Quantum Anomalous Hall Effect, Domain Walls, and Disorder in Bilayer Graphene

Fabian R. Geisenhof

München 2022

Quantum Anomalous Hall Effect, Domain Walls, and Disorder in Bilayer Graphene

Fabian R. Geisenhof

Dissertation
durchgeführt an der Fakultät für Physik
der Ludwig-Maximilians-Universität
München

vorgelegt von
Fabian R. Geisenhof
aus Marktoberdorf

München, den 14.10.2022

Erstgutachter: Prof. Dr. Thomas Weitz
Zweitgutachter: Prof. Dr. Alexander Högele
Tag der mündlichen Prüfung: 06.12.2022

Zusammenfassung

Seit seiner Entdeckung im Jahr 2004 ist das zweidimensionale Material Graphen Gegenstand vieler theoretischer sowie experimenteller Studien, wobei außergewöhnliche mechanische und elektrische Eigenschaften entdeckt wurden. Im Vergleich zur Monolage zeichnet sich Bilagen Graphen durch ähnlich herausragende Qualitäten aus, besitzt dabei aber noch größere Vielseitigkeit, beispielsweise durch eine variierbare Bandlücke. Zudem ist Bilagen Graphen, auf Grund seiner unter gewissen Umständen nicht verschwindenden Zustandsdichte bei Ladungsneutralität, besonders anfällig für korrelierte Zustände. Diese treten durch Elektron-Elektron Wechselwirkungen auf, wobei bestimmte Symmetrien des Systems gebrochen werden und sich das Energiespektrum verändert. Theoretische Studien nennen beispielsweise fünf verwandte Quanten-Hall-Zustände, die durch Brechung der chiralen Symmetrie entstehen können und bei Ladungsneutralität miteinander konkurrieren. Obwohl nach und nach einige dieser Zustände durch die immer besser werdende Qualität der Proben experimentell bestätigt werden konnten, gibt es diesbezüglich noch viele offene Fragestellungen. Insbesondere konnte einer dieser Quanten-Hall-Zustände, die exotische „ALL“-Phase, welche eine teilweise Polarisierung der zum Transport beitragenden Ladungsträger in eine der Graphenlagen und ein orbitales magnetischen Moment aufweist, bisher noch nicht eindeutig beobachtet werden. Des Weiteren ist bisher noch weitestgehend unklar, welche der fünf Quanten-Hall-Phasen der eigentliche Grundzustand von Bilagen Graphen ist, da die bis zum jetzigen Zeitpunkt veröffentlichten Studien keine eindeutigen experimentellen Beobachtungen liefern. Neben dem Auftreten von konkurrierenden Quanten-Hall-Zuständen könnte die Existenz von Fehlern in der Stapelfolge der zwei Graphenlagen eine mögliche Erklärung für die unterschiedlichen Signaturen in Quantentransportmessungen sein. Die Detektion dieser Kristallfehler wurde erst vor Kurzem durch präzise Techniken, wie beispielsweise optische Rasternahfeldmikroskopie, ermöglicht. Obwohl schon eindrucksvoll quantisierter Ladungstransport entlang solcher Kristallfehler im Experiment gezeigt wurde, bleibt ihr Einfluss auf die bei Ladungsneutralität auftretenden Quanten-Hall-Zustände weitestgehend unerforscht.

Um die aufgeführten Fragestellungen genauer zu untersuchen, werden in dieser Arbeit Quantentransportmessungen in Bilagen Graphen bei niedrigen Temperaturen präsentiert. Diese wurden an Feldeffekttransistoren, bestehend aus ultrareinem, freischwebenden Bilagen Graphen, dessen elektrische Eigenschaften durch zwei Gate-Elektroden manipulierbar sind, durchgeführt. Besonderes Augenmerk wurde dabei auf die Existenz von Fehlern in der Stapelfolge innerhalb der untersuchten Graphen Flocken gelegt. Sind diese nicht vorhanden, konnte die exotische „ALL“-

Phase bei niedrigen Magnetfeldern beobachtet werden, wobei der Zustand in achtfacher Ausführung in Form eines anomalen Quanten-Hall-Effekts mit einer Leitfähigkeit von $\pm 2\, e^2\, h^{-1}$ (e ist dabei die Elementarladung und h das Plancksche Wirkungsquantum) auftritt. Die Entdeckung stellt einen überzeugenden Nachweis für orbitalen Magnetismus in Bilagen Graphen dar und verdeutlicht, dass das vermeintlich triviale System einen anomalen Quanten-Hall-Effekt aufweist, ohne dass die Realisierung eines fragilen Moiré-Gitters notwendig ist. Außerdem wurde der Quantentransport entlang Fehlern in der Stapelfolge von Bilagen Graphen untersucht. Dabei wurde ein komplexes Zusammenspiel zwischen topologisch geschütztem Quantentransport entlang eines Kristallfehlers und Quantentransport in Randkanälen, induziert durch den Quanten-Hall-Effekt, entdeckt. Die Messungen zeigen den maßgeblichen Einfluss der häufig vorkommenden Kristallfehler und verdeutlichen, wie wichtig es ist, diesen in zukünftigen Studien zu beachten. Zuletzt wurden die Auswirkungen von Unordnung sowie Fehlern in der Stapelfolge auf den Grundzustand und auf verschiedene Phasenübergänge zwischen Zuständen mit gebrochener Symmetrie in Bilagen Graphen untersucht. Die Ergebnisse helfen schwer erklärbare Signaturen in Quantentransport-messungen aus der Literatur zu verstehen und tragen somit zur eindeutigen Identifikation des Grundzustands von Bilagen Graphen bei. Durch die hier präsentierten Ergebnisse wurden bedeutende Fortschritte im Verständnis komplexer physikalischer Phänomene in Bilagen Graphen erzielt, was zudem die Wichtigkeit weiterer experimenteller Studien an dem Material verdeutlicht.

Abstract

Since the discovery of graphene in 2004, the two-dimensional material has been subject of extensive theoretical and experimental research revealing exceptional electronic and mechanical properties. Bilayer graphene, while inheriting most advantages of its monolayer counterpart, provides even more tunability, e.g. due to its tunable band gap. Moreover, as consequence of the non-vanishing density of states near charge neutrality under certain circumstances, bilayer graphene is susceptible to exotic interaction-driven broken-symmetry states that modify the energetic spectrum. For example, theoretical studies propose the emergence of a family of five competing quantum Hall states at charge neutrality owing to chiral symmetry breaking. Although some of the phases have already been observed experimentally with an increasing level of device quality, bilayer graphene retains many related unanswered questions. For instance, the exotic ALL phase, a quantum anomalous Hall phase with partial layer polarization and substantial orbital moment, has not been pinpointed clearly. Moreover, it is still under debate which of the five broken-symmetry phases is the true ground state, as ambiguous experimental results have been reported from literature. Besides the emergence of competing phases, a possible cause for distinct signatures in quantum transport measurements could be the influence of stacking domain walls in bilayer graphene. Their detection has only become possible recently using precise scanning techniques such as scattering-type scanning near-field optical microscopy. Although quantum transport along such dislocations has been shown, their impact on broken-symmetry states emerging within the zero energy Landau level remains unclear.

To shed light on these unexplored aspects, low-temperature transport measurements on high-quality dually gated freestanding bilayer graphene are presented in this thesis, with special attention given to any stacking domain walls present within the bilayer graphene flakes. In their absence, the exotic ALL phase, appearing as an octet of quantum anomalous Hall phases with a conductance of $\pm 2\ e^2\ h^{-1}$ (where e is the electronic charge and h is Planck's constant), was tracked to low magnetic fields, providing compelling evidence for orbital magnetism in bilayer graphene. The findings demonstrate that the seemingly simple Bernal-stacked bilayer graphene exhibits the quantum anomalous Hall effect without the need of fabricating delicate moiré heterostructures. In addition, the quantum transport along stacking domain walls was investigated revealing an intriguing interplay between topological valley and quantum Hall edge transport. The measurements highlight the influence of the commonly occurring stacking domain walls and demonstrate that their impact inevitably needs to be regarded in future experiments. Lastly, the role of disorder and stacking domain walls on the emergence of the spontaneously gapped ground state and various phase

transitions between broken-symmetry states was examined. The results contribute to solving the debate about the ground state of bilayer graphene and help to explain related ambiguous observations in literature. All in all, the presented measurements provide major advances in understanding the complex physical phenomena in the seemingly trivial Bernal-stacked bilayer graphene and highlight the importance of continuous experimental effort.

Table of Contents

1 Introduction

Although subject of theoretical calculations already in 1947[1], two-dimensional (2D) materials were long presumed to not exist freely in nature[2]. Hence, the first isolation and examination of graphene, a single two-dimensional layer of carbon atoms arranged in a hexagonal lattice, by K.S. Novoselov and A.K. Geim in 2004 was even more a surprise[3]. Rapidly, graphene gained more and more interest owing to its exceptional electronic[4] and mechanical properties[5]. This development was further fostered by its accessibility for experimental physics owing to the simple fabrication procedure using mechanical exfoliation[3] as well as uncomplicated identification with conventional optical microscopy[6]. Its discovery not only demonstrated that 2D crystals can naturally occur but in fact initiated the exploration of a whole family of 2D materials[7,8]. In less than two decades, a growing diversity of materials and their respective characteristics have been revealed, ranging from exceptional insulators such as hexagonal boron nitride[9,10], to molybdenum disulfide, a semiconductors with a sizeable band gap[11] as well as extraordinary electrical properties[12], and tungsten ditelluride, a material with superconducting[13] and topological insulating behavior[14]. The key for their in-plane stability are strong covalent bonds, however, weak van der Waals forces play a crucial role in holding several layers vertically together[7]. It took not long to discover a technique of reliably stacking 2D materials[15–18] analogous to Lego blocks[7]. This recently developed method represents a further step towards creating devices with atomic precision. Especially for electronic and optoelectronic applications, the possibility of combining the properties of individually stacked 2D materials into heterostructures provides a new level of freedom to material engineering and device design[8].

Despite these major advances and the almost unlimited possibilities arising from the diversity of 2D materials, graphene-based systems have always been in the forefront in fundamental research because of their exceptional physical properties. For instance, a monolayer of graphene provides unexcelled electrical[19,20] as well as thermal conductivity[21], shows extraordinary mechanical robustness[5] and has the ability to sustain extremely high current densities[22]. Adding an additional layer yields the simplest van der Waals structure, bilayer graphene, which inherits most of these advantages[23] but provides even more tunability[3,24,25]. In contrast to the monolayer with its linear dispersion at low energies[4], bilayer graphene exhibits non-linear touching bands with massive chiral quasiparticles[23] and the possibility of opening a tunable band gap via gating[25,26]. Moreover, the stacking order of the two graphene layers provides yet another parameter to manipulate the

electronic properties. Recent advances[27,28] demonstrated this by assembling two graphene sheets, twisted by an angle of about 1.1 degree. As a result, flat bands arise in these delicate structures, which foster the emergence of exotic correlated states including superconductivity[28] and orbital ferromagnetism[29,30]. However, even the naturally occurring Bernal-stacked bilayer graphene can be a playground for correlated physics. In fact, bilayer graphene has been predicted to be susceptible to a wide range of correlated states that spontaneously break one or more symmetries of the system[31–34]. Indeed, by increasing the level of cleanliness and quality of bilayer graphene flakes[19,22,35], numerous studies have revealed broken-symmetry states[36–41] arising from many-body interactions. Although bilayer graphene has been subject of extensive research for more than a decade, it has retained many unanswered questions. For instance, at charge neutrality, where electron-electron interactions are especially strong[42], a family of five competing quantum Hall states caused by chiral symmetry breaking has been predicted[32,33]. Despite the fact that each of the states possesses unique properties[33], their identification by examining the resulting signatures in quantum transport remains challenging. So far, evidence of some of the phases has been observed experimentally, including the quantum valley Hall[39,41], the layer antiferromagnetic[40,43] as well as the quantum anomalous Hall phase[35,44]. Yet, the most exotic out of the five states, the so-called ALL phase, exhibiting substantial charge, spin and valley Hall conductivities of 2 $e^2\ h^{-1}$ as well as a net layer polarization and orbital moment[33], has not been pinpointed clearly. So far, it is unclear if it truly survives to zero magnetic field, which is especially interesting for a state exhibiting a quantum anomalous Hall effect, as its persistence would provide quantized resistance in the absence of any external magnetic field[45]. Moreover, it is still under debate which of the five broken-symmetry phases is the true ground state since ambiguous experimental results are reported in literature. Observations range from a vanishing[36–41] to a finite conductance[36,46] at charge neutrality and zero external electric as well as magnetic fields. In addition, it is unclear, if intrinsic effects such as disorder can mask the ground state or, alternatively, drive the system into another phase[47]. In this matter, a rather unexplored aspect is the influence of stacking domain walls, which are one-dimensional lattice dislocations separating regions of AB and BA stacking in bilayer graphene[48,49]. They alter the quantum transport drastically, as topological valley transport can occur along such dislocations[50–53], even though the bulk of the bilayer is gapped. Easily, they could be one of the major causes[54] for discrepancies in experimental reports about quantum transport in bilayer graphene. Moreover, their impact on the behavior of broken-symmetry quantum Hall states emerging within the zero energy Landau levels is unknown. The main reason for their disregard is their challenging detection, which has only recently been possible with the help of precise scanning techniques[48,50]. For instance, scattering-type scanning near-field optical microscopy[55] offers a versatile and non-destructive way of detecting and locating these stacking domain walls[50,56,57]. Combining this additional pre-characterization technique with devices of extraordinary quality allows for the observation of correlated physics and the role of stacking domain walls in bilayer graphene.

To pursue these open questions, low-temperature transport measurements on high-quality dually gated freestanding bilayer graphene are presented within this thesis. Freestanding devices were chosen since they excel in offering excellent quality and provide a low dielectric environment for unimpeded electron-electron interactions. Moreover, special attention was given to any stacking domain walls present within the bilayer graphene flakes. To this end, scattering-type scanning near-field optical microscopy was used as additional characterization technique. Three different topics were investigated: First, in the absence of any stacking domain walls, the ALL phase, one of the five competing quantum Hall states, has been tracked for the first time to vanishing magnetic field. Appearing as an octet of quantum anomalous Hall phases, it provides compelling evidence of orbital magnetism in bilayer graphene. Second, quantum transport along stacking domain walls was examined in the presence of broken-symmetry states within the zero energy Landau level. An intriguing interplay between topological valley and quantum Hall edge transport was observed. Lastly, the role of disorder and stacking domain walls on broken-symmetry states in bilayer graphene was studied and compared in several devices. The suppression of the insulating layer antiferromagnetic ground state could be correlated to broad phase transitions between different broken-symmetry states. Hereby, electric field disorder inducing the spontaneous formation of domains within the device were determined as common cause.
All in all, the presented investigations led to the experimental revelation of the most exotic of the five predicted competing quantum Hall phases at charge neutrality and to major advances in understanding the role of stacking domain walls and disorder in the presence of broken-symmetry states. Although in recent years, the attention has moved towards twisted bilayer graphene[27,28], the observations unambiguously proof that the naturally occurring Bernal-stacked bilayer retains many unexplored and intriguing physical phenomena. Very recent studies even revealed superconductivity[58] and new strongly correlated phases[58–60] in Bernal-stacked bilayer graphene at high electric fields, further highlighting that the material is worth to be subject of continuous experimental effort.

The outline of the cumulative thesis is as follows: In Chapter 2, the theoretical background is presented. After outlining the basic electronic properties of both mono- and bilayer graphene, the quantum Hall effect in general and its characteristics in bilayer graphene are explained. Special attention is laid on the competing ground phases and the role of electron-electron interactions in the quantum Hall regime. Moreover, stacking domain walls and their impact on the electronic band structure of bilayer graphene are explained. In the last two sections, the general concepts of near-field optical microscopy and dually gated field effect transistors are given. In Chapter 3, the experimental methods to fabricate and characterize dually gated freestanding bilayer graphene devices are illustrated in sequential order. This includes the description of exfoliating and preselecting suitable flakes as well as the investigation with near-field optical microscopy.

Furthermore, the actual fabrication techniques and the electrical measurement setup as well as the routine of device calibration are illustrated. Then, Chapter 4 summarizes the experimental findings about the quantum anomalous Hall effect in bilayer graphene. In Appendix A.1 the corresponding publications is attached in full. Chapter 5 is dedicated to the investigations on domain walls in bilayer graphene and their impact on the quantum transport. Appendix A.2 and B.1 show the related publication and supplementary information, respectively. Chapter 6 discusses the observations made about the role of electric field disorder on the ground state and on phase transitions between different broken-symmetry states in bilayer graphene. Here, the corresponding publication and supplementary information are given in Appendix A.3 and B.2, respectively. Lastly, Chapter 7 concludes the thesis with a summary as well as a short outlook.

2 Theoretical Fundamentals

In this chapter, the theoretical fundamentals of this thesis are discussed. First, an introduction to 2D materials and in particular to mono- and bilayer graphene is given. In the second part, the Hall effect as well as its appearance in bilayer graphene is explained. Thirdly, the influence of electron-electron interactions on quantum transport and the resulting emergence of broken-symmetry states in bilayer graphene is described. In the fourth section, domain walls and their impact on the electronic structure are discussed. Then, the principles of near-field microscopy and the underlying physical mechanisms are briefly explained. The last section gives a short overview of the basic functionality of a dually gated graphene field-effect transistor.

2.1 Two-Dimensional Materials

In the last decades, the family of 2D materials has both grown in variety and versatility, since more and more two-dimensional systems[7] as well as new astonishing properties[7,12,14,26,61] have been revealed. Although the research field has extended far beyond simple carbon-based materials[7], graphene, since its first isolation and identification in 2004[3], has always been on the front line owing to its exceptionally good mechanical[5] and electronic[19,20] characteristics. Stacking multiple layers of graphene adds even more complexity, e.g. due to a tunable band structure[26] and the emergence of strongly correlated states caused by an enhancement of electron-electron interactions[27,28,32,36,38,39,62]. In the following, the crystal structure as well as the electronic structure of mono- and bilayer graphene are discussed.

2.1.1 Monolayer Graphene

Graphene consists of carbon atoms arranged in a hexagonal crystal lattice, which form a two-dimensional layer[4,63] (see Figure 2.1a). The structure is a result from the sp^2 – hybridization of one s and two p orbitals forming strong covalent σ – bonds between neighboring carbon atoms[4,63]. These in-plane bonds are responsible for the exceptional mechanical robustness of the crystalline structure[4]. The remaining p_z orbital, which is perpendicular to the graphene plane, forms π – bonds with neighboring atoms[4]. These bonds give rise to a delocalized π – electronic system, which dictates the electronic properties of graphene.

The hexagonal structure of graphene can be treated as a triangular lattice with a basis of two atoms

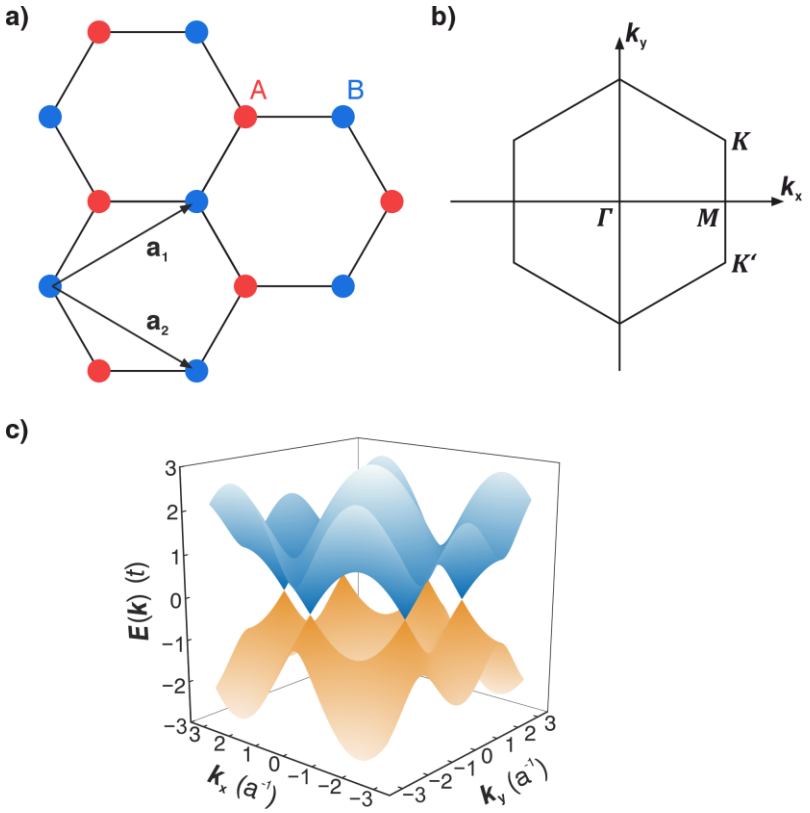

Figure 2.1 Crystal and band structure of monolayer graphene. a) *The hexagonal lattice of graphene with two atoms per unit cell. Atoms corresponding to sublattice A (B) are shown in red (blue). The unit cell vectors a_1 and a_2 are illustrated by arrows. [Figure adapted from Ref.[4]].* ***b)*** *First Brillouin zone of graphene with high-symmetry points $\boldsymbol{K}$ and $\boldsymbol{K}'$ as well as other important points $\boldsymbol{\Gamma}$ and $\boldsymbol{M}$ highlighted. [Figure adapted from Ref.[4]].* ***c)*** *Band structure of graphene calculated using a tight-binding approach. The energy is shown in units of the nearest neighbor hopping energy t, and the momentum vectors $\boldsymbol{k}_x$ and $\boldsymbol{k}_y$ in units of the inverse lattice constant a. At the $\boldsymbol{K}$ and $\boldsymbol{K}'$ points, the conduction (blue) and valence band (orange) touch and the dispersion is linear.*

per unit cell[63], resulting in two distinct sublattices A and B. The corresponding lattice vectors are given by

$$\boldsymbol{a_1} = \frac{a}{2}(3, \sqrt{3}), \qquad \boldsymbol{a_2} = \frac{a}{2}(3, -\sqrt{3}) \tag{2.1}$$

with $a \approx 1.42$ Å being the carbon-carbon distance[63]. The related reciprocal lattice is also triangular[63]. The first Brillouin zone is illustrated in Figure 2.1b. Of peculiar relevance for low-energy physics in graphene are the two inequivalent high-symmetry points $\boldsymbol{K}$ and $\boldsymbol{K}'$ at the positions

$$\boldsymbol{K} = \left(\frac{2\pi}{3a}, \frac{2\pi}{3\sqrt{3}a}\right), \qquad \boldsymbol{K}' = \left(\frac{2\pi}{3a}, -\frac{2\pi}{3\sqrt{3}a}\right) \tag{2.2}$$

in momentum space[4,63].

Using a tight-binding approach and considering only nearest- and next-nearest-neighbor hopping,

the Hamiltonian takes the following form[4]

$$H = -t \sum_{\langle i,j\rangle,\sigma} \left(a^{\dagger}_{\sigma,i} b_{\sigma,j} + H.c.\right) - t' \sum_{\langle i,j\rangle,\sigma} \left(a^{\dagger}_{\sigma,i} a_{\sigma,j} + b^{\dagger}_{\sigma,i} b_{\sigma,j} + H.c.\right), \tag{2.3}$$

where $a_{\sigma,i}$ ($b_{\sigma,i}$) annihilates and $a^{\dagger}_{\sigma,i}$ ($b^{\dagger}_{\sigma,i}$) creates an electron with spin $\sigma = \uparrow, \downarrow$ on site R_i on sublattice A (B). Moreover, t and t' represent the nearest and next-nearest neighbor hopping energies, respectively. The energy bands derived from the Hamiltonian are given by[4]

$$E_{\pm}(\boldsymbol{k}) = \pm t\sqrt{3 + f(\boldsymbol{k})} - t' f(\boldsymbol{k}), \tag{2.4}$$

with

$$f(\boldsymbol{k}) = 2\cos\left(\sqrt{3} k_y a\right) + 4\cos\left(\frac{\sqrt{3}}{2} k_y a\right)\cos\left(\frac{3}{2} k_x a\right), \tag{2.5}$$

where $\pm$ denotes the conduction and valence band, respectively. The full band structure is shown in Figure 2.1c. Overall, it consists of two cosine-like energy bands, each can be attributed to one of the sublattices[2,64]. The two energy bands intersect at the high-symmetry points $\boldsymbol{K}$ and $\boldsymbol{K}'$, resulting in a gapless dispersion. At the touching point of the conduction and valence band, electronic states are a superposition of states of the two different sublattices[2]. The sublattice can be viewed as an additional degree of freedom, called pseudospin[2,23], analogous to spin but with up/down referring to sublattice A/B. By expanding the Hamiltonian Eq. (2.3) close to the high-symmetry position $\boldsymbol{K}$, i.e. $\boldsymbol{k} = \boldsymbol{K} + \boldsymbol{q}$ with $|\boldsymbol{q}| \ll |\boldsymbol{K}|$, it takes the form[4,63]

$$H_{\boldsymbol{K}} = \hbar v_F \begin{pmatrix} 0 & (q_x - i q_y) \\ (q_x + i q_y) & 0 \end{pmatrix}, \tag{2.6}$$

with $\boldsymbol{q} = (q_x, q_y)$ being the momentum relatively to the $\boldsymbol{K}$ point and $v_F = 3ta/2$ the Fermi velocity. Then, the energy eigenvalues result in a conical band structure [4,63,65]

$$E_{\pm}(\boldsymbol{q}) \approx \pm \hbar v_F |\boldsymbol{q}|. \tag{2.7}$$

Rewriting the Hamiltonian near the $\boldsymbol{K}$ point using the Pauli vector $\boldsymbol{\sigma} = (\sigma_x, \sigma_y)$ with the Pauli matrices $\sigma_x = \begin{pmatrix} 0 & 1 \\ 1 & 0 \end{pmatrix}$ and $\sigma_y = \begin{pmatrix} 0 & -i \\ i & 0 \end{pmatrix}$ as well as the replacements $q_x \to -i\frac{\partial}{\partial x}$ and $q_y \to -i\frac{\partial}{\partial y}$ gives[4,63]

$$H_{\boldsymbol{K}} = -i\hbar v_F \boldsymbol{\sigma} \cdot \boldsymbol{\nabla}. \tag{2.8}$$

Correspondingly, the result yields the transposed Hamiltonian $H_{\boldsymbol{K}'} = {H_{\boldsymbol{K}}}^{T}$ for quasiparticles near the $\boldsymbol{K}'$ point[63]. Most strikingly, the Hamiltonian is analogous for massless Dirac fermions in two dimensions, with the speed of light replaced by v_F[4,63]. Therefore, $\boldsymbol{K}$ and $\boldsymbol{K}'$ are called Dirac points or valleys. Lastly, the eigenfunctions of Eq. (2.8) can be derived:

$$\psi_{\pm,\boldsymbol{K}}(\boldsymbol{k}) = \frac{1}{\sqrt{2}} \begin{pmatrix} e^{-\frac{i\theta_{\boldsymbol{k}}}{2}} \\ \pm e^{\frac{i\theta_{\boldsymbol{k}}}{2}} \end{pmatrix}, \psi_{\pm,\boldsymbol{K}'}(\boldsymbol{k}) = \frac{1}{\sqrt{2}} \begin{pmatrix} e^{\frac{i\theta_{\boldsymbol{k}}}{2}} \\ \pm e^{-\frac{i\theta_{\boldsymbol{k}}}{2}} \end{pmatrix}, \tag{2.9}$$

with the polar angle in momentum space $\theta_{\boldsymbol{k}} = \arctan\binom{k_x}{k_y}$, and $\pm$ denoting the conduction and valence band, respectively.

The quasiparticles in graphene have several interesting characteristics worth noting. Quasiparticles in the inequivalent $\boldsymbol{K}$ and $\boldsymbol{K}'$ valleys are described by distinct Hamiltonians and wavefunctions. However, they are closely related by time-reversal symmetry[4]. In pristine graphene the two valleys are decoupled[63], i.e. scattering between them is weak. This can be accounted for by adding a valley degeneracy of two[65]. However, introducing valley scattering can lift this degeneracy.

Another interesting property of graphene results from the unique band structure and the interconnection between electron and holes: For every electron state with energy $+E$ and momentum $\boldsymbol{q}$ there exists a hole state with energy $-E$ and momentum $-\boldsymbol{q}$ within the same energy branch (i.e. sublattice)[2,64]. In other words, the two quasiparticles share the same pseudospin but move in opposite direction, i.e. the projection of the pseudospin on the direction of movement is always positive for electrons and negative for holes[64]. This characteristic is called chiral, and the symmetry between electron and holes is called chiral symmetry. Mathematically, chiral symmetry can be described as follows[66]: When $\psi(\boldsymbol{k})$ is an eigenstate of the Hamiltonian $H_{\boldsymbol{K}}$ with eigenenergy E and $H_{\boldsymbol{K}}$ commutes with the Pauli matrix $\sigma_z = \begin{pmatrix} 1 & 0 \\ 0 & -1 \end{pmatrix}$, i.e. $[H_{\boldsymbol{K}}, \sigma_z] = 0$, then

$$H_{\boldsymbol{K}}\sigma_z\psi(\boldsymbol{k}) = -\sigma_z H_{\boldsymbol{K}}\psi(\boldsymbol{k}) = -\sigma_z E\psi(\boldsymbol{k}) = -E\sigma_z\psi(\boldsymbol{k}) \,, \qquad (2.10)$$

that means there exists an eigenstate $\sigma_z\psi(\boldsymbol{k})$ of $H_{\boldsymbol{K}}$ with eigenenergy $-E$.

Moreover, the nature of the band structure of graphene causes the following: In case a quasiparticle moves along a closed orbit around $\boldsymbol{K}$, which corresponds to a rotation of $\theta_{\boldsymbol{k}}$ by 2π, the wave function changes sign, see Eq. (2.9). In other words, the quasiparticles acquire a phase of π[4,24,63], called Berry's phase. It is opposite for electron and holes as well as for the $\boldsymbol{K}$ and $\boldsymbol{K}'$ valley[33]. Often Berry's phase is referred to the integral over the Berry curvature[67]. Put simply, the Berry curvature can be seen as in-built magnetic field, and Berry's phase as the phase a charge particles acquires when encircling a magnetic flux with a closed loop in this field[67]. Overall, when considering the sum of the Berry curvature over all bands, it is zero. The quantity becomes relevant for example in case an external magnetic field is applied and the charge carriers move in cyclotron orbits, altering the appearance of the quantum Hall effect in graphene compared to conventional two-dimensional systems without Berry's phase[24].

2.1.2 Bilayer Graphene

Bilayer graphene consists of two monolayers on top of each other coupled by weak van der Waals forces[4]. The energetically most stable configuration of the two layers is AB – or Bernal stacking order[4,63], where the top layer is shifted by the carbon-carbon distance a in a way that one of its atoms sits directly in the middle of the honeycomb of the underlying layer (see Figure 2.2a).

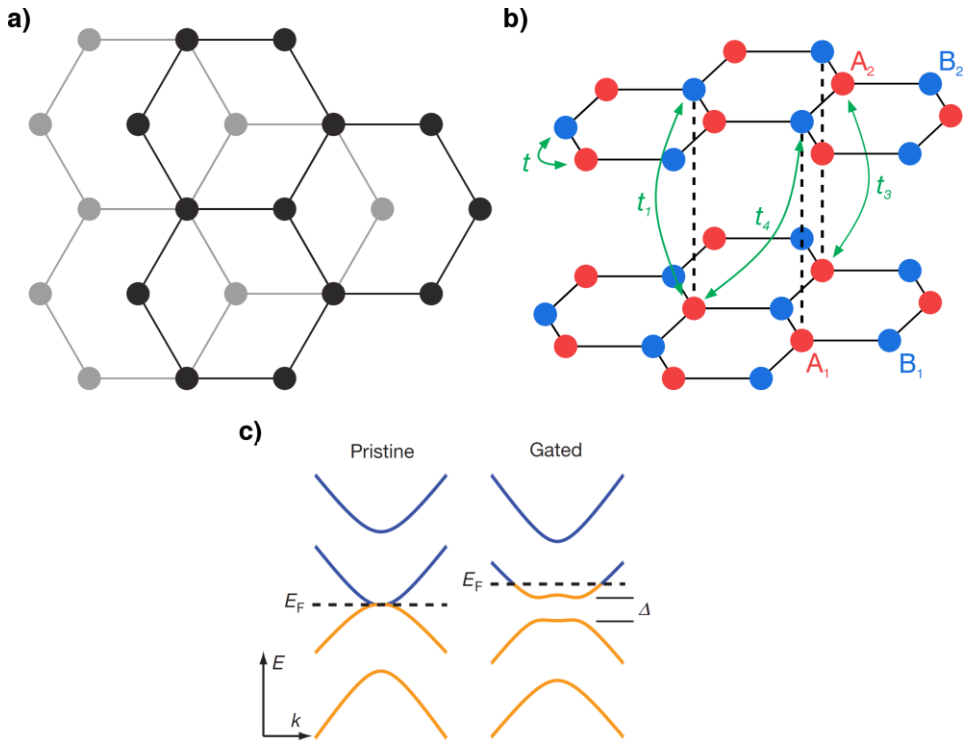

Figure 2.2 Crystal and band structure of bilayer graphene. a) *Top view of the crystal structure of Bernal-stacked bilayer graphene. The upper layer (black) is shifted relatively to the lower layer (grey). [Figure adapted from Ref.[23]].* ***b)*** *Side view of Bernal-stacked bilayer graphene with the most important hopping parameters indicated in green. The sublattices A_1 (A_2) and B_1 (B_2) correspond to the bottom (top) layer. [Figure adapted from Ref.[23]].* ***c)*** *Schematic band structure of bilayer graphene without (left) and with a gate voltage applied (right). E_F and Δ label the Fermi energy and the non-zero band gap, respectively. [Figure taken from Ref.[26]].*

In order to derive the band structure of bilayer graphene using a tight-binding approach hopping between the two layers needs to be considered[4]. In Figure 2.2b, the most important hopping parameters are schematically shown. Here, t is the intralayer hopping energy, t_1 describes interlayer hopping between atoms sitting directly on top of each other, whereas t_3 and t_4 connect the same (e.g. A_1 to A_2) or distinct (e.g. A_1 to B_2) sublattices in different layers[4]. The Hamiltonian can be written as[4]

$$H = -t \sum_{\langle i,j\rangle,m,\sigma} \left(a^{\dagger}_{m,i,\sigma} b_{m,j,\sigma} + H.c.\right) - t_1 \sum_{j,\sigma} \left(a^{\dagger}_{1,j,\sigma} a_{2,j,\sigma} + H.c.\right)$$
$$-t_4 \sum_{j,\sigma} \left(a^{\dagger}_{1,j,\sigma} b_{2,j,\sigma} + a^{\dagger}_{2,j,\sigma} b_{1,j,\sigma} + H.c.\right) - t_3 \sum_{j,\sigma} \left(b^{\dagger}_{1,j,\sigma} b_{2,j,\sigma} + H.c.\right), \qquad (2.11)$$

where $a_{m,i,\sigma}$ ($b_{m,i,\sigma}$) annihilates and $a^{\dagger}_{m,i,\sigma}$ ($b^{\dagger}_{m,i,\sigma}$) creates an electron with spin $\sigma = \uparrow, \downarrow$ on site R_i, in layer $m = 1, 2$ and sublattice A (B). Notably, the interlayer hopping terms t_3 and t_4 are only relevant under certain circumstances (e.g. when interaction effects are weak). In this special case,

t_3 can for example lead to a more complex band structure[4,68]. The effect is called trigonal warping and was experimentally observed in recent studies[58–60]. However, when interaction effects are dominant[33], the approximation of considering only t and t_1 leads already to qualitatively good results[63]. The observations made in the course of this thesis are in particular well explained by this assumption and therefore it is used in the following.

The wave function describing bilayer graphene is a four-component spinor[4], accounting for the inequivalent sublattices A and B in layer $m = 1, 2$. Calculating the eigenvalue yields four energy bands[23], however, two bands are gapped by $2|t_1|$ (with $t_1 \approx 0.4\,eV$[63]) and are consequently irrelevant for low-energy physics[63]. Focusing only on the low-energy bands, an effective Hamiltonian for bilayer graphene can be derived near the $\boldsymbol{K}$ point[63], analogously to Eq. (2.6) for monolayer graphene:

$$H_{\boldsymbol{K}} = \frac{\hbar^2}{2m^*}\begin{pmatrix} V/2 & (q_x - iq_y)^2 \\ (q_x + iq_y)^2 & -V/2 \end{pmatrix}, \tag{2.12}$$

with the effective mass $m^* = t_1/(2{v_F}^2)$. Here, an interlayer bias V causing a shift in the electrochemical potential between the two layers has been accounted for by adding a term $V/2\,\boldsymbol{\sigma}_z$ to the Hamiltonian[4,65]. In case of $V = 0$, the dispersion relation near the $\boldsymbol{K}$ and $\boldsymbol{K}'$ points[63] is given by:

$$E_{\pm}(\boldsymbol{q}) \approx \pm {v_F}^2 \frac{\boldsymbol{q}^2}{t_1} = \pm \frac{\hbar^2 \boldsymbol{q}^2}{2m^*}. \tag{2.13}$$

Notably, when ignoring the interlayer hopping terms t_3 and t_4, Bernal-stacked bilayer graphene exhibits parabolic bands touching at the Dirac points (see Figure 2.2c) with massive charge carriers. Using the Pauli matrices and the same transformations as for monolayer graphene, the Hamiltonian can be rewritten as[23,24,33]

$$H_{\boldsymbol{K}} = -\frac{\boldsymbol{p}^2}{2m^*}[\sigma_x \cdot \cos(2\theta) + \sigma_y \cdot \cos(2\theta)] = -\frac{\boldsymbol{p}^2}{2m^*}\boldsymbol{\sigma} \cdot \boldsymbol{n}(\theta)\,, \tag{2.14}$$

with $\boldsymbol{p} = \hbar\boldsymbol{q}$ and $\boldsymbol{n}(\theta) = (\cos(2\theta), \sin(2\theta))$. The eigenstates are given by[63]

$$\psi_{\pm,\boldsymbol{K}}(\boldsymbol{k}) = \frac{1}{\sqrt{2}}\begin{pmatrix} e^{-i\theta_{\boldsymbol{k}}} \\ \pm e^{i\theta_{\boldsymbol{k}}} \end{pmatrix}, \psi_{\pm,\boldsymbol{K}'}(\boldsymbol{k}) = \frac{1}{\sqrt{2}}\begin{pmatrix} e^{i\theta_{\boldsymbol{k}}} \\ \pm e^{-i\theta_{\boldsymbol{k}}} \end{pmatrix}, \tag{2.15}$$

describing also chiral quasiparticles but with a Berry's phase of $\pm 2\pi$ instead of $\pm\pi$[24,65].

The shape of the band structure of bilayer can, however, be altered by breaking the equivalence of the two layers, i.e. the inversion symmetry[4]. For example, by applying an electric field perpendicular to the graphene plane[65], i.e. $V \neq 0$, a gap opens in the energy spectrum[63], since the dispersion of the low-energy bands in the vicinity of the $\boldsymbol{K}$ and $\boldsymbol{K}'$ points changes to[4,63]

$$E_{\pm}(\boldsymbol{q}) \approx \pm\left(\frac{V}{2} - \frac{V\hbar^2 {v_F}^2}{{t_1}^2}\boldsymbol{q}^2 + \frac{\hbar^4 {v_F}^4}{{t_1}^2 V}\boldsymbol{q}^4\right), \tag{2.16}$$

assuming $\hbar v_F q \ll V \ll |t_1|$. The resulting dispersion has a minimum at $q = V/(\sqrt{2}\hbar v_F)$ with a band

gap tunable by the interlayer bias[4,63]. Experimentally, an electric field can be implemented by applying a gate voltage, however, this causes not only the opening of a band gap but also shifts the Fermi level[26] (see Figure 2.2c). To disentangle both mechanisms, a dually gated device is needed (see Section 2.7).

2.2 Quantum Hall Effect

In 1980, Klaus v. Klitzing discovered that the Hall effect shows precisely quantized Hall resistance in case the electrons are confined in a two-dimensional system and strong magnetic fields are applied perpendicular to it at low temperatures[69]. Surprisingly, the so-called quantum Hall effect is solely dependent on fundamental physical constants and independent of irregularities within the material. Besides its emergence in two-dimensional electron gases in conventional semiconductors, the discovery of two-dimensional materials revealed a new versatile platform to study quantum Hall physics[70]. In the following, the classical Hall effect is briefly outlined. Then the quantum Hall effect in general and its occurrence in bilayer graphene are discussed to lay a basis for the observations made in the magnetotransport measurements.

2.2.1 Classical and Quantum Hall Effect

In case an electron current I_e flows through a conductor with a magnetic field B perpendicular to it (see Figure 2.3a), the charge carriers are deflected by the Lorentz force[71]. A voltage across the conductor builds up until an equilibrium is reached, i.e. when the Lorentz force is exactly compensated[71].

Assuming a constant drift velocity of the electrons along the x – and no current flow in z – direction, the longitudinal σ_{xx} and transversal conductivity σ_{xy} are given by[71]

$$\sigma_{xx} = \frac{n_{3D}e}{B}\frac{\tau eB/m^*}{1+\tau^2(eB/m^*)^2} \qquad (2.17)$$

and

$$\sigma_{xy} = -\frac{n_{3D}e}{B_z}\frac{\tau^2(eB/m^*)^2}{1+\tau^2(eB/m^*)^2}, \qquad (2.18)$$

where n_{3D} is the number of charge carriers per volume, m^* the effective mass and τ the relaxation time, i.e. the mean free time between two scattering events of the charge carrier[71]. Using the relation between conductivity and resistivity tensors $\sigma_{xx} = \rho_{xx}/({\rho_{xx}}^2 + {\rho_{xy}}^2)$ and $\sigma_{xy} = \rho_{xy}/({\rho_{xx}}^2 + {\rho_{xy}}^2)$ results in[71]

$$\rho_{xx} = \frac{m^*}{n_{3D}e^2\tau} \qquad (2.19)$$

and

$$\rho_{xy} = \frac{B}{n_{3D} e}, \qquad (2.20)$$

for the longitudinal ρ_{xx} and transversal resistivity ρ_{xy}. Most importantly, the former depends only on intrinsic properties of the material, whereas the latter is linearly dependent on the magnetic field.

The charge transport signatures change drastically in case the charge carriers are localized into a 2D system at low temperatures and high magnetic fields[71]. When they can freely travel in for example the xy – plane but are confined in z – direction in a thin sheet of thickness d, a quasi-two-dimensional electron gas forms. Applying a magnetic field perpendicular to it, forces the electrons to move in discrete cyclotron orbits[71]. Consequently, the energy eigenstates E_N of the system are quantized into the so-called Landau levels[71,72]:

$$E_N = E_0 + \left(N + \frac{1}{2}\right)\hbar\omega_C\,, \qquad N = 0, 1, 2, \dots\,, \qquad (2.21)$$

where $\omega_C = eB/m^*$ is the cyclotron frequency and E_0 accounts for the confinement in z – direction. Since the density of states has to be conserved during the process, each Landau level possesses a degeneracy of $g = eB/h$, i.e. for low temperatures each Landau level below the Fermi energy is occupied by g electrons[71,72]. Tuning B not only changes the energetic separation between two neighboring Landau levels but also varies their degree of degeneracy[72]. The transversal resistance of the Nth – Landau level can then be calculated using the degeneracy and the classical formula of Eq. (2.20)[71,72]:

$$R_{xy} = \frac{\rho_{xy}}{d} = \frac{B}{ne} = \frac{B}{\nu g e} = \frac{h}{\nu e^2} = \frac{R_K}{\nu}, \qquad \nu = 0, 1, 2, \dots\,, \qquad (2.22)$$

when the present charge carriers fill exactly ν Landau levels, with ν is called the filling factor. Here, n denotes the charge carrier density in the quasi 2D electron gas and R_K the von Klitzing constant. Most importantly, the resistance is quantized to a fraction of R_K in case a Landau level is completely filled. Hence, the phenomenon is called quantum Hall effect.

Nonetheless, to fully understand the behavior of longitudinal R_{xx} and transversal resistance R_{xy} the impact of impurities on the Landau levels needs to be considered. The density of states corresponding to the Landau levels does not exhibit discrete δ – functions but broadened distributions owing to localized states induced by residual disorder[71] (Figure 2.3b). Only states in the center of the Landau level are delocalized[71], as indicated in Figure 2.3b. Moreover, closed cyclotron orbits corresponding to the Landau levels are only possible in the bulk of the channel. At the edge of the material, the additional spatial confinement leads to a drastic increase of the energy of the Landau levels (see Figure 2.3c) as the charge carriers are elastically reflected. This gives rise to a net charge transport along edge channels[71,72] (see Figure 2.3d). Even in case a charge carrier is scattered from a defect, the Lorentz force redirects it in the forward direction[72]. Furthermore, since edge

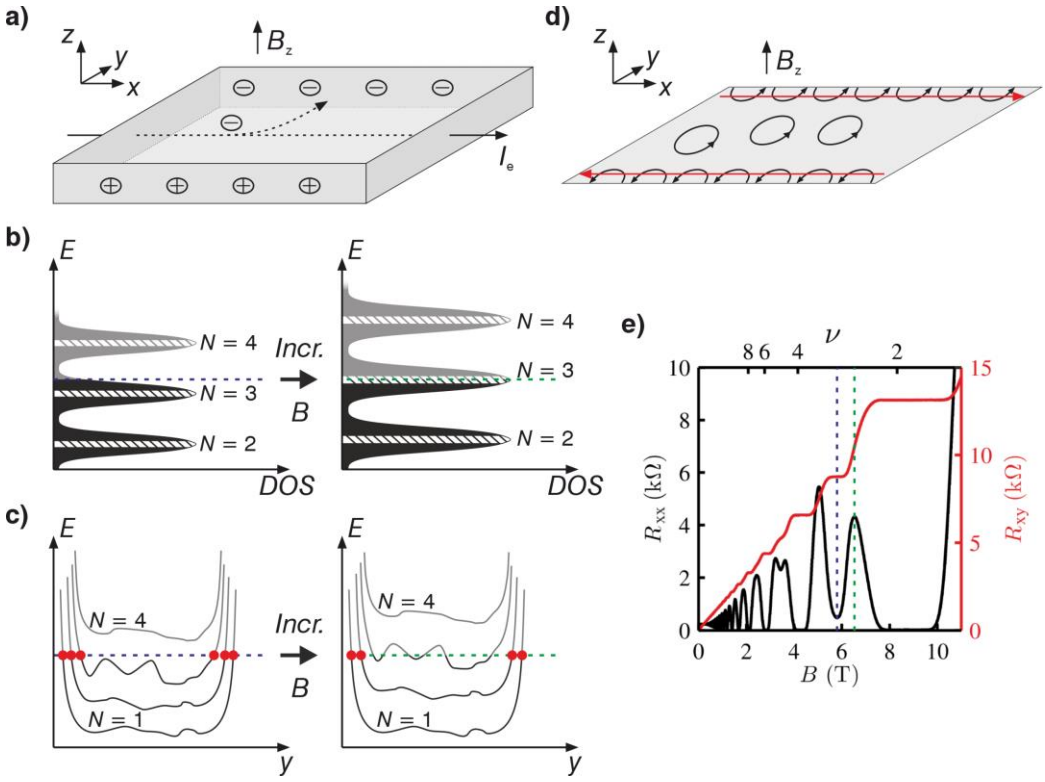

Figure 2.3 Classical and quantum Hall effect. a) *Conductor with an electron current I_e flowing in x – direction and a magnetic field B_z applied in z – direction. The charge carriers are deflected in y – direction due to the Lorentz force, building up a voltage across the voltage. [Figure adapted from Ref.[71]].* ***b)*** *Density of states as a function of energy for a 2D electron gas with some disorder present in a perpendicular magnetic field. The (de-) localized states for each Landau level N are shown in solid (hatched) color. The green/blue lines indicate the Fermi level with (un-) occupied states shown in black (grey). From the left to right panel, the magnetic field is increased. [Figure adapted from Ref.[71]].* ***c)*** *Energetic landscape of the Landau levels shown over the spatial extend of the 2D electron gas in y – direction. At the border, the energy of the Landau level is drastically increased due to the confinement. Residual disorder in the device causes fluctuations in the energetic landscape. The green/blue lines indicate the Fermi level, with (un-) occupied states shown in black (grey). The magnetic field is increased from the left to right panel. The red dots indicate ballistic edge channels. [Figure adapted from Ref.[71]].* ***d)*** *Schematic representation of electron trajectories in the quantum Hall effect. In the bulk, the electrons move in closed cyclotron orbits, whereas at the edge skipping orbits lead to edge channels, which are illustrated in red. [Figure adapted from Ref.[71]].* ***e)*** *Longitudinal R_{xx} (black) and transversal R_{xy} resistance (red) as a function of magnetic field measured in a 2D electron gas at low temperatures. The blue and green lines correspond to the position of the Fermi level shown in (b) and (c). The top axis illustrates the filling factor. [Figure taken from Ref.[73]].*

channels forming at either side of the channel are antiparallel, the forward and backward transport is spatially separated[71,73]. Hence, backscattering is highly suppressed resulting in a quasi-ballistic

transport within the directional edge channels[71,72].

Finally, the behavior of R_{xx} and R_{xy} measured for a 2D electron gas at low temperatures (Figure **2.3**e) can be explained. For low magnetic fields, the resistances behave as described in the classical Hall effect. However, with increasing magnetic fields a step-like behavior of the R_{xy} appears, whereas R_{xx} features oscillations. At certain magnetic fields, R_{xy} shows a plateau and R_{xx} vanishes (blue line in Figure 2.3e). In this case, the Fermi energy lies within the localized states between two Landau levels (blue line in Figure 2.3b). The localized states give rise to closed cyclotron orbits within the bulk and consequently no conduction between the two edges of the sample is possible[71]. However, owing to the additional spatial confinement at the edge of the material, a specific number of ballistic edge channels emerge. Consequently, R_{xx} vanishes, whereas R_{xy} is quantized. Increasing the magnetic field broadens the density of states of each Landau level and moves them towards higher energies. When a Landau level reaches the Fermi energy (green line in Figure 2.3b), delocalized states become available enabling transport between the two edges of the sample[72]. Backscattering is possible, and consequently R_{xx} is finite but R_{xy} increases, since one Landau level is depleted of charge carriers (green line in Figure 2.3e). Raising the magnetic field further repeats the process, depleting the Landau levels one by one. Similar observations can be made when the Fermi level instead of the magnetic field is tuned.

Whereas the section above discusses four-terminal measurements, in the course of this thesis mostly two-terminal devices were examined. For a two-terminal configuration, the conductance of a square-shaped device comparable to the ones used in this thesis (see Section 3.3.2) is given by[74]

$$\sigma_{two-terminal} = \sqrt{{\sigma_{xx}}^2 + {\sigma_{xy}}^2}\,, \tag{2.23}$$

or, with the relation between resistivity and conductance, by

$$\sigma_{two-terminal} = \frac{1}{\sqrt{{\rho_{xx}}^2 + {\rho_{xy}}^2}}\,. \tag{2.24}$$

Consequently, a two-terminal measurement exhibits, although only resolving a combination of longitudinal and transverse conductance, the same plateaus as R_{xy}.

2.2.2 Quantum Hall Effect in Bilayer Graphene

With a nearly parabolic energy dispersion at low energies in case trigonal warping is ignored (see Section 2.1.2), the charge carriers in bilayer graphene resemble a regular 2D electron gas[65]. However, its charge carriers are chiral with a Berry's phase of 2π. Although not distinguishable from zero, the Berry's phase causes an anomalous sequence of Landau levels to appear[24,65]. A magnetic field perpendicular to the graphene plane $\boldsymbol{B} = (0, 0, -B)$ can be accounted for by the transformation $\hbar\boldsymbol{q} \rightarrow -i\hbar\boldsymbol{\nabla} + e\boldsymbol{A}$, with the vector potential $\boldsymbol{A} = \boldsymbol{\nabla} \times \boldsymbol{B}$, in the effective Hamiltonian of bilayer graphene, see Eq. (2.12)[23,68]. Then, the energy of the Landau levels is given by[23,24,68]

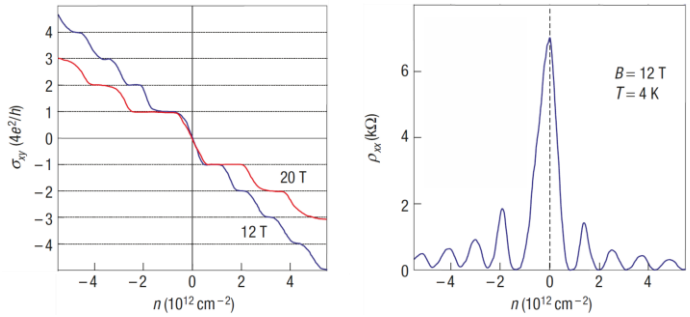

Figure 2.4 Unconventional quantum Hall effect in bilayer graphene. *σ_{xy} (left) and ρ_{xx} (right) as a function of charge carrier density measured at fixed B and T = 4 K. The quantum Hall plateaus appear for σ_{xy} at integer values of 4 $e^2\ h^{-1}$, but with a step of 8 $e^2\ h^{-1}$ across zero density due to the degeneracy of the zero energy Landau levels. [Figure taken from Ref.[24]].*

$$E_N^{BLG} = \pm\hbar\omega_C\sqrt{N(N-1)}\,,\ N = 0, 1, 2, \dots\,, \qquad (2.25)$$

N is called orbital index and $\pm$ refers to electron and holes states, respectively. The energy states have a distinct behavior compared to monolayer graphene or conventional two-dimensional electron systems[23,65]. Most prominently, the ground state ($N = 0$) as well as the first excited state ($N = 1$) are fixed at zero energy[23,65,68] leading to an unconventional quantum Hall effect in bilayer graphene. The $N = 0, 1$ Landau levels, lying at the border of electron and hole gases, provide an eightfold degeneracy, when taking spin ($\uparrow, \downarrow$), valley ($\boldsymbol{K}$, $\boldsymbol{K}'$) and the additional orbital degeneracy ($N = 0, 1$) into account. Contrarily, higher Landau levels with $N \geq 2$ move in energy for varying magnetic field and have each a fourfold degeneracy, due to the spin and valley index[23,68]. Notably, electron and hole states behave symmetrically around zero energy.

As a consequence, the Hall conductance σ_{xy} measured in bilayer graphene exhibits quantized plateaus at integer values of 4 $e^2\ h^{-1}$, but with a step of 8 $e^2\ h^{-1}$ across zero density due to the additional orbital degeneracy of the zero energy Landau levels[23,24]. Consistent with theory, experimental data confirmed the unusual sequence[24] (see Figure 2.4). Worth to note is that the sequence holds true only if interaction effects are neglected and any valley, spin or orbital splitting is negligible compared to temperature and Landau level broadening[23].

2.3 Competing Broken-Symmetry Ground Phases in Bilayer Graphene

So far, the quantum Hall effect in bilayer graphene was explained in the absence of any many-body effects. However, their consideration is important, since they can drastically alter the behavior of the Landau levels[23,41,44,65,75–78] and lead to the emergence of various broken-symmetry quantum Hall phases[31–33,36–39]. In particular, Coulomb interactions dominate in altering the spectrum[41,44,75–78].

These electron-electron interactions are especially strong at low charge carrier densities, as their strength is given by the ratio between Coulomb E_C and kinetic energy E_K resulting in[42,79]

$$r_S = \frac{E_C}{E_K} \propto {}^{1}/_{\sqrt{n}} \qquad (2.26)$$

for bilayer graphene. Hence, at low density the Coulomb energy dominates over the kinetic energy and interactions become increasingly important[42]. As a consequence, bilayer graphene – owing to the non-zero density of states at charge neutrality in case trigonal warping is neglectable[68], and a substantial Berry phase of $\pm 2\pi$ – is susceptible to spontaneous symmetry breaking at zero external fields[33]. This can be accounted for by adding a spontaneous mass term m to the Hamiltonian for the low-energy bands in bilayer graphene[33,39], see Eq. (2.14). Then, the Hamiltonian in the $\boldsymbol{K}$ valley changes to[33]

$$H_{\boldsymbol{K}}^{Int} = H_K + m\boldsymbol{\sigma}\,, \qquad (2.27)$$

where $\boldsymbol{\sigma}(\sigma_x, \sigma_y, \sigma_z)$ is the Pauli vector. The question is whether the spontaneous mass term is directed in-plate, i.e. $m(\sigma_x, \sigma_y)$, or out-of-plane, expressed by $m\sigma_z$. An in-plane mass term would break rotational symmetry giving rise to gapless nematic states[33,39,46]. In contrast, an out-of-plane mass term breaks chiral symmetry, since $[H_{\boldsymbol{K}}^{Int}, \sigma_z] \neq 0$, see Eq. (2.10). This results in the emergence of a family of gapped quantum Hall phases[32,33] with a spontaneous energy gap of $2m$ at $\boldsymbol{p} = 0$. Experiments[36–41,43] suggest that these gapped states corresponding to an out-of-plane mass term are favored, hence the focus is laid on chiral symmetry breaking rather than on the emergence of nematic states.

The sign of the out-of-plane mass term $m\sigma_z$ can be dependent on the spin and valley index, i.e. its implications need to be considered for all four species arising from the combinations of the valley ($\boldsymbol{K}/\boldsymbol{K}'$) and spin indices (↑/↓). In case of broken chiral symmetry, each of the four species spontaneously polarizes in a specific layer, depending on the sign of the mass term[32,33]. Moreover, the touching energy bands become gapped, resulting in a non-zero Berry curvature[33], which is related to

$$\Omega_z^{(\alpha)}(\boldsymbol{p}, \tau_z, s_z) \propto -\alpha\tau_z \mathrm{sgn}(m)\,, \qquad (2.28)$$

where $\tau_z = \pm 1$ indicates the $\boldsymbol{K}$ and $\boldsymbol{K}'$ valley, respectively, and $\alpha = +(-)$ labels the conduction (valence) band. Hence, it changes sign when the valley index τ_z, the mass term or the band index α is inverted. The consequence of a non-zero Berry curvature is that quasiparticles in an in-plane electric field acquire an anomalous transverse velocity proportional to the Berry curvature. This gives rise to a magnetic moment and an intrinsic Hall conductivity, with their sign specified for each spin-valley flavor[33]. The orbital magnetic moment carried by a quasiparticle shows the following dependence:

$$M_z(\boldsymbol{p}, \tau_z, s_z) \propto -\tau_z \mathrm{sgn}(m)\mu_B\,, \qquad (2.29)$$

with the Bohr magneton μ_B. Analogously to the Berry curvature, the orbital magnetic moment changes sign when the valley index τ_z or the mass term changes sign, however, it is independent on the band index α. Overall, considering the contributions from the four spin-valley flavors, a net orbital magnetization can persist for specific mass terms[33]. The intrinsic Hall conductivity is given by[32,33]

$$\sigma_H^{(\alpha)}(\tau_z, s_z) = \frac{e^2}{h}\tau_z\left(m\left(\sqrt{m^2 + \frac{(v_F p_F)^4}{{t_1}^2}}\right)^{-1} - \frac{m}{|m|}\delta_{\alpha,+}\right) \propto \frac{e^2}{h}\tau_z\,\mathrm{sgn}(m)\,, \qquad (2.30)$$

where p_F is the momentum of a quasiparticle at the Fermi level. When the Fermi level lies within the spontaneous gap, each spin-valley flavor adds $\pm e^2\,h^{-1}$, where the sign of its contribution is dependent on τ_z, $\mathrm{sgn}(m)$ and the band index α[33]. Taking into account the sign of all four $\sigma_H^{(\alpha)}(\tau_z, s_z)$ terms for one band α, an effective charge Hall conductivity $\sigma^{(CH)}$ can be derived[33]:

$$\sigma_{(\alpha)}^{(CH)} = \sum_{\tau_z, s_z} \sigma_H^{(\alpha)}(\tau_z, s_z)\,. \qquad (2.31)$$

Likewise, in case a valley and/or spin polarization is present, a net valley Hall conductivity

$$\sigma_{(\alpha)}^{(VH)} = \sum_{s_z} \sigma_H^{(\alpha)}(\tau_z = +1, s_z) - \sum_{s_z} \sigma_H^{(\alpha)}(\tau_z = -1, s_z) \qquad (2.32)$$

and/or spin Hall conductivity

$$\sigma_{(\alpha)}^{(SH)} = \sum_{\tau_z} \sigma_H^{(\alpha)}(\tau_z, s_z = +1) - \sum_{\tau_z} \sigma_H^{(\alpha)}(\tau_z, s_z = -1) \qquad (2.33)$$

can arise. Considering the dependence of the sign of the spontaneous mass term on the valley and spin indices, a total of five broken chiral symmetry states can emerge, each with a specific mass term and distinct charge, spin and valley dependent quantum Hall conductivities[32,33]: the quantum valley Hall (QVH), the quantum anomalous Hall (QAH), the layer antiferromagnetic (LAF) and the ALL as well as the quantum spin Hall (QSH) phase. These phases are schematically described in Figure 2.5. Moreover, their respective spontaneous mass term as well as the corresponding layer polarization of the four spin-valley species and the resulting Hall conductivities, following Eqs. (2.31), (2.32) and (2.33), are listed in Table 2.1. In addition, it is indicated whether the phases possess an overall layer polarization and/or orbital magnetization, see Eq. (2.29).

In the following, the five phases are explained in more detail: Firstly, in the quantum valley Hall phase (see Figure 2.5a) each spin-valley flavor polarizes in the same layer[32,33], i.e. the phase is fully layer polarized. It can be described by a spontaneous mass term of $m\sigma_z$. Since the $\boldsymbol{K}$ and $\boldsymbol{K}'$ valley contribute to the Hall conductivity and orbital magnetization with opposite sign, it shows zero charge and spin Hall but a non-zero valley Hall conductivity of 4 $e^2\,h^{-1}$. Secondly, the quantum anomalous Hall phase shows a polarization of the two valleys in different layers[33] (see Figure 2.5b). With the mass term taking the form $m\tau_z\sigma_z$, all four Hall conductivity and orbital magnetization contributions are of the same sign[33]. Hence, the QAH phase exhibits a charge Hall conductivity of 4

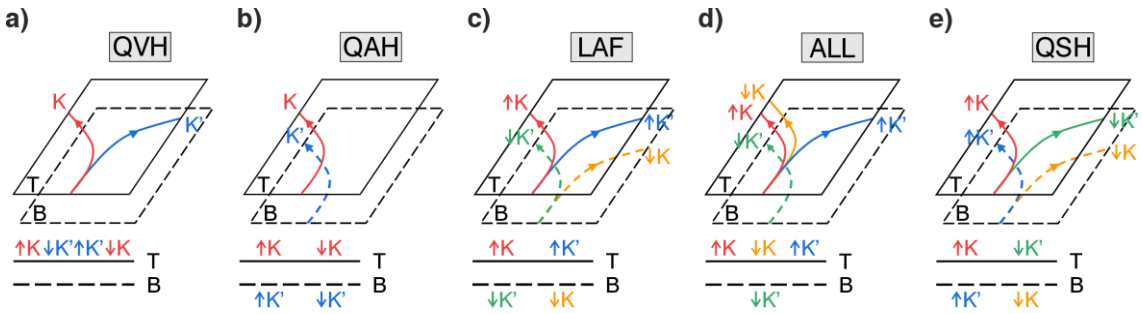

Figure 2.5 Five competing broken-symmetry quantum Hall ground phases in bilayer graphene. a) – e) *Top: Schematic of the spontaneous quantum Hall effect for the five different phases. Bottom: Layer polarization for the corresponding spin-valley flavors. T and B label the top and bottom graphene layer, respectively. [Figure adapted from Refs.[33,83]].*

Phase	Spin-valley flavor				Hall conductivities $(e^2\,\mathrm{h}^{-1})$			Lay. pol./ orb. magn.	Spontaneous mass term
	$\uparrow \boldsymbol{K}$	$\downarrow \boldsymbol{K}$	$\uparrow \boldsymbol{K'}$	$\downarrow \boldsymbol{K'}$	$\sigma^{(\mathrm{CH})}$	$\sigma^{(\mathrm{SH})}$	$\sigma^{(\mathrm{VH})}$		
QVH	T	T	T	T	0	0	4	yes / no	$m\sigma_z$
QAH	T	T	B	B	4	0	0	no / yes	$m\tau_z\sigma_z$
LAF	T	B	T	B	0	0	0	no / no	$ms_z\sigma_z$
ALL	T	T	T	B	2	2	2	yes / yes	$m\left(\frac{1+\tau_z}{2} + \frac{1-\tau_z}{2}s_z\right)\sigma_z$
QSH	T	B	B	T	0	4	0	no / no	$m\tau_z s_z\sigma_z$

Table 2.1 Characteristics of the five competing broken-symmetry quantum Hall ground phases in bilayer graphene. *Summary of the layer polarization of the four spin-valley flavors as well as the resulting charge $\sigma^{(CH)}$, spin $\sigma^{(SH)}$, and valley Hall conductivity $\sigma^{(VH)}$ in units of $e^2\ h^{-1}$ for each of the five quantum Hall ground phases. T and B relate to the top and bottom graphene layer, respectively. Moreover, it is indicated if the phases possess any net layer polarization and/or orbital magnetization. In addition, the corresponding spontaneous mass term for each of the five quantum Hall phases is shown. Here, $\tau_z = \pm 1$ corresponds to valley $\boldsymbol{K}/\boldsymbol{K'}$ and $s_z = \pm 1$ to spin ↑/↓. [Table adapted from Refs.[33,83]].*

$e^2\ h^{-1}$ and a substantial orbital magnetization[33] but the resulting spin and valley Hall conductivities are zero. Thirdly, the layer antiferromagnetic phase appears when the two spin species spontaneously polarize in opposite layers[33] (see Figure 2.5c). It can be seen as the two spin species showing an opposite QVH effect and the two layers exhibiting an opposite spin polarization. The corresponding spontaneous mass term is given by $ms_z\sigma_z$. The resulting Hall conductivity

contributions lead to all three charge, spin and valley conductivities being zero[33]. The most exotic out of the five states is the ALL phase, in which one spin-valley flavor polarizes in the opposite layer as the other three[33] (see Figure 2.5d). It can be understood in a way that one spin species shows a QVH effect, whereas the other forms a QAH effect. The mass term is given by $m\left(\frac{1+\tau_z}{2}+\frac{1-\tau_z}{2}s_z\right)\sigma_z$, resulting in a net layer polarization and orbital magnetization[33]. Intriguingly, the Hall conductivity contributions of the four spin-valley flavors yield charge, spin and valley conductivities of 2 $e^2\ h^{-1}$. Hence, its name is 'ALL' phase. Lastly, the quantum spin Hall phase has opposite QAH effects in the two spin species[33]. With a spontaneous mass term of $m\tau_z s_z \sigma_z$, this phase possesses zero charge and valley Hall conductivity but a substantial spin Hall conductivity of 4 $e^2\ h^{-1}$.

Since all five broken-symmetry quantum Hall phases compete at zero charge carrier density and zero external fields, it is per se not clear which of these phases actually emerge. Importantly, since three of the five phases are insulating, it is not sufficient to examine the charge Hall conductivity of any appearing phases in experiments. Instead, they can only be distinguished when considering their respective combination of charge, spin and valley Hall conductivities and related properties such as orbital moment and layer polarization (see Table 2.1). So far, evidence has been found for four of the five phases: Phases with a layer polarization (i.e. with substantial valley Hall conductivity) are expected to be stabilized by an externally applied electric field, which breaks inversion symmetry[33]. Under this condition, the QVH phase with its full layer polarization has been observed experimentally[33,39,41]. On the contrary, a perpendicular magnetic field strengthens phases with an orbital moment since the latter couples to the magnetic field[33]. With increasing magnetic field, these phases exhibit – in contrast to the insulating phases – a slope in the $n-B-$ space and eventually evolve smoothly into quantum Hall states with a filling factor matching their charge Hall conductivity[33] (see Section 2.4). Therefore, the QAH phase, with its unique charge Hall conductivity of 4 $e^2\ h^{-1}$, has been revealed by tracking the $\nu=\pm 4$ quantum Hall states towards zero magnetic field[35,44]. However, it is not clear if the phase survives to $B=0$. In fact, experiments suggest that the LAF phase is stabilized in this regime and is possibly the true ground state of bilayer graphene for zero electric field[40,43], however, contradicting studies reporting a finite conductance state have also been published[36,46]. In the presence of a small magnetic field, it evolves into the canted antiferromagnetic (CAF) phase, in which the spins are canted due to the applied magnetic field[62,80,81]. A detailed investigation to solve the debate about the ground state was conducted in this thesis (see Chapter 6). Lastly, the exotic ALL phase with its unique charge Hall conductance of 2 $e^2\ h^{-1}$ combines both a partial layer polarization and a substantial orbital moment[33]. Hence, it is expected to be stabilized by perpendicular magnetic and intermediately strong electric fields. Although experiments revealed evidence for its emergence[82], the resulting orbital magnetism and its appearance towards zero magnetic field was firstly revealed in the course of this thesis[83] (see Chapter 4).

2.4 Broken-Symmetry Quantum Hall States at Finite Magnetic Field

Even for finite magnetic field, electron-electron interactions can drastically alter the appearance of the Landau levels by lifting their fourfold (or eightfold when considering the $N = 0, 1$ zero energy levels) degeneracy[23,41,44,65,75–78] giving rise to a multitude of quantum Hall states[34,41,44,75–77,82,84]. Since the energetic width of the Landau levels are limited by disorder, a high cleanliness of the material further supports electron-electron interactions[85]. With a sufficient high quality of bilayer graphene and the applying of external fields[34], it is possible to observe all integer filling factors, i.e. filling factors in the range of $-4 \leq \upsilon \leq 4$ for the lowest octet of broken-symmetry states[41,75–77]. A simplistic Landau level diagram can help to describe the behavior of the different quantum Hall states and their phase transitions[41,75,76]. In the following picture, $\boldsymbol{K}/\boldsymbol{K}'$ label the valleys and $0/1$ as well as ↑/↓ mark states of orbital index $N = 0/1$ and spin up/down, respectively. Experimental effort has been made to derive the behaviors of the energy gaps related to the different symmetry breakings on the magnetic and electric field[76]. Valley imbalances breaking the valley degeneracy[75,76] are linear dependent on an externally applied electric field with a weak dependence on the magnetic field[76], i.e. the valley splitting follows $\Delta_{\boldsymbol{v}} \propto a_1 E + a_2 B$, where a_1 and a_2 are constants[76]. On the contrary, the interaction-induced ordering of the spins is solely dependent on the magnetic field[75,76]: $\Delta_s \propto a_3 B$, where a_3 is constant[76] with $a_3 > a_2$. Lastly, Coulomb interactions as well as band structure effects cause both weak electric and magnetic field dependencies of the energies of different orbital index (i.e. $N = 0$ and $N = 1$)[75,76,85].

With this information, a schematic Landau level diagram has been derived (see Figure 2.6). Assuming a finite magnetic field is applied to sufficiently clean bilayer graphene, at zero electric field the spin degeneracy is lifted owing to the magnetic field but also states with distinct orbital index $N = 0/1$ differ energetically. Neglecting the weak dependence of the valley splitting on the magnetic field, the valley degeneracy is still intact and only broken by increasing E. In addition, applying an electric field affects the splitting of states with distinct orbital indices but not of states with opposite spins. As a result, assuming the electric field direction favors states at the $\boldsymbol{K}'$ valley, states in the $\boldsymbol{K}/\boldsymbol{K}'$ valley move upward/downward in energy, whereas distinct slopes of states corresponding to the $N = 0/1$ orbital index are observed. This results in the emergence of broken-symmetry quantum Hall phases with specific electric field behaviors and phase transitions. Experiments confirmed the occurrence of the following states and their phase transitions with electric field: layer unpolarized $\nu = \pm 4$ states[41,75] without any phase transition and layer polarized $\nu = \pm 3$ states with a phase transition around zero electric field[85,86]. Moreover, layer polarized $\nu = \pm 2$ states at high electric fields have been observed[75,82,85,86] undergoing a phase transition at finite electric fields to layer unpolarized phases[82,85,86], which persist down to $E = 0$. Similarly, the layer polarized $\nu = \pm 1$ states

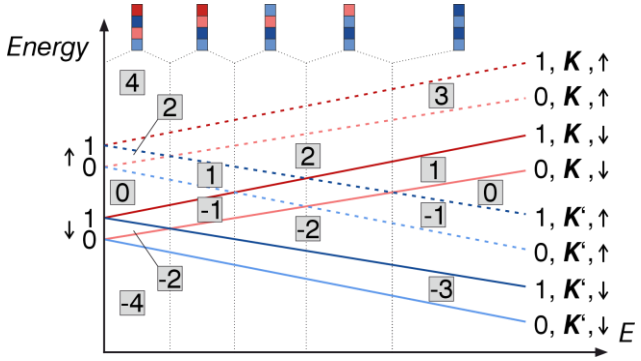

Figure 2.6 Schematic representation of the Landau level evolution with electric field and the appearing quantum Hall states. *Landau level behavior as a function of electric field at finite magnetic field and sufficient high cleanliness of the device. The levels within the lowest Landau level octet are coded and their corresponding orbital* $(0/1)$ *and valley indices* $(\boldsymbol{K}/\boldsymbol{K}')$ *as well as spin* $(\uparrow/\downarrow)$ *are indicated. The appearing quantum Hall states are labeled with numerals. Moreover, it is assumed that the direction of the electric field favors states in the* $\boldsymbol{K}'$ *valley. The color bars in the top of the graph illustrate the filling sequence from the* $\nu = -4$ *to the* $\nu = 0$ *state as a function of electric field. [Figure adapted from Refs.*[75,76]*].*

for high electric fields exhibit a phase transition at finite electric fields[85,86], yet they vanish around $E = 0$[84–86]. In addition, layer polarized $\nu = 0$ phases for high electric fields and a layer unpolarized $\nu = 0$ phase at low electric fields have been observed[39,41,62,87].

Overall, the simple Landau level schematic gives a good qualitative understanding of the appearing quantum Hall phases and their phase transitions with electric field. Furthermore, it correctly explains the complex filling sequence of the Landau levels of the lowest octet depending on the electric field[76,85] (the sequence from $\nu = -4$ to $\nu = 0$ is illustrated in the top of Figure 2.6). However, it certainly fails in other aspects. In particular, the picture does neither capture filling factor dependent many-body screening effects[76], nor does it correctly predict the nature of all appearing phases. As an example, it suggests a spin ferromagnet for the $\nu = 0$ phase[76] for $E = 0$, but experiments revealed a canted antiferromagnetic phase instead[62]. In the course of this thesis, the model with the predicted states as well as their expected phase transitions was used to identify the unique sequence of broken-symmetry quantum Hall states in bilayer graphene.

2.5 Domain Walls in Bilayer Graphene

As explained in Section 2.1.2, Bernal stacking is the most stable stacking order in bilayer graphene. It can occur in two energetically equivalent forms[48,49]: AB and BA stacking, both appearing equally frequently. They differ by the shift of one layer by a carbon-carbon distance along a certain direction in respect to the adjacent layer[48–50]. Even a simultaneous occurrence of both stacking orders within one bilayer graphene flake is possible. This requires the formations of domains, which are separated

by one-dimensional dislocations[48–50,57,88]. At these so-called domain walls, the stacking order transitions smoothly from AB to BA stacking (or vice versa) by either tensile or shear strain[48,57,88] (see Figure 2.7a and b). Due to the energetic equivalence of both stacking forms, no forces develop to reduce the area of the stacking fault[49], which results in an overall common occurrence of domain walls in bilayer graphene[48,57]. Since they possess only a width of 6 – 11 nm[48], domain walls can only be detected by techniques with sufficient high-resolution, such as transition electron microscopy[48,49] or scattering-type scanning near-field optical microscopy[56,57,88]. The latter is explained in more detail in Section 2.6.

Based on the common occurrence of domain walls in bilayer graphene flakes, it is essential to consider the consequences of their presence and understand their remarkable electronic properties. In case a perpendicular electric field is applied to bilayer graphene, a band gap opens within the bulk of bilayer graphene[26] (see Section 2.1.2), which can also be explained by the emergence of the quantum valley Hall phase at zero charge carrier density[41,62]. However, in a uniformly applied electric field, AB and BA domains show opposite valley polarization, since the energetic favoring of the $\boldsymbol{K}$ or $\boldsymbol{K}'$ valley is reversed at the dislocation[53,89,90]. As a consequence, gapless states emerge at the stacking fault[53,89], as schematically shown in Figure 2.7c. The states are chiral, hence electrons in the $\boldsymbol{K}$ and $\boldsymbol{K}'$ valley are counterpropagating[50]. Overall, since two states (both doubly spin degenerate) emerge within each valley, four valley-projected, one-dimensional channels are present. This results in a conductance of 4 $e^2\,h^{-1}$ along the domain wall for each direction[50,53,89] (see Figure 2.7d). In principle, intervalley scattering could lead to mixing of the counterpropagating modes and hence a reduction in conductance. However, domain walls consist of a defect free, smooth transition from AB to BA stacking over several hundred atoms. Hence, backscattering caused by intervalley mixing, which would require a large momentum change, is highly suppressed[50,91]. As a consequence, ballistic transport along the dislocation is possible[50].

An equivalent to these stacking domain walls are artificially created, electrostatically confined channels between two bilayer regions with the same stacking order but with electric fields of opposite polarity applied[51,53,89,92]. These antiparallel electric fields lead to regions with inverse layer (valley) polarization and hence to the emergence of chiral gapless modes[53], analogous to the ones observed between domains of AB and BA stacking when applying a uniform electric field. These artificial domain walls have been successfully demonstrated in experiments[51] and even potential applications such as valley polarizers and electron beam splitters have been realized[92,93]. Although they exhibit an advantageous tunability, as they can be switched on and off via gate voltages[51,92], the presence of an electric field is inevitable for their emergence[53]. On the contrary, stacking domain walls are an actual deformation of the lattice and are consequently also present in the low electric field regime. However, the question is whether the arising topologically protected states at the stacking domain wall also persist in this regime, where a multitude of broken-symmetry states

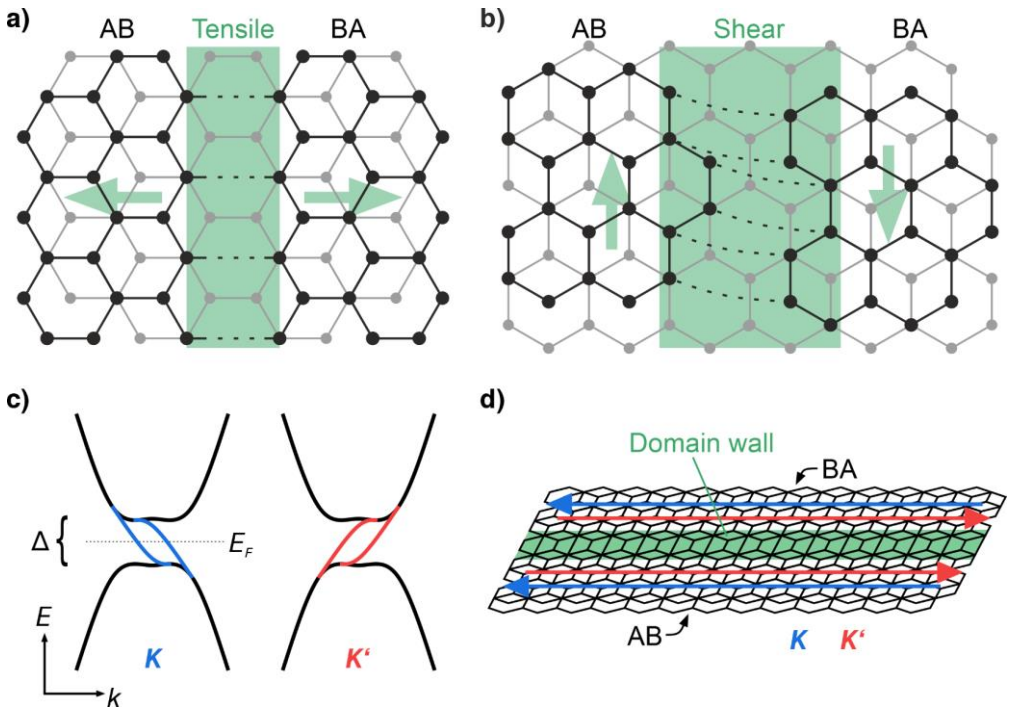

Figure 2.7 Stacking domain walls in bilayer graphene. a),b) *Schematic top view of the crystal structure of Bernal-stacked bilayer graphene with a tensile (a) and shear strain domain wall (b). The green rectangle illustrates the domain wall region in which the AB stacking smoothly transitions into a BA stacking domain. The upper (lower) graphene layer is shown in black (grey) and the green arrows indicate the direction of the strain. [Figure adapted from Ref.[57]].* ***c)*** *Electronic band structure of bilayer graphene for a non-zero electric field applied with a domain wall present.* E_F *and* Δ *label the Fermi energy and the non-zero band gap, respectively. The blue (red) lines indicate topologically protected, doubly spin degenerate chiral states at the* $\boldsymbol{K}(\boldsymbol{K}')$*-valley. [Figure adapted from Ref.[50]].* ***d)*** *Schematic side view of an AB-BA domain wall in bilayer graphene. Topological valley transport in the* $\boldsymbol{K}$ *and* $\boldsymbol{K}'$ *valley along the domain boundary is shown in blue and red, respectively. [Figure adapted from Ref.[50]].*

emerges[41,75,77,82]. So far, the quantum transport along stacking domain walls was mainly examined for zero magnetic field[50]. Hence, in this thesis the focus was laid on revealing the interplay between topological valley and quantum Hall edge transport[94] (see Chapter 5).

2.6 Near-Field Microscopy

In order to identify domain walls in bilayer graphene special techniques are necessary. This has mainly two reasons: first, owing to their small width of 6 – 11 nm[48], they escape the detectability of conventional optical methods. And second, the stacking order transition happens only in the graphene plane, hence domain walls are unobservable in purely topographic measurements. Here, scattering-type scanning near-field optical microscopy[56,57,88] (s-SNOM) combines a reliable

identification of domain walls in bilayer graphene with the advantage of being a non-destructive technique[95]. In the course of this thesis, it has been used to detect stacking dislocations.

In conventional optical microscopy, the spatial resolution is limited by the diffraction limit, or Abbe limit, which prevents resolving two individual points separated by roughly less than half of the incident wavelength[96]. However, there are several possible ways of circumventing this limit to gain information of a sample with even higher resolution. One possibility is to use scanning probe microscopy techniques[97]. Hereby, a probe is brought into close proximity of the sample surface to extract local properties of the sample. Then, by scanning the device, i.e. by moving either the sample or the probe, images are created. One commonly used example for this technique is atomic force microscopy (AFM)[98]. A sharp tip acts as the probe interacting with the underlying material by attractive and repulsive forces, e.g. van der Waals force and Pauli repulsion[97]. By fixing the probe-sample distance and simultaneously monitoring the movement of the tip, information about the sample topography can be gathered. In addition, it is possible to further extend this technique to measure more device characteristics such as local optical properties: In scattering-type (or apertureless) scanning near-field optical microscopy (s-SNOM)[95] the tip is metallic and side-illuminated from a focused laser beam. Consequently, it acts as nano-antenna[55] to focus the incident electric field onto the sample surface. A near- (or evanescent) field is created[55], modified by the interaction with the surface of the sample. The interaction decays exponentially with the tip-surface distance[99]. The back-scattered light, which can be detected in the far-field, carries information about local optical parameters of the sample. Hence, optical and topography information are simultaneously gained. Moreover, the resolution is no longer limited by the incoming wavelength, which would be several microns for mid-infrared light, but only dependent on the apex of the tip[95]. This process, schematically illustrated in Figure 2.8a, can be qualitatively explained with a simple dipole model[55,99]. Assuming the incident light with wavelength λ and electric field E_{in} is only polarized parallel to the tip axis (any component orthogonal induces an inferior signal level[99]) an initial dipole

$$p_0 = \alpha E_{\mathrm{in}} \qquad (2.34)$$

is induced in the apex of the tip. Describing the tip as point dipole with radius R (with $R \ll \lambda$), its dipole polarizability equals[100]

$$\alpha = 4\pi R^3 \frac{\varepsilon_{\mathrm{t}} - 1}{\varepsilon_{\mathrm{t}} + 2}, \qquad (2.35)$$

with ε_{t} being the dielectric constant of the tip. As a consequence, a mirror dipole is formed within the sample with a strength of[100]

$$p' = \beta p_0 , \qquad (2.36)$$

where $\beta = (\varepsilon_{\mathrm{s}} - 1)/(\varepsilon_{\mathrm{s}} + 1)$ is the dielectric surface response function[55] and ε_{s} the dielectric constant of the sample. The mirror image induces an additional dipole p_{i} within the tip, leading to a

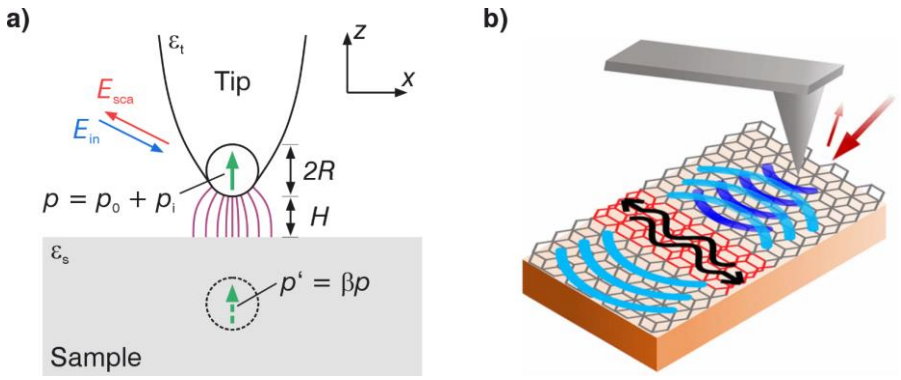

Figure 2.8 Point-dipole model and surface plasmon polaritons in near-field optical microscopy. a) *A schematic illustration of the s-SNOM tip and the sample is shown. The incident light E_{in} induces a dipole p_0 (green arrow) in the tip (dielectric constant: ε_t), which is modeled by a sphere with radius R. In the sample (dielectric constant: ε_s) in close distance H to it, a mirror dipole p' (dashed green arrow) is created interacting with the initial dipole in the tip and changing it by p_i. β and E_{sca} are the dielectric surface response function and the back scattered light, respectively. The interaction is schematically shown in purple. [Figure adapted from Ref.[55]].* ***b)*** *Plasmons are launched from the tip with a circular wavefront (dark blue). At a domain wall (red region) in bilayer graphene, they are partially transmitted and reflected (light blue) causing standing-wave interference pattern. [Figure taken from Ref.[56]].*

consecutive enhancement of dipole in the tip $p = p_0 + p_\mathrm{i}$ and the sample $p' = \beta(p_0 + p_\mathrm{i})$. Taking these near-field interactions into account[55] leads to an effective polarizability

$$\alpha_\mathrm{eff} = \frac{\alpha}{1 - \frac{\alpha\beta}{16\pi(R+H)^3}} \qquad (2.37)$$

of the tip, where H is the distance between tip and sample surface. Since the electric field scattered at a point dipole E_sca is directly proportional to its polarizability[55]

$$E_\mathrm{sca} \propto \alpha_\mathrm{eff} E_\mathrm{in}\,, \qquad (2.38)$$

relative changes in the scattered light are caused by changes in the local dielectric constant of the sample. Numerous extensions can been made to improve the model, such as considering a finite-dipole model[101] or taking light scattered at the surface of the sample into account[102]. Nonetheless, the simple model already allows for intuitively understanding the mechanism between the scattered light and optical properties of the sample. The technical details of the measuring process are explained in Section 3.2.2.

In graphene, the complex dielectric function, or the optical conductivity directly related to it[103], is dependent on layer number as well as stacking order[104] and, hence, the near-field signal changes from e.g. mono- to bilayer graphene. Moreover, since the scattered light is confined at the nanoscale to a much lower scale than the optical wavelength, the electric field strength and light-matter interactions are highly enhanced[105,106]. At the interface between graphene and a dielectric,

collective oscillations of free charge carriers, so called surface plasmon polaritons, can be excited[107,108]. These excitations, with a charge carrier density dependent plasmon wavelength[107], are launched from the apex of the tip. Owing to the isotropic conductivity tensor in graphene[106], they form a circular wavefront and propagate in-plane up to several times of their wavelength even at room temperature[107,108]. At the edge of a graphene flake, standing wave patterns can be observed due to back reflection and interference of plasmons[107,108]. Most importantly for this thesis, the same phenomena can be observed at stacking domain walls in bilayer graphene[50,56,57], see Figure 2.8b. Even though plasmon are reflected only partially at the defects, standing-wave interference patterns can be observed[56,57], albeit weaker than at the edge of the flake. Consequently, the dislocations are indirectly visible in the near-field microscope. Moreover, different types of dislocations (i.e. shear or tensile stacking domain walls) induce different phase shifts for the reflection[56,57]. Empirically, effective phase shifts of π and $\pi/2$ have been determined for tensile and shear dislocations[57], respectively. The consequences are distinguishable interference pattern allowing for a differentiation with s-SNOM.

2.7 Dually Gated Bilayer Graphene Field-Effect Transistor

The field-effect is the modulation of the electrical conductivity of a material by applying an external electric field, firstly demonstrated in experiment by J. Bardeen, W. Brattain and W. Shockley in 1947[72]. The effect can be exploited in a field-effect transistor to reliably probe the electronic properties of a material, which works also in graphene[3,109]. In the course of this thesis, a two-terminal device geometry was used, in which the active graphene channel is connected to source-drain contacts and its electronic properties are tuned via two gate electrodes. The dually gated structure (see Figure 2.9a) provides significant advantages over a device with a single gate, since both charge carrier density and electric field can be adjusted independently[41]. This is of particular importance in bilayer graphene as, in contrast to monolayer graphene, an electric field breaks the inversion symmetry of the bilayer, which can significantly alter its transport properties[26].
In a dually gated device, the net charge carrier density n is the sum of the components n_t and n_b induced by the top V_t and bottom gate voltage V_b, respectively[41,86]:

$$n = (n_t + n_b) = \frac{C_t(V_t - V_t^0) + C_b(V_b - V_b^0)}{e} = \frac{C_b}{e}\left(\alpha(V_t - V_t^0) + (V_b - V_b^0)\right). \qquad (2.39)$$

Here, V_t^0 and V_b^0 indicate the effective offset voltages due to residual charge carrier doping, i.e. charge neutrality at zero electric field is at $V_t = V_t^0$ and $V_b = V_b^0$. Moreover, α denotes the ratio between top C_t and bottom capacitance per unit area C_b of the respective gate electrode to the graphene sheet, and e is the electron charge. In the freestanding devices fabricated in the course of this thesis, the top gate is separated from the graphene by vacuum, whereas the bottom capacitor

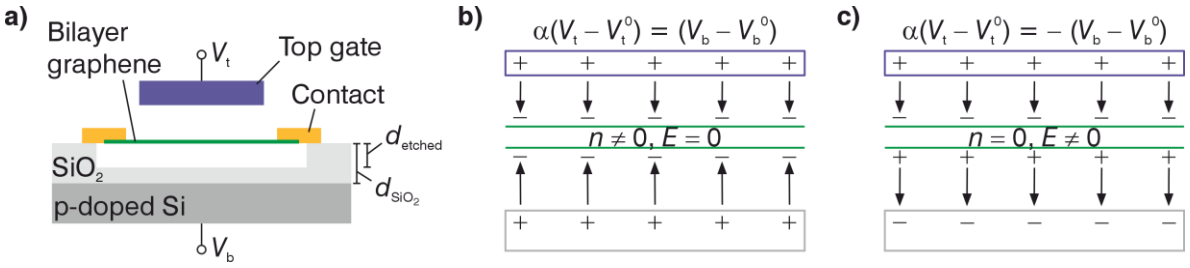

***Figure 2.9 Dually gated bilayer graphene field effect transistor**. **a)** Schematic cross section of the finalized device. The bilayer graphene (green) is freestanding and attached to the source-drain contacts (yellow). It is separated from the top gate (blue) by vacuum, and from the bottom gate by a layer of vacuum and SiO_2 (light grey), with thicknesses of d_{etched} and d_{SiO_2}, respectively. V_t and V_b indicate the voltages applied to the top and bottom gate electrodes, with the latter being highly doped silicon (grey). **b),c)** Schematic working principle of the dual-gate structure. The same color-coding as in (a) is used. For $\alpha(V_t - V_t^0) = (V_b - V_b^0)$, a net charge carrier density is induced in the bilayer graphene, but no electric field is applied, as illustrated in (b). In contrast, for $\alpha(V_t - V_t^0) = -(V_b - V_b^0)$, the total charge carrier density is zero, whereas a non-zero electric field is applied, as shown in (c). [Figure adapted from Ref.[112]].*

consists partly of vacuum and partly of silicon dioxide, see Figure 2.9a. Hence, the latter can be described by the sum of two in-series capacitances:

$$C_b = \varepsilon_0 \frac{{d_{etched}}^{-1} \cdot \varepsilon_{SiO_2}(d_{SiO_2} - d_{etched})^{-1}}{{d_{etched}}^{-1} + \varepsilon_{SiO_2}(d_{SiO_2} - d_{etched})^{-1}}, \qquad (2.40)$$

where ε_0 denotes the vacuum permittivity, ε_{SiO_2} is the permittivity of SiO_2, d_{SiO_2} indicates the overall thickness of the initially unetched SiO_2 layer and d_{etched} is the etching depth.

The perpendicular electric field E is the mean value of the electric field components E_t and E_b applied by the top and bottom gate[26]:

$$E = \frac{1}{2}(E_t + E_b) = \frac{C_b}{2\varepsilon_0}\left(\alpha(V_t - V_t^0) - (V_b - V_b^0)\right). \qquad (2.41)$$

Figure 2.9b and c illustrate two special cases: when the relation $\alpha(V_t - V_t^0) = (V_b - V_b^0)$ is true, $n \neq 0$ and $E = 0$ hold, whereas $n = 0$ and $E \neq 0$ applies for $\alpha(V_t - V_t^0) = -(V_b - V_b^0)$. However, since n and E are linearly independent, any possible combination of charge carrier density and electric field can be set by applying the corresponding V_t and V_b, see Eqs. (2.39) and (2.41).

3 Device Fabrication and Characterization Methods

In this chapter, the laboratory techniques for fabricating and examining the devices used in this thesis are described. Mainly delicate dually gated, freestanding bilayer graphene devices were fabricated and investigated using state-of-the-art procedures. At first, the process of exfoliation of high-quality graphene is presented. Secondly, pre-characterization methods such as optical and near-field microscopy are explained. Thirdly, the procedure of fabricating dually gated, freestanding bilayer graphene field effect devices is demonstrated. Lastly, the setup of electrical measurement for investigating the quantum transport is illustrated and the process of current annealing as well as device calibration is explained.

3.1 Wafer Preparation and Graphene Exfoliation

As substrate for all devices commercial highly p-doped silicon wafers (Silicon Materials) with an insulating layer of 300 nm Silicon dioxide (SiO_2) on top were used. Since the underlying silicon acted as bottom gate electrode during cryogenic measurements, the high doping level was necessary to ensure that the silicon possessed low resistivity even at temperatures close to absolute zero.
Small 4x4 mm^2 pieces cut from the wafers were rinsed in acetone as well as isopropanol. Subsequently, solvent residues were evaporated using dry air. Shortly prior to exfoliation, the substrates were additionally cleaned using an oxygen plasma (PICO Plasma Cleaner, Diener) for 5 min at 50 W with an oxygen gas flow of 10 sccm. Directly afterwards, mechanical exfoliation[2], a very simple yet successful technique to obtain graphene flakes with excellent quality[19], was used to fabricate bilayer graphene flakes from a highly oriented pyrolytic graphite block (Momentive Performance Materials Inc.). As a first step, while the substrates were heated to 110 – 130 °C to ensure the evaporation of any residual water, an adhesive tape (Magic Tape, Scotch) was slightly pressed onto the graphite surface and subsequently peeled off. Hereby, thin layers of graphite stuck to the tape by van der Waals force[4]. Secondly, using an additional piece of tape and placing it on the section with graphite on the initial tape, the graphite is further thinned. The procedure was repeated up to five times. Lastly, the tape with a desired graphite thickness was pressed onto the pre-heated substrates for ten seconds and was then carefully removed. During this process, some of the flakes

were randomly transferred to the substrates. After exfoliation, the substrates were cleaned again in acetone as well as isopropanol and blow-dried with dry air to dissolve most of the glue residues originating from the tape.

3.2 Optical and Near-Field Microscopy

In order to select suitable bilayer graphene flakes, two different microscopy techniques were conducted before fabricating the actual dually gated devices. First, optical microscopy was used to locate bilayer graphene flakes. Subsequently, the preselected flakes were investigated with scattering-type scanning near-field optical microscopy. The obtained topography images provided information about their homogeneity and cleanliness, whereas any stacking domain walls present in the flakes were detected within the optical channel. In the following, the aforementioned methods are presented in detail.

3.2.1 Optical Microscopy

After exfoliation, an optical microscope (LD EC Epiplan-Neofluar 100x, Zeiss) was used to locate and preselect suitable bilayer graphene flakes. Under ideal conditions, the absorbance of monolayer graphene is almost independent on the wavelength of the incident visible light and is given by $\pi\alpha \approx 2.3$ %, with α being the fine structur constant[6]. In addition, for a low number of layers, it increases linearly with additional graphene sheets[110], which can be used to estimate the number of layers of preselected flakes. To this end, optical images were taken, see Figure 3.1a. The optical contrast was identified by measuring the value of the green channel divided by the background value, see Figure **3.1**b. Although the optical contrast in a microscopy image is not solely dependent on the absorbance but also on the used substrate[110] as well as the wavelength of the incident light, the difference between mono- and bilayer graphene is sufficient to determine the layer number (see Figure 3.1b). The results were confirmed in quantum transport measurements with the unique sequence of quantum Hall states in bilayer graphene (see Section 2.4).

Besides layer number, this technique provides a fast and easy way to gain information about homogeneity and size of the flakes. Only rather isolated flakes with a homogenous looking surface were selected to enable an easy contacting procedure. In addition, special care was taken on the geometrical measures of the flakes for the following reasons: Firstly, freestanding graphene devices allow only for a certain width to be stable during suspension, hence, bilayer graphene flakes with a width of 0.5 – 3 µm were chosen. Secondly, of importance are also the aspect ratio of the devices (i.e. the ratio between channel length and width) as well as the ratio between channel length and contact width, as discussed in Chapter 6. Hence, appropriate flakes suitable for the experiments needed to be selected. Worth to note is that an additional etching step to shape flakes was avoided in order to maintain the high quality of the edges for quantum transport[19].

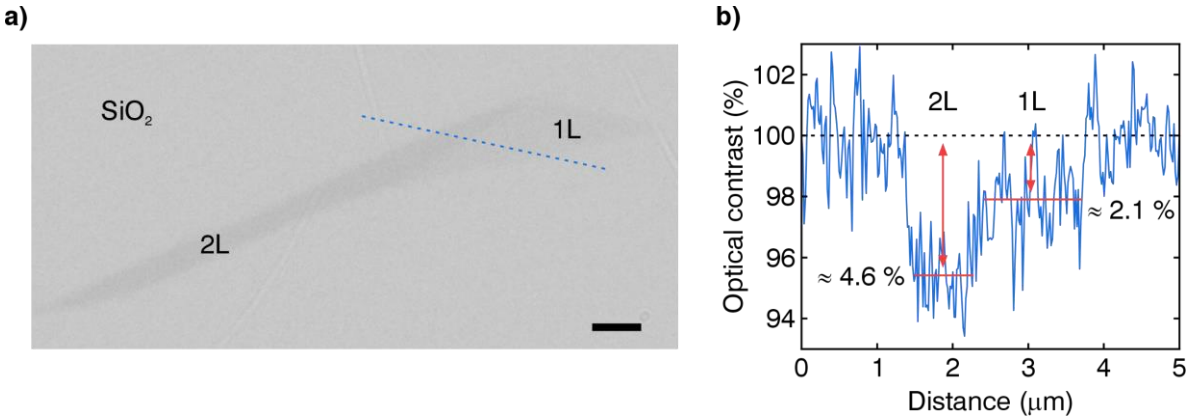

Figure 3.1 Optical microscopy. a) *Background corrected optical microscope image of a graphene flake on a SiO_2(300nm)/Si substrate. Mono- (1L) and bilayer graphene (2L) parts of it are labeled. The dashed line illustrates the position of the line trace shown in (b). Scale bar: 2 µm.* ***b)*** *Line trace of the normalized optical contrast across the flake shown in (a). The red lines are constant fits to the respective contrast levels of 1L and 2L graphene in the data. In this example, the difference in absorbance of mono- and bilayer graphene compared to the substrate is 2.1 % and 4.6 %, respectively. This is sufficient for a differentiation with optical microscopy.*

3.2.2 Scattering-Type Scanning Near-Field Optical Microscopy

After preselecting suitable bilayer graphene flakes, a customized scattering-type scanning near-field optical microscope (neaSNOM, neaspec) was used to scan the topography of the flakes with high resolution and simultaneously reveal any stacking defects. Essentially, the s-SNOM is an atomic force microscope operating in tapping mode with an infrared laser source coupled to it[55], see Section 2.6. In Figure 3.2, the setup is illustrated schematically. Its basic functionality is explained in the following.

An infrared laser (CO_2 Laser Merit G, Access Laser Company) beam with a tunable wavelength in the range of 9.2 – 10.8 µm goes through a neutral density filter, which allows for adapting the intensity of the light. Subsequently, it is guided using multiple mirrors onto a beam splitter. In addition, a green laser diode can be coupled in the same beam path for alignment purposes of the invisible infrared laser. One part of the beam is focused with a parabolic mirror onto the metal-coated tip (Pt/Ir, Arrrow NCPT-50, Nanoworld), which is oscillating with a frequency of $\Omega \approx 250 - 270$ kHz and a tapping amplitude of 60 – 80 nm. After interacting with the sample surface (see Section 2.6), the scattered light is collected and collimated by the same parabolic mirror. The second part of the beam goes into a reference interferometer, called pseudo-heterodyne[111] (ps-het) module, which consists of a mirror perpendicular to the incident beam oscillating with a frequency M causing an interference pattern with the scattered light from the tip at the beam splitter. The combined signal is then guided and focused onto a liquid nitrogen cooled HgCdTe detector using multiple standard

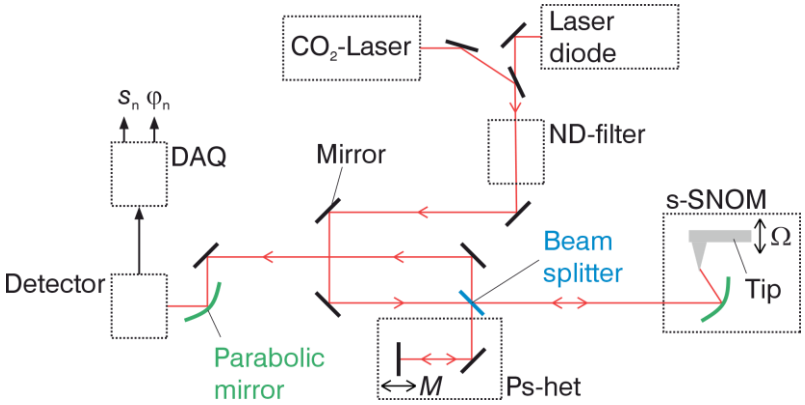

Figure 3.2 Scattering-type scanning near-field optical microscopy setup. *The CO_2 laser beam goes through a neutral-density (ND-) filter and is focused with multiple mirrors onto a beam splitter (blue). One part of the beam is focused with a parabolic mirror (green) onto the metal coated tip, which oscillates with a frequency Ω. After interacting with the sample, the scattered light is collected and collimated back to the beam splitter. The other part is guided into the reference path (ps-het module) and gets back reflected at an oscillating mirror with frequency M. The two parts get superposed at the beam splitter and are subsequently focused onto the detector using multiple standard and one parabolic mirror. A data acquisition card reads out the signal. A green laser diode shares the same beam path for alignment purposes.*

and one parabolic mirror. This pseudo-heterodyne technique provides an almost background-free, simultaneous detection of the near-field amplitude and phase[111]. Qualitatively, it works as follows. The detector measures the intensity of the incoming signal[111]

$$I \propto \left|E_{\mathrm{sca,nf}} + E_{\mathrm{sca,bg}} + E_{\mathrm{ref}}\right|^2, \tag{3.1}$$

which is related to the electric field components associated with the near-field interaction $E_{\mathrm{sca,nf}}$, a large additive background signal $E_{\mathrm{sca,bg}}$ caused by elastic reflection from the tip shaft or sample surface[111] and the reference signal E_{ref}. Since the tip oscillates vertically with a frequency of $\Omega \approx 250 - 270$ kHz, $E_{\mathrm{sca,nf}}$ and $E_{\mathrm{sca,bg}}$ are modulated at Ω and its higher harmonics[111]. On the contrary, in the pseudo-heterodyne module, the mirror oscillates with a much lower frequency $M \approx 300$ Hz in the propagation direction of the laser beam leading to a phase modulation of E_{ref}. Due to the interference of both components, the spectrum of the superposition shows sidebands at Ω and its n-th harmonic $n\Omega$ at frequencies of $f_{\mathrm{n,m}} = n\Omega \pm mM$, where m is an integer[111]. According to Ref.[111], the background-free near-field amplitude s_{n} and phase contrast value φ_{n} can then be obtained from the detector signals $u_{\mathrm{n},1}$ and $u_{\mathrm{n},2}$ measured at the first $f_{\mathrm{n},1}$ and second sideband $f_{\mathrm{n},2}$, respectively. The quantities are given by

$$s_{\mathrm{n}} = 2.16k\sqrt{{u_{\mathrm{n},1}}^2 + {u_{\mathrm{n},2}}^2} \tag{3.2}$$

and

$$\varphi_{\mathrm{n}} = \arctan\left(2.16k\frac{u_{\mathrm{n},2}}{u_{\mathrm{n},1}}\right), \qquad (3.3)$$

with k being a constant. The equations are only true for sufficient high harmonic order $n > 1$. In the course of this thesis, the signal was usually demodulated at the third or fourth harmonic of Ω, which was done by a data acquisition card connected to the detector.

The main goal for using the s-SNOM was to detect stacking domain walls within the preselected bilayer graphene flakes. These defects are only indirectly visible owing to plasmon reflections at the stacking domain boundaries (see Section 2.6). Since this effect is much weaker compared to reflections at the edge of graphene, and the spatial extend of the interference pattern is in the order of a few hundred nanometers[57], excellent alignment and an impeccable quality of the tip are crucial.

3.3 Dually Gated Freestanding Device Fabrication

In the course of this thesis, a dually gated, freestanding device geometry was used to achieve high quality, high tunable bilayer graphene samples free of any influence from the substrate. The technique was first developed by K.I. Bolotin et al.[19] and further improved by R.T. Weitz et al.[41], over a decade ago. It involves multiple steps of electron-beam lithography and physical vapor deposition as well as subsequently chemical wet etching with hydrofluoric acid, etching SiO_2 but leaving the graphene and the metal contacts intact. The procedure is explained in the following in detail.

3.3.1 Contact and Top Gate Patterning

After the initial optical characterizations, the selected bilayer graphene flakes were contacted directly with chromium/gold contacts using electron-beam lithography. The process is schematically shown in Figure 3.3. Hereby, special attention was laid on domain walls detected in the flakes with the near-field microscope. The contacts were designed in three different configurations: i) domain walls were present in the channel and connected by source-drain contacts on both ends, ii) domain walls were present in the channel but not connecting both contacts, and iii) domain walls were completely absent. The devices were fabricated as follows. A positive resist polymethylmethacrylat (PMMA) 950 k dissolved in anisole (AR-P 672.045, Allresist) in a 4.5 wt.% solution was spin coated onto the devices (see Figure 3.3a) in a two-step process: at first, the sample rotated at 800 rpm for 1 s and immediately after at 4000 rpm for 30 s. The procedure resulted in a homogenous layer of resist with roughly 230 nm thickness. Afterwards, a soft bake at 150 °C for 3 min was performed, illustrated in Figure 3.3b. Subsequently, small (big) contact leads were exposed with an electron-beam using an acceleration voltage of 10 kV and a 10 (60) µm aperture with a dose of 110 (170) µC cm^{-2} (see Figure 3.3c). The width of the designed contact leads was designed to be not smaller than 1 µm to ensure mechanical robustness during suspension. Consecutively, the devices

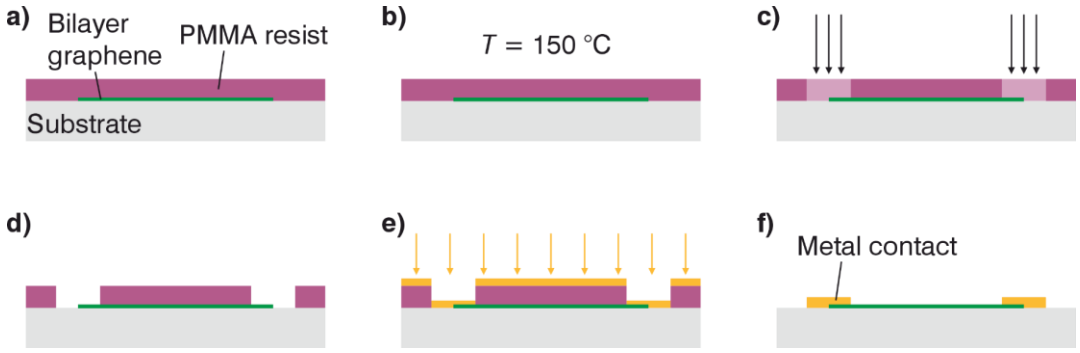

Figure 3.3 Procedure of electron-beam lithography. a) *PMMA resist (purple) is spin coated onto the substrate (grey) with a preselected bilayer graphene flake (green).* ***b)*** *A softbake at T = 150 °C is performed.* ***c)*** *Desired parts of the resist are exposed with an electron-beam.* ***d)*** *Rinsing the device in a developer dissolves the exposed parts.* ***e)*** *Metals (yellow) are deposited using electron-beam evaporation.* ***f)*** *The resist is dissolved using acetone and the metal remains only at the previously exposed sections.*

were developed in a 1:3 solution of methylisobutylketon (MIBK) and isopropanol for 2 min dissolving the exposed PMMA sections, then immersed in isopropanol and blow-dried with dry air (see Figure 3.3d). Subsequently, metals were deposited using electron-beam physical vapor deposition (PVD) at low pressure ($< 3 \times 10^{-7}$ mbar), as illustrated in Figure 3.3e. Successively, an adhesion layer of 5 nm chromium and a 100 nm gold layer were deposited with deposition rates of 0.1 – 0.2 Å s^{-1} and 1.0 – 1.2 Å s^{-1}, respectively. Afterwards, the devices were rinsed in warm acetone to lift-off the remaining resist, leaving only the designed contact patterns (see Figure 3.3f). Consecutively, the devices were immersed in isopropanol and blow-dried with dry air.

After patterning the contact leads, two additional electron-beam lithography and PVD steps were used to fabricate the top gate structure. First, a SiO_2 spacer was patterned. To this end, the aforementioned procedure of electron-beam lithography was used again, however, to prevent problems during lift-off owing to the greater thickness of the spacer than the contacts, both, the spin coating of the PMMA resist and the consecutive soft bake were performed twice. After exposure with unchanged parameters, an increased development time of 3:30 min was used. Then, SiO_2 was deposited at a rate of 1.0 – 2.0 Å s^{-1} and the resist was lifted-off. Second, to fabricate the top gate, the spin coating procedure was again conducted twice, and the desired structure was patterned using an electron-beam. After 3:30 min of development, an adhesive layer of 5 nm chromium and a 160 nm layer of gold were deposited with deposition rates of 0.1 – 0.2 Å s^{-1} and 1.1 – 1.3 Å s^{-1}, respectively. The subsequent lift-off revealed the processed but not yet freestanding structure, as shown schematically in Figure 3.4a.

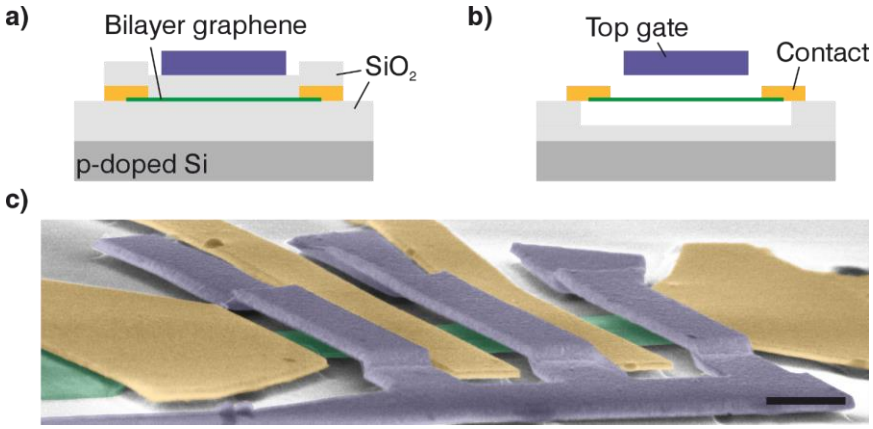

***Figure 3.4 Dually gated freestanding bilayer graphene device**. **a),b)** Schematic cross section of the device architecture prior (a) and after suspending the device (b). In the final state, the bilayer graphene (green) is suspended and attached underneath the gold contacts (yellow) with a freestanding top gate (blue) above. The SiO_2 and highly doped silicon substrate are shown in light grey and grey, respectively. **c)** False-color scanning electron microscope image of an exemplary dually gated freestanding device with multiple channels. The colors match the ones used in (a) and (b). Scale bar: 1 µm.*

3.3.2 Wet Etching and Critical Point Drying

In order to finalize the devices and suspend both the bilayer graphene as well as the top gate, a wet etching procedure was used. Figure 3.4a,b illustrates a schematic cross section of a device before and after the process. The devices were immersed in a 1:7 buffered oxide etch based on hydrofluoric acid for 100 s, which uniformly removed about 150 nm of SiO_2. The latter happens even under the flake due to a rapid propagation of the acid along the SiO_2/graphene interface[19]. Consequently, the bilayer graphene flake is suspended and only attached underneath the gold contacts. The parts of SiO_2 masked by chromium/gold are impenetrable for the acid and are only etched horizontally. Therefore, the contact leads do not collapse. In addition, the evaporated SiO_2 spacer between the bilayer graphene and the top gate is also etched. This occurs almost instantaneously due to the low quality of the deposited dielectric. As a result, the top gate is also suspended above the channel of the device. After etching, the devices were immersed in water twice and subsequently three times in ethanol without drying them in between.

As a last step, to prevent the collapse of the device during drying due the surface tension of the liquid[19], the devices were placed directly from ethanol into a critical point dryer (K850, Quorum Technologies). Within the pressure chamber of the dryer, the devices were cooled down in ethanol to 12 °C. Then, the solvent was slowly replaced with liquid CO_2 during multiple rinsing cycles at constant temperature. Afterwards, temperature and pressure within the chamber were raised to approximately 35 °C and 80 bar, which ensured the surpassing of the critical point of CO_2. By

consecutively venting the chamber at constant temperature a phase transition between the liquid and vapor phase was avoided. A false-color scanning electron microscopy image of a fully processed, dually gated freestanding bilayer graphene device is shown in Figure 3.4c.

3.3.3 Bonding

Prior to loading the devices in the cryostat, they were glued onto a sample holder using conductive silver paint. Gold pads connected to the top gate and contact leads were successively bonded to pins attached to the sample holder using a wedge bonder (MEI 1204W, Marpet Enterprises). The bonding was carefully performed using only low power ultrasonic pulses as well as proper grounding to avoid a collapse of the fragile structures and any electrostatic discharge.

3.3.4 Current Annealing

Due to the involved electron-beam lithography, the suspended bilayer graphene devices were exposed to lots of contaminants and usually exhibited high amounts of residues, e.g. of the PMMA resist. Consequently, the quality and especially the quantum transport characteristics of the devices were initially relatively poor. To overcome this problem, a current annealing technique[19,22,41] was used to greatly reduce the amount of residual dirt. The procedure was conducted at a temperature of 1.6 K after loading the device into the cryostat. By ramping up a large d.c. source-drain voltage $V_{\mathrm{d.c.}}$, a high current $I_{\mathrm{d.c.}}$ runs through the two-terminal device. As a consequence, it heats up to very high temperatures due to dissipation, which removes the contaminants[22]. Successively after each $V_{\mathrm{d.c.}}$ ramp, the quality of the device was analyzed with a back gate voltage V_{b} sweep.

Figure 3.5 demonstrates the technique for an exemplary device, with several labeled annealing cycles. After the initial step (1), which involved applying approximatively 4.5 V and a resulting current of 0.5 mA (see Figure 3.5a), the resistance does not show any saturation (see Figure 3.5b). Moreover, the device is still highly doped, as the resistance increases monotonically as a function of V_{b} and shows no charge neutrality point (see Figure 3.5c). A second cycle (2) with much more current flowing (> 1 mA) reveals the begin of current saturation. Moreover, the charge neutrality point is visible in the accessible back gate voltage range. However, to achieve a high quality of the device, further cycles of current annealing were performed (3) – (5). Minimal higher currents can greatly improve the characteristics, remarkable in the reduction of contact resistance (i.e. the resistance offset for high back gate voltages) as well as in the narrowing of the resistance peak at charge neutrality (see Figure 3.5c). The best results were achieved when a current of approximatively 0.35 mA per width of the channel (in µm) and per layer number was flowing and a source-drain voltage with an extra of 0.5 – 2.0 V above the onset of the saturation was used. However, significant higher currents (i.e. additional 150 – 250 % of current) were needed in devices with a low overall resistance to achieve similar annealing temperatures and a comparable quality of the devices. In particular, devices with a domain wall present connecting source and drain showed significant lower

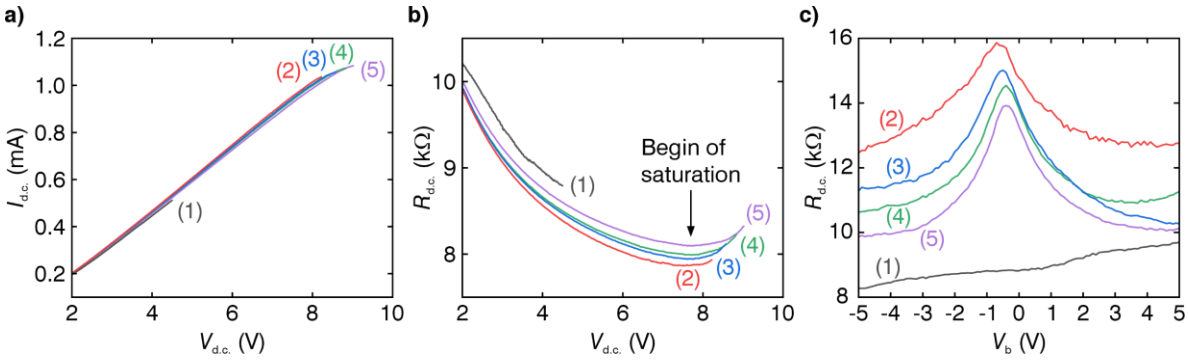

Figure 3.5 Current annealing technique. a),b) *D.c. Current $I_{d.c.}$ (a) and resistance $R_{d.c.}$ (b) as a function of applied d.c. source-drain voltage $V_{d.c.}$ for five consecutive annealing cycles shown in black, red, blue, green and purple. The cycles are additionally labeled with numerals.* ***c)*** *$R_{d.c.}$ versus bottom gate voltage V_b, subsequently measured after each annealing cycle. The colors match the sequence shown in (a) and (b).*

resistance and, hence, much higher current was needed in order to obtain similar results from the annealing procedure.

3.4 Electrical Characterization

After annealing the devices, the quantum transport characteristics of the flakes were investigated. All measurements were conducted in a cryogen-free dilution refrigerator measurement system (Dilution Refrigerator BF-LD250, Bluefors) with a base temperature of 7 mK. Most measurements were performed at base temperature, however, in some experiments, the temperature was raised up to 10 K. In addition, a perpendicular magnetic field of up to 14 T could be applied. In-series low-pass filters were used to minimize high-frequency noise. Due to the device geometry, only two-terminal measurements were performed. However, to bypass in-series resistances originating from the filters and wiring, four connections with two interconnected at the bonding pins were used to measure the voltage drop relatively close to the actual device. Standard lock-in techniques were used for all measurements, apart from the conducted d.c. measurements for current annealing and the in-situ monitoring the device quality (see Section 3.3.4).

In Figure 2.6, the electrical measurement setup is illustrated. First, an a.c. reference signal V_{Ref} provided from a lock-in amplifier (SR830, Stanford Research Systems) was modulated onto an optional d.c. bias $V_{\mathrm{d.c.}}$ from a d.c. source (SMU GS610, Yokogawa) using a transformer. Second, a high resistance R_{S} was used to convert the applied a.c.–d.c. voltage into a current signal, resulting in an excitation current of $I_{\mathrm{exc.\,(a.c.)}} = 1 - 10$ nA with a frequency of 78 Hz running through the device (plus an optional d.c. current). 78 Hz was chosen to suppress any high frequency effects and 50 Hz noise. The a.c. voltage drop $V_{\mathrm{a.c.}}$ across the device was measured using a second lock-in amplifier (SR865, Stanford Research Systems) linked via V_{Ref} to the first one. To consider the actual

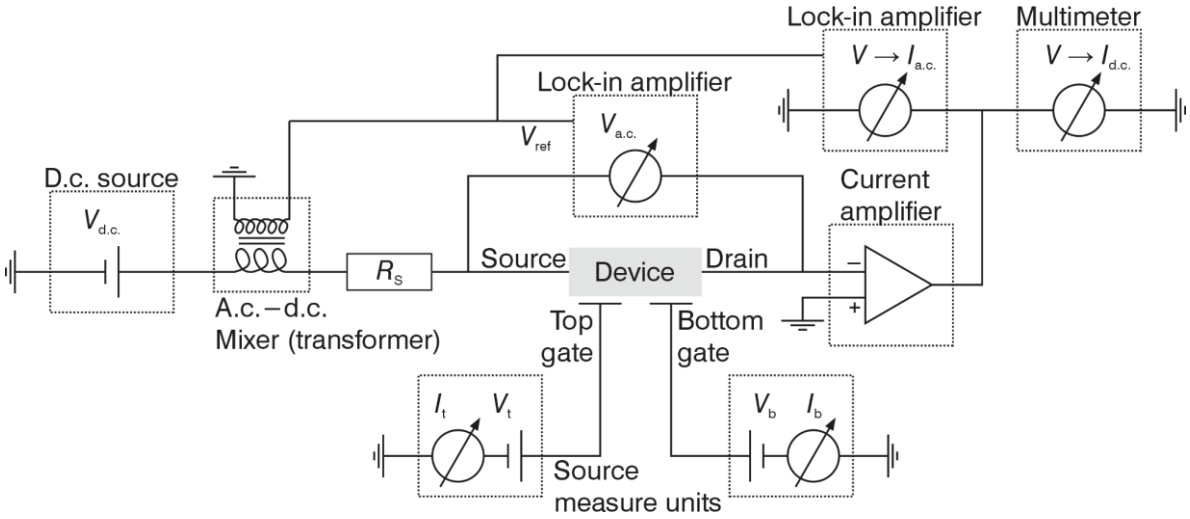

Figure 3.6 Electrical measurement setup. *Lock-in techniques were used in the setup to measure the differential resistance as well as conductance. It included the following units: a d.c. source, two lock-in amplifiers, a current amplifier as well as a multimeter and two source measure units. In addition, a transformer was used to mix the a.c. and d.c. signals, and a resistor to convert the applied source-drain voltages to current.*

current flowing through the device, it was amplified by a current amplifier (Model 1211, DL Instruments) and its a.c. $I_{\mathrm{a.c.}}$ and d.c. component $I_{\mathrm{d.c.}}$ were measured using the first lock-in amplifier as well as a multimeter (Multimeter 34461A, Keysight), respectively. With the measured $V_{\mathrm{a.c.}}$ and $I_{\mathrm{a.c.}}$, the differential resistance and conductance of the devices could be calculated. To manipulate the gates, two source measure units (SourceMeter 2450, Keithley) were used to apply the top V_{t} and bottom gate voltages V_{b} and simultaneously measure the corresponding leakage currents, I_{t} and I_{b}.

In order to control all electrical devices and specify their settings as well as to collect the data during the electrical measurements, a software developed by Felix Winterer[112] was used.

3.5 Device Calibration

For each device, a set of calibration measurements were conducted to find its charge neutrality point, to convert the top and bottom gate voltages into charge carrier density and electric field as well as to calculate the contact resistance of the sample.

At first, a top and bottom gate voltage sweep was performed at zero magnetic field (see Figure 3.7a). The line of highest resistance value $R_{max}(V_{\mathrm{b}})$ for each V_{t} (dashed line in Figure 3.7a) indicates charge neutrality. Moreover, the slope of the diagonal yields the gate coupling ratio α, see Section 2.7. Second, Eqs. (2.39) and (2.41) were used to define the dependence of n and E on the top and bottom gate voltage:

$$V_t = \frac{en + 2\varepsilon_0 E}{2\alpha C_b} + V_t^0 \qquad (3.4)$$

and

$$V_b = \frac{en - 2\varepsilon_0 E}{2C_b} + V_b^0\,, \qquad (3.5)$$

which were specified in the measurement software. Afterwards, precise charge carrier density and electric field sweeps were conducted (see Figure 3.7b and c). Hereby, V_t^0 as well as V_b^0 were initially set to zero and only an estimate of the bottom capacitance C_b was used, calculated from the etching time and following Eq. (2.40). Subsequently, Lorentzian functions were fitted to both data sets to determine their respective offsets n_{off} and E_{off}. Using Eqs. (3.4) and (3.5), the position of the CNP at $E = 0$ could be derived by

$$V_t^0 = -\frac{en_{off} + 2\varepsilon_0 E_{off}}{2\alpha C_b} \qquad (3.6)$$

and

$$V_b^0 = -\frac{en_{off} - 2\varepsilon_0 E_{off}}{2C_b}\,. \qquad (3.7)$$

To obtain the correct value for C_b and hence a precise calibration of the $n-$ and $E-$ axis, a fan diagram was recorded (see Figure 3.7d). The appearing quantum Hall states could be linked to integer filling factors υ in sequential order. Subsequently, linear functions following $B = hC_b\big(\alpha(V_t - V_t^0) + (V_b - V_b^0)\big)/(e^2\upsilon)$ were plotted for each $-4 \leq \upsilon \leq 4$ state. The true C_b, see Eq. (2.40), could be determined by tuning d_{SiO_2} and d_{etched} in a way that the linear functions lie in the center of the corresponding quantum Hall plateaus (dashed lines in Figure 3.7d).

Finally, in two-terminal transport measurements there always persists an in-series contact resistance, and its calculation as well as subtraction are crucial. For this purpose, a density sweep at $B = 2$ T and $E = 20$ mV nm^{-1} was performed. Figure 3.7e shows the conductance for hole doping. Note, that the case for electron doping behaves similarly. At this magnetic field, all integer quantum Hall states are fully visible. The applied finite electric field ensures the emergence of layer polarized states. The appearing quantum Hall states were compared to the unique Landau level diagram of bilayer graphene (see Section 2.4) and linked to integer filling factors in sequential order. Then, a constant fit to each plateau was conducted to obtain their respective conductance (or resistance) values, which were subsequently plotted against the corresponding inverse filling factor (see Figure 3.7f). A linear fit to the data yields the contact resistance R_c as its intercept and the von Klitzing constant as its slope. The former was subtracted to all measurements, whereas the latter acted as sanity check.

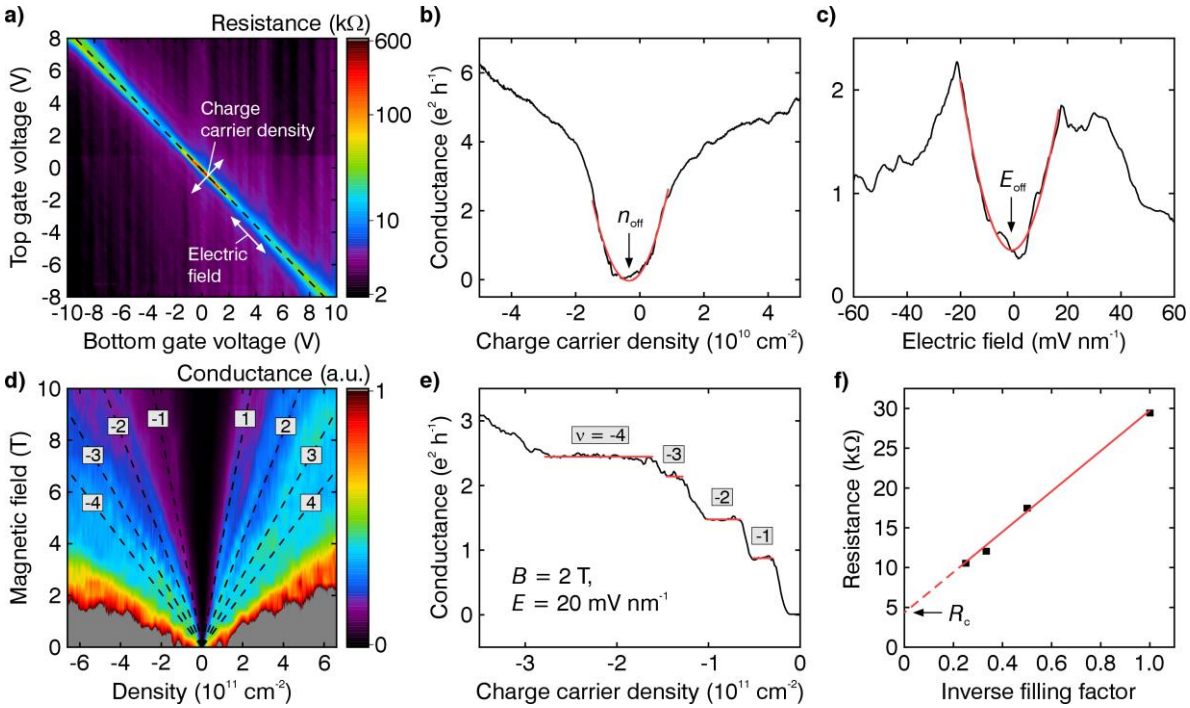

Figure 3.7 Device calibration procedure. a) *Resistance as a function of top and bottom gate voltage. The directions of both charge carrier density and electric field are indicated. The dashed line illustrates charge neutrality.* ***b),c)*** *Conductance as a function of charge carrier density (b) and electric field (c) in the uncalibrated device. In both cases, a Lorentzian fit (in red) to parts of the data and the respective offsets n_{off} and E_{off} are shown.* ***d)*** *Conductance as a function of magnetic field and charge carrier density at zero electric field. The appearing quantum Hall states can be linked to integer filling factors of sequential order. Linear fits (dashed lines) to the appearing quantum Hall states help to calculate the correct C_b and are labeled with the corresponding filling factor.* ***e)*** *Conductance as a function of negative charge carrier density (i.e. hole doping) for $B = 2\ T$ and $E = 20\ mV\ nm^{-1}$. To each appearing quantum Hall plateau, a constant function is fitted (red lines). The states are labeled with their respective filling factor.* ***f)*** *The resistance values obtained from the fits in (e) plotted versus the corresponding inverse filling factor. A linear fit to the data (solid red line) allows for the calculation of the contact resistance R_c, which is the intercept of curved red line. The dashed red line is a guide to the eye.*

4 Quantum Anomalous Hall Effect in Bilayer Graphene

Part of the findings presented in this chapter have been published in Ref.[83]. The full article can be found in Appendix A.1.

4.1 Summary

The quantum anomalous Hall effect has only been observed in magnetically doped topological insulators[45,113,114] and precisely aligned moiré heterostructures[29,30,115–117]. However, it has been theoretically predicted to occur also in pure Bernal-stacked bilayer graphene[31–33]. In Ref.[83], which is part of this thesis, states with a conductance of $\pm 2\ e^2\ h^{-1}$ were observed that survive down to anomalously small magnetic fields as well as up to temperatures of 5 K and show a magnetic hysteresis providing compelling evidence of orbital magnetism.

In the study, dually gated freestanding bilayer graphene devices were fabricated and current annealing was used to obtain ultraclean samples. Near-field optical microscopy was used to ensure the absence of any domain walls in the devices. The dual-gate structure was exploited to tune charge carrier density and electric field independently. By varying n and B for various E, quantum Hall states with a conductance of $\pm 2\ e^2\ h^{-1}$ were tracked down to vanishing magnetic fields. Notably, they appear only within a specific range of intermediately strong electric fields. Their emergence is consistent with a theoretically reported octet of exotic ALL phases, which are quantum anomalous Hall phases with a partial layer polarization as well as a substantial orbital moment[33] (see Section 2.3). So far, evidence of this phase has only been found for magnetic fields of $B > 1.2$ T[82], however, as one of the competing quantum Hall ground phases in bilayer graphene, it is predicted to survive down to zero magnetic field[33]. Moreover, owing to the substantial orbital moment and resulting quantum anomalous Hall character, a magnetic hysteresis is expected. In Ref.[83], exactly this behavior was confirmed, with a hysteresis appearing only for a specific filling factor around $\upsilon = \pm 2$ and, again, intermediately strong electric fields, consistent with the properties of the ALL phase. In addition, the temperature dependence of the $\upsilon = \pm 2$ quantum anomalous Hall phase compared to the $\upsilon = 0, \pm 4$ states were examined at $B = 0.5$ T. The resulting activation energy gap of the $\upsilon = -2$

state shows a specific electric field dependence consistent with its partial layer polarization. The surprising robustness of the $\upsilon = -2$ state, which is on par to the one of the $\upsilon = -4$ state, illustrates the coupling of electric and magnetic fields to the layer polarization and substantial orbital moment, respectively.

Notably, the here observed QAH phase differs from the QAH effect in magnetically doped topological insulators[45,113,114]. In these materials, it arises from a combination of topological properties (caused by spin-orbit coupling) and broken time-reversal symmetry (owing to magnetic dopants), whereas in bilayer graphene it is ought to be of orbital nature due to a vanishing spin-orbit coupling. Moreover, the ALL phase is caused by spontaneous chiral symmetry breaking[33], unlike in moiré heterostructures[29,30,115–117], in which the orbital magnetism is obtained by artificially designing the band structure. Besides a quantized charge Hall conductivity, the QAH phase in bilayer graphene possesses also spin, valley and spin-valley QAH effects[32,33] (see Section 2.3), more unique features which distinguish it from the QAH effects in other materials.

4.2 Outlook

The observation of the quantum anomalous Hall octet in bilayer graphene is only the first step towards understanding its nature. Several aspects of it are worth future studies: first, a four-terminal device geometry would greatly help to examine the ALL phases, since its implementation would enable the independent determination of longitudinal and Hall resistance. One way would be to fabricate heterostructures consisting of graphene and hexagonal boron nitride[18]. Processing multiterminal devices is standard in this type of devices[62,118], however, the strength of electron-electron interactions, and hence the observation of the $\upsilon = \pm 2$ quantum anomalous Hall octet, could be affected by embedding the bilayer graphene in a material with high dielectric constant[42]. Yet, even in freestanding devices the realization of a multiterminal device is possible and has been successfully established previously in a cross-like geometry[35,43,119,120]. Moreover, also a Hall bar structure with several voltage probes and two current leads (see Figure 4.1a) could be possible. Although the fabrication of such devices with a top gate is in principle feasible, the annealing of multiterminal devices is very challenging, as the cleaning process seems to happen inhomogenously[120]. This could hamper the observation of spontaneously broken-symmetry states[120]. All in all, if a sufficiently clean, multiterminal freestanding device can be realized, the determination of the actual quantization of the Hall conductance should be the first goal. Moreover, the full exploration of the magnetic hysteresis, one of the major aspects of the quantum anomalous Hall effect, would be facilitated. In particular, properties such as the coercive magnetic field and its temperature dependence could be measured properly. Both have been explored in moiré systems[29,30,115,116] and greatly helped to understand the underlying phenomena.

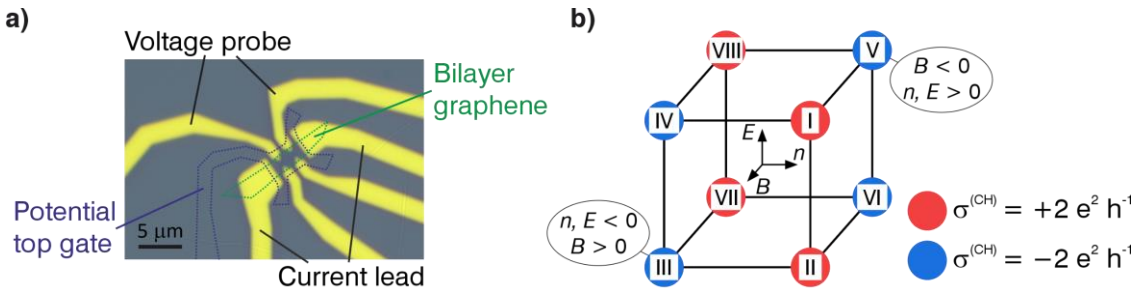

c)

ALL phase in ABC-like graphene ($l \geq 2$)	Hall conductivities ($e^2\ h^{-1}$)		
	$\sigma^{(CH)}$	$\sigma^{(SH)}$	$\sigma^{(VH)}$
	l	l	l

Figure 4.1 Aspects of the quantum anomalous Hall octet in bilayer graphene suitable as subjects for future studies. a) *Optical microscopy image of a multiterminal bilayer graphene device. The bilayer graphene flake (dashed, green) is contacted in a Hall bar geometry with four voltage probes and two current leads. A designed but not realized top gate (dashed, blue) is illustrated. The device is not yet freestanding.* ***b)*** *Schematic cube illustrating the tunability of the quantum anomalous Hall octet. Each corner represents one of the eight ALL phases (labeled with roman numerals) with a unique combination of polarities of n, E and B as well as a charge Hall conductivity of either $+2\ e^2\ h^{-1}$ (red) or $-2\ e^2\ h^{-1}$ (blue). The phases are tunable by n, E and B. [Figure adapted from Ref.[83]].* ***c)*** *Charge $\sigma^{(CH)}$, spin $\sigma^{(SH)}$, and valley Hall conductivity $\sigma^{(VH)}$ in units of $e^2\ h^{-1}$ for the ALL phase in ABC-like graphene multilayers with a layer number of $l \geq 2$. [Figure adapted from Ref.[33]].*

A second intriguing aspect is the tunability of the phase. Since it shows a partial layer polarization, the phase is not solely defined by the magnetic field and the sign of the filling factor (i.e. positive or negative charge carrier density), but also by the direction of the electric field[32,33]. In fact, eight ALL phases, each unique in its combination of polarities of n, E and B, form together a quantum anomalous Hall octet (see Figure 4.1b). By tuning one of the three physical quantities, the system can be switched into another ALL phase. Four of the phases are expected to show a conductance of $+2\ e^2\ \mathrm{h}^{-1}$, whereas the other half exhibit a conductance of opposite sign. Although reversing the direction of the electric field will not change the conductance but only the layer polarization, inverting the charge carrier density or the magnetic field does switch it from $+2\ e^2\ h^{-1}$ to $-2\ e^2\ h^{-1}$ (or vice versa). This tunability by charge carrier density could be exploited to control a magnetic state electrically by gate voltages. Experimentally, this has been realized in moiré heterostructures[115]. Another possibility to control the magnetic state could be the application of a d.c. bias current, which also has been demonstrated in moiré heterostructures[29,30]. It seems that a

d.c. current can modify the magnetization of the quantum anomalous Hall phase, acting in a similar way as an external magnetic field[29,30]. Enabling the tunability of a magnetic state by either a gate voltage or a d.c. current in such a simple system as bilayer graphene would be a great achievement. In case the effect could be stabilized for higher temperatures, an application as a magnetic memory in logic devices comes immediately in mind[115]. However, even for low temperatures interesting applications are possible[115,121].

Lastly, since the quantum anomalous Hall octet is not uniquely tied to bilayer graphene, but is instead universal to ABC-like graphene stacks[32,33], it is well worth to examine the phases in rhombohedral multilayer flakes with a layer number of $l \geq 3$. Although the fabrication of devices with rhombohedral stacking is more difficult due to its instability towards Bernal stacking during processing[122], electron-electron interactions are expected to be enhanced for an increasing amount of layers in ABC-like graphene stacks[42,79], at least up to a certain number of layers[32,33]. In fact, the ratio between Coulomb and kinetic energy follows[79]

$$r_S \propto n^{-(l-1)/2}, \qquad (4.1)$$

i.e. at charge neutrality it diverges faster for a high number of layers than in bilayer graphene. This indicates even stronger electron-electron interactions in systems with more layers, up to a critical value[32,33]. It would be interesting to examine the ALL phases and in particular their parameters such as critical temperature and coercive magnetic field as a function of l. Moreover, the charge, spin and valley Hall conductivities of the quantum anomalous Hall octet depend on the layer number[32], see Figure 4.1c. Thus, adding layers to an ABC-like system provides a unique way to tune some of the properties of the appearing ALL phases. In a first follow-up study, the quantum anomalous Hall octet has been revealed in rhombohedral trilayer graphene[123]. As expected, it exhibits a charge Hall conductivity of $\pm 3\ e^2\ h^{-1}$ and a magnetic hysteresis indicating the presence of orbital magnetism. However, these observations are only the first step towards examining the evolution of the ALL phases in ABC-like graphene stacks with increasing layer number.

5 Topological Valley and Quantum Hall Edge Transport

Part of the findings presented in this chapter have been published in Ref.[93]. The full publication can be found in Appendix A.2 and the corresponding supplementary material in Appendix B.1.

5.1 Summary

The possibility to manipulate the valley degree of freedom in bilayer graphene to achieve valley-polarized quantum transport has been predicted[53] and successfully realized in experiments by locally inverting the direction of an applied electric field[51,92]. An analogous effect emerges at stacking domain walls in Bernal-stacked bilayer graphene. Here, topologically protected valley-helical states emerge in case a uniform electric field is applied[50,89,124]. In Ref.[93], which is part of this thesis, the robustness of these kink states is examined in the presence of various broken-symmetry states within the manifold of the eight-fold degenerate zeroth Landau level. An intriguing interplay between topological domain wall and quantum Hall edge transport is observed.

In the study, dually gated freestanding bilayer graphene devices were fabricated with two distinct configurations: devices with a domain wall contacted on both ends and pristine devices without any dislocation as reference. After current annealing the devices, the dual-gate structure was exploited to tune charge carrier density and electric field independently. In a first set of measurements, the behavior of the two-terminal resistance was examined under an electric field to confirm the presence of gapless kink states (see Section 2.5), as observed in previous studies[50,51,92]. In fact, for increasing electric field the resistance saturates at $R \approx 8.5$ kΩ. With a device length of $L = 0.7$ µm and four valley-projected, one-dimensional channels (i.e., a theoretically expected conductance of $\sigma_0 = 4\, e^2\, h^{-1}$) this results in a mean free path of $\lambda_m \approx 2.2$ µm. Since $\lambda_m > L$, ballistic charge transport supported by the domain wall is confirmed. The long mean free path highlights the high quality of the device comparable to previous studies[50,51,92]. Then, the focus was laid on the behavior of the kink states within certain broken-symmetry phases, which has not been examined so far due to the following reasons: Investigations on artificially constructed domain walls can only be conducted at non-zero applied electric field as a matter of principle[51,53,92]. More specifically, as

locally inverted electric fields are needed to realize the valley-polarized quantum transport in these designed structures, the regime around zero electric field is inaccessible. Furthermore, the quantum transport along stacking domain walls was mainly examined for zero magnetic field and in devices with lower quality[50]. To this end, a second set of measurements was conducted at various magnetic fields. Measuring the conductance as a function of electric field and charge carrier density at low magnetic fields reveals an almost constant value of approximately $4\ e^2\ h^{-1}$ within the eight-fold degenerate zeroth Landau level of bilayer graphene. Starting at $\upsilon = 0$, for increasing filling factor the initial four kink states per direction are successively traded for quantum Hall edge states with higher quality. Hence, the conductance is decreasing only slightly. However, at stronger magnetic fields, the domain wall conductance is suppressed owing to the formation of minigaps (for the case of the $\upsilon = 0$ canted antiferromagnetic phase) or intervalley backscattering (for the case of the $\upsilon = \pm 1, \pm 2$ quantum Hall states). Overall, a complex interplay between topological domain wall and quantum Hall edge transport can be observed. Lastly, a set of temperature dependent measurements confirm both a metallic behavior of the domain wall as well as its negligible impact on the quantum transport within the $\upsilon = \pm 4$ quantum Hall phases.

5.2 Outlook

Although the domain walls have recently gained a lot of interest owing to their ubiquity in magic-angle twisted bilayer graphene[125,126], they are rather unexplored in various aspects: in addition to the low electric field versus charge carrier density regime, which was examined in the present study, the impact of domain walls on higher Landau levels is worth further investigations. Theoretical calculation predict an influence of both stacking and artificial domain walls on the energetic landscape of higher Landau levels[94,124]. The otherwise energetically flat Landau levels display ripples and resonances caused by the presence of domain walls[124]. Under certain circumstances, they could provide additional charge channels and alter the conductance of the quantum Hall states. However, to resolve states with higher filling factors $|\upsilon| > 4$ as a function of magnetic field, large charge carrier densities need to be applied. Since the achievable electric field and charge carrier density regime in freestanding devices is rather limited, the use of heterostructures consisting of bilayer graphene and hexagonal boron nitride[18] are inevitable to examine higher Landau levels[75].

In addition, the $\upsilon = 0$ ferromagnetic phase at high in-plane magnetic fields[62,87] in the presence of a stacking domain wall is worth further investigations. In bilayer graphene, the $\upsilon = 0$ state at zero charge carrier density and electric field transitions for increasing magnetic field from the layer antiferromagnetic[43,81] to the canted antiferromagnetic[62,127] and finally to the ferromagnetic phase[62,80,81,127]. The corresponding energetic edge gap is maximal for the LAF state, shows a smaller value for the CAF phase, and vanishes in the FM phase, where gapless states with opposite spin emerge[62,80]. This evolution is in stark contrast to the expected behavior of the kink states. In the

present study it was revealed that chiral states are present in the layer antiferromagnetic phase, but evidence of a minigap was found in case the spins are canted. However, stacking domain walls do not necessarily correspond to a topological domain wall in the order parameter and the absence of gapless states was predicted for the $\upsilon = 0$ FM phase. Future experiments investigating the evolution of the chiral states at the kink alongside the transition of the $\upsilon = 0$ phase and its edge states is worth considering. For this purpose, high in- and out-of-plane magnetic fields are needed[62,87].

Moreover, domain walls provide a flexible platform to study correlated physics[128,129]. As the charge transport along the dislocations is one-dimensional, Coulomb interactions are expected to cause strong perturbations and the quasiparticles should behave like a Luttinger liquid[128,130]. Experimental consequences are for example a specific power-law dependence of the differential conductance[128]:

$$\sigma \propto T^{\alpha} \text{ , for } eV_{d.c.} \ll k_B T \text{ ,} \qquad (5.1)$$

and

$$\sigma \propto (V_{d.c.})^{\alpha} \text{ , for } eV_{d.c.} \gg k_B T \text{ ,} \qquad (5.2)$$

where k_B is the Boltzmann constant and α a constant. This means, the behavior of the conductance depends on the relation between applied d.c. voltage $V_{d.c.}$ and temperature T. First steps towards examining these dependencies have been conducted in this thesis. Figure 5.1a shows the conductance as a function of d.c. current $I_{d.c.}$ along the domain wall measured at $n = E = B = 0$ for various temperatures on a log-log scale. As expected[130,131], the curves for different temperatures collapse in a single curve in the high current (or voltage) regime and can be described by a power-law function $\sigma \propto (I_{d.c.})^{\alpha}$ for $eV_{d.c.} \gg k_B T$, with $\alpha \approx 0.48$. However, the true voltage dependency could not be measured due to the usage of in-series resistors for low-pass filtering. Furthermore, an excitation current rather than a voltage is applied in the setup (see Section 3.4). Moreover, to verify the temperature dependence of the conductance in the $eV_{d.c.} \ll k_B T$ regime, higher temperatures than the $T \leq 10$ K used are needed. Thus, the measurement shown in Figure 5.1a are only a first step and modifications to the electrical setup as well as detailed measurements at higher temperatures are necessary to fully explore the expected Luttinger liquid in stacking domain walls in bilayer graphene.

More exotically, in case a certain combination of electric field and out-of-plane as well as high in-plane magnetic fields is applied, a so-called spin ladder has been proposed[129]. Hereby, the spin of the four chiral states on each side of the domain wall is locked to the direction of movement, i.e. chiral quasiparticles with opposite charge have opposite spins[129]. Consequently, a two-leg spin ladder forms on each side of the domain wall, weakly coupled to each other[129]. In each leg, two counterpropagating modes with opposite chirality are present but spin and direction of movement are locked in the same way. Due to the spin-charge coupling, exotic correlated phases such as charge density wave or super fluidic phases are theoretically proposed[129]. Experimentally, the phases are

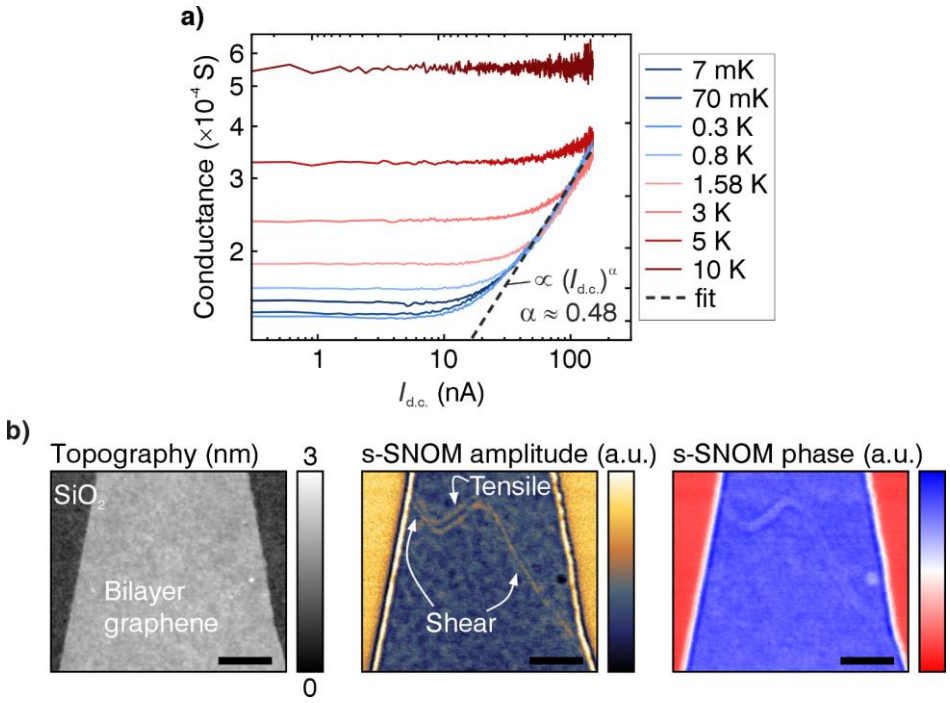

Figure 5.1 Aspects of stacking domain walls in bilayer graphene interesting for future studies. a) *Log-log plot of the differential conductance as a function of applied d.c. current at* $n = E = B = 0$ *for various temperatures. The data collapses in a single curve to which a power-law function* $\sigma \propto (I_{d.c.})^{\alpha}$ *is fitted (dotted line).* ***b)*** *Topography (left), s-SNOM amplitude (mid) and phase (right) image of a bilayer graphene flake. A stacking domain wall is present, visible in the amplitude and phase images. With sufficiently good alignment, regions with shear and tensile strain transitions can be differentiated. Scale bars: 0.5 µm.*

expected to exhibit special temperature dependencies of the conductance and to be tunable by electric and magnetic fields[129].

Another interesting but unexplored aspect of dislocations in bilayer graphene is the influence of their exact species. As explained in Section 2.5, the stacking order can change within a smooth, defect-free transition region in two different ways: either by tensile or shear strain[57]. Their differentiation is possible with near-field optical microscopy[57,132] (see Figure 5.1b), since the two species result in distinct boundary conditions and hence interference pattern of the plasmons. Usually, a shear domain wall features one main amplitude maxima and two secondary ones, whereas a tensile strain transition shows two equally pronounced maxima. However, the patterns are doping and gate-dependent[57] and the overall procedure is challenging, since a perfect alignment of the setup is needed to distinguish the different plasmon reflection patterns of tensile and shear strain solitons. Previous studies differentiating the species focused on optical properties[57] and charge carrier transmission[132] and confirmed distinct behaviors. However, investigations regarding the quantum transport are still missing and worth further effort.

6 Electric Field Disorder in Ultraclean Bilayer Graphene

Part of the findings presented in this chapter have been published in Ref.[133]. The full publication can be found in Appendix A.3 and the corresponding supplementary material in Appendix B.2.

6.1 Summary

Bilayer graphene, owing to its various internal degrees of freedom and non-vanishing density of states at the charge neutrality point when trigonal warping[68] is neglected, exhibits a rich variety of broken-symmetry states[36–41,46,62]. Coherent experimental determination of the exchange-induced ground state has up to now been challenging due to the interplay between interaction and disorder effects[47]. In Ref.[133], which is part of this thesis, the strength of the spontaneously gapped layer antiferromagnetic ground state can be correlated to the behavior of phase transition between various broken-symmetry states at finite magnetic field. Spatial variations in the interlayer potential difference allowing for the spontaneous formation of domains of different broken-symmetry states are determined as common cause.

In the study, dually gated freestanding bilayer graphene devices were fabricated, and special care was taken on the presence of any stacking domain walls. Overall, eleven devices, two with stacking domain walls within the channel but not connecting the two contacts, were investigated. After current annealing the devices, bottom gate voltage sweeps at various fixed top gate voltages already revealed major differences in the transport signatures at $T = 1.5$ K. Measurements at base temperature ($T < 10$ mK) support this observation. In particular, some devices exhibit an insulating phase at charge neutrality with a nonmonotonic behavior of the resistance for increasing electric field. Contrarily, in other devices the spontaneously gapped phase is absent, and the resistance increases monotonically for increasing electric field. The measurements reflect well the ambiguous observations from literature, which report either a vanishing or a finite conductance at charge neutrality[36–41,46]. However, considering the behavior of all examined devices, a continuous spectrum of the resistance (or conductance) rather than a bimodal distribution[36] is observed.

At first, the spontaneously gapped state at charge neutrality and zero electric field shows insulating behavior with phase transitions appearing at $|E| > 0$. Hence, according to these signatures, it can be identified as the interaction-driven layer antiferromagnetic state in bilayer graphene[32,40,43] (see Section 2.3). Secondly, in case the LAF state is present, the conductance at charge neutrality σ_{CNP} shows an activated T dependence and the width of the ground state in electric field ΔE^{SP} increases for decreasing T. As both quantities correlate with the critical temperature T_c for several devices, they can be taken as measures of the strength of the LAF state. As a result, the spectrum of σ_{CNP} and ΔE^{SP} observed across all devices demonstrates a continuous weakening of the spontaneously gapped state. As possible cause for this distribution, differences in the fabrication process or in the residual charge disorder present can be excluded since no systematic dependencies can be detected. Moreover, both devices with a stacking domain wall show an intermediately strong LAF ground state, hence their presence cannot explain its weakening or absence, although their presence has been made responsible for unusual transport signatures in the past[36,134]. Furthermore, the appearance of additional stacking domain walls owing to high current annealing as reported in literature[134] can be excluded by measurements prior and after the annealing procedure.

Nonetheless, ΔE^{SP} depends on the current density required to observe saturation during annealing. The heat generated by the electric current during annealing leads to partial evaporation[22] and most likely to a redistribution of contaminants within each layer towards the cooler contacts, instead of between the two layers. Thus, the process effectively removes lateral charge fluctuations producing spatially varying in-plane electric fields[135] (i.e. residual charge disorder), yet charge imbalances between the two layers creating spatially varying out-of-plane electric fields[135,136] (i.e. electric field disorder) remain. Hereby, devices with shorter channels exhibit higher shares of contaminated regions near the contacts compared to devices with long channels. Moreover, the contacts act as heat sink[22], i.e. the wider the contacts the more likely the movement of contaminations towards them. Hence, electric field disorder is expected to be primarily present in devices with short channels and wide contacts. This can explain the observed dependency of ΔE^{SP} on the device geometry, since the presence of electric field disorder allows for the formation of domains of competing spontaneously gapped states other than a uniform LAF state[52] within a device. Then, the LAF state is effectively suppressed, which results in a smaller ΔE^{SP}. Spontaneous DWs separating these domains, which are known to carry gapless edge modes[52], result in a finite σ_{CNP}.

To find further proof of electric field disorder, the quantum Hall regime was investigated. Conductance maps as a function of charge carrier density and electric field at $B = 3$ T reveal distinct behaviors of the phase transitions between (partially) layer polarized $\upsilon = \pm 1, \pm 2$ broken-symmetry states of opposite layer polarization around zero electric field, when comparing all devices. For example, the width of the phase transition in electric field between the $\upsilon = -2$ state at $E > 0$ and the one at $E < 0$, $\Delta E^{\nu=-2}$, ranges from peak-like to a broad phase transition region with high

conductance. Again, a continuous distribution of $\Delta E^{\nu=-2}$ is observed. Since $\Delta E^{\nu=-2}$ correlates well to ΔE^{SP}, electric field disorder as common cause seems likely. Moreover, a varying number of spontaneously formed domains with states of opposite layer polarization present can again explain the continuous distribution. The resulting spontaneous domain walls carry charge[54], which results in the enhanced conductance at the transition regions. Similar findings are made when examining the phase transition between the canted antiferromagnetic and fully layer polarized $\upsilon = 0$ phases. To this end, conductance maps as a function of electric and magnetic field at zero charge carrier density were recorded. Again, the extend of the phase transition in electric field ranged from peak-like to broadened and correlates to ΔE^{SP}. Once more, the picture electric field disorder causing the formation of multiple domains of CAF and FLP states in the transition region is plausible[75].
Overall, the results provide a unique insight into the role of electric field disorder on broken-symmetry states and contribute to solving the debate about the interaction-driven ground state of ultraclean bilayer graphene.

6.2 Outlook

The measurements show that mainly electric field disorder determines the electric field dependence of various broken-symmetry states. Although stacking DWs were present in some of the devices, it seems they play only a minor role in e.g. suppressing the LAF ground state. In principle, stacking and spontaneously arising DWs should affect the quantum transport in a similar way, however, the number of domains might be crucial. Presumably, the spontaneously emerging domain walls arise in a complex network, whereas the examined devices with stacking fault possessed only a single one, which might well be the reason why the quantum transport was not as strongly affected. In fact, when increasing the number of dislocations, the consequences could be more drastic and comparable to the case of spontaneously arising domains. To examine the influence of the number of domains present within a device, graphene flakes with network-like structures of stacking DWs could be used. Clearly, they can occur naturally[48,57] and have also been found in the course of this thesis (see Figure 6.1). One major difficulty might be, however, the mobility of stacking DWs. Although single dislocations seem to be stable during processing and current annealing[133], in case several are close to each other, they could possibly merge, as reported in literature[48,88].
Another interesting aspect worth further experimental effort is the magnetic field dependence of the investigated phase transition regions. In the present study, phase transitions between distinct (partially) layer polarized $\upsilon = \pm 1, \pm 2$ phases and between the canted antiferromagnetic and fully layer polarized $\upsilon = 0$ phases were examined. The explanation for the increased conductance within the transition regions is the formation of domains, as reported in literature[54,75]. However, in both regimes, evidence for the emergence of new phases at high magnetic fields have been found: Around zero electric field, where the (partially) layer polarized $\upsilon = \pm 1, \pm 2$ phases are unstable,

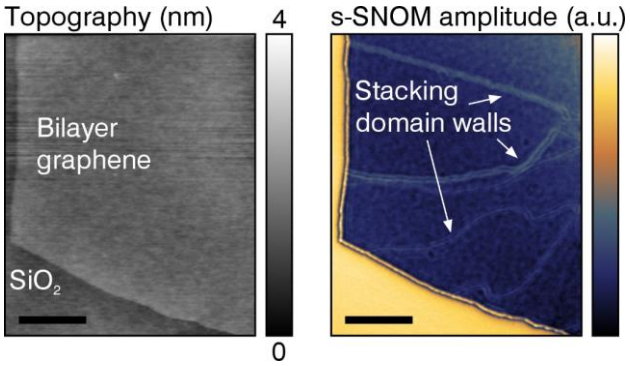

Figure 6.1 Network of stacking domain walls in bilayer graphene. *Topography (left) and s-SNOM amplitude image (right) of a bilayer graphene flake with a network-like structure of stacking domain walls present. Scale bars: 1 µm.*

layer unpolarized $\upsilon = \pm 1$ and ± 2 phases appear[82,84]. Similarly, within the transition region of the canted antiferromagnetic to the fully layer polarized phase, an intermediate phase has been reported[76,85]. In both cases, the additional phases only occur for very high magnetic fields. Future measurements could examine the emergence of these phases and how they are affected by disorder. Presumably, spontaneously formed domains and/or the presence of stacking DWs have an impact on the critical magnetic field needed for their emergence. Hence, investigating the magnetic field dependence of the conductance within these regimes could be worth additional effort. Measurements at very high magnetic fields would be needed on several devices with different amounts of disorder present.

Moreover, an interesting subject for future studies is the influence of spontaneously forming domains on the quantum transport in heterostructures consisting of hexagonal boron nitride and bilayer graphene. The phase transitions between the canted antiferromagnetic and fully layer polarized $\upsilon = 0$ phases show similarities to the ones observed in freestanding devices, since a peak-like[62,76,87] and an extended region of enhanced conductance in electric field[87] have been identified. This suggests that an analogous, underlying phenomena controls the appearance of the phase transitions in heterostructures. However, a major difference to freestanding devices lies of course in the fabrication process. In particular, current annealing is redundant in heterostructures, as on the one hand the bilayer graphene flakes are not exposed to PMMA or something alike during processing[18], and on the other hand applying a current will hardly move any residues trapped within the heterostructures. Still, examining the phase transition within hexagonal boron nitride/bilayer graphene devices could be worth further effort. This hold true for phase transitions of higher Landau levels, since they are mostly inaccessible when using freestanding devices owing to the limited voltage and hence charge carrier density range applicable. Similar to the broken-symmetry states of the zeroth Landau level, they exhibit multiple phase transitions in electric field[75], which might be susceptible to the spontaneous formation of domains.

7 Conclusion

In the course of this thesis, the quantum transport in ultraclean, freestanding Bernal-stacked bilayer graphene was investigated. Special attention was given to any stacking domain walls present within the examined bilayer graphene flakes. To this end, scattering-type scanning near-field optical microscopy was conducted prior to contacting to detect any stacking faults present in the selected flakes. Subsequently, dually gated field-effect transistors were fabricated. The dual-gate geometry was exploited to independently tune charge carrier density and electric field in the bilayer graphene during magnetotransport measurements at low temperatures.

In the first part, clean bilayer graphene devices without any domain wall present were used to investigate the most exotic of the competing quantum Hall phases, which appear owing to spontaneous chiral symmetry breaking close to charge neutrality towards zero electric and magnetic field. To this end, quantum Hall states with a conductance of $\pm 2\ e^2\ h^{-1}$ were tracked for decreasing magnetic field. It was found that they survive down to anomalously small magnetic fields within a certain range of electric fields. Moreover, a magnetic hysteresis of the conductance was observed, only appearing at a specific filling factor of $\nu = \pm 2$ and intermediately strong electric field. These findings are consistent with the emergence of an octet of quantum anomalous Hall phases and can be explained by the coupling of electric and magnetic field to the partial layer polarization and substantial orbital moment of the appearing phases. Each of the phases is unique in its combination of polarities of applied electric as well as magnetic field and charge carrier density. In addition, temperature dependent investigations of the $\nu = -2$ QAH phase indicate a surprisingly high stability, as its activation energy gap is comparable to the one observed for the robust $\nu = -4$ state. The observed quantum anomalous Hall effect in Bernal-stacked bilayer graphene differs from the one observed in magnetically doped topological insulators, as it is primarily of orbital nature due to vanishing spin-orbit coupling. Moreover, it is caused by spontaneous chiral symmetry breaking, unlike the quantum anomalous Hall effect appearing in the artificially designed band structure of moiré heterostructures.

In the second part, devices with a stacking domain wall connecting the source-drain contacts were examined and compared to defect-free samples. Tracking the resistance as a function of electric field for zero magnetic field revealed a saturation at $R \approx 8.5$ kΩ in case a stacking fault is present. This observation confirms topologically valley transport along the domain wall separating AB and

BA stacking regions, as reported in previous studies. With a mean free path of $\lambda_m \approx 2.2$ µm, the gapless kink states show a surprisingly high quality. By additionally applying a magnetic field, a complex interplay between topological valley transport originating from the domain wall and quantum Hall edge transport arising from the emerging broken-symmetry quantum Hall phases was observed. More precisely, for low magnetic fields, the conductance remains almost constant at approximately $4\,e^2\,h^{-1}$ within the complete eight-fold degenerate zeroth Landau level, since the initial four kink states per direction within the $\upsilon = 0$ state are successively traded with increasing filling factor for quantum Hall edge states. However, the conductance originating from the kink states decreases at high magnetic fields. Possible explanations are the formation of minigaps in the case of the $\upsilon = 0$ canted antiferromagnetic phase and the occurrence of intervalley backscattering for the $\upsilon = \pm 1, \pm 2$ quantum Hall states. Lastly, a set of temperature dependent measurements confirmed both a metallic behavior of the domain wall as well as a negligible impact of the domain wall on the quantum transport within the $\upsilon = \pm 4$ quantum Hall states. Overall, the presence of dislocations drastically alters the quantum transport in bilayer graphene, as both topological valley and quantum Hall edge transport need to be considered in the vicinity of the eight-fold degenerate zeroth Landau level.

In the third part, in total eleven devices, two of which exhibit a stacking domain wall but not connecting source and drain, were fabricated to investigate the true interaction-driven ground state of bilayer graphene. Comparing the transport signatures at charge neutrality for all devices revealed major discrepancies ranging from the emergence of an insulating state to a finite conductance and a resulting nonmonotonic or monotonic behavior of the resistance for increasing electric field, respectively. In the former case, an activated temperature dependence of the conductance as well as an expanding of the insulating phase in electric field with decreasing temperature was found. The gapped phase could be attributed to the layer antiferromagnetic state, and the distribution of behaviors across all devices to its continuous weakening. Any stacking domain walls present in a device seem not to be the major cause for the weakening. Instead, the continuous behavior can be explained by a variable amount of electric field disorder present, which seems uncorrelated to residual charge disorder but rather depends on the device geometry. Its presence allows for the spontaneous formation of domains of competing spontaneously gapped states other than a uniform LAF state within a device. Further proof for the presence of electric field disorder was found in the quantum Hall regime: Phase transitions between the broken-symmetry $\upsilon = \pm 1, \pm 2$ states of opposite layer polarization arising around zero electric field as well as phase transitions between the canted antiferromagnetic and the two fully layer polarized $\upsilon = 0$ phases show similar distributions of behaviors when comparing several devices. The widths of the phase transitions in electric field correlate well with the strength of the layer antiferromagnetic ground state, highlighting their common cause. The observations provide a unique insight into the role of electric field disorder on the appearance of broken-symmetry states and contribute to solving the debate

about the interaction-driven ground state of bilayer graphene.

In summary, the results presented in this thesis give new insights into correlated physics in the naturally occurring Bernal-stacked bilayer graphene, and proof that it retains many unexplored and intriguing physical phenomena despite being subject of intensive research for more than a decade. At first, the findings demonstrate that the seemingly simple system can exhibit exotic phases such as the quantum anomalous Hall effect without the need of delicate moiré heterostructures. Here, more effort on the fabrication of four-terminal devices is needed in the future to enable the differentiation of longitudinal and Hall resistance. In addition, new discoveries on the quantum anomalous Hall effect are expected since the observed phase is not uniquely tied to bilayer graphene but is instead universal to its rhombohedral cousins. Secondly, the measurements on structural domain walls show that they can greatly impact the quantum transport and emphasizes the inevitable need to regard them in future studies. It might be worth to consider precise near-field imaging, which would allow distinction between tensile and shear domain walls and their unique impact on the quantum transport in bilayer graphene. Lastly, the extensive studies on eleven dually gated devices help in solving the longstanding debate about the ground state in bilayer graphene and explain the corresponding ambiguous observations from literature. Moreover, the observations underline the importance of further investigations on the impact of electric field disorder in general, as it should be universal to all two-dimensional materials.
Together, the results highlight bilayer graphene as a highly tunable platform to investigate fundamental many-body phenomena and open the possibility for exciting developments in low-dissipation electronics or quantum information science.

A Publications

In the following, the publications in which I contributed are listed chronologically and sorted for being part or not being part of this thesis.

Peer-reviewed first author publications which are part of this cumulative thesis:

Quantum Anomalous Hall Octet Driven by Orbital Magnetism in Bilayer Graphene
F. R. Geisenhof, F. Winterer, A. M. Seiler, J. Lenz, T. Xu, F. Zhang, and R. T. Weitz
Nature **598**, 53 – 58 (2021)
Ref.[83], the full article is shown in Appendix A1 including the extended data.

Interplay between Topological Valley and Quantum Hall Edge Transport
F. R. Geisenhof, F. Winterer, A. M. Seiler, J. Lenz, I. Martin, and R. T. Weitz
Nat. Commun. **13**, 4187 (2022)
Ref.[94], the full article is shown in Appendix A2, the supplementary information in Appendix B1.

Impact of Electric Field Disorder on Broken-Symmetry States in Ultraclean Bilayer Graphene
F. R. Geisenhof, F. Winterer, A. M. Seiler, J. Lenz, and F. Zhang, and R. T. Weitz
Nano Lett. **22**, 7378 – 7385 (2022)
Ref.[133], the full article is shown in Appendix A3, the supplementary information in Appendix B2.

Further peer-reviewed publications:

Vertical, Electrolyte-Gated Organic Transistors Show Continuous Operation in the MA cm^{-2} Regime and Artificial Synaptic Behavior
J. Lenz, F. del Giudice, **F. R. Geisenhof**, F. Winterer, and R. Thomas Weitz
Nat. Nanotechnol., **14**, 579–585 (2019)

Appendix A: Publications

Anisotropic Strain-Induced Soliton Movement Changes Stacking Order and Band Structure of Graphene Multilayers: Implications for Charge Transport
F. R. Geisenhof, F. Winterer, S. Walkolbinger, T. D. Gokus, Y. C. Durmaz, D. Priesack, J. Lenz, F. Keilmann, K. Watanabe, T. Taniguchi, R. Guerrero-Avilés, M. Pelc, A. Ayuela, and R. T. Weitz
ACS Appl. Nano Mater. **2**, 6067–6075 (2019)

Locally-Triggered Hydrophobic Collapse Induces Global Interface Self-Cleaning in van-der-Waals Heterostructures at Room-Temperature
S. Wakolbinger, **F. R. Geisenhof**, F. Winterer, S. Palmer, J. G. Crimmann, K. Watanabe, T. Taniguchi, F. Trixler, and R. T. Weitz
2D Mater. **7**, 035002 (2020)

Synthesis of Large-Area Rhombohedral Few-Layer Graphene by Chemical Vapor Deposition on Copper
C. Bouhafs, S. Pezzini, **F. R. Geisenhof**, N. Mishra, V. Mišeikis, Y, Niu, C. Struzzi, R. T. Weitz, A. A. Zakharov, S. Forti, C. Coletti
Carbon **177**, 282-290 (2021)

High-Performance Vertical Organic Transistors of Sub-5 nm Channel Length
J. Lenz, A. M. Seiler, **F. R. Geisenhof**, F. Winterer, K. Watanabe, T. Taniguchi, and R. T. Weitz
Nano Lett. **21** (10), 4430-4436 (2021)

Spontaneous Gully-Polarized Quantum Hall States in ABA Trilayer Graphene
F. Winterer, A. M. Seiler, A. Ghazaryan, **F. R. Geisenhof**, K. Watanabe, T. Taniguchi, M. Serbyn, and R. T. Weitz
Nano Lett. **22** (8), 3317-3322 (2022)

Quantum Cascade of Correlated Phases in Trigonally Warped Bilayer Graphene
A. M. Seiler, **F. R. Geisenhof**, F. Winterer, K. Watanabe, T. Taniguchi, T. Xu, F. Zhang, and R. T. Weitz
Nature **608**, 298–302 (2022).

Rhombohedral Trilayer Graphene Being More Stable Than Its Bernal Counterpart
R. Guerrero-Avilés, M. Pelc, **F. R. Geisenhof**, R. T. Weitz, and A. Ayuela
Nanoscale **14**, 16295-16302 (2022)

A.1 Quantum Anomalous Hall Octet Driven by Orbital Magnetism in Bilayer Graphene

Fabian R. Geisenhof, Felix Winterer, Anna M. Seiler, Jakob Lenz, Tianyi Xu, Fan Zhang, and R. Thomas Weitz

Nature **598**, 53 – 58 (2021)
DOI: 10.1038/s41586-021-03849-w

Abstract

The quantum anomalous Hall (QAH) effect—a macroscopic manifestation of chiral band topology at zero magnetic field—has been experimentally realized only by the magnetic doping of topological insulators [1–3] and the delicate design of moiré heterostructures [4–8]. However, the seemingly simple bilayer graphene without magnetic doping or moiré engineering has long been predicted to host competing ordered states with QAH effects [9–11]. Here we explore states in bilayer graphene with a conductance of 2 $e^2\ h^{-1}$ (where e is the electronic charge and h is Planck's constant) that not only survive down to anomalously small magnetic fields and up to temperatures of five kelvin but also exhibit magnetic hysteresis. Together, the experimental signatures provide compelling evidence for orbital-magnetism-driven QAH behavior that is tunable via electric and magnetic fields as well as carrier sign. The observed octet of QAH phases is distinct from previous observations owing to its peculiar ferrimagnetic and ferrielectric order that is characterized by quantized anomalous charge, spin, valley and spin–valley Hall behavior [9].

References:

[1] Chang, C.-Z. et al. *Science* **340**, 167–170 (2013).
[2] Tenasini, G. et al. *Phys. Rev. Res.* **2** (2020).
[3] Zhao, Y.-F. et al. *Nature* **588**, 419–423 (2020).
[4] Tschirhart, C. L. et al. *Science* **372**, 1323–1327 (2021).
[5] Sharpe, A. L. et al. *Science* **365**, 605–608 (2019).
[6] Serlin, M. et al. *Science* **367**, 900–903 (2020).
[7] Polshyn, H. et al. *Nature* **588**, 66–70 (2020).
[8] Chen, G. et al. *Nature* **579**, 56–61 (2020).
[9] Zhang, F., Jung, J., Fiete, G. A., Niu, Q. & MacDonald, A. H. *Phys. Rev. Lett.* **106**, 156801 (2011).
[10] Zhang, F. *Synth. Met.* **210**, 9–18 (2015).

[11] Nandkishore, R. & Levitov, L. *Phys. Rev. B* **82** (2010).

Contribution

I fabricated all devices, conducted all measurements, and performed the data analysis. The first draft, apart from some theoretical sections, was written by me. Furthermore, I produced the final version of the publication and designed all figures.

Article

Quantum anomalous Hall octet driven by orbital magnetism in bilayer graphene

https://doi.org/10.1038/s41586-021-03849-w

Received: 16 April 2021

Accepted: 22 July 2021

Published online: 6 October 2021

Check for updates

Fabian R. Geisenhof[1], Felix Winterer[1], Anna M. Seiler[1], Jakob Lenz[1], Tianyi Xu[2], Fan Zhang[2]✉ & R. Thomas Weitz[1,3,4,5]✉

The quantum anomalous Hall (QAH) effect—a macroscopic manifestation of chiral band topology at zero magnetic field—has been experimentally realized only by the magnetic doping of topological insulators[1–3] and the delicate design of moiré heterostructures[4–8]. However, the seemingly simple bilayer graphene without magnetic doping or moiré engineering has long been predicted to host competing ordered states with QAH effects[9–11]. Here we explore states in bilayer graphene with a conductance of $2\,e^2\,h^{-1}$ (where e is the electronic charge and h is Planck's constant) that not only survive down to anomalously small magnetic fields and up to temperatures of five kelvin but also exhibit magnetic hysteresis. Together, the experimental signatures provide compelling evidence for orbital-magnetism-driven QAH behaviour that is tunable via electric and magnetic fields as well as carrier sign. The observed octet of QAH phases is distinct from previous observations owing to its peculiar ferrimagnetic and ferrielectric order that is characterized by quantized anomalous charge, spin, valley and spin–valley Hall behaviour[9].

Intricate interplay between single-particle effects such as the band topology and many-body effects such as the electron–electron interaction determines the electronic ground states of many low-dimensional systems. An especially interesting class are systems in which quasiparticle Berry curvature gives rise to orbital instead of spin magnetic moments, with the consequence that effects usually requiring substantial spin–orbit coupling and/or intentional magnetic doping can occur spontaneously[9,10]. A prominent example is the quantum anomalous Hall (QAH) phase that displays quantized Hall resistance at zero magnetic field owing to the presence of orbital magnetic order. The QAH effect is characterized by a finite number of topologically protected chiral edge channels. So far, it has been experimentally realized in two distinct types of systems. In magnetically doped topological insulators[1–3], topological properties and broken time-reversal symmetry (caused by spin–orbit coupling and aligned magnetic dopants, respectively) lead to topologically non-trivial Chern bands[12,13]. In these spin Chern insulators, magnetism occurs mainly owing to ordering of electron spin moments. However, a Chern insulator can also emerge solely owing to a spontaneous polarization of the orbital magnetic moments[9,10,14], as recently observed in delicately designed moiré heterostructures[4–8]. In these orbital Chern insulators, orbital magnetism arises because of spontaneous gap opening in the half-filled quasiparticle Dirac bands[9–11,14]. Gapped Dirac bands with non-trivial Berry-curvature-induced orbital magnetic moments have also been predicted[9,15] and observed in naturally occurring purely carbon-based systems such as bilayer graphene[16,17] and its rhombohedral cousins[18]. However, orbital magnetism[9] has not been clearly pinpointed experimentally in such a simple system as pure bilayer graphene, despite theoretical studies[9–11] predicting that some of the competing ground states should exhibit non-vanishing exchange-interaction-driven quantized Hall conductivities at zero magnetic field.

Here we report the observation of filling factor $\nu = \pm 2$ states at anomalously small magnetic fields of about 20 mT in suspended dually gated bilayer graphene devices. In addition, we observe field tuning and magnetic hysteresis, which strongly evidences that the $\nu = \pm 2$ states are ferrimagnetic, ferrielectric, QAH phases driven by orbital magnetism in pure bilayer graphene. Using bilayer graphene flakes free of electronically active domain walls[19–21] and previously established processing[22] (Methods, Extended Data Fig. 1), suspended dually gated bilayer graphene devices were fabricated (Fig. 1a).

Sweeping both top and bottom gate voltages, V_t and V_b, at zero magnetic field yields the well known map of the differential conductance, including the interlayer electric-field-induced insulating states as well as the exchange-interaction-induced gapped phase near zero electric field (Fig. 1b)[23–25]. The observation of the latter and the location of the charge neutrality point at $V_t \approx V_b \approx 0$ demonstrates the high quality of the device (note that such a spontaneous gap is universal for rhombohedral few-layer and Bernal even-layer graphene[9,18,26]). The dual-gate structure allows independent tunability of the charge carrier density n and the perpendicular electric field $E_\perp$ (Methods). Sweeping n at $E_\perp = 0$ reveals a residual charge density inhomogeneity of less than 10^9 cm^{-2} (Fig. 1b, inset), underlining the high quality of the device[27] (Methods).

Varying both n and $E_\perp$ while applying a perpendicular magnetic field of $B = 3$ T (Fig. 1c) reveals the lowest quantum Hall plateaus in bilayer graphene with the integer filling factors ranging from $\nu = -4$ to $\nu = 4$ (refs. [23,28–32]), resulting from the spontaneous symmetry breaking in the anomalous $N = 0$ Landau levels. As identified previously, only the $\nu = 0$ and $\nu = \pm 4$ quantum Hall states are resolved at $E_\perp = 0$ (Fig. 1c), whereas

[1]Physics of Nanosystems, Department of Physics, Ludwig-Maximilians-Universität München, Munich, Germany. [2]Department of Physics, University of Texas at Dallas, Richardson, TX, USA. [3]Center for Nanoscience (CeNS), Munich, Germany. [4]Munich Center for Quantum Science and Technology (MCQST), Munich, Germany. [5]1st Physical Institute, Faculty of Physics, University of Göttingen, Göttingen, Germany. ✉e-mail: zhang@utdallas.edu; thomas.weitz@uni-goettingen.de

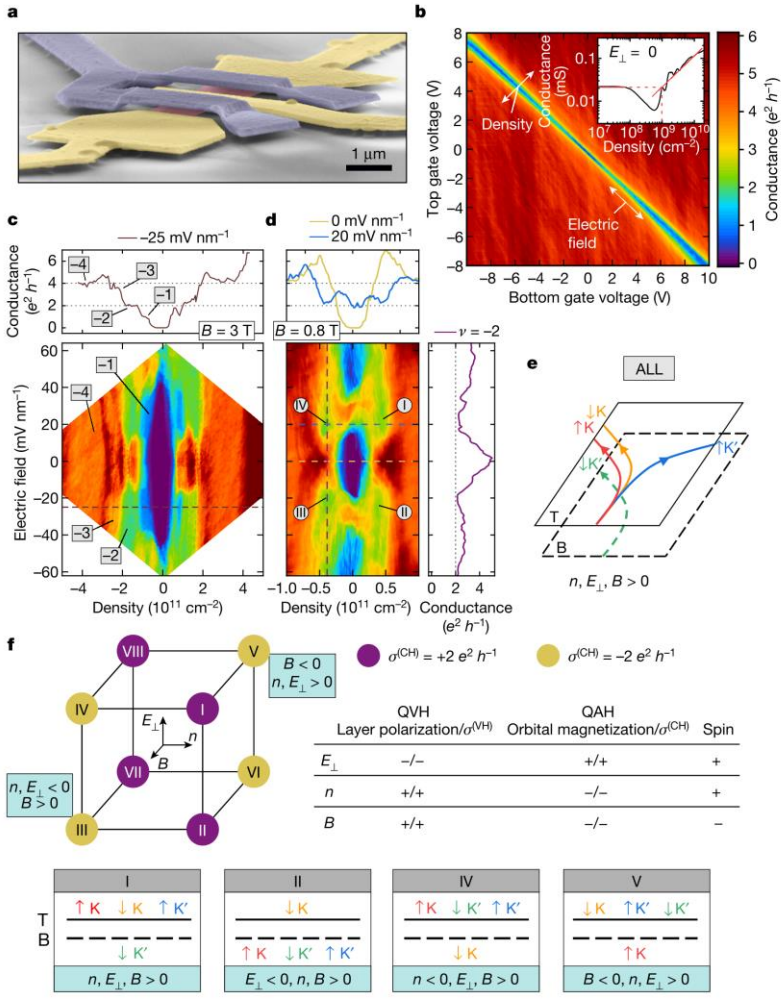

Fig. 1 | Exchange-interaction-driven quantum Hall states in dually gated, freestanding bilayer graphene. a, False-colour scanning electron microscope image of a suspended bilayer graphene device. Contacts, top gate and bilayer graphene are shown in yellow, blue and red, respectively. **b**, Conductance map as a function of top gate voltage and bottom gate voltage at $B = 0$ and $T < 10$ mK. Inset: conductance as a function of charge carrier density at $E_\perp = 0$. The red lines are linear fits and the dashed red lines are guides to the eye, indicating the residual charge carrier inhomogeneity in the device. **c**, **d**, Maps of the conductance as a function of $E_\perp$ and n at $B = 3$ T (**c**) and $B = 0.8$ T (**d**). The roman numerals in **d** label the 'ALL' phases labelled by the same numerals in **f**. **e**, Schematic representation of one 'ALL' QAH phase showing the classical counterpart of its corresponding spontaneous quantum Hall effect for n, $E_\perp$, $B > 0$. T and B refer to the top and bottom graphene layers, respectively. **f**, Top: schematic of the eight different 'ALL' phases and their corresponding Hall conductance $\sigma^{(CH)}$ and how they can be accessed by tuning n, $E_\perp$ and/or B. The table shows the properties of the QVH and QAH species of the 'ALL' octet: the layer polarization and orbital magnetization as well as the valley and charge Hall conductivities, $\sigma^{(VH)}$ and $\sigma^{(CH)}$. +/− indicates whether the observables are even/odd under flipping n, $E_\perp$ or B. Bottom: schematics of the layer polarizations of the four spin–valley species for four exemplary 'ALL' phases.

the $\nu = \pm1$, $\nu = \pm2$ and $\nu = \pm3$ states emerge only at a larger finite electric field[23,32,33]. At a lower magnetic field of $B = 0.8$ T (Fig. 1d), only the $\nu = 0$, $\nu = \pm2$ and $\nu = \pm4$ states emerge. Surprisingly, in contrast to the $\nu = \pm4$ states, the $\nu = \pm2$ states are only stable in an intermediate range of electric field (four green regions in Fig. 1d), that is, both larger and smaller electric fields can destabilize the $\nu = \pm2$ states.

QAH phases in bilayer graphene

Although the $\nu = \pm2$ states in bilayer graphene have been observed previously at $B > 1.2$ T (refs. [23,32]), their exact nature—especially with lowering the magnetic field towards the $B = 0$ limit where one can expect intricate QAH phases and phase transitions as function of electric field—has not been identified previously. The order parameters of these states are particularly interesting, as they can unveil the yet unclear ground state of bilayer graphene in the $B = 0$ limit[9–11,34]. Owing to the quadratic band touching and non-trivial winding numbers, the exchange interaction in bilayer graphene is peculiarly strong and produces non-trivial quasiparticle topological properties[10]; various symmetry-broken states have been suggested as gapped competing ground states[9,11] (Methods, Extended Data Fig. 2, Table 1), with two families of QAH phases exhibiting orbital magnetism[9]. One family manifesting a Hall conductance of 4 e^2 h^{-1} (where

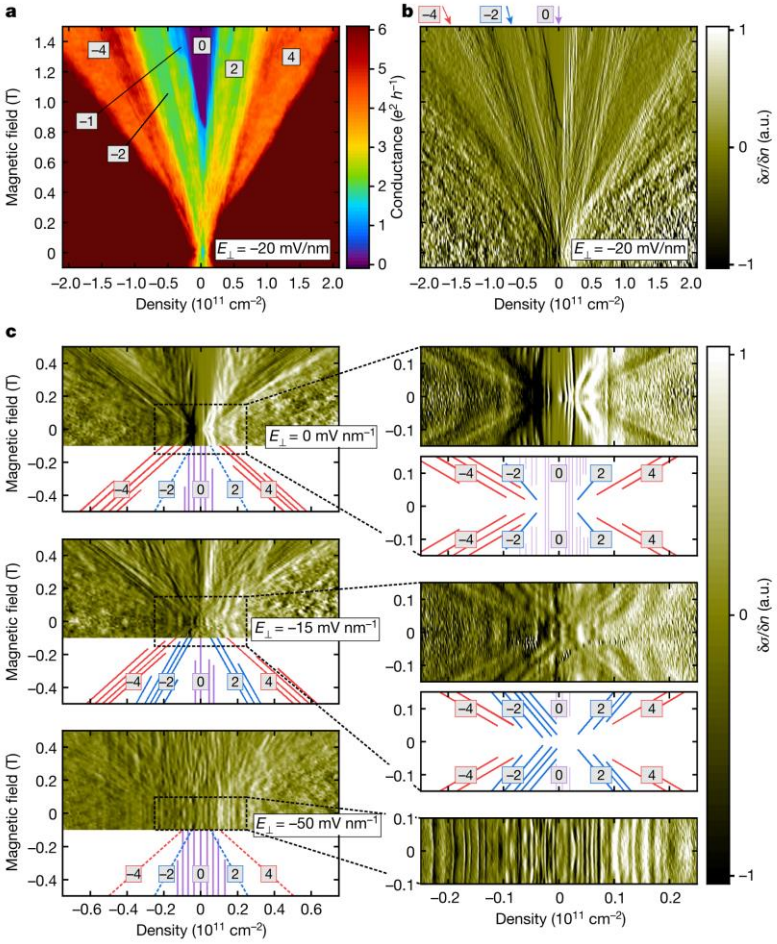

Fig. 2 | Extraordinary stability of the tunable $\nu = \pm 2$ quantum Hall states towards zero magnetic field. a, **b**, Fan diagrams of the differential conductance (**a**) and its derivative $\delta\sigma/\delta n$ (**b**) at $E_\perp = -20$ mV nm^{-1}. The slopes of the $\nu = 0$, $\nu = -2$ and $\nu = -4$ states are indicated with purple, blue and red arrows, respectively. **c**, Left: $\delta\sigma/\delta n$ plotted as a function of magnetic field and density for various $E_\perp$. Right: high-resolution measurements around zero magnetic field. The schematics indicate transconductance fluctuations corresponding to the $\nu = 0$, $\nu = -2$ and $\nu = -4$ states that are shown with purple, blue and red lines, respectively. Solid (dashed) lines indicate the slopes of the respective states in case they are present (absent). All measurements were taken at $T < 10$ mK.

e is the electronic charge and h is Planck's constant), simply termed the QAH phase, is a bilayer counterpart of the Haldane QAH state, in which electrons from different valleys spontaneously polarize to different layers resulting in a Z_2 orbital ferromagnetic order. The other family manifesting Hall conductance of $2\,e^2/h$, termed the 'ALL' phase[9], is even more exotic; as quasiparticles of one spin can choose either one of the two quantum valley Hall (QVH) phases—electrons from both valleys polarize to the same layer resulting in a Z_2 ferroelectric order—whereas quasiparticles of the other spin can choose either one of the two aforementioned QAH phases (Fig. 1e, Methods, Extended Data Fig. 2). In total, there are eight different ALL phases forming an octet with Chern number $C = \pm 2$ or Hall conductance $\sigma^{(CH)} = \pm 2\,e^2/h$ (Extended Data Fig. 3). Markedly, each ALL phase exhibits quantized anomalous charge, spin, valley and spin–valley Hall effects and hence the name[9,10]. Owing to its partial layer polarization, each ALL phase can be stabilized with an interlayer electric field, which fits well with our observations. At very high electric fields, the phase vanishes again, losing stability against a fully layer-polarized QVH phase. Furthermore, applying a perpendicular magnetic field should lower its energy as the field can couple to the quasiparticle orbital magnetization[9,10]. Therefore, switching the sign(s) of the applied n, $E_\perp$ and/or B results in a quantum phase transition between two different ALL phases, as sketched in Fig. 1f. By flipping $E_\perp$ and n, the layer polarization of the QVH species and the orbital magnetization of the QAH species become opposite, respectively. By flipping B, both the orbital magnetization and the spin of the QAH species become opposite. Comparing the measurement at $B = 3$ T (Fig. 1c) and $B = 0.8$ T (Fig. 1d), we find that the electric field range at which the octet emerges at $B = 3$ T expands towards higher electric fields. This demonstrates the enhanced stability of the octet with increasing magnetic field (see Extended Data Fig. 4 for more data on the evolution of these phases in magnetic field).

Tracing the $\nu = \pm 2$ QAH phases to $B = 0$

So far, we have examined the stability of the $\nu = \pm 2$ QAH phases at small but finite magnetic fields. As these phases are driven by the exchange-interaction-induced orbital magnetism, they should, however, also

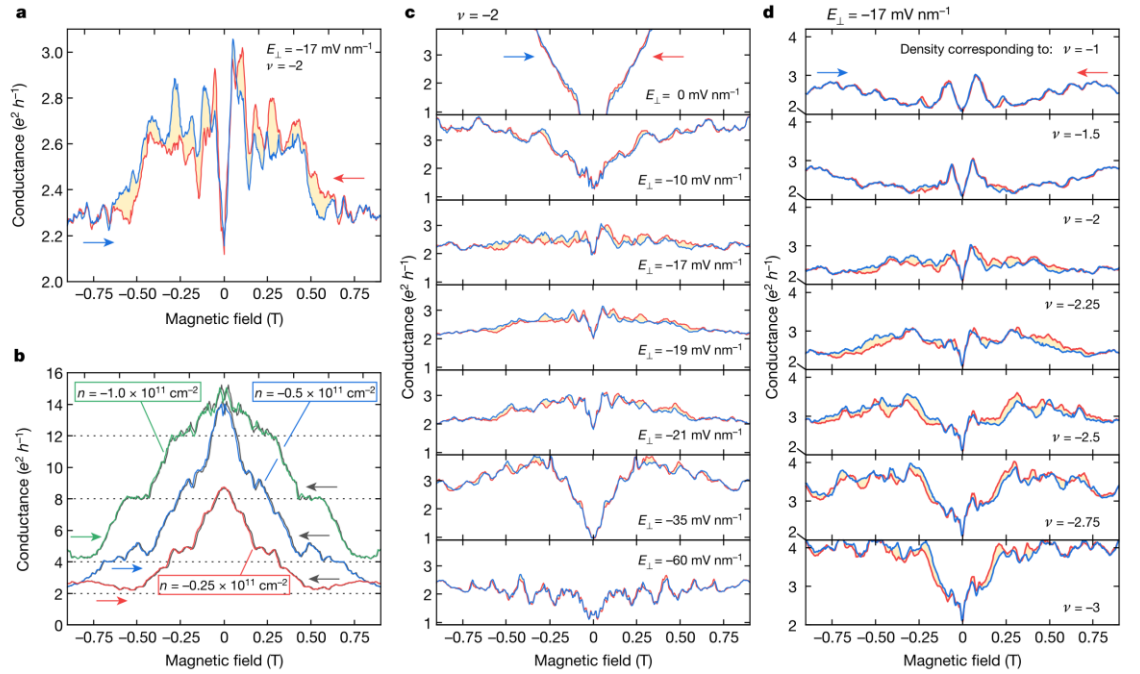

Fig. 3 | Magnetic hysteresis observable in the quantum anomalous Hall ν = −2 in bilayer graphene. a, Two-terminal conductance hysteresis measured for ν = −2 and $E_\perp$ = −17 mV nm^{-1}. The hysteresis loop area is shaded for clarity. The blue and red arrows indicate the forward and reverse sweep, respectively. **b**, Magnetic field dependence of the conductance measured for variable filling factor but fixed charge carrier density at $E_\perp$ = −17 mV nm^{-1}. The forward sweep for n = −0.25 × 10^{11} cm^{-2}, n = −0.5 × 10^{11} cm^{-2} and n = −1.0 × 10^{11} cm^{-2} is shown in red, blue and green, respectively. The reverse sweeps are shown in black. **c**, **d**, Hysteresis of the conductance as a function of electric field at fixed ν = −2 (**c**) and for various filling factors at fixed $E_\perp$ = −17 mV nm^{-1} (**d**). Note that the varying ν in **d** labels the ν = −2 phase at slightly different densities rather than different quantum Hall states. The forward and reverse sweeps are shown in blue and red, respectively, as indicated by the arrows. All measurements were taken at T < 10 mK.

be stable towards B = 0. To this end, we have recorded multiple fan diagrams around B = 0 at various electric fields (Fig. 2). From the fan diagram at $E_\perp$ = −20 mV nm^{-1} (Fig. 2a, b) we can see that both the ν = ±2 and ν = ±4 states emerge already at unusually small magnetic field. We focus here on the ν = ±2 QAH phases, as they previously escaped observation at such low magnetic fields[30,32,35], and because they are the most exotic ones among the competing ground states of bilayer graphene at B = 0: quasiparticles of one spin form a QVH phase whereas those of the other spin form a QAH phase[9–11] (Fig. 1e, Methods). Carefully examining the derivative of the conductance (Fig. 2b) to track fluctuations near incompressible quantum states provides more insight[36,37], as the traceable fluctuations are assignable to specific filling factors using their slopes and can appear even before the corresponding quantum Hall states emerge in conventional magneto-transport measurements. Investigating the derivative of the differential conductance at various electric fields (Fig. 2b, c) demonstrates that both the ν = ±2 and ν = ±4 states already emerge at magnetic fields well below B = 100 mT, but that they differ in their electric field dependences. In contrast to the number of fluctuations at finite B corresponding to the ν = ±4 states, which decreases with increasing negative electric field (Fig. 2c, left), the ν = ±2 states are prominent at $E_\perp$ = −15 mV nm^{-1} but disappear at zero and very high negative electric fields. In addition, high-resolution scans around zero magnetic field (Fig. 2c, right) reveal that the ν = ±2 states are also present for B < 100 mT. In fact, they do persist to B < 20 mT, which is even further than the ν = ±4 states. This provides strong evidence that the QAH ν = ±2 phases are potential ground states of bilayer graphene at B = 0 in addition to the previously identified ν = 0 layer antiferromagnet (LAF) and ν = ±4 QAH phases[23–25,30,35].

The observation that the ν = ±2 states can be stabilized by a combination of B and $E_\perp$ fields is consistent with their partial layer polarizations and orbital magnetic characters. Finally, for very high electric fields, fluctuations with an infinite slope that trace the fully layer-polarized ν = 0 QVH phase dominate the fan diagram (see Extended Data Fig. 5 for more data showing fan diagrams in electric fields).

Orbital-magnetism-driven hysteresis

Although the electric and magnetic field dependences and the stability down to $B \approx 0$ T support the presence of the QAH phases, we have looked for more direct proof of the presence of their orbital magnetism. Indeed, hysteretic behaviour indicative of magnetism is observable in the samples, even though in our two-terminal measurements the absolute contributions of both longitudinal and Hall resistances are measured simultaneously (Methods). As can be seen in Fig 3a, by sweeping the magnetic field at constant ν = −2 and $E_\perp$ = −17 mV nm^{-1}, we have recorded a magnetic hysteresis. Forward and reverse sweeps are mirror symmetric with respect to the B = 0 line, with the hysteretic behaviour starting at about B = ±650 mT. In addition, the hysteresis is highly reproducible upon repeated sweeps and we also observe it in a second device (Extended Data Fig. 6). Sweeping a smaller range than that between B = ±650 mT reduces the hysteresis (Extended Data Fig. 7). This magnetic hysteresis provides consistent evidence for the emergence of orbital magnetism in pure bilayer graphene; notably, such hysteretic behaviour is rare for moiréless purely carbon-based two-dimensional systems[18]. Given the vanishing spin–orbit coupling in bilayer graphene, the magnetism is primarily of orbital nature, which

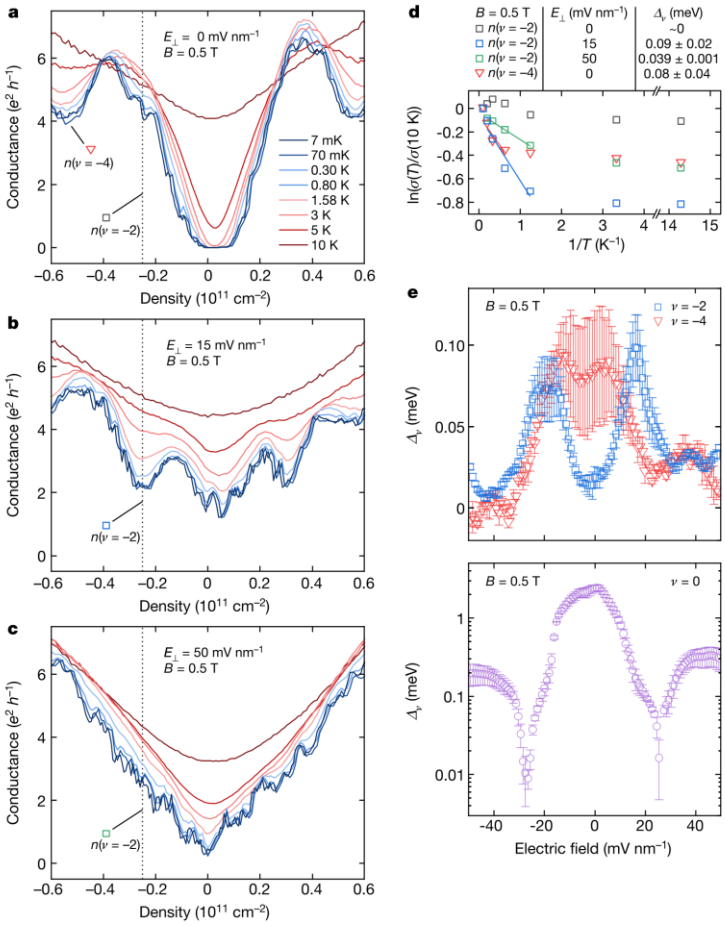

Fig. 4 | Temperature dependence of the $\nu = \pm 2$ and $\nu = \pm 4$ states show distinct electric field dependence. a–**c**, Conductance as a function of n measured for various temperatures for $B = 0.5$ T and fixed electric fields of $E_\perp = 0$ mV nm^{-1} (**a**), $E_\perp = 15$ mV nm^{-1} (**b**) and $E_\perp = 50$ mV nm^{-1} (**c**). The density $n(\nu = -2) = -0.25 \times 10^{11}$ cm^{-2} corresponding to $\nu = -2$ at $B = 0.5$ T is indicated by the vertical line in each plot. **d**, Arrhenius plots of the conductance (normalized by its value at 10 K) measured at $n(\nu = -2)$ for $E_\perp = 0$ mV nm^{-1} (black squares), 15 mV nm^{-1} (blue squares) and 50 mV nm^{-1} (green squares) are shown. In addition, the data at $n(\nu = -4)$ and $E_\perp = 0$ mV nm^{-1} are shown with red triangles. The coloured lines are linear fits to the corresponding datasets. **e**, Electric field evolution of the activation gaps in the $\nu = 0$, $\nu = -2$ and $\nu = -4$ states. The error bars originate from the uncertainty from the linear fits.

stems from the opposite mean-field gaps in the two valleys in one of the two spin species[9–11] (Fig. 1e, Methods).

The intimate relation of the orbital magnetism to the $\nu = \pm 2$ QAH phases can be further validated by a series of test measurements. First, cyclic B sweeps for fixed n (and consequently varying ν) do not show hysteretic behaviour (Fig. 3b). These measurements were performed at $n = -0.25 \times 10^{11}$ cm^{-2}, $n = -0.5 \times 10^{11}$ cm^{-2} and $n = -1.0 \times 10^{11}$ cm^{-2} corresponding to the quantum Hall states of $\nu = -1$, $\nu = -2$ and $\nu = -4$ at $B = 1$ T, respectively. This implies that when the magnetic field is swept towards $B = 0$, the sample leaves the $\nu = -2$ QAH phase and reaches quantum Hall states with higher filling factors up to $\nu = -12$ for $n = -1.0 \times 10^{11}$ cm^{-2}, far away from the $\nu = -2$ QAH phase.

A second set of test measurements addresses the electric field dependence in the region where the $\nu = -2$ QAH phase is stable (Fig. 3c). Consistently, at $E_\perp = 0$, we do not observe any hysteretic behaviour as a $\nu = -2$ state is not observable here. At $E_\perp = -10$ mV nm^{-1}, in agreement with the observations from the fan diagrams (Fig. 2), hysteretic behaviour starts to emerge, and the hysteresis loop area reaches its maximum at $E_\perp = -17$ mV nm^{-1}. With increasing negative electric field, the hysteresis decreases again and vanishes completely at $E_\perp = -60$ mV nm^{-1}, where the fully layer-polarized $\nu = 0$ QVH phase dominates. These observations are consistent with the electric field dependence of the $\nu = -2$ state in Fig. 2 and the partial layer polarization of the $\nu = -2$ QAH phase in Fig. 1e.

Finally, the hysteretic behaviour vanishes at constant finite electric field if the filling factor is detuned substantially away from $\nu = -2$ (Fig. 3d). As the $\nu = -1$ and $\nu = -3$ quantum Hall states do not emerge at $B < 1$ T, all nominal fillings in the range of $-1 < \nu < -3$ correspond to the $\nu = -2$ state. In this range, we observe hysteresis with the loop area reaching its maximum at $\nu = -2.5$. At higher or lower nominal filling, for example, $\nu = -1$ or $\nu = -3$, the hysteresis almost vanishes.

Activation gaps depending on electric field

As a final test of the stability of the $\nu = -2$ QAH phase, we have investigated its temperature dependence at various electric fields at $B = 0.5$ T (Fig. 4); see Extended Data Fig. 8 for the full temperature-dependent

transport data. Although a quantitative estimation of the bulk gap in the $\nu = -2$ state via calculation of its activation energy $\Delta_{\nu=-2}$ is challenging due to the potential presence of disorder, we use such estimates for a relative judgement of the stability of the various observed phases. Figure 4d shows an Arrhenius plot[8] of the conductance at $n(\nu = -2)$ and various electric fields. As the temperature dependence of the conductance[23] follows $\sigma \propto \exp(-\Delta_\nu/(2k_BT))$, where T is the temperature and k_B is Boltzmann constant, in the semi-log graph we can use a linear fit to calculate the energy gap. At zero electric field (Fig. 4a), the $\nu = -2$ state does not persist to $B = 0.5$ T as we have seen in the fan diagrams, and consequently the temperature dependence is very small, indicating a vanishing energy gap. By contrast, at a finite electric field of $E_\perp = 15$ mV nm^{-1}, there is an evident temperature dependence (Fig. 4b) with an energy gap of $\Delta_{\nu=-2} = (0.09 \pm 0.02)$ meV. Applying an even higher electric field of $E_\perp = 50$ mV nm^{-1} (Fig. 4c), the $\nu = -2$ state becomes less stable with a smaller $\Delta_{\nu=-2} = (0.039 \pm 0.001)$ meV, again consistent with its predicted partial layer polarization. We point out that the gap energies measured by activation only give lower bounds for the real gaps due to the presence of local disorder (Methods), but their absolute magnitudes can be put into perspective by comparing them with the gaps of the $\nu = \pm 4$ and $\nu = 0$ states as functions of electric field, as shown in Fig. 4e. The behaviour of the $\nu = 0$ state with a large gap of $\Delta_{\nu=0} = 3$ meV at zero electric field, a vanishing gap for an intermediate electric field and a reappearance for a high electric field is consistent with the observation of the phase transition from the interaction-driven layer-balanced gapped LAF phase to the electric-field-induced fully layer-polarized gapped QVH state[23,24]. The activation gaps of the $\nu = -4$ and $\nu = -2$ states show very different electric field dependencies but rather similar magnitudes, with $\Delta_{\nu=-4} = (0.08 \pm 0.04)$ meV at $E_\perp = 0$ mV nm^{-1} and $\Delta_{\nu=-2} = (0.09 \pm 0.02)$ meV at $E_\perp = 15$ mV nm^{-1}. This observation is surprising, as in previous experiments $\Delta_{\nu=-4} > \Delta_{\nu=-2}$ has been found[30,32,38]. Whereas these previous measurements of the $\nu = \pm 2$ and $\nu = \pm 4$ states were performed at larger magnetic fields or without an independent control of $E_\perp$ and n, where the QAH $\nu = \pm 2$ phases may be unstable, the surprising robustness of the $\nu = \pm 2$ states evidenced by the larger activation gaps arises from the electric field coupling to the layer polarization and the magnetic field coupling to the orbital magnetization of the quasiparticles.

Outlook

Since the current measurements have been performed on two-terminal devices, future measurements using a four-terminal geometry[35,39] could distinguish between longitudinal and Hall resistances and determine possible switching mechanisms of the exotic ordering of such $\nu = \pm 2$ QAH phases by using both magnetic and electric fields. Finally, applications in low-dissipation electronics or quantum information science[40] could be exciting developments.

Online content

Any methods, additional references, Nature Research reporting summaries, source data, extended data, supplementary information, acknowledgements, peer review information; details of author contributions and competing interests; and statements of data and code availability are available at https://doi.org/10.1038/s41586-021-03849-w.

1. Chang, C.-Z. et al. Experimental observation of the quantum anomalous Hall effect in a magnetic topological insulator. *Science* **340**, 167–170 (2013).
2. Tenasini, G. et al. Giant anomalous Hall effect in quasi-two-dimensional layered antiferromagnet $Co_{1/3}NbS_2$. *Phys. Rev. Res.* **2** (2020).
3. Zhao, Y.-F. et al. Tuning the Chern number in quantum anomalous Hall insulators. *Nature* **588**, 419–423 (2020).
4. Tschirhart, C. L. et al. Imaging orbital ferromagnetism in a moiré Chern insulator. *Science* **372**, 1323–1327 (2021).
5. Sharpe, A. L. et al. Emergent ferromagnetism near three-quarters filling in twisted bilayer graphene. *Science* **365**, 605–608 (2019).
6. Serlin, M. et al. Intrinsic quantized anomalous Hall effect in a moiré heterostructure. *Science* **367**, 900–903 (2020).
7. Polshyn, H. et al. Electrical switching of magnetic order in an orbital Chern insulator. *Nature* **588**, 66–70 (2020).
8. Chen, G. et al. Tunable correlated Chern insulator and ferromagnetism in a moiré superlattice. *Nature* **579**, 56–61 (2020).
9. Zhang, F., Jung, J., Fiete, G. A., Niu, Q. & MacDonald, A. H. Spontaneous quantum Hall states in chirally stacked few-layer graphene systems. *Phys. Rev. Lett.* **106**, 156801 (2011).
10. Zhang, F. Spontaneous chiral symmetry breaking in bilayer graphene. *Synth. Met.* **210**, 9–18 (2015).
11. Nandkishore, R. & Levitov, L. Quantum anomalous Hall state in bilayer graphene. *Phys. Rev. B* **82** (2010).
12. Yu, R. et al. Quantized anomalous Hall effect in magnetic topological insulators. *Science* **329**, 61–64 (2010).
13. Zhang, F., Kane, C. L. & Mele, E. J. Surface state magnetization and chiral edge states on topological insulators. *Phys. Rev. Lett.* **110**, 46404 (2013).
14. Zhu, J., Su, J.-J. & MacDonald, A. H. Voltage-controlled magnetic reversal in orbital Chern insulators. *Phys. Rev. Lett.* **125**, 227702 (2020).
15. Xiao, D., Yao, W., Niu, Q. Valley-contrasting physics in graphene: magnetic moment and topological transport. *Phys. Rev. Lett.* **99**, 236809 (2007).
16. Lee, Y. et al. Tunable valley splitting due to topological orbital magnetic moment in bilayer graphene quantum point contacts. *Phys. Rev. Lett.* **124**, 126802 (2020).
17. Ju, L. et al. Tunable excitons in bilayer graphene. *Science* **358**, 907–910 (2017).
18. Shi, Y. et al. Electronic phase separation in multilayer rhombohedral graphite. *Nature* **584**, 210–214 (2020).
19. Jiang, L. et al. Soliton-dependent plasmon reflection at bilayer graphene domain walls. *Nat. Mater.* **15**, 840–844 (2016).
20. Ju, L. et al. Topological valley transport at bilayer graphene domain walls. *Nature* **520**, 650–655 (2015).
21. Geisenhof, F. R. et al. Anisotropic strain-induced soliton movement changes stacking order and band structure of graphene multilayers. Implications for charge transport. *ACS Appl. Nano Mater.* **2**, 6067–6075 (2019).
22. Moser, J., Barreiro, A. & Bachtold, A. Current-induced cleaning of graphene. *Appl. Phys. Lett.* **91**, 163513 (2007).
23. Weitz, R. T., Allen, M. T., Feldman, B. E., Martin, J. & Yacoby, A. Broken-symmetry states in doubly gated suspended bilayer graphene. *Science* **330**, 812–816 (2010).
24. Velasco, J. et al. Transport spectroscopy of symmetry-broken insulating states in bilayer graphene. *Nat. Nanotechnol.* **7**, 156–160 (2012).
25. Freitag, F., Trbovic, J., Weiss, M. & Schönenberger, C. Spontaneously gapped ground state in suspended bilayer graphene. *Phys. Rev. Lett.* **108**, 76602 (2012).
26. Nam, Y., Ki, D.-K., Soler-Delgado, D. & Morpurgo, A. F. A family of finite-temperature electronic phase transitions in graphene multilayers. *Science* **362**, 324–328 (2018).
27. Nam, Y., Ki, D.-K., Soler-Delgado, D. & Morpurgo, A. F. Electron–hole collision limited transport in charge-neutral bilayer graphene. *Nat. Phys.* **13**, 1207–1214 (2017).
28. Zhao, Y., Cadden-Zimansky, P., Jiang, Z. & Kim, P. Symmetry breaking in the zero-energy Landau level in bilayer graphene. *Phys. Rev. Lett.* **104**, 66801 (2010).
29. Li, J., Tupikov, Y., Watanabe, K., Taniguchi, T. & Zhu, J. Effective Landau level diagram of bilayer graphene. *Phys. Rev. Lett.* **120**, 47701 (2018).
30. Martin, J., Feldman, B. E., Weitz, R. T., Allen, M. T. & Yacoby, A. Local compressibility measurements of correlated states in suspended bilayer graphene. *Phys. Rev. Lett.* **105**, 256806 (2010).
31. Lee, K. et al. Bilayer graphene. Chemical potential and quantum Hall ferromagnetism in bilayer graphene. *Science* **345**, 58–61 (2014).
32. Velasco, J. et al. Competing ordered states with filling factor two in bilayer graphene. *Nat. Commun.* **5**, 4550 (2014).
33. Shi, Y. et al. Energy gaps and layer polarization of integer and fractional quantum Hall states in bilayer graphene. *Phys. Rev. Lett.* **116**, 56601 (2016).
34. Zhang, J., Nandkishore, R. & Rossi, E. Disorder-tuned selection of order in bilayer graphene. *Phys. Rev. B* **91**, 1–6 (2015).
35. Ki, D.-K. & Morpurgo, A. F. High-quality multiterminal suspended graphene devices. *Nano Lett.* **13**, 5165–5170 (2013).
36. Lee, D. S., Skákalová, V., Weitz, R. T., Klitzing, K. von & Smet, J. H. Transconductance fluctuations as a probe for interaction-induced quantum Hall states in graphene. *Phys. Rev. Lett.* **109**, 56602 (2012).
37. Kumar, M., Laitinen, A. & Hakonen, P. Unconventional fractional quantum Hall states and Wigner crystallization in suspended Corbino graphene. *Nat. Commun.* **9**, 2776 (2018).
38. Velasco, J. et al. Transport measurement of Landau level gaps in bilayer graphene with layer polarization control. *Nano Lett.* **14**, 1324–1328 (2014).
39. Ki, D.-K., Fal'ko, V. I., Abanin, D. A. & Morpurgo, A. F. Observation of even denominator fractional quantum Hall effect in suspended bilayer graphene. *Nano Lett.* **14**, 2135–2139 (2014).
40. Lian, B., Sun, X.-Q., Vaezi, A., Qi, X.-L. & Zhang, S.-C. Topological quantum computation based on chiral Majorana fermions. *Proc. Natl Acad. Sci. USA* **115**, 10938–10942 (2018).

Methods

Device fabrication

The graphene flakes were exfoliated from a highly ordered pyrolytic graphite block onto silicon/silicon dioxide (Si/SiO_2) substrates. Using optical microscopy, suitable bilayer flakes were preselected by examining the optical contrast. The flakes were scanned with scanning near-field optical microscopy to avoid any structural domain walls within the channel[19–21] that might mask fragile quantum Hall phases. The electrodes (Cr/Au, 5 nm/100 nm), top gate (Cr/Au, 5 nm/160 nm) and spacer (SiO_2, 140 nm) were fabricated by multiple steps of standard lithography techniques and electron beam evaporation. To suspend both the top gates and the bilayer graphene flakes, hydrofluoric acid was subsequently used to etch about 150–200 nm of the SiO_2. Finally, the suspended dual-gated bilayer graphene devices were loaded into a dilution refrigerator.

Electrical transport measurements

The two-terminal conductance measurements were carried out in a dilution refrigerator with a base temperature of 7 mK. Unless stated otherwise, the measurements were performed with an a.c. bias current of 0.1–10 nA at 78 Hz using Stanford Research Systems SR865A and SR830 lock-in amplifiers at a temperature of $T < 10$ mK. Gate voltages were applied using multiple Keithley 2450 SourceMeters. Several homebuilt low-pass resistor–capacitor (RC) filters were used in series to reduce high-frequency noise.

Device annealing and characterization

Current annealing procedure. Before any measurements can be performed, a current annealing procedure is used to clean the samples. Multiple cycles of current annealing at 1.6 K are performed, during which the d.c. resistance $R_{d.c.}$ of the sample is tracked (Extended Data Fig. 1a). In general, for an increasing applied d.c. voltage $V_{d.c.}$, the resistance of the sample decreases. However, when a saturation of the drain current is reached, $R_{d.c.}$ consequently increases again. The maximum current flowing was approximately 0.35 mA μm^{-1} per layer.

Measurement details. The dual-gate structure allows independent tunability of the charge carrier density n and the perpendicular electric field $E_\perp$. We can define n and $E_\perp$ as a function of the top gate voltage V_t and the bottom gate voltage V_b as follows[23]:

$$n = \frac{C_b}{e}(\alpha V_t + V_b)$$

and

$$E_\perp = \frac{C_b}{2\varepsilon_0}(\alpha V_t - V_b),$$

where ε_0 is the vacuum permittivity and $\alpha = \frac{C_t}{C_b}$ is the ratio between the top gate capacitance C_t and the bottom gate capacitance C_b. Hence, by changing V_t and V_b simultaneously, we can directly sweep n or $E_\perp$. A Lorentzian fit to a density sweep and a precise electric field sweep were used to find the exact charge neutrality point.

For the hysteresis measurements, the filling factor reads

$$\nu = \frac{nh}{e|B|} = \frac{C_b(\alpha V_t + V_b)h}{e^2|B|},$$

where h is Planck's constant and B is the magnetic field. Hence, to sweep the magnetic field while fixing the filling factor, V_t, V_b and B need to be varied simultaneously.

Calculation of the contact resistance. As in two-terminal transport measurements there always pertains a contact resistance, we calculated and subtracted it in our data. This was done by recording a resistance versus density sweep at $B = 2$ T and $E_\perp = 20$ mV nm^{-1}. Appearing resistance plateaus were assigned to a filling factor. Plotting the resistance of the quantum Hall plateaus as a function of the inverse filling factor (Extended Data Fig. 1b) gives a linear behaviour. Using a linear fit demonstrates that the slope per filling factor (25,604 ± 712) Ω fits well to the von Klitzing constant, while giving a contact resistance of $R_C = (3{,}545 \pm 161)$ Ω. For all measurements shown in this paper (except Fig. 1b), we subtracted R_C.

Quality of the device. Extended Data Fig. 1c shows the conductance of the device as a function of charge carrier density for zero and finite electric field. The narrow width and low conductance of the device at $E_\perp = 0$ mV nm^{-1} suggest a high quality of the device. Besides calculating the residual charge disorder (Fig. 1b, inset), we additionally have calculated the electron/hole mobility $\mu_{e/h} = 120{,}000/130{,}000$ $cm^2 (Vs)^{-1}$ at $n = \pm 5 \times 10^9$ cm^{-2}, emphasizing the high quality of the device.

Theoretical fundamentals regarding the ALL QAH phases

Competing ground states in bilayer graphene at $n = E_\perp = B = 0$. In bilayer graphene at $n = E_\perp = B = 0$, when spin is ignored only two different types of competing ground states can be distinguished[9–11]: one in which the K and K′ valleys are layer-polarized in the opposite sense producing a QAH phase with broken time-reversal symmetry (Θ), orbital magnetization and quantized charge Hall conductivity ($\pm 2\, e^2 h^{-1}$ without counting spin degeneracy), and one in which the two valleys have the same sense of layer polarization producing a QVH phase with broken inversion symmetry (P), net layer polarization and non-trivial valley Hall conductivity. When spin is included, there are three additional types, namely the LAF phase, the ALL phase and the quantum spin Hall phase[9,10]. The five distinct phases in the spinful case can be obtained by each spin species choosing to be one of the two QVH phases or one of the two QAH phases, as depicted in Extended Data Fig. 2. These phases are distinguished[9,10] by their charge, spin, valley and spin–valley Hall conductivities, by their layer polarizations, by their orbital magnetizations, and by their broken symmetries, as summarized in Extended Data Table 1.

Quasiparticle orbital magnetism in bilayer graphene. In ABC-stacked N-layer graphene, the presence of a spontaneous gap at the Brillouin zone corners K and K′ produces non-trivial momentum-space Berry curvature, and the Berry curvature gives rise to non-trivial orbital magnetic moments of quasiparticles. The orbital magnetic moment of the quasiparticle state in band α of spin s_z, valley τ_z and momentum $\mathbf{p}$ reads[9,10]

$$m_z^{(\alpha)}(\mathbf{p}, \tau_z, s_z) = \left[-\tau_z \frac{\lambda}{h_t^2}\left(\frac{\partial h_\parallel}{\partial p}\right)^2 m_e \right]\mu_B,$$

where $h_\parallel = (v_0 p)^N/\gamma_1^{N-1}$, $h_t = (\lambda^2 + h_\parallel^2)^{1/2}$, $\gamma_1 \approx 0.4$ eV is the nearest-neighbour interlayer coupling, m_e is the electron mass, v_0 is the Fermi velocity in monolayer graphene, $\lambda\tau_z$ is the spontaneous gap term in Extended Data Table 1, $\alpha = \pm$ denote the two low-energy bands and μ_B is the Bohr magneton. Note that in the presence of a particle–hole symmetry, the moments of the particle and hole states are the same; in other words, the orbital magnetic moment does not depend on the band index α.

For AB bilayer graphene, the orbital magnetic moment reads

$$m_z^{(\alpha)}(\mathbf{p}, \tau_z, s_z) = \left[-\tau_z \frac{4\lambda m_e v_0^4 p^2}{\lambda^2\gamma_1^2 + v_0^4 p^4} \right]\mu_B,$$

With a Wannier function $|W^{(\alpha)}(\mathbf{R})\rangle = M^{-1/2}\sum_{\mathbf{k}} |\psi^{(\alpha)}(\mathbf{k})\rangle e^{i\mathbf{k}\cdot\mathbf{R}}$ at the lattice vector $\mathbf{R}$ and an energy cutoff $v_0 p \approx \gamma_1 \gg |\lambda|$, it follows that the total orbital magnetization per unit area can be defined as

Article

$$\langle W^{(\alpha)}(\mathbf{R})|m_{\hat{z}}^{(\alpha)}|W^{(\alpha)}(\mathbf{R})\rangle/A_{\text{unitcell}} = \int m_{\hat{z}}^{(\alpha)}(p,\tau_z,s_z)\frac{\mathrm{d}\mathbf{k}}{(2\pi)^2} = -\tau_z\frac{\Lambda m_e}{\pi\hbar^2}\ln\left(\frac{\gamma_1}{|\lambda|}\right)\mu_B,$$

where A_{unitcell} is the area of a unit cell and $\hbar$ is the reduced Planck's constant. For a spontaneous gap of 10 meV, 1 meV and 0.1 meV, the orbital magnetization per unit cell for each spin–valley species is 8.0 mμ_B, 1.3 mμ_B and 0.18 mμ_B, respectively.

Eight possible ALL QAH phases in bilayer graphene. The ALL phase in Extended Data Table 1 and Extended Data Fig. 2 can be viewed as a phase in which one spin–valley species polarizes into one layer whereas the other three species polarize into the opposite layer, or alternatively as a phase in which one spin species is in one of the two possible QVH phases (that have opposite layer polarization, for example, Extended Data Fig. 3a, b) whereas the other spin species is in one of the two possible QAH phases (that have opposite Chern numbers, for example, Extended Data Fig. 3a, f). Based on either viewpoint, one can find eight different ALL phases in total, as depicted in Extended Data Fig. 3.

Evolution of the $\nu = \pm 2$ state in electric and magnetic field

Here we show additional data on how the $\nu = \pm 2$ state behaves in an electric and magnetic field. We have recorded multiple electric field versus density conductance maps at various magnetic fields (Extended Data Fig. 4a–h). Extended Data Fig. 4a–d shows the conductance map for lower magnetic fields $B = 0.1$ T, $B = 0.2$ T and $B = 0.5$ T as well as a map with a reversed field of $B = -0.5$ T, respectively. Of the four domains observed at $B = 0.8$ T, only three show a quantized conductance of $2\,e^2\,h^{-1}$ at lower fields. The domain at negative electric field and positive density shows a higher conductance, possibly due to residual disorder providing additional channels for charge transport. Still, this domain behaves like the other three, as we also see in the fan diagrams in Fig. 2.

Changing the direction of the magnetic field (Extended Data Fig. 4c, d) shows the other four ALL phases (see also Extended Data Fig. 3).

Furthermore, from the conductance map as a function of electric field and density at different magnetic fields (Extended Data Fig. 4a–h) and the conductance map as a function of electric and magnetic fields at a fixed filling factor $\nu = -2.25$ (Extended Data Fig. 4i), we can see the evolution of the ALL phases (for example, the $\nu = -2$ state) in electric and magnetic fields. The required minimum and maximum electric fields and the electric field range for the $\nu = -2$ state to emerge increase slightly with increasing the magnetic field. At a very low magnetic field, the $\nu = -2$ state is only stable in a very limited electric field range, as at larger electric fields a fully layer-polarized $\nu = 0$ state dominates over the partially layer polarized $\nu = -2$ state. However, as the magnetic field increases, the $\nu = -2$ state becomes more and more stabilized, that is, the electric field range increases.

Lastly, we turn to the relevant physics at high magnetic fields. The $\nu = \pm 2$ states discussed in this current work appears near zero magnetic field, whereas in previous studies higher magnetic fields were applied. In fact, there are two types of $\nu = \pm 2$ quantum Hall ferromagnetic state at large magnetic fields: one without layer polarization (layer XY-like) that appears near zero electric field and the other with layer polarization (layer Ising-like) that requires a finite electric field. This was mentioned in a theoretical study[41] and observed in dual-gated devices[31,32,42]. The ALL states adiabatically evolve into the layer-polarized $\nu = \pm 2$ quantum Hall ferromagnetic states with increasing magnetic field. Although there is no transition, the required electric field range does evolve with the magnetic field.

Additional fan diagrams showing a complete electric field series

Extended Data Fig. 5 shows additional fan diagrams, demonstrating the behaviour of quantum Hall states towards zero magnetic field for various electric fields. The strength of each Landau level is indicated by the number of coloured lines with the corresponding slope in the top of each picture.

As the $\nu = \pm 4$ state is a non-layer-polarized phase, it is less and less pronounced for increasing electric field. On the contrary, as discussed already in the main text, the $\nu = \pm 2$ state is strongest for a finite range of electric fields. However, it does not emerge at $E_\perp = 0$ but appears for increasing electric fields. For $E_\perp = -10$ mV nm^{-1}, it does finally emerge for the complete magnetic field range shown here. The highest number of fluctuations corresponding to it appears at $E_\perp = -15$ mV nm^{-1} to $E_\perp = -20$ mV nm^{-1}, whereas for higher negative fields they disappear again. Lastly, the $\nu = 0$ state is strong for low electric fields (canted antiferromagnetic phase) and for very high electric fields, where it is a fully layer-polarized phase.

Evidence of the QAH effect in a second device

Extended Data Fig. 6 shows the quantum transport data measured in a second device. Extended Data Fig. 6a, b shows the conductance map for low magnetic fields of $B = 0.2$ T and $B = 0.5$ T, respectively. Although the sample is less clean than the one shown in the main text, we still see four domains with a conductance of $\pm 2\,e^2\,h^{-1}$ (four green regions in Extended Data Fig. 6a, b) even at these low magnetic fields. Furthermore, the $\nu = \pm 2$ states have the same behaviour when applying an electric field and magnetic field. Extended Data Fig. 6c shows the conductance as a function of electric and magnetic field for a fixed filling factor $\nu = -2$. The $\nu = -2$ state emerges for only intermediate applied electric fields and the range at which it appears increases with increasing magnetic field. Lastly, also in this device we see magnetic hysteresis (Extended Data Fig. 6d) when sweeping B around zero while fixing $\nu = -2$ and $E_\perp = -19$ mV nm^{-1}. However, the hysteresis is less prominent and the conductance breaks down for low magnetic fields, presumably due to the lower quality of the device.

More details on the hysteresis

At first sight, the observation of magnetic hysteresis with two-terminal measurements might be surprising, as only absolute values are measured without resolving the two components, σ_{xx} and σ_{xy}. However, following the previous derivation of the two-terminal conductance[43]

$$\sigma_{\text{two-terminal}} \propto \sqrt{{\sigma_{xx}}^2 + {\sigma_{xy}}^2}$$

or, in terms of the longitudinal ρ_{xx} and Hall resistivity ρ_{xy}

$$\sigma_{\text{two-terminal}} \propto \frac{1}{\sqrt{{\rho_{xx}}^2 + {\rho_{xy}}^2}},$$

one can observe a hysteresis if $\sigma^{\text{forward}}_{\text{two-terminal}} \neq \sigma^{\text{backward}}_{\text{two-terminal}}$. This is true around the coercive field, where a transition between two different ALL phases occurs, that is, $|\rho_{xx}^{\text{forward}}| \neq |\rho_{xx}^{\text{backward}}|$ and/or $|\rho_{xy}^{\text{forward}}| \neq |\rho_{xy}^{\text{backward}}|$. Around zero magnetic field, the hysteresis vanishes in two-terminal measurements, as $\rho_{xx}^{\text{forward}} = \rho_{xx}^{\text{backward}} = 0$ and $\rho_{xy}^{\text{forward}} = -\rho_{xy}^{\text{backward}}$, even though opposite orbital magnetizations (with $\rho_{xy} = \pm h/2e^2$) are present and distinguishable in four-terminal measurements[6].

To further prove the presence of the magnetic hysteresis, we have measured it for different ranges of magnetic fields, as shown in Extended Data Fig. 7. The degree of the hysteresis increases with the field range of the cycle. When the magnetic field is only swept in a small range ($-0.25\ \text{T} \le B \le 0.25$ T), there is almost no hysteretic behaviour. However, when the magnetic field is swept from a larger field towards zero ($-0.5\ \text{T} \le B \le 0.5$ T), the hysteresis appears partially. The fact that a sufficiently large magnetic field is needed to observe a hysteresis has been seen in twisted bilayer graphene[5,6]. The maximum degree of hysteresis is reached at $|B| \le 1$ T and then remains nearly the same with further increasing the magnetic field range.

Temperature-dependent transport data

Extended Data Fig. 8 shows maps of the conductance as a function of electric field and density for various temperatures. The temperature-dependent data shown in Fig. 4 are taken from these measurements, with the position of the linecuts indicated by dashed lines in the top left image. In general, we see that for $T \leq 0.3$ K, the maps are basically the same, whereas for higher temperatures, the $\nu = \pm 2$ and $= \pm 4$ as well as the $\nu = 0$ states get less and less well resolved, as fluctuations due to increasing temperatures broaden all phase transitions. We point out that gap energies measured by activation can only give lower bounds for the real gaps due to the presence of local disorder. As a consequence, in some measurements (for example, Chen et al.[8]) activation gaps are—like in our case—smaller than the temperature range they are measured in. To give an estimate of thermodynamic gaps, direct measurements of the inverse compressibility would be required (Martin et al.[30]). Our gap energies should be thus understood as lower bounds and can give an estimate to compare the strength of the different phases against one another within the same sample and to get a feeling for the dependence of the gap strength as function of applied perpendicular electric field.

Data availability

The data that support the findings of this study are available from the corresponding authors upon reasonable request.

41. Barlas, Y., Côté, R., Nomura, K. & MacDonald, A. H. Intra-Landau-level cyclotron resonance in bilayer graphene. *Phys. Rev. Lett.* **101**, 97601 (2008).
42. Zibrov, A. A. et al. Tunable interacting composite fermion phases in a half-filled bilayer-graphene Landau level. *Nature* **549**, 360–364 (2017).
43. Abanin, D. A. & Levitov, L. S. Conformal invariance and shape-dependent conductance of graphene samples. *Phys. Rev. B* **78** (2008).

Acknowledgements R.T.W. and F.R.G. acknowledge funding from the Center for Nanoscience (CeNS) and by the Deutsche Forschungsgemeinschaft (DFG, German Research Foundation) under Germany's Excellence Strategy-EXC-2111-390814868 (MCQST). F.Z. and T.X. acknowledge support from the Army Research Office under grant number W911NF-18-1-0416 and by the National Science Foundation under grant numbers DMR-1945351 through the CAREER programme and DMR-1921581 through the DMREF programme.

Author contributions F.R.G. fabricated the devices and conducted the measurements and data analysis. F.Z. and T.X. contributed the theoretical part. All authors discussed and interpreted the data. R.T.W. supervised the experiments and the analysis. The manuscript was prepared by F.R.G., F.Z. and R.T.W with input from all authors.

Competing interests The authors declare no competing interests.

Additional information
Supplementary information The online version contains supplementary material available at https://doi.org/10.1038/s41586-021-03849-w.

Correspondence and requests for materials should be addressed to Fan Zhang or R. Thomas Weitz.

Peer review information *Nature* thanks Kayoung Lee, Sergey Slizovskiy and the other, anonymous, reviewer(s) for their contribution to the peer review of this work. Peer reviewer reports are available.

Article

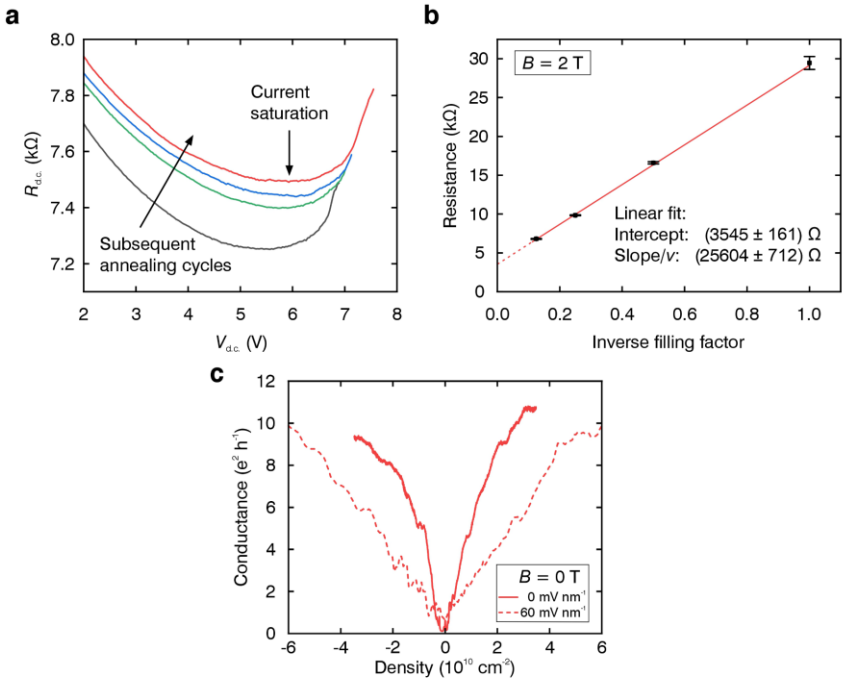

Extended Data Fig. 1 | Current annealing, contact resistance and device quality. a, $R_{d.c.}$ as a function of $V_{d.c.}$ during multiple annealing cycles. **b**, The resistance of quantum Hall plateaus shown as a function of inverse filling factor at $B = 2$ T and $E_\perp = 20$ mV nm^{-1}. **c**, The conductance as a function of density for $E_\perp = 0$ mV nm^{-1} and 60 mV nm^{-1} at $B = 0$ T.

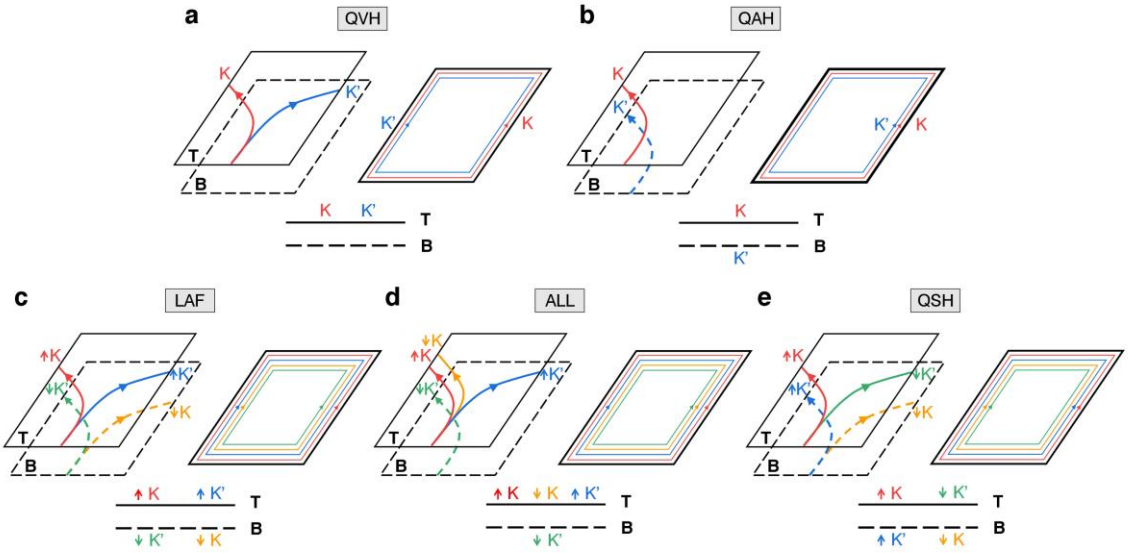

Extended Data Fig. 2 | Representatives of the five competing broken symmetry ground states in bilayer graphene at $n = E_\perp = B = 0$. a–e, Bottom panel: layer polarizations of the four spin-valley species. Top-left and top-right panels: bulk (classical) and edge (quantum) pictures of the corresponding spontaneous quantum Hall effect. Note that the edge roughness can produce couplings between counter-propagating edge states (of the same spin but different valleys) and thus gap them. Spin degeneracy is implicit in **a** and **b**. See the text for details. T and B refer to the top and bottom graphene layers, respectively.

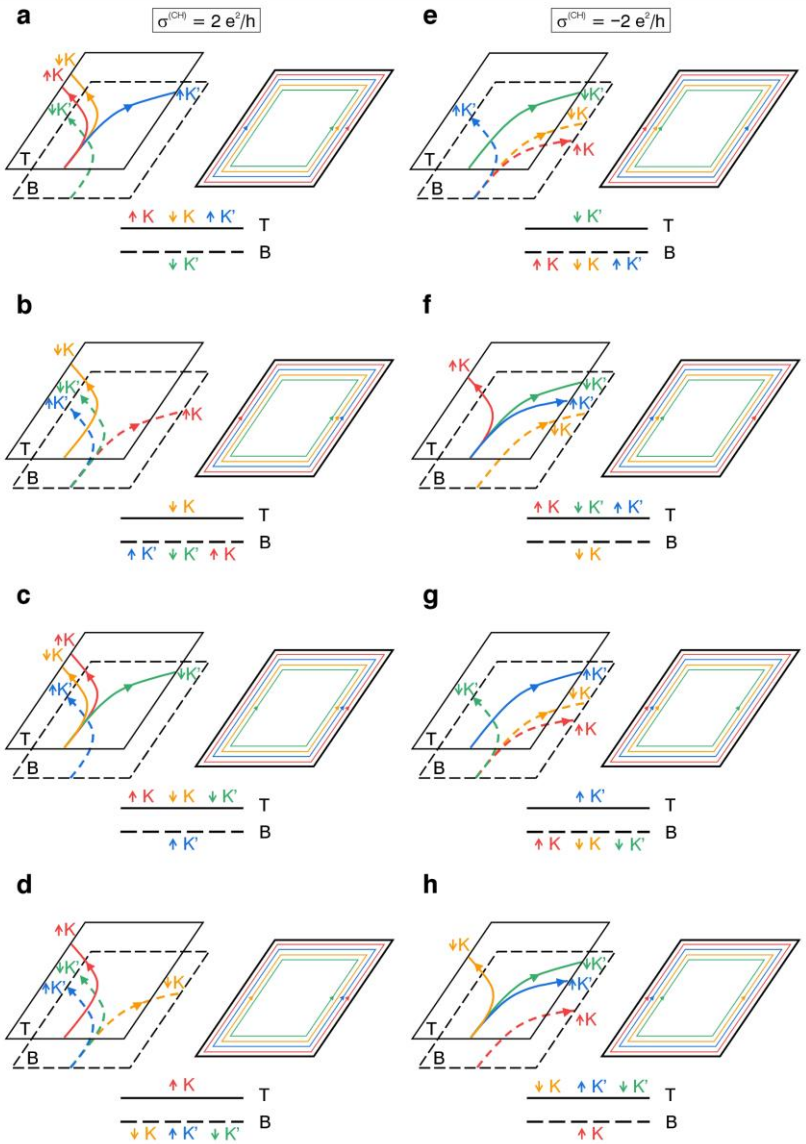

Extended Data Fig. 3 | Possible 'ALL' quantum anomalous Hall phases in bilayer graphene. a–h, Eight different 'ALL' phases that can be classified by the layer polarizations of their two spin species, by which spin species being in which QAH or QVH phases, and by their charge Hall conductivities.

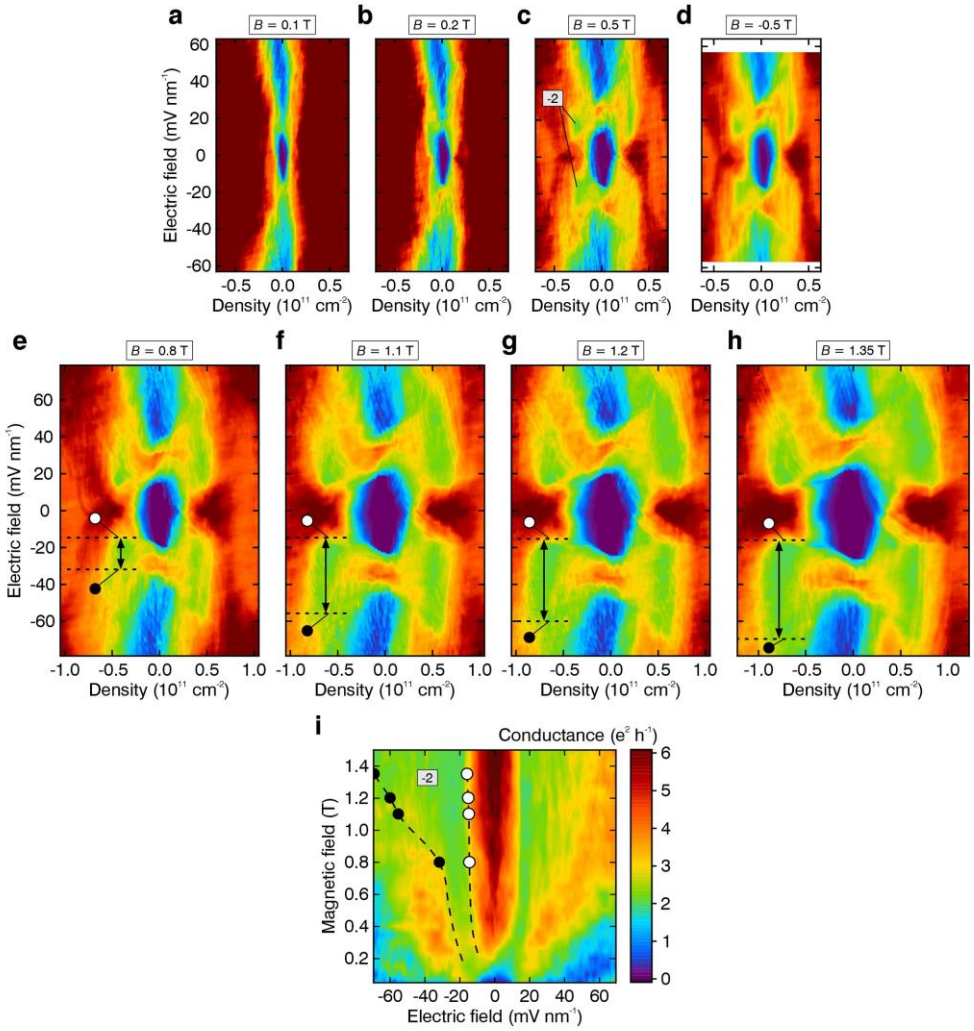

Extended Data Fig. 4 | Additional measurements showing the electric and magnetic field dependence of the $\nu = \pm 2$ state. a–h, Maps of the conductance as a function of electric field and density for various magnetic fields. The dashed lines in **e–h** are guides to the eye, and the arrows indicate the range of negative electric field at which the $\nu = -2$ state emerges. **i**, Conductance as a function of electric and magnetic fields at a fixed filling factor near $\nu = -2$ (at exactly $\nu = -2.25$). The black (white) dots indicating the maximum (minimum) electric field for the $\nu = -2$ to emerge are extracted from the data shown in **e–h**. The dashed lines are guides to the eye, highlighting the region where the $\nu = -2$ state emerges at negative electric fields.

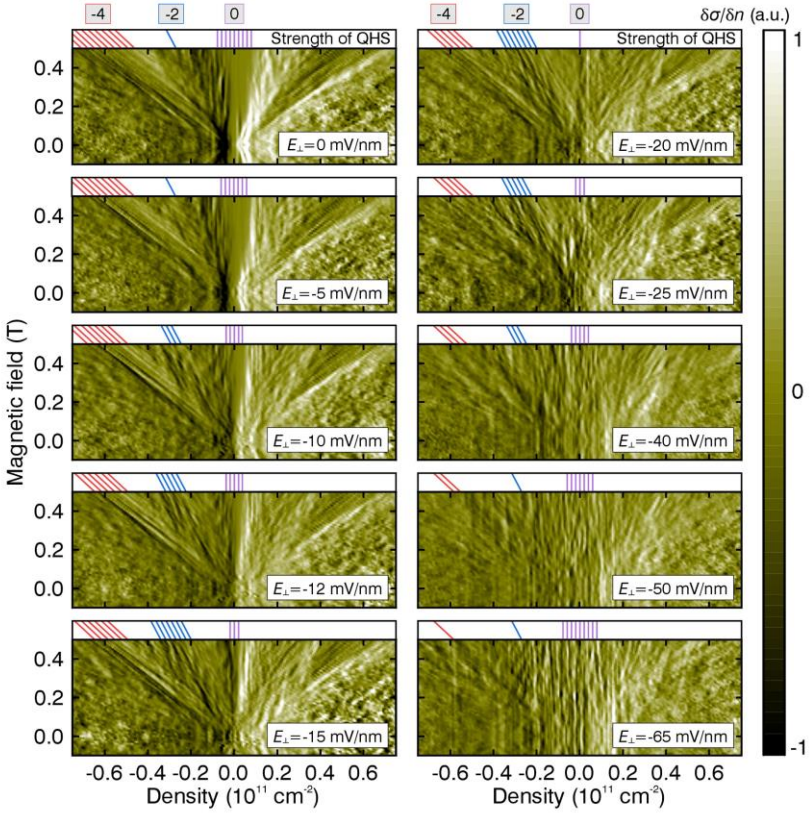

Extended Data Fig. 5 | Tracing quantum Hall states towards zero magnetic field. Derivative of the differential conductance $\delta\sigma/\delta n$ plotted as a function of magnetic field and density for various $E_\perp$. The amount of conductance fluctuations corresponding to the $\nu = 0, -2$ and -4 state are indicated by the number of white, blue and yellow lines in the top of each image.

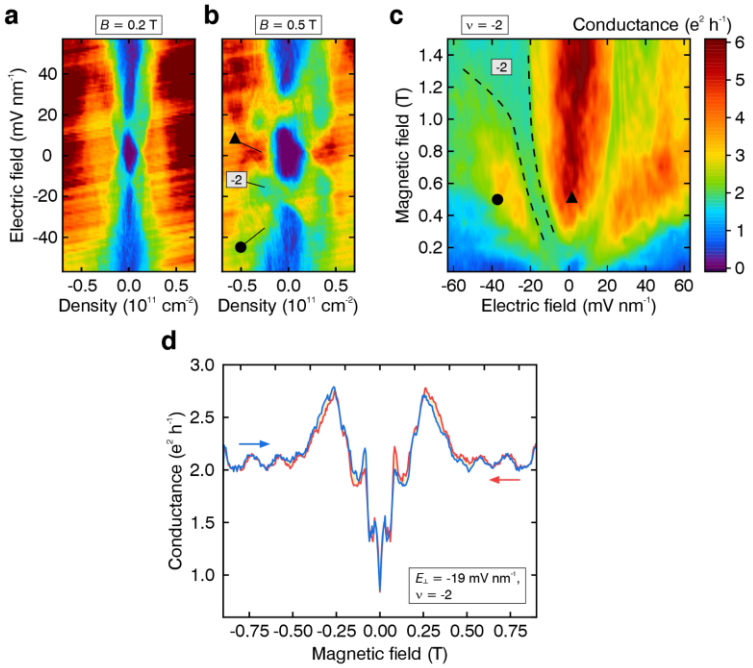

Extended Data Fig. 6 | Quantum transport data in a second device. **a**, **b**, Maps of the conductance as a function of $E_\perp$ and n for $B = 0.2$ T and 0.5 T, respectively. **c**, Conductance as a function of electric and magnetic field for fixed filling factor of $\nu = -2$. The dashed lines indicate the region where the $\nu = -2$ state at negative electric fields emerges with a conductance of $2\,e^2/h^{-1}$. **d**, Two-terminal conductance hysteresis measured for $\nu = -2$ and $E_\perp = -19$ mV nm^{-1}. The hysteresis loop area is shaded for clarity. The forward (reverse) sweep is shown in blue (red), as indicated by the arrows.

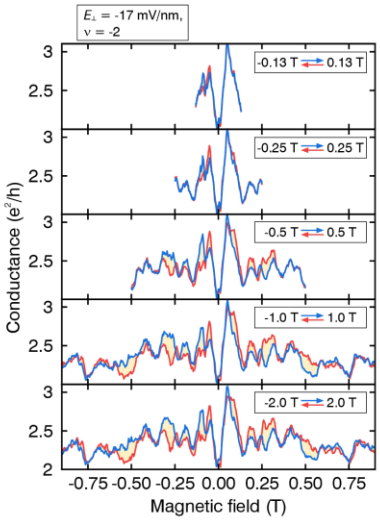

Extended Data Fig. 7 | Magnetic hysteresis loop for different magnetic field ranges. Two-terminal conductance hysteresis measured for different magnetic field ranges at $\nu = -2$ and $E_\perp = -17$ mV nm^{-1}. The hysteresis loop areas are shaded for clarity. The forward (reverse) sweep is shown in blue (red), as indicated by the arrows.

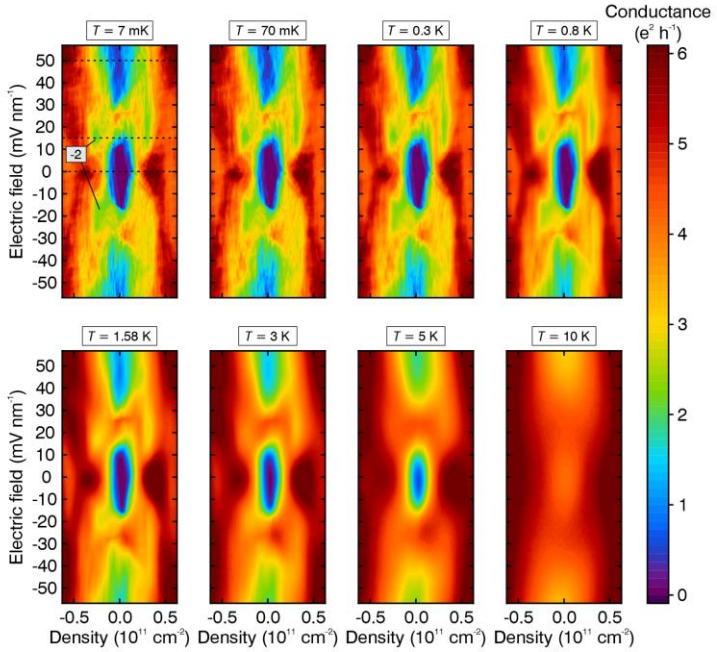

Extended Data Fig. 8 | Temperature dependence of the quantum Hall states at $B = 0.5$ T. Map of the conductance as a function of density and electric field for various temperatures. The dashed lines in the top left images indicate the position of the linecuts shown in Fig. 4 in the main manuscript.

Article

Extended Data Table 1 | Classification of the five competing broken symmetry ground states in bilayer graphene at $n = E = B = 0$

Phase	K ↑	K ↓	K′ ↑	K′ ↓	Broken symm.	Mass ($\lambda\tau_z$)	$\sigma^{(CH)}$	$\sigma^{(SH)}$	$\sigma^{(VH)}$	$\sigma^{(SVH)}$
QVH	T	T	T	T	P	$m\sigma_z$	0	0	$2N$	0
QAH	T	T	B	B	Θ	$m\tau_z\sigma_z$	$2N$	0	0	0
LAF	T	B	T	B	$\Theta, P, SU(2)$	$ms_z\sigma_z$	0	0	0	$2N$
QSH	T	B	B	T	$SU(2)$	$m\tau_z s_z\sigma_z$	0	$2N$	0	0
"ALL"	T	T	T	B	$\Theta, P, SU(2)$	$m\left(\frac{1+\tau_z}{2}+\frac{1-\tau_z}{2}s_z\right)\sigma_z$	N	N	N	N

These phases are distinguished by their spin-valley layer polarizations, by the symmetries they break, by their order parameters, and by their charge Hall (CH), spin Hall (SH), valley Hall (VH), and spin-valley Hall (SVH) conductivities. The results are general for ABC-stacked N-layer graphene[8,10,18] and with $N=2$ for AB bilayer graphene.

A.2 Interplay between Topological Valley and Quantum Hall Edge Transport

Fabian R. Geisenhof, Felix Winterer, Anna M. Seiler, Jakob Lenz, Ivar Martin, and R. Thomas Weitz
Nat. Commun. **13**, 4187 (2022)
DOI: 10.1038/s41467-022-31680-y

Abstract
An established way of realising topologically protected states in a two-dimensional electron gas is by applying a perpendicular magnetic field thus creating quantum Hall edge channels. In electrostatically gapped bilayer graphene intriguingly, even in the absence of a magnetic field, topologically protected electronic states can emerge at naturally occurring stacking domain walls. While individually both types of topologically protected states have been investigated, their intriguing interplay remains poorly understood. Here, we focus on the interplay between topological domain wall states and quantum Hall edge transport within the eight-fold degenerate zeroth Landau level of high-quality suspended bilayer graphene. We find that the two-terminal conductance remains approximately constant for low magnetic fields throughout the distinct quantum Hall states since the conduction channels are traded between domain wall and device edges. For high magnetic fields, however, we observe evidence of transport suppression at the domain wall, which can be attributed to the emergence of spectral minigaps. This indicates that stacking domain walls potentially do not correspond to a topological domain wall in the order parameter.

Contribution
I fabricated all devices, conducted all measurements, and performed the data analysis. The first draft, apart from some theoretical sections, was written by me. Furthermore, I produced the final version of the publication and designed all figures.

nature COMMUNICATIONS

ARTICLE

https://doi.org/10.1038/s41467-022-31680-y OPEN

Check for updates

Interplay between topological valley and quantum Hall edge transport

Fabian R. Geisenhof[1], Felix Winterer[1], Anna M. Seiler[1,2], Jakob Lenz[1], Ivar Martin[3] & R. Thomas Weitz[1,2,4,5]✉

An established way of realising topologically protected states in a two-dimensional electron gas is by applying a perpendicular magnetic field thus creating quantum Hall edge channels. In electrostatically gapped bilayer graphene intriguingly, even in the absence of a magnetic field, topologically protected electronic states can emerge at naturally occurring stacking domain walls. While individually both types of topologically protected states have been investigated, their intriguing interplay remains poorly understood. Here, we focus on the interplay between topological domain wall states and quantum Hall edge transport within the eight-fold degenerate zeroth Landau level of high-quality suspended bilayer graphene. We find that the two-terminal conductance remains approximately constant for low magnetic fields throughout the distinct quantum Hall states since the conduction channels are traded between domain wall and device edges. For high magnetic fields, however, we observe evidence of transport suppression at the domain wall, which can be attributed to the emergence of spectral minigaps. This indicates that stacking domain walls potentially do not correspond to a topological domain wall in the order parameter.

[1] Physics of Nanosystems, Department of Physics, Ludwig-Maximilians-Universität München, Munich, Germany. [2] 1st Physical Institute, Faculty of Physics, University of Göttingen, Göttingen, Germany. [3] Materials Science Division, Argonne National Laboratory, Lemont, IL, USA. [4] Center for Nanoscience (CeNS), LMU Munich, Munich, Germany. [5] Munich Center for Quantum Science and Technology (MCQST), Munich, Germany. ✉email: thomas.weitz@uni-goettingen.de

Electrons near the Fermi surface of two-dimensional hexagonal materials typically occupy two or more distinct electronic valleys. The valley index adds to the carrier's charge and spin, enabling additional channels for spontaneous symmetry breaking at low temperatures, whereby valleys are polarised independently or in combination with charge and spin degrees of freedom[1,2]. The most direct way to induce non-trivial valley response is by breaking sublattice symmetry. This occurs naturally in boron nitride, which makes it a quantum valley Hall insulator[3]. In Bernal-stacked bilayer graphene, the same effect is achieved by applying an interlayer bias[4]. Moreover, by spatially varying its sign, topological domain walls can be created, which exhibit one-dimensional (1D) electronic channels with quantised conductance[4], resilient to backscattering[5]. These electronic domain-wall states provide a flexible platform to study 1D transport[6–8] and correlated physics[9–11]. However, creating them by electrostatic gating is technically challenging. Fortunately, similar physics transpire at stacking domain walls (DWs) in bilayer graphene, where the stacking arrangement of graphene layers changes from AB to BA[12]. Such domain walls are common in naturally Bernal-stacked bilayer graphene[13–15] and even ubiquitous in twisted bilayer graphene[16,17], which is known for hosting superconductivity at a certain twist angle[18]. When a uniform electric field is applied to a bilayer graphene flake with a DW, topologically protected valley-helical states emerge along the dislocation, surrounded by insulating bulk[12,14,19]. Critically for the present work, stacking domain walls can have much richer interplay with spontaneous symmetry breaking in bilayer graphene[20–27] compared to artificially created ones, as not being forced by applied bias to have charge imbalance between layers. The interplay between stacking domain walls and spontaneous symmetry breaking is of peculiar interest in the presence of a quantising magnetic field, since bilayer graphene exhibits a very rich phase diagram owing to the eightfold degeneracy of the zero-energy Landau levels[28–30] (coming from two valleys, two orbital Landau level indices, and two spins – neglecting Zeeman splitting). Interactions lift the degeneracy by generating orderings, leading to quantum Hall plateaus at all integer filling fractions between -4 and 4[24,28–32]. This complex and intriguing regime shows a large variety of ways the internal symmetry can break spontaneously in the absence of externally induced layer polarisation. Within this manifold, the valley, sublattice, and layer index are rigidly locked. Since at the stacking domain wall the roles of the layers are exchanged, any ordering that is not a valley singlet is guaranteed to be affected.

In this work, the goal is to study this interplay by means of transport measurements. It cannot be fully explored in the artificial electrostatic domain walls as a matter of principle. We chose freestanding dually gated bilayer graphene devices as an ideal and versatile platform, since on the one side—as indicated by our measurements below—DWs remain stable during processing and suspension, and, on the other side, suspending enables the investigation of quantum transport unaffected by surroundings.

Results and discussion

Topological valley transport in the presence of an electric field induced gap. At first, suitable bilayer graphene flakes were preselected using optical microscopy and subsequently investigated with scattering scanning near-field optical microscopy[14,15,33]. Even though flakes show a smooth surface in the topography (Fig. 1a), the corresponding near-field amplitude image (Fig. 1b) can reveal stacking domain walls. Second, contacts were designed in two different configurations, as schematically illustrated in Fig. 1c. Either a DW was contacted on both ends (i.e. the DW goes along the channel separating two distinct domains, one with AB and one with BA stacking), or, alternatively, no domain wall was within the channel. Two devices are discussed exemplarily in the following: D1-DW of the former and D2 (which has been also investigated in ref. [27].) of the latter type. Data from additional domain-wall containing devices are shown in the Supplementary Information.

Using the dual-gate structure and sweeping the top V_t and bottom gate voltage V_b while tracking the resistance for the two configurations reveals differences in their signatures (Fig. 1d, e). Device D2 (Fig. 1e) shows, consistent with previous measurements, the spontaneously gapped state at the charge neutrality point[20–24] and a phase transition to the insulating fully layer polarised state for increasing electric field[23,24]. The resistance in device D1-DW (Fig. 1d) shows an overall similar behaviour, but with very different values. This becomes more apparent when examining line traces (see Fig. 1f, g). Although the resistance in both devices behaves non-monotonically as a function of increasing V_t, which indicates the emergence of the layer antiferromagnetic (LAF) ground state with opposite spins in two layers[1,34,35] at charge neutrality and zero electric field (at $V_t \approx V_b \approx 0$), it remains low in device D1-DW. As discussed below, this is caused by additional charge channels, which mask the insulating phase. Moreover, consistent with previous measurements[7,14], the resistance saturates for an increasing electric field (here at $R \approx 8.5\,k\Omega$), which unambiguously demonstrates the presence of zero-energy line modes[4,12,19]. In other words, although the perpendicular applied electric field induces a bandgap within the system[36], topologically-protected states at the K/K′ valleys persist, giving rise to helical valley transport (see the insets of Fig. 1d, e). The length-dependent conductance follows the Landau-Büttiker formula[14] $\sigma = \sigma_0\left(1 + \frac{L}{\lambda_m}\right)^{-1}$, which yields a mean free path of $\lambda_m \approx 2.2\,\mu$m with a channel length of $L = 0.7\,\mu$m and the theoretical conductance of the domain wall of $\sigma_0 = 4\,e^2\,h^{-1}$ (where e is the electronic charge and h Planck's constant). With $\lambda_m > L$, ballistic charge transport supported by the domain wall is confirmed, highlighting the high quality of the device[8,14]. Worth to note, away from charge neutrality both devices show low resistance. In this regime, which is dominated by contact resistance, we expect no influence of the domain wall.

Behaviour of the kink states in the presence of broken-symmetry phases at low magnetic field. Whereas artificially constructed domain walls can only be investigated in the presence of a perpendicular electric field[4,7,8] in a limited range of electric fields and densities, quantum transport along stacking domain walls have mostly been studied in zero magnetic field[14]. Hence, we focus here on the interplay of topological domain walls and quantum Hall edge transport. Figure 2a, b shows the conductance in the devices D1-DW and D2 as a function of charge carrier density n and electric field E at a magnetic field of $B = 3$ T. In both devices, the broken-symmetry states within the lowest Landau level octet[24,28–31] appear, however, with very different conductance values (see Fig. 2c). The emerging quantum Hall states in device D1-DW, although exhibiting unusual conductance values, can unambiguously be identified by examining their slope in fan diagrams (see Supplementary Fig. 1). Thus, the stacking domain wall in device D1-DW contributes additional charge transport channels in parallel to the quantum Hall edge states altering the overall conductance of the device. In fact, tracking the conductance of both devices as a function of density (Fig. 2c) reveals a conductance offset for most of the appearing states. In device D1-DW, the $\nu = 0$ state at zero electric field, which has previously been identified as an insulating canted antiferromagnetic (CAF) state[37,38], shows a rather high conductance of $\sigma \approx 2.9\,e^2\,h^{-1}$ (see Fig. 2d). CAF states have been

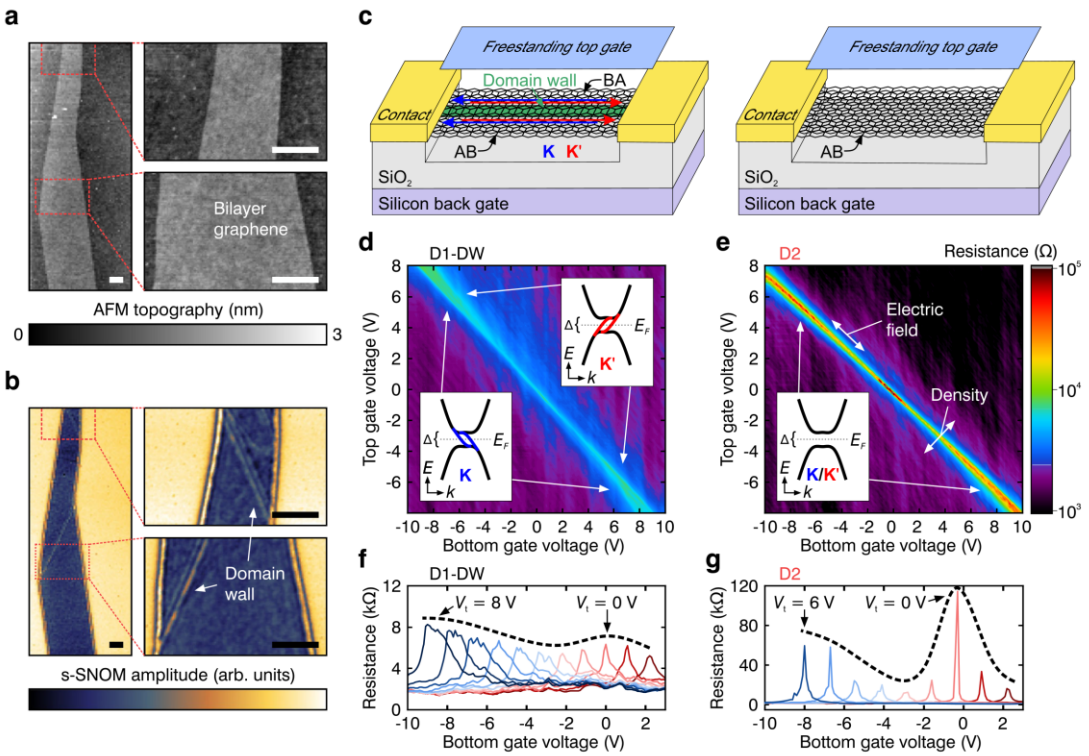

Fig. 1 Topologically-protected states in bilayer graphene. a, **b** Atomic force microscopy image (**a**) and scattering-type scanning near-field microscopy image (**b**) of a bilayer graphene flake, with high-resolution zoom-in scans on the right. The scale bars are 0.5 µm. **c** Freestanding dually gated bilayer graphene devices schematically shown with (left) and without domain wall (right) connecting the contacts. Topological valley transport along the domain wall is shown in blue and red in the K- and K′-valley, respectively. **d**, **e** Resistance map as a function of top and bottom gate voltage for device D1-DW (**d** with domain wall) and D2 (**e** without domain wall). Insets: Electronic band structure of bilayer graphene with (**d**) and without a domain wall (**e**) for an applied electric field. Δ is the electric field induced bandgap, E_F the Fermi level and the blue (red) lines indicate topologically protected, doubly spin degenerate chiral states in the K(K′)-valley. **f**, **g** Trace of the resistance as a function of V_b for various V_t with steps of 1 V shown for device D1-DW (**f**) and D2 (**g**). The dashed lines indicate the envelope of the resistance and are a guide to the eye.

observed to have low edge conductance, attributed to the opening of a spectral minigap at the sample edges[2,37,38]. The observed high conductance is thus consistent with the maximum possible —four—kink states at the DW contributing to the charge transport (with a finite $\lambda_m \approx 1.9\,\mu$m), as is also the case in the layer polarised (LP) $\nu = 0$ phase (see Supplementary Fig. 2 for more details) at high E. For an increasing filling factor, the conductance changes to $\sigma \approx 3.5, 4.0$ and $3.9\,e^2\,h^{-1}$ for the $\nu = -1, -2$, and -4 states (see Fig. 2d), respectively. This near constancy of conductance can be naturally explained: In the simplest model (see Fig. 2e), ignoring spin and orbital index for clarity, changing the Fermi level for an applied electrical field leads to the topological domain-wall channels being traded for quantum Hall edge channels. Changing the filling factor from the electron to the hole side, exchanges the positions of the valley polarised channels. More precisely (see Fig. 2f), when increasing the filling factor, a domain-wall channel disappears whereas an additional quantum Hall edge channel emerges. Hence, the conductance follows $\sigma = (4 - |\nu|)\sigma_{DW} + |\nu|\sigma_{QH}$ for $|\nu| \le 4$, where σ_{DW} is the conductance supported by a single kink state, and $\sigma_{QH} = e^2\,h^{-1}$ is the conductance of a quantum Hall edge channel. A linear fit to the data further supports this hypothesis (see Fig. 2d): for D2, it shows the expected slope of 1.0 $e^2\,h^{-1}$ per filling factor as there are only quantum Hall edge states present. On the contrary, it yields a slope of 0.23 $e^2\,h^{-1}$ per filling factor for device D1-DW. Although in all $|\nu| \le 4$ states four quantised channels contribute in total to the charge transport, the non-zero slope corresponds to the difference in conductance of the kink and edge states and shows that for increasing filling factor kink states with a conductance of $\sigma_{DW} \approx 0.77\,e^2\,h^{-1}$ are traded for higher-quality quantum Hall edge states with $\sigma_{QH} = e^2\,h^{-1}$. Discrepancies from the linear behaviour of the conductance in device D1-DW could indicate a distinct magnetic dependency of the conductance within the $|\nu| \le 4$ states, as shown below. The $\nu = \pm 4$ states seem to be free of the influence of the domain wall (see Fig. 2f). A more detailed consideration of the band structure reveals that stacking domain walls can affect even the higher Landau levels, albeit more weakly (see Supplementary Fig. 3). In our free-standing devices, these states are at higher magnetic field outside the accessible density regime needed to observe the quantum Hall states.

Emergence of a spectral minigap for high magnetic fields. A more in-depth understanding of the intricate interplay between the quantum Hall edge modes and domain walls can be gained by investigating the charge transport at varying magnetic fields (see

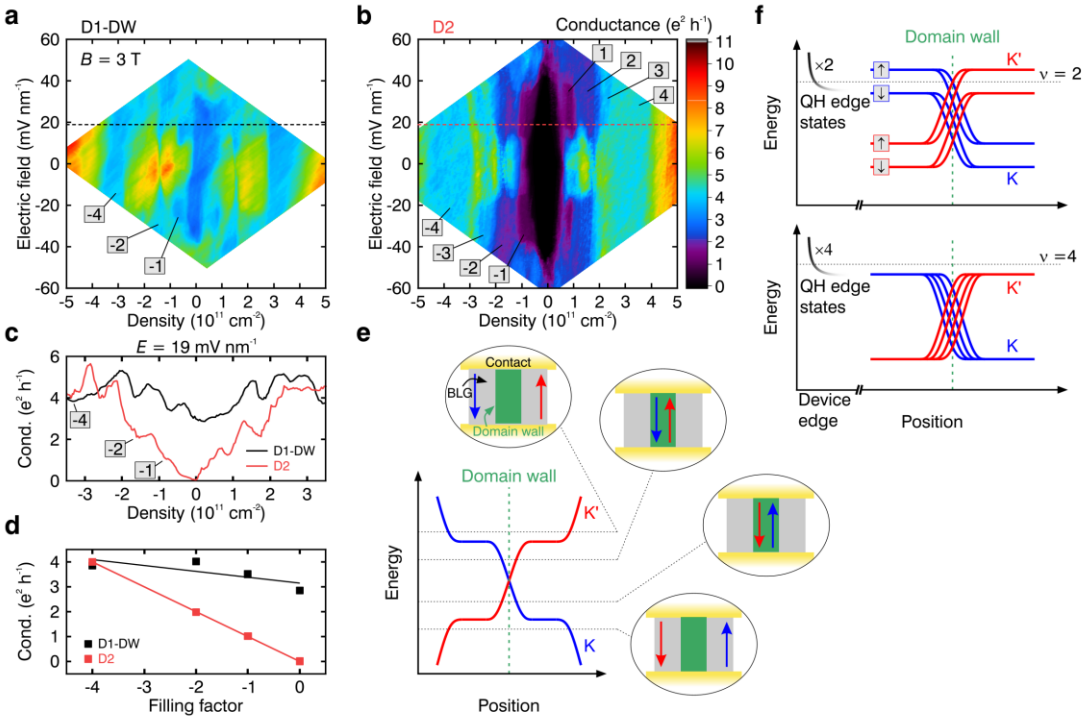

Fig. 2 Interplay between topological valley and quantum Hall edge transport at low magnetic fields. a, **b** Maps of the conductance in units of $e^2\,h^{-1}$ as a function of applied electric field E and charge carrier density n at a magnetic field of $B = 3$ T for devices D1-DW (**a**) and D2 (**b**). The dashed lines indicate the position of the data shown in **c**. Certain filling factors are indicated. **c** Line traces of the conductance as a function of n taken at constant E in device D1-DW (black) and D2 (red). **d** Conductance of quantum Hall states as a function of filling factor for device D1-DW (black) and D2 (red). The values are averaged over the electric field range at which the individual states emerge. The solid lines are linear fits to the corresponding data. **e** Schematic band structure (spin and orbital index omitted) in bilayer graphene in the presence of a stacking domain wall as a function of position. The dashed lines indicate distinct positions of the Fermi level and the corresponding encircled pictures schematically demonstrate the evolution of directions and locations of the one-dimensional channels within the device. **f** Schematic band structure as a function of position across the device with a domain wall shown for the $\nu = 2$ (top) and $\nu = 4$ (bottom) QH state in the presence of an interlayer electric field (spin and orbital flavours have been reinstated).

Fig. 3 and Supplementary Fig. 4 for more data). Line traces of the conductance as a function of filling factor measured in device D1-DW at zero and finite electric field show the $\nu = 0, \pm 1, \pm 2$ states (see Fig. 3a). In addition, we plot the conductance as a function of magnetic field for the individual states shown in Fig. 3b. Note that the conductance was averaged over the electric field range at which the respective state emerges, i.e. for the $\nu = 0$ CAF phase around zero electric fields, for the $\nu = -1$ and -2 at $|E| \geq 10\,\mathrm{mV\,nm^{-1}}$ and $|E| \geq 15\,\mathrm{mV\,nm^{-1}}$, respectively, and for the $\nu = -4$ state at all electric fields.

Most prominently, we see a sharp dip to very low conductance around zero charge carrier density within the $\nu = 0$ phase at high magnetic fields of $B \geq 8$ T (marked with a cross in Fig. 3a), which can also be tracked as function of magnetic field (see Fig. 3b). The feature is reproducible upon repeated sweeps and persists between different cooldowns of the device (see Supplementary Fig. 5). Towards $B = 0$, the $\nu = 0$ state corresponds to the layer antiferromagnetic phase with spin and valley indices locked[1,34,35]. In general, we find high conductance in this regime, suggesting the presence of zero-energy line modes at the kink. This observation would be consistent with the LAF order parameter experiencing an order parameter reversal as illustrated in Fig. 3c. The 1D modes persist within the gap because counterpropagating states in the same valley have opposite spin, and hence scattering is suppressed. However, as the magnetic field is increased, spins cant and the LAF phase evolves into the canted antiferromagnetic phase[37,38]. Then, the counterpropagating modes in the same valley become partially spin aligned and can hybridise causing the emergence of a minigap. This is similar to the effect at the device edge. However, in the latter case the termination and backscattering off atomic scale defects can also couple opposite valleys[5], leading to further suppression of conductance. Our experimental data are indeed consistent with the opening of a gap and—when the Fermi level is located in this gap—a decrease in conductance. Outside of the gap, we expect a finite conductance, with a value determined by a sequence of the crossing bands and gap openings (see Fig. 3c). Since canting of spins gets stronger with magnetic field, one can expect the size of the minigap to grow with increasing B. This is consistent with our experimental observations of decreasing conductance (see Fig. 3a, b and Supplementary Fig. 4) and could be the reason why we can only resolve the minigap at $B \geq 8$ T. Eventually, for an infinite perpendicular or a finite in-plane magnetic field the CAF phase is expected to evolve into the ferromagnetic phase[37,38], in which the stacking domain wall has little or no effect on the Landau level energy (see Fig. 3c), making the stacking domain wall effectively invisible (this regime was not investigated experimentally in this study).

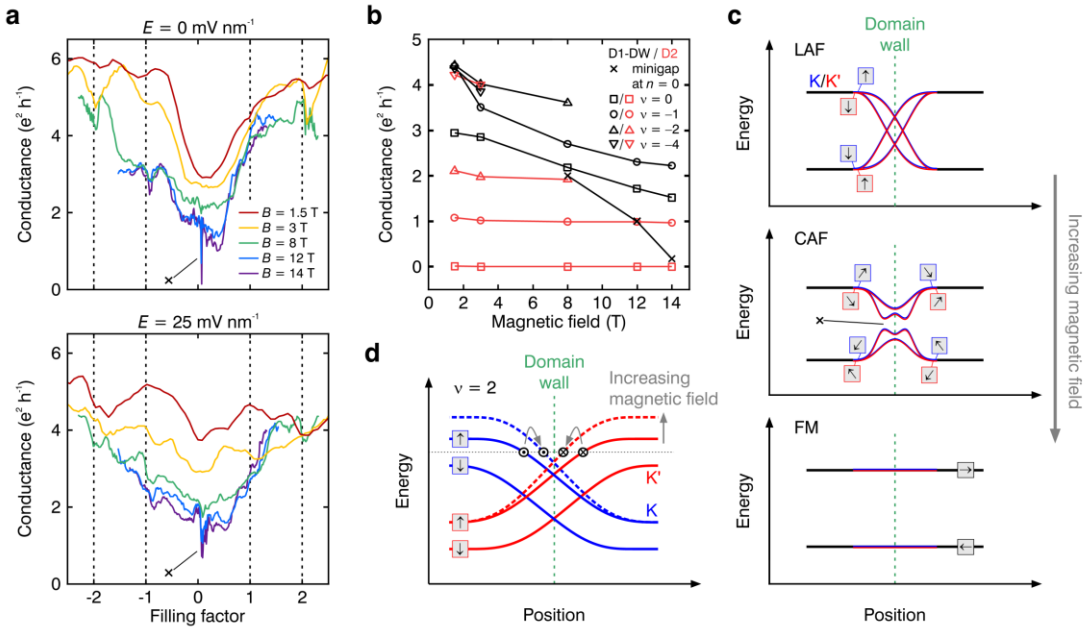

Fig. 3 Behaviour of the kink states for varying magnetic field. a Conductance as a function of filling factor shown for various magnetic fields at $E = 0$ (top) and $E = 25$ mV nm^{-1} (bottom) measured in device D1-DW. The cross indicates the sharp conductance dip caused by the opening of a minigap. Note, that the state emerging around zero density is the LAF/CAF state, only at $E = 25$ mV nm^{-1} the data curve for $B = 1.5$ T shows the transition between LAF/CAF and LP phase, see also Supplementary Fig. 2. **b** Conductance of the $\nu = 0, -1, -2, -4$ quantum Hall states as well as within the minigap as a function of magnetic field. The data for device D1-DW (D2) is shown in black (red). **c** Schematic band structure around the domain wall shown for the LAF, CAF and FM $\nu = 0$ phases. The blue (red) lines indicate the chiral states in the K(K′)-valley. The cross indicates the spectral minigap emerging in the CAF phase. **d** Schematic band structure for $\nu = 2$ (orbital index is implicit) in the presence of layer-polarising bias. The domain wall retains only two pairs of valley helical (spin polarised) states, indicated by black circles with in-plane and out-of-plane directions. Their backscattering rate at the chemical potential (thin horizontal line) depends on their spatial separation and width. Both are generally expected to change as a function of magnetic field, leading to a change in DW conductance. The influence of the magnetic field is indicated by grey arrows. A similar effect was observed in artificial domain walls[7].

Notably, the conductance of the $\nu = \pm 1, \pm 2$ states also decrease with increasing B (Fig. 3a, b), whereas device D2 shows the expected constant values as a function of B for each QH state (see Fig. 3b). These quantum Hall states occur in sufficiently large electric field, and thus the valley polarisation is expected to change sign across the domain wall. In contrast, the spin polarisation remains constant across domain walls, pinned to the direction of magnetic field (see Fig. 2f). Therefore, the counter-propagating states at the domain wall belong to opposite valleys but same spin and can only be destroyed by local defects that can provide large momentum scattering. That is in contrast to the CAF state at $\nu = 0$ and $E = 0$, where a minigap can open owing to the hybridisation of states within the same valley and without the need for short range scattering. The measurements indicate that increasing the magnetic field increases the intervalley scattering, although the exact mechanism at this point remains unclear. One possible explanation could be the change in relative spatial arrangement of the counterpropagating channels as a function of magnetic field (see Fig. 3d). Clearly, increasing the channel separation should suppress backscattering, and vice versa. An effect of this type has already been observed at domain walls, where application of magnetic field or change of the chemical potential was found to affect the domain-wall conductance[7,39]. Another possibility could be the that increasing magnetic field pushes the system towards other broken-symmetry states[40,41], which would change the order parameter and hence the behaviour of the kink states. However, these states have been observed only at very high magnetic fields and since we see no evidence of phase transitions in sample D2 for the same parameters, this possibility appears unlikely. Given that the measurements were performed in a two-terminal configuration, one should also make sure that the effect that we observe is not a consequence of a magnetic field dependent contact resistance of the kink states. However, we do not observe this behaviour for quantum Hall edge states (see Fig. 3b), and it is likely that the contact resistance of both types of one-dimensional channels behaves similarly. Additional devices revealed similar behaviours of the domain-wall conductance with increasing magnetic field (see Supplementary Fig. 6).

Temperature dependence of the domain-wall states. As final investigation to establish the interplay between edge and domain walls, we have conducted temperature dependent measurements. In Fig. 4, the conductance is shown as a function of temperature measured in different phases: in the layer antiferromagnetic, the canted antiferromagnetic as well as the layer polarised $\nu = 0$ phases and in the $\nu = -4$ phase. In contrast to device D2, which shows an activated temperature dependence of the conductance in all phases, D1-DW exhibits a much weaker temperature dependence and, most importantly, a finite conductance at low temperatures for the insulating LAF, CAF, and LP phases (see

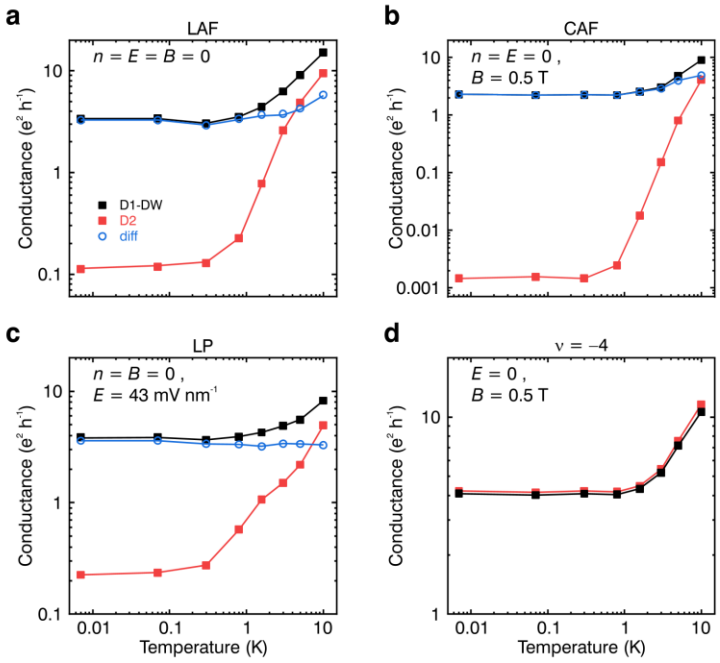

Fig. 4 Temperature dependence of the conductance in various broken-symmetry phases. a–d Temperature dependence of the conductance measured for the LAF phase at $n = E = B = 0$ (**a**), the CAF phase for $n = E = 0$ and $B = 0.5$ T (**b**), the LP phase at $n = B = 0$ and $E = 43$ mV nm^{-1} (**c**) and the $\nu = -4$ phase at $E = 0$ and $B = 0.5$ T (**d**). The data corresponding to device D1-DW (D2) is shown in black (red). Moreover, in **a**–**c**, the difference of conductance between the two devices $\sigma_{diff}(T) = \sigma_{D1-DW}(T) - \sigma_{D2}(T)$ is shown as a function of temperature in blue. Note that the temperature dependence was measured in a different loading and annealing cycle than the measurements shown in Figs. 1–3 leading to small disparities in the conductance.

Fig. 4a–c, respectively). As the charge channels induced by the stacking domain wall contribute in parallel to any edge channels, we can subtract the data measured in both devices to reveal the underlying temperature dependence of the domain-wall $\sigma_{DW}(T) \approx \sigma_{diff}(T) = \sigma_{D1-DW}(T) - \sigma_{D2}(T)$, assuming that the activated charge transport behaves similarly in both devices. Notably, in all three $\nu = 0$ phases the difference $\sigma_{diff}(T)$ shows an approximately constant behaviour at low temperatures with $\sigma_{diff} \approx 2.5 - 3.5\ e^2\,h^{-1}$ and only a slight increase in the LAF and CAF phases for $T \geq 3$ K. Overall, this weak temperature dependence is expected for 1D charge transport and suggests weakly localised metallic behaviour[42]. On the contrary, the $\nu = -4$ phase (see Fig. 4d) shows the same activated temperature dependence and very similar conductance values in both devices, indicating that the domain wall has negligible influence on the quantum transport in this phase.

In conclusion, we have investigated the impact of stacking domain walls on the eightfold degenerate zero-energy Landau level in bilayer graphene. For future measurements, high in-plane magnetic fields would be beneficial to explore the behaviour of domain walls within the $\nu = 0$ ferromagnetic phase[38]. Moreover, the usage of encapsulated devices is essential to investigate the behaviour of domain walls in heterostructures[43] and their impact on the energy landscape of correlated states in higher Landau levels. Furthermore, having established that in the lowest Landau level the edge states and domain-wall channels co-exist, one can imagine investigating their mutual interaction[44] in narrow samples. Lastly, a direct imaging[39] of topological valley and quantum Hall edge channels would be very illuminating.

Methods

Bilayer graphene was exfoliated from a highly ordered pyrolytic graphite (HOPG) block onto Si/SiO_2 substrates and suitable flakes were preselected using optical microscopy. Afterwards, infrared nano-imaging[45] was performed in a scattering-type scanning near-field microscope (s-SNOM, neaspec GmbH) in tapping mode to detect any stacking domain walls. Hereby, an infrared CO_2 laser beam (with a wavelength of 10.5 µm) was focused onto a metal-coated atomic force microscopy tips (Pt/Ir, Arrow NCPT-50, Nanoworld), which was oscillating with a frequency and amplitude of 250–270 kHz and 50–80 nm, respectively. With this method, we were able to obtain topographic and infrared nano-images simultaneously. Electrodes (Cr/Au, 5/100 nm) in two distinct configurations, a top gate (Cr/Au, 5/160 nm) as well as a spacer (SiO_2, 140 nm) were fabricated using several steps of standard lithography techniques and electron beam evaporation. Subsequently, the devices were submersed in hydrofluoric acid to etch about 150–200 nm of the SiO_2 and consequently suspend both the top gates and bilayer graphene flakes. After loading the freestanding dually gated bilayer graphene devices into a dilution refrigerator current annealing was performed at 1.6 K. In devices without domain wall best results were obtained when using a current of about 0.35 mA µm^{-1} per layer. In devices with domain wall 150–250% more current was needed to achieve a current saturation due to their lower resistance and shorter channels. All quantum transport measurements were conducted at the base temperature of the cryostat ($T < 10$ mK), if not noted differently. Moreover, an excitation a.c. bias current of 0.1–10 nA at 78 Hz and Stanford Research Systems SR865A and SR830 lock-in amplifiers were used for the measurements, as well as Keithley 2450 SourceMeters to apply the gate voltages. Low-pass filters were used in series to reduce high frequency noise.

Data availability

All data supporting the findings of this study are available within the article, as well as the Supplementary Information file, or available from the corresponding authors on request.

Received: 1 November 2021; Accepted: 21 June 2022;
Published online: 20 July 2022

References

1. Zhang, F., Jung, J., Fiete, G. A., Niu, Q. & MacDonald, A. H. Spontaneous quantum Hall states in chirally stacked few-layer graphene systems. *Phys. Rev. Lett.* **106**, 156801 (2011).
2. Kharitonov, M. Canted antiferromagnetic phase of the ν = 0 quantum Hall state in bilayer graphene. *Phys. Rev. Lett.* **109**, 46803 (2012).
3. Volovik, G. E. *The Universe in a Helium Droplet* (Oxford University Press, 2009).
4. Martin, I., Blanter, Y. M. & Morpurgo, A. F. Topological confinement in bilayer graphene. *Phys. Rev. Lett.* **100**, 36804 (2008).
5. Qiao, Z., Jung, J., Niu, Q. & MacDonald, A. H. Electronic highways in bilayer graphene. *Nano Lett.* **11**, 3453–3459 (2011).
6. Chen, H. et al. Gate controlled valley polarizer in bilayer graphene. *Nat. Commun.* **11**, 1202 (2020).
7. Li, J. et al. Gate-controlled topological conducting channels in bilayer graphene. *Nat. Nanotechnol.* **11**, 1060–1065 (2016).
8. Li, J. et al. A valley valve and electron beam splitter. *Science* **362**, 1149–1152 (2018).
9. Killi, M., Wu, S. & Paramekanti, A. Graphene: kinks, superlattices, Landau levels and magnetotransport. *Int. J. Mod. Phys. B* **26**, 1242007 (2012).
10. Killi, M., Wei, T.-C., Affleck, I. & Paramekanti, A. Tunable Luttinger liquid physics in biased bilayer graphene. *Phys. Rev. Lett.* **104**, 216406 (2010).
11. Mazo, V., Shimshoni, E., Huang, C.-W., Carr, S. T. & Fertig, H. A. Helical quantum Hall edge modes in bilayer graphene: a realization of quantum spin-ladders. *Phys. Scr.* **T165**, 14019 (2015).
12. Vaezi, A., Liang, Y., Ngai, D. H., Yang, L. & Kim, E.-A. Topological edge states at a tilt boundary in gated multilayer graphene. *Phys. Rev. X* **3**, 021018 (2013).
13. Alden, J. S. et al. Strain solitons and topological defects in bilayer graphene. *Proc. Natl Acad. Sci. USA* **110**, 11256–11260 (2013).
14. Ju, L. et al. Topological valley transport at bilayer graphene domain walls. *Nature* **520**, 650–655 (2015).
15. Jiang, L. et al. Soliton-dependent plasmon reflection at bilayer graphene domain walls. *Nat. Mater.* **15**, 840–844 (2016).
16. Sunku, S. S. et al. Photonic crystals for nano-light in moiré graphene superlattices. *Science* **362**, 1153–1156 (2018).
17. Huang, S. et al. Topologically protected helical states in minimally twisted bilayer graphene. *Phys. Rev. Lett.* **121**, 37702 (2018).
18. Cao, Y. et al. Unconventional superconductivity in magic-angle graphene superlattices. *Nature* **556**, 43–50 (2018).
19. Zhang, F., MacDonald, A. H. & Mele, E. J. Valley Chern numbers and boundary modes in gapped bilayer graphene. *Proc. Natl Acad. Sci. USA* **110**, 10546–10551 (2013).
20. Bao, W. et al. Evidence for a spontaneous gapped state in ultraclean bilayer graphene. *Proc. Natl Acad. Sci. USA* **109**, 10802–10805 (2012).
21. Freitag, F., Trbovic, J., Weiss, M. & Schönenberger, C. Spontaneously gapped ground state in suspended bilayer graphene. *Phys. Rev. Lett.* **108**, 76602 (2012).
22. Nam, Y., Ki, D.-K., Soler-Delgado, D. & Morpurgo, A. F. A family of finite-temperature electronic phase transitions in graphene multilayers. *Science* **362**, 324–328 (2018).
23. Velasco, J. et al. Transport spectroscopy of symmetry-broken insulating states in bilayer graphene. *Nat. Nanotechnol.* **7**, 156–160 (2012).
24. Weitz, R. T., Allen, M. T., Feldman, B. E., Martin, J. & Yacoby, A. Broken-symmetry states in doubly gated suspended bilayer graphene. *Science* **330**, 812–816 (2010).
25. Zhang, F. Spontaneous chiral symmetry breaking in bilayer graphene. *Synth. Met.* **210**, 9–18 (2015).
26. Nandkishore, R. & Levitov, L. Quantum anomalous Hall state in bilayer graphene. *Phys. Rev. B* **82**, 115124 (2010).
27. Geisenhof, F. R. et al. Quantum anomalous Hall octet driven by orbital magnetism in bilayer graphene. *Nature* **598**, 53–58 (2021).
28. Hunt, B. M. et al. Direct measurement of discrete valley and orbital quantum numbers in bilayer graphene. *Nat. Commun.* **8**, 948 (2017).
29. Li, J., Tupikov, Y., Watanabe, K., Taniguchi, T. & Zhu, J. Effective Landau level diagram of bilayer graphene. *Phys. Rev. Lett.* **120**, 47701 (2018).
30. Zhao, Y., Cadden-Zimansky, P., Jiang, Z. & Kim, P. Symmetry breaking in the zero-energy Landau level in bilayer graphene. *Phys. Rev. Lett.* **104**, 66801 (2010).
31. Lee, K. et al. Bilayer graphene. Chemical potential and quantum Hall ferromagnetism in bilayer graphene. *Science* **345**, 58–61 (2014).
32. Nomura, K. & MacDonald, A. H. Quantum Hall ferromagnetism in graphene. *Phys. Rev. Lett.* **96**, 256602 (2006).
33. Geisenhof, F. R. et al. Anisotropic strain-induced soliton movement changes stacking order and band structure of graphene multilayers. implications for charge transport. *ACS Appl. Nano Mater.* **2**, 6067–6075 (2019).
34. Freitag, F., Weiss, M., Maurand, R., Trbovic, J. & Schönenberger, C. Spin symmetry of the bilayer graphene ground state. *Phys. Rev. B* **87**, 161402 (2013).
35. Veligura, A. et al. Transport gap in suspended bilayer graphene at zero magnetic field. *Phys. Rev. B* **85**, 1–8 (2012).
36. Zhang, Y. et al. Direct observation of a widely tunable bandgap in bilayer graphene. *Nature* **459**, 820–823 (2009).
37. Kharitonov, M. Edge excitations of the canted antiferromagnetic phase of the ν = 0 quantum Hall state in graphene: a simplified analysis. *Phys. Rev. B* **86**, 075450 (2012).
38. Maher, P. et al. Evidence for a spin phase transition at charge neutrality in bilayer graphene. *Nat. Phys.* **9**, 154–158 (2013).
39. Yin, L.-J., Jiang, H., Qiao, J.-B. & He, L. Direct imaging of topological edge states at a bilayer graphene domain wall. *Nat. Commun.* **7**, 11760 (2016).
40. Shi, Y. et al. Energy gaps and layer polarization of integer and fractional Quantum Hall States in bilayer graphene. *Phys. Rev. Lett.* **116**, 56601 (2016).
41. Velasco, J. et al. Competing ordered states with filling factor two in bilayer graphene. *Nat. Commun.* **5**, 4550 (2014).
42. Gogolin, A. Electron localization in quasi-one-dimensional organic conductors. *Phys. Rep.* **166**, 269–351 (1988).
43. Sunku, S. S. et al. Dual-gated graphene devices for near-field nano-imaging. *Nano Lett.* **21**, 1688–1693 (2021).
44. Kang, W., Stormer, H. L., Pfeiffer, L. N., Baldwin, K. W. & West, K. W. Tunnelling between the edges of two lateral quantum Hall systems. *Nature* **403**, 59–61 (2000).
45. Keilmann, F. & Hillenbrand, R. In *Nano-optics and Near-field Optical Microscopy* (eds Zayats, A. V. & Richards, D.) pp. 235–265 (Artech House, 2009).

Acknowledgements

R.T.W. and F.R.G. acknowledge funding from the Centre for Nanoscience (CeNS) and by the Deutsche Forschungsgemeinschaft (DFG, German Research Foundation) under Germany's Excellence Strategy-EXC-2111-390814868 (MCQST). I.M. was supported by the Materials Sciences and Engineering Division, Basic Energy Sciences, Office of Science, U.S. Dept. of Energy. We also thank Y.C. Durmaz and F. Keilmann for experimental assistance with the near-field optical microscopy.

Author contributions

F.R.G. fabricated the devices and conducted the measurements and data analysis. I.M contributed the theoretical part. F.R.G., F.W, A.M.S, J.L, I.M., and R.T.W. discussed and interpreted the data. R.T.W. supervised the experiments and the analysis. The paper was prepared by F.R.G., I.M., and R.T.W with input from all authors.

Funding

Open Access funding enabled and organized by Projekt DEAL.

Competing interests

The authors declare no competing interests.

Additional information

Supplementary information The online version contains supplementary material available at https://doi.org/10.1038/s41467-022-31680-y.

Correspondence and requests for materials should be addressed to R. Thomas Weitz.

Peer review information *Nature Communications* thanks the other, anonymous reviewer(s) for their contribution to the peer review of this work. Peer reviewer reports are available.

Reprints and permission information is available at http://www.nature.com/reprints

Publisher's note Springer Nature remains neutral with regard to jurisdictional claims in published maps and institutional affiliations.

A.3 Impact of Electric Field Disorder on Broken-Symmetry States in Ultraclean Bilayer Graphene

Fabian R. Geisenhof, Felix Winterer, Anna M. Seiler, Jakob Lenz, Fan Zhang, and R. Thomas Weitz
Nano Lett. **22**, 7378 – 7385 (2022)
DOI: 10.1021/acs.nanolett.2c02119

Abstract

Bilayer graphene (BLG) has multiple internal degrees of freedom and a constant density of states down to the charge neutrality point when trigonal warping is ignored. Consequently, it is susceptible to various competing ground states. However, a coherent experimental determination of the ground state has been challenging due to the interaction–disorder interplay. Here we present an extensive transport study in a series of dually gated freestanding BLG devices and identify the layer-antiferromagnet as the ground state with a continuous strength across all devices. This strength correlates with the width of the state in the electric field. We systematically identify electric-field disorder–spatial variations in the interlayer potential difference–as the main source responsible for the observations. Our results pinpoint for the first time the importance of electric-field disorder on spontaneous symmetry breaking in BLG and solve a long-standing debate on its ground state. The electric-field disorder should be universal to all 2D materials.

Contribution

I fabricated all devices, conducted all measurements, and performed the data analysis. The first draft was written by me. Furthermore, I produced the final version of the publication and designed all figures.

NANO LETTERS

pubs.acs.org/NanoLett Letter

Impact of Electric Field Disorder on Broken-Symmetry States in Ultraclean Bilayer Graphene

Fabian R. Geisenhof, Felix Winterer, Anna M. Seiler, Jakob Lenz, Fan Zhang, and R. Thomas Weitz*

Cite This: *Nano Lett.* 2022, 22, 7378−7385 Read Online

ACCESS | Metrics & More | Article Recommendations | Supporting Information

ABSTRACT: Bilayer graphene (BLG) has multiple internal degrees of freedom and a constant density of states down to the charge neutrality point when trigonal warping is ignored. Consequently, it is susceptible to various competing ground states. However, a coherent experimental determination of the ground state has been challenging due to the interaction−disorder interplay. Here we present an extensive transport study in a series of dually gated freestanding BLG devices and identify the layer-antiferromagnet as the ground state with a continuous strength across all devices. This strength correlates with the width of the state in the electric field. We systematically identify electric-field disorder—spatial variations in the interlayer potential difference—as the main source responsible for the observations. Our results pinpoint for the first time the importance of electric-field disorder on spontaneous symmetry breaking in BLG and solve a long-standing debate on its ground state. The electric-field disorder should be universal to all 2D materials.

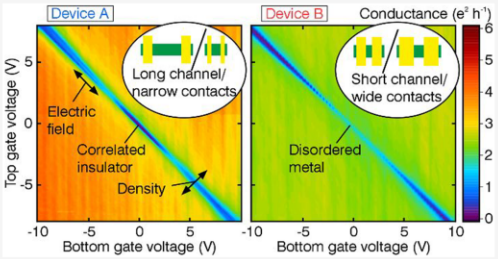

KEYWORDS: *bilayer graphene, ground state, domain wall, disorder, broken-symmetry state*

Bernal bilayer graphene (BLG) has quadratic band touching at the charge neutrality point (CNP) and constant density of states in the single-particle spectrum, when trigonal warping[1] is ignored. This implies that BLG is susceptible to exchange interaction-driven broken-symmetry states.[2−13] Such exotic states have been observed at finite magnetic field B[3,13−18] and, more intriguingly, also in its absence.[2,6−12] To clearly identify their underlying orders is, however, a long-standing challenge. States at vanishing magnetic field are especially intricate as they are degenerate in mean-field theory[4,5,19] despite their distinct spin-valley orders. Experimentally, these competing ground states can be characterized by the stability of their resistance against external changes in charge carrier density and electromagnetic field. However, while a vanishing conductance at the CNP suggesting an insulating state[2,6−11] associated with the layer antiferromagnetic (LAF) state[4,9,10] was found in some devices, finite conductance was seen in others.[6,7,20] Moreover, disparate observations at finite magnetic fields were also reported; for example, a recent study assigned a new quantum Hall state to the transition region between the layer polarized and canted antiferromagnetic $\nu = 0$ states,[21] while others did not spot this state.[2]

Evidently, at both zero and finite magnetic fields, there is no consensus whether the different experimental signatures originate from different interaction-driven states or from disorder.[19] Charge impurities from substrate or fabrication are one source of disorder. It can be minimized by suspending BLG above a substrate or by encapsulating BLG in hexagonal boron nitride. However, encapsulation embeds BLG in a dielectric medium with $\varepsilon \sim 3-4$, which substantially reduces the interaction effects compared to the case of suspended devices. Indeed, the spontaneously gapped states have so far not been observed in encapsulated devices. In suspended devices, disorder can be further minimized by current annealing.[2,22] Another source of disorder are domain walls (DW) that can either naturally occur as stacking defects[23−25] or emerge spontaneously due to the interplay between exchange interaction and thermal fluctuation.[26] The former, as line defects between AB and BA stacking domains, is not only common in BLG[24,27] but universal to twisted BLG.[28−30] Appealingly, these DWs can host topologically protected states.[23,25,31] The spontaneous DWs are expected to have similar topological properties,[26] and they often bind to spatial variation in the potential difference between layers and can proliferate thermally;[26] however, they are extremely difficult to identify and control in experiment. Because of these challenges, up to now the impact of DWs on the discussed interaction-driven states and their phase transitions has not been studied

Received: May 25, 2022
Revised: September 13, 2022
Published: September 16, 2022

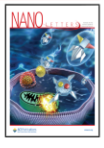

experimentally, although they are expected to alter the quantum transport characteristics in BLG.[26,32]

To reveal the origin of the experimental discrepancies in the interaction-driven states at finite and vanishing magnetic fields in BLG, we have carefully examined 11 dually gated suspended BLG devices, of which a representative SEM image is shown in Figure 1a. BLG flakes were first identified by their optical contrast and subsequently imaged by scattering-type scanning near-field optical microscopy[23,27] (s-SNOM) to detect stacking DWs within the flakes (Figure S1). Two out of the 11 devices investigated show clearly pronounced DWs. After fabrication, we performed multiple cycles of current annealing at a temperature of T = 1.6 K in a dilution refrigerator until a saturation of the current was visible (Figure S2).

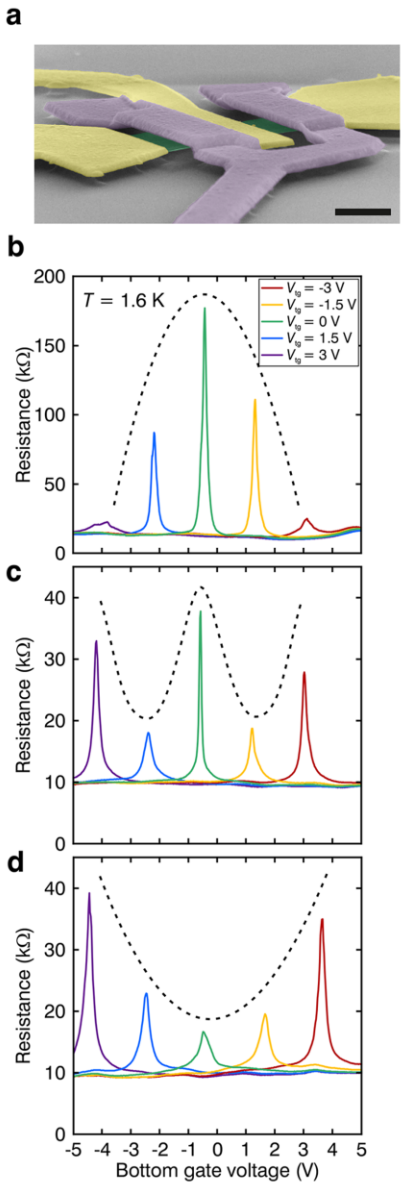

Figure 1. Resistance at charge neutrality in bilayer graphene. a, False-color scanning electron microscope image of a typical suspended bilayer graphene device. Scale bar, 1 μm. b–d, Resistance as a function of V_b measured for a series of V_t at T = 1.6 K for three different devices. The dashed lines indicate the envelope of the data as a guide to the eye.

We first focus on the comparison of different devices with respect to their behavior at B = 0. After current annealing, already at T = 1.6 K, bottom gate voltage V_b sweeps at various fixed top gate voltages V_t reveal differences in the transport signature of the devices (Figure 1b–d). For example, the resistance at the CNP can be very high (>150 kΩ) and decreases with increasing V_t (Figure 1b), can be quite low (<20 kΩ) and increases with V_t (Figure 1d), or can lie in between these two extremes (Figure 1c). Similar behavior has been described in the literature before[2,6−11,20] and led to a lively debate on the competing ground states and concomitant experimental signatures (e.g., the presence or absence of a gap or edge states).

To gain more insight into the different experimental signatures at the CNP, we mapped the full bottom and top gate voltage range at the base temperature of our cryostat, T < 10 mK (Figure 2a). Notably, in 10 out of the 11 devices an insulating state appears at the CNP, while only one device remains metallic. In the following, we will discuss the two most extreme devices, A and B, in which the insulating state is dominant and absent, respectively. For further analysis, we transform V_b and V_t to the perpendicular electric field E and the charge carrier density.n[12] Figure 2b shows the E dependence of the resistance at n = 0, where device A shows the insulating state[2,6−11] with a resistance of several 100 kΩ around E = 0. According to its signatures, we identify the insulating state as the interaction-driven LAF state[4,9,10] (see Supplementary Note). Examining the magnitude of the conductance at the CNP, σ_{CNP}, and the width of the spontaneously gapped state in the electric field, ΔE^{SP}, as functions of the temperature reveals an activated T dependence of σ_{CNP} and concomitantly an increase of ΔE^{SP} with decreasing T, as can be observed in device A (see Figure 2c). Moreover, we can see that σ_{CNP} and ΔE^{SP} correlate with the critical temperature across four devices (see Figure S3). We conclude that smaller σ_{CNP} and larger ΔE^{SP} indicate a more pronounced LAF state and decreasing temperature strengthens this spontaneously gapped state.[2,7] On the contrary, in device B the resistance monotonically increases with E (Figure 2b), and no significant temperature dependence of σ_{CNP} is observed (Figure 2c). Hence, the spontaneously gapped state is absent, even for T < 10 mK. (We note in passing that we also see a nonmonotonic behavior in the magnetic field of the conductance in device A, which could indicate the transition from the LAF state at B = 0 to the canted antiferromagnetic state at finite B and differences between their edge transport;[33] see Figure S4). In the literature, distinct observations have been made, such as an insulating state[2,8−11] associated with the LAF state,[5] a finite conductance,[20] or even a bimodal distribution of conductivities at charge neutrality.[6,7] Across our investigated devices, however, we observe continuous distributions of σ_{CNP} and ΔE^{SP} both at T < 10 mK and T = 1.6 K (Figure 2d), suggesting a continuous variation of the strength of the LAF state. Our analysis in the remainder of the manuscript is dedicated to deciphering the origin of these distributions.

https://doi.org/10.1021/acs.nanolett.2c02119
Nano Lett. 2022, 22, 7378−7385

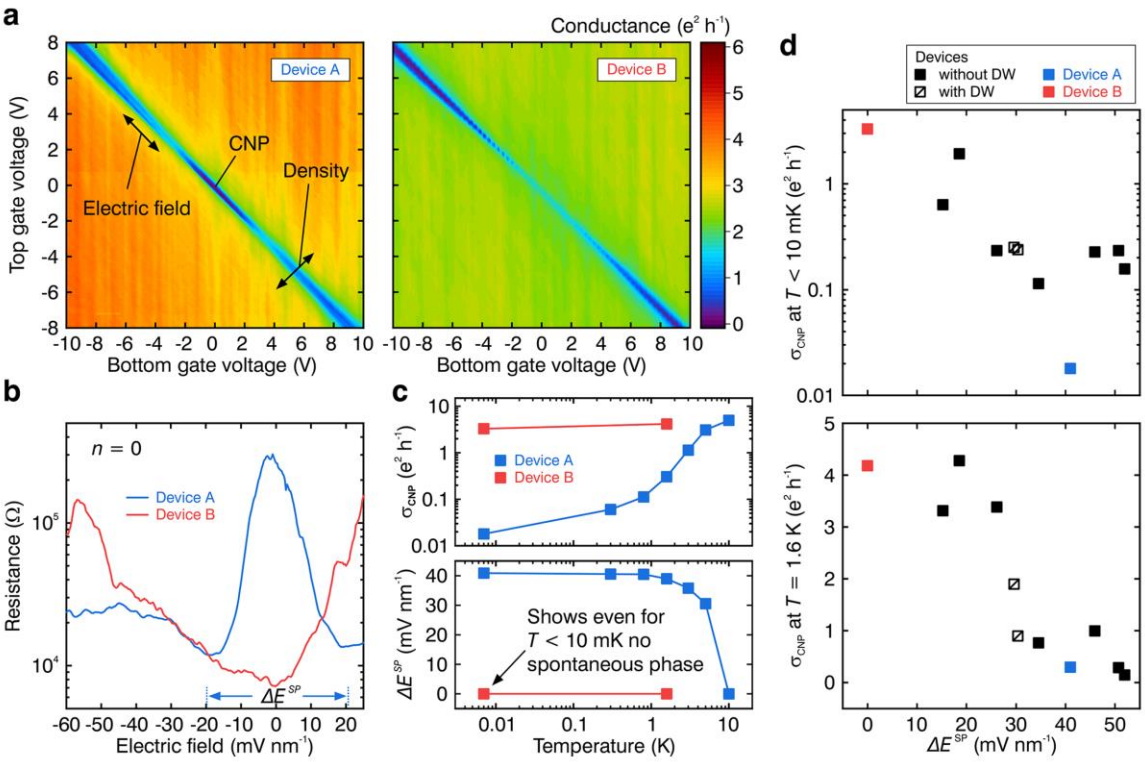

Figure 2. Presence or absence of the spontaneously gapped LAF ground state in bilayer graphene. a, Conductance map as a function of top and bottom gate voltages for devices A and B. b, Trace of the resistance at charge neutrality as a function of E for devices A (blue) and B (red). The electric field range of the insulating spontaneous state is indicated by ΔE^{SP}. c, Conductance at the charge neutrality point σ_{CNP} (top) as well as ΔE^{SP} (bottom) for various temperatures for devices A (blue) and B (red). d, σ_{CNP} measured at $T < 10$ mK (top) and $T = 1.6$ K (bottom) as a function of ΔE^{SP} for all measured devices. Devices with (without) a stacking domain wall within the channel are shown with open (solid) squares. Device A (B) is shown in blue (red).

A first possible cause for the observed distribution of σ_{CNP} could be uncontrollable variations in sample fabrication. Such fluctuations of process contaminants are, however, very unlikely since we processed all our devices in the same way. Moreover, we have even found different types of gate dependency when measuring two neighboring contact pairs sharing the same flake, while we have identified similar behavior for two independently processed flakes. A second possible explanation could be the presence of uniaxial strain. However, strain neither opens a spontaneous gap[8] nor broadens quantum Hall transitions. In fact, to apply substantial uniaxial strain, a special effort is often needed,[34] which is not our current case. A third possible reason could be the presence of structural DWs. Such DWs have previously been held responsible for unusual conduction behavior close to the CNP.[35] Our experiments, however, demonstrate that DWs are not the cause for suppressing the interaction-driven insulating ground state, since the two devices with DWs show an intermediate strong LAF state, which is consistent with recent experiments revealing that even in the extreme case when a stacking DW directly connects the contacts, the LAF state can still be present.[31] The arguments hold only with the assumption that the DWs remain stable and do not move during current annealing. Recent literature, however, showed that such stacking DWs can be mobile at high temperatures,[24] and even the formation of new stacking boundaries during current annealing resulting in a finite or vanishing conductance at the CNP has been reported.[35] To clarify the behavior of stacking DWs under processing and device cleaning, we have conducted a set of test measurements. Since near-field microscopy is impossible to conduct for our dually gated devices, the tests were made on BLG flakes on a substrate without a top gate. At first, we examined the stability of stacking DWs during the fabrication of contacts: in contrast to multilayer graphene,[36] they appeared stable and immobile in BLG during processing, verified by their presence prior to and after processing (see Figure S5). This observation is consistent with the prediction that AB and BA stackings are energetically equivalent[24] and consequently—unlike DWs between ABC and ABA stacks[36,37]—there should be no driving force for DW movement by the strain induced during processing. Second, contacted flakes with stacking DWs between the contacts were annealed at large currents and reinvestigated subsequently with near-field microscopy (see Figure S6). We did not observe any systematic movement of the stacking DWs or any development of new ones. We conclude that current annealing and processing do not create, remove, or move stacking DWs systematically. The observed stability implies that two of the investigated devices did indeed have a DW each, which neither

https://doi.org/10.1021/acs.nanolett.2c02119
Nano Lett. 2022, 22, 7378−7385

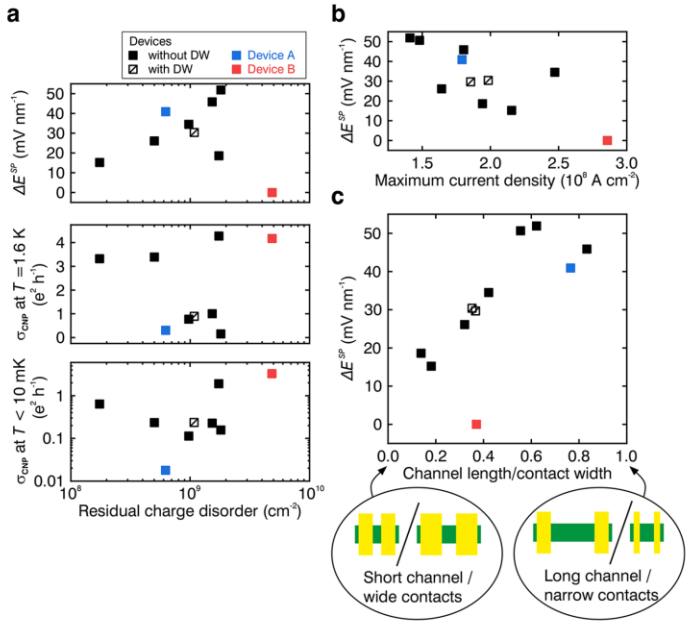

Figure 3. Role of disorder and annealing on the emergence of the gapped LAF ground state in bilayer graphene. a, ΔE^{SP} and σ_{CNP} at T < 10 mK and T = 1.6 K as functions of the residual charge disorder shown for nine devices. b, ΔE^{SP} as a function of the maximum current density J_{max} applied during the current annealing procedure shown for nine devices. c, ΔE^{SP} plotted versus the ratio of channel length and contact width of the corresponding device. The schematics in the bottom illustrate the ratio, with the contacts shown in yellow and the bilayer graphene flakes in green.

systematically alters the conductivity of the ground state nor explains the observed continuous spectrum of behavior.

Another possible explanation could be the residual charge disorder in BLG devices. It is often assumed that disorder can be removed via current annealing to a device-independent minimum. Hence, we should be able to clean all devices such that they have similarly low conductance. This is, however, at odds with our experimental findings. Even though we can identify that σ_{CNP} depends on the cleanliness of the device (i.e., the degree of current annealing) and can be changed by more than 1 order of magnitude by further annealing, the overall transport signature (i.e., the monotonic or nonmonotonic behavior of the E dependence of conductance that indicates the absence or presence of the LAF state) does not change once the CNP lies in the accessible V_b range (Figure S7). In other words, the emergence of the spontaneously gapped ground state is independent of the number of current annealing cycles in our experiments. Moreover, in the cleanest state accessible by current annealing (i.e., when a current saturation is visible[38]), ΔE^{SP} and σ_{CNP} do not systematically depend on the residual charge disorder across all devices, which is in general very low in all ultraclean devices (Figure 3a). Therefore, residual charge disorder cannot be the cause, and current annealing itself does not have any effect on the overall transport signatures (Figure S7).

Nonetheless, the current density required to observe saturation during annealing, J_{max}, varies significantly in the range of 1.4−2.9 × 10^8 A cm^{-2} between devices. Moreover, the strength of the spontaneously gapped state, ΔE^{SP}, systematically depends on J_{max} (Figure 3b). Specifically, when a high current density is needed for current saturation, the device shows a weaker (or no) gapped ground state. Intriguingly, besides residual charge disorder, there is a different type of disorder:[39,40] Whereas charge fluctuations produce spatially varying in-plane electric fields that lead to charge puddles,[39] i.e., residual charge disorder, charge imbalance between the two layers creates spatially varying out-of-plane electric fields, i.e., electric field disorder.[39,40] Moreover, the two types of disorder are most likely uncorrelated.[39]

One may wonder from where the electric field disorder originates and why it is not removed during annealing. During the current annealing procedure, the heat generated by the electric current leads to partial evaporation and redistribution of contaminants to colder parts of the devices,[38] which in our experiments are the contacts. During fabrication the top layer is exposed to a resist, whereas the bottom layer is in contact with residues initially present on the SiO_2 surface. Hereby, current annealing is more likely to redistribute contaminants within each layer toward the contacts, instead of between the two layers, and we expect the electric field disorder to depend on the device geometry. This hypothesis is ready to be tested by our large number of devices with varying geometries. Indeed, ΔE^{SP} scales with the ratio of channel length to contact width, as shown in Figure 3c. Evidently, the shorter the graphene channel and/or the wider the contacts, the less effective the current annealing procedure, i.e., the more current is needed to minimize residual charge disorder, and the more electric field disorder is present. Specifically, devices with shorter channels exhibit higher shares of contaminated regions near the contacts compared to devices with longer channels. Moreover, the contacts act as heat sinks,[38] and their widths determine the cooling effectiveness during current annealing, i.e., the wider the contacts the more likely the movement of contaminations toward them. Hence, electric field disorder is

https://doi.org/10.1021/acs.nanolett.2c02119
Nano Lett. 2022, 22, 7378−7385

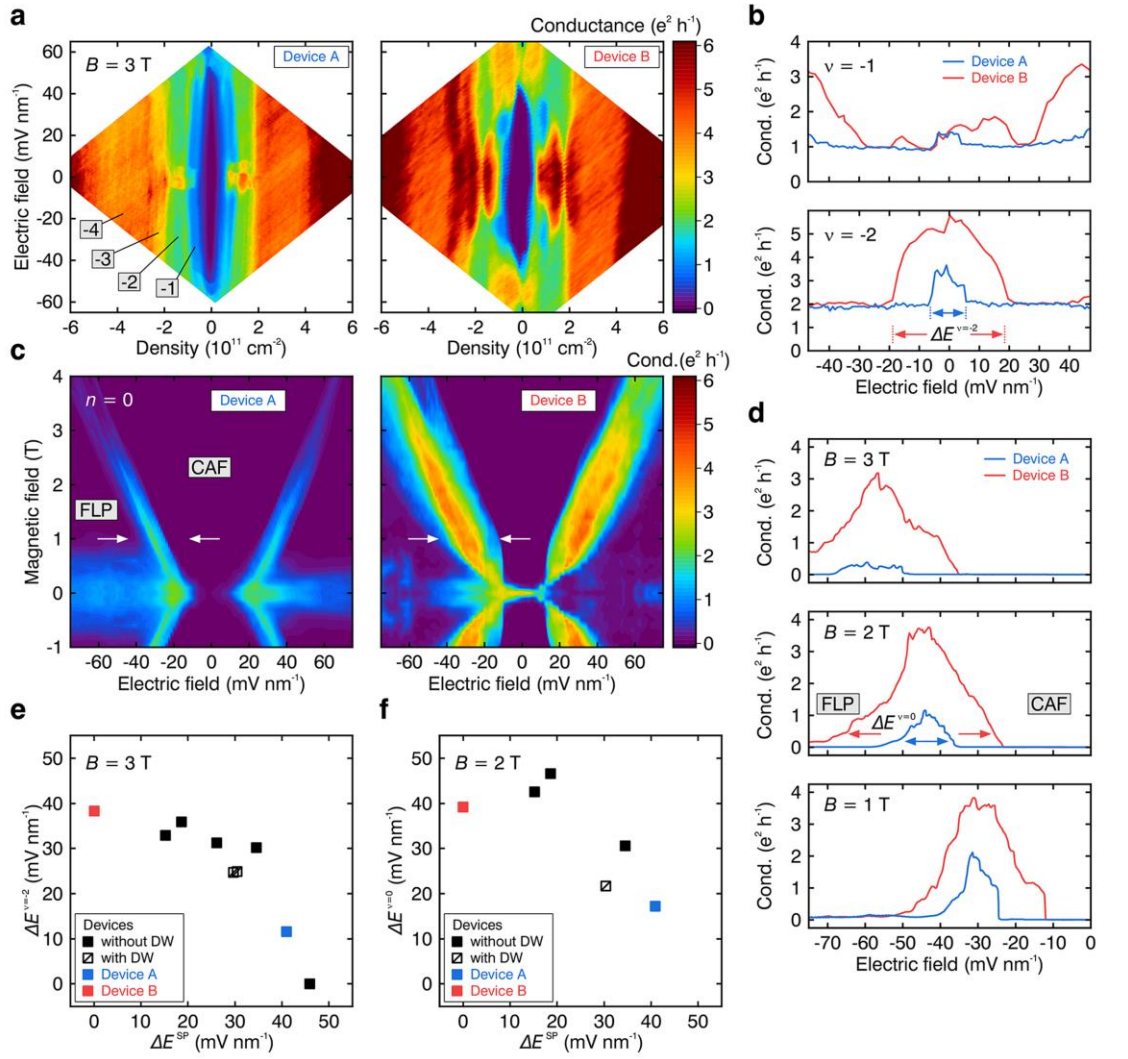

Figure 4. Phase transition between broken-symmetry quantum Hall states and distinct $\nu = 0$ states in bilayer graphene. a, Maps of conductance as a function of E and n at $B = 3$ T for devices A and B. b, Line traces of the conductance taken at $B = 3$ T and constant filling factors $\nu = -1$ and -2 as a function of E for devices A (blue) and B (red). The width of the phase transition between $\nu = -2$ states of opposite layer polarization in electric field ($\Delta E^{\nu=-2}$) is indicated. c, Maps of conductance as a function of E and B at zero charge carrier density for devices A and B. The first-order phase transition between the canted antiferromagnetic (CAF) and the fully layer polarized (FLP) states is characterized by a region with increased conductance, indicated by the white arrows. d, Line traces across the $\nu = 0$ phase transition at negative electric fields for $B = 1$, 2, and 3 T shown for devices A (blue) and B (red). The width of the $\nu = 0$ phase transition at negative electric fields $\Delta E^{\nu=0}$ is indicated for $B = 2$ T. e, $\Delta E^{\nu=-2}$ at $B = 3$ T as a function of ΔE^{SP} shown for several devices. Devices with (without) a stacking domain wall within the channel are shown with open (closed) squares. Device A (B) is shown in blue (red). f, $\Delta E^{\nu=0}$ at $B = 2$ T as a function of ΔE^{SP} shown for several devices.

primarily present in devices with short channels and wide contacts. Its presence allows for the formation of domains of competing spontaneously gapped states other than a uniform LAF state[26] within a device. Spontaneous DWs separating these domains are known to carry gapless edge modes.[26] These can explain the observation of finite σ_{CNP} and small ΔE^{SP}.

An estimate of the upper bound of the electric field disorder that completely suppresses the LAF state can be half of ΔE^{SP} in the cleanest device, namely, ~25 mV nm^{-1}. This corresponds to a charge imbalance of about 1.4×10^{11} cm^{-2} in device B, which is surprisingly large given that the charge disorder is an order of magnitude smaller (Figure 3a). However, the critical disorder strength could be much weaker, as the domain walls between LAF/FLP states are expected to proliferate at the critical point (just like at the critical temperature[26]). Moreover, the two types of disorder are uncorrelated.[39]

To find more proof of electric field disorder, we have conducted magneto-transport measurements, since the formation of domains is expected to impact transitions between broken-symmetry quantum Hall states.[32] The conductance as a

https://doi.org/10.1021/acs.nanolett.2c02119
Nano Lett. 2022, 22, 7378−7385

function of n and E at B = 3 T for devices A and B are shown in Figure 4a (see Figure S8 for data at 1.5 T). Although both devices show the full splitting of the lowest Landau level octet, major differences in the appearance of the $\nu = \pm 1$ and ± 2 states arise. In particular, transitions to the layer polarized $\nu = \pm 1$ and ± 2 states around zero electric field can be identified as regions of increased conductance (see Figure 4a,b), as observed previously.[2,8,17,41] In general, if electric field disorder is strong, around zero electric field, domains of states with opposite layer polarization can be present. Moreover, DWs separating these domains can host one-dimensional conducting states,[26,32] increasing the conductance. Whereas the transition regions are narrow in electric field in device A, in device B they are drastically extended and feature enhanced conductance, consistent with many domains and consequently a network of conducting DW states present. Generally, the more domains of states with different layer polarization within a device occur, the more DW states contribute to the charge transport and the more electric field that is needed to uniformly favor a layer-polarized state. On a broader basis, we take the extent of the region of increased conductance in electric field for the $\nu = -2$ state ($\Delta E^{\nu=-2}$) as an indication for the density of conductive DWs and plot it as a function of the width of the LAF ground state in the electric field ΔE^{SP} for several devices (Figure 4e). Systematically, the devices with larger $\Delta E^{\nu=-2}$ also have weaker LAF states at B = 0, consistent with the relevance of the electric field disorder with a concomitant formation of domains in both states. This correlation further corroborates our findings and their explanation at zero magnetic field. Worth mentioning is that these phase-transition regions vanish for very high magnetic fields, since additional layer-balanced, spin-polarized $\nu = \pm 1, \pm 2$ states emerge around zero electric field.[17,18]

Finally, we turn to another electric-field induced quantum phase transition between two ν = 0 states,[3] the canted antiferromagnetic (CAF) phase at low electric fields and the fully layer polarized (FLP) phase at high electric fields. Conductance maps as functions of the applied electric and magnetic fields at zero density are shown for devices A and B in Figure 4c. We find the two ν = 0 insulating states separated by a region with increased conductance, as reported in the literature.[2,3,21] This first order phase transition has a slope in the E−B plane. By taking line traces along negative E at specific B (Figure 4d), one can clearly reveal differences between device A, which displays a sharper transition, and device B, where the phase transition not only has a higher conductance but also extends over a wider range of electric field $\Delta E^{\nu=0}$. Although a recent study attributed the broad transition to the emergence of a new phase,[21] our data is consistent with the presence of electric field disorder causing the formation of multiple domains of CAF and FLP phases in the transition region.[15] DWs separating the layer unpolarized CAF and the FLP states host one-dimensional conducting states[26,32] and consequently cause an increase in conductance at the transition. The step-like features likely indicate the switching of individual domains (Figure 4d). To correlate this observation with the strength of the spontaneously gapped ground state at B = 0 (i.e., the LAF state), we plot the width of the ν = 0 transition at negative electric field $\Delta E^{\nu=0}$ at B = 2 T versus ΔE^{SP} for six devices (Figure 4f). Again, devices with a more pronounced spontaneous gap at B = 0 also exhibit a narrower transition between the two ν = 0 states, consistent with the detrimental impact of the electric field disorder.

OUTLOOK

Having identified the electric field disorder as the source for creating domains of different spontaneously gapped ground states at zero magnetic field and broadening the electric field-induced phase transitions both at zero magnetic field and in the quantum Hall ferromagnetic regime in BLG poses interesting questions for future investigations. How can one fabricate noninvasive contacts in suspended devices beyond the existing four-terminal ones?[42] How does the electric field disorder impact the thermal proliferation of spontaneous DWs[26] in suspended devices? How does the electric field disorder address the interplay between trigonal warping and Coulomb interaction and the resulting cascade of correlated phases, including fractional metals[13,43,44] and Wigner crystals?[13] Finally, we note that the existence of electric field disorder should be universal to all 2D materials, and its unique impacts await exploration.

ASSOCIATED CONTENT

Supporting Information

The Supporting Information is available free of charge at https://pubs.acs.org/doi/10.1021/acs.nanolett.2c02119.

Methods used for sample fabrication and characterization, a Supplementary Note with the discussion about the layer antiferromagnetic state, scanning near-field optical microscopy images of the 11 devices (Figure S1), current annealing procedure and the appearance of fractional quantum Hall states (Figure S2), correlation among σ_{CNP}, ΔE^{SP}, and the critical temperature of the spontaneous ground phase (Figure S3), behavior of the LAF phase with increasing magnetic field (Figure S4), stability of stacking domain walls during processing (Figure S5), stability of stacking domain walls during current annealing (Figure S6), stability of the quantum transport signatures during multiple current annealing cycles (Figure S7), and behavior of the quantum Hall states at B = 1.5 T (Figure S8) (PDF)

AUTHOR INFORMATION

Corresponding Author

R. Thomas Weitz − *Physics of Nanosystems, Department of Physics, Ludwig-Maximilians-Universität München, Munich 80539, Germany; Center for Nanoscience (CeNS), Munich 80799, Germany; Munich Center for Quantum Science and Technology (MCQST), Munich 80799, Germany; 1st Physical Institute, Faculty of Physics, University of Göttingen, Göttingen 37077, Germany;* orcid.org/0000-0001-5404-7355; Email: thomas.weitz@uni-goettingen.de

Authors

Fabian R. Geisenhof − *Physics of Nanosystems, Department of Physics, Ludwig-Maximilians-Universität München, Munich 80539, Germany;* orcid.org/0000-0002-3623-1906

Felix Winterer − *Physics of Nanosystems, Department of Physics, Ludwig-Maximilians-Universität München, Munich 80539, Germany;* orcid.org/0000-0002-8344-1615

Anna M. Seiler − *Physics of Nanosystems, Department of Physics, Ludwig-Maximilians-Universität München, Munich 80539, Germany; 1st Physical Institute, Faculty of Physics, University of Göttingen, Göttingen 37077, Germany*

Jakob Lenz − *Physics of Nanosystems, Department of Physics, Ludwig-Maximilians-Universität München, Munich 80539, Germany*

Fan Zhang − *Department of Physics, University of Texas at Dallas, Richardson, Texas 75080, United States;* orcid.org/0000-0003-4623-4200

Complete contact information is available at: https://pubs.acs.org/10.1021/acs.nanolett.2c02119

Author Contributions

F.R.G. fabricated the devices and conducted the measurements. F.R.G. and R.T.W. analyzed the data. F.Z. contributed the theoretical part. All authors discussed and interpreted the data. R.T.W. supervised the experiments and the analysis. The manuscript was prepared by F.R.G., F.Z., and R.T.W with input from all authors.

Notes

The authors declare no competing financial interest.

■ ACKNOWLEDGMENTS

R.T.W. and F.R.G. acknowledge funding from the Center for Nanoscience (CeNS) and by the Deutsche Forschungsgemeinschaft (DFG, German Research Foundation) under Germany's Excellence Strategy EXC-2111-390814868 (MCQST). F.Z. acknowledges support from the Army Research Office under Grant No. W911NF-18-1-0416 and the National Science Foundation under grant numbers DMR-1945351 through the CAREER program, DMR-2105139 through the CMP program, and DMR-1921581 through the DMREF program. We also thank Y.C. Durmaz, F. Keilmann, and T.D. Gokus for experimental assistance with the near-field optical microscopy measurements.

■ REFERENCES

(1) McCann, E.; Fal'ko, V. I. Landau-Level Degeneracy and Quantum Hall Effect in a Graphite Bilayer. *Phys. Rev. Lett.* **2006**, *96*, 086805.
(2) Weitz, R. T.; Allen, M. T.; Feldman, B. E.; Martin, J.; Yacoby, A. Broken-Symmetry States in Doubly Gated Suspended Bilayer Graphene. *Science* **2010**, *330*, 812−816.
(3) Maher, P.; Dean, C. R.; Young, A. F.; Taniguchi, T.; Watanabe, K.; Shepard, K. L.; Hone, J.; Kim, P. Evidence for a spin phase transition at charge neutrality in bilayer graphene. *Nat. Phys.* **2013**, *9*, 154−158.
(4) Zhang, F.; Jung, J.; Fiete, G. A.; Niu, Q.; MacDonald, A. H. Spontaneous Quantum Hall States in Chirally Stacked Few-Layer Graphene Systems. *Phys. Rev. Lett.* **2011**, *106*, 156801.
(5) Zhang, F. Spontaneous chiral symmetry breaking in bilayer graphene. *Synth. Met.* **2015**, *210*, 9−18.
(6) Freitag, F.; Trbovic, J.; Weiss, M.; Schönenberger, C. Spontaneously Gapped Ground State in Suspended Bilayer Graphene. *Phys. Rev. Lett.* **2012**, *108*, 076602.
(7) Bao, W.; Velasco, J.; Zhang, F.; Jing, L.; Standley, B.; Smirnov, D.; Bockrath, M.; MacDonald, A. H.; Lau, C. N. Evidence for a Spontaneous Gapped State in Ultraclean Bilayer Graphene. *Proc. Natl. Acad. Sci. U.S.A.* **2012**, *109*, 10802−10805.
(8) Velasco, J.; Jing, L.; Bao, W.; Lee, Y.; Kratz, P.; Aji, V.; Bockrath, M.; Lau, C. N.; Varma, C.; Stillwell, R.; Smirnov, D.; Zhang, F.; Jung, J.; MacDonald, A. H. Transport Spectroscopy of Symmetry-Broken Insulating States in Bilayer Graphene. *Nat. Nanotechnol.* **2012**, *7*, 156−160.
(9) Veligura, A.; van Elferen, H. J.; Tombros, N.; Maan, J. C.; Zeitler, U.; van Wees, B. J. Transport Gap in Suspended Bilayer Graphene at Zero Magnetic Field. *Phys. Rev. B* **2012**, *85*, 155412.
(10) Freitag, F.; Weiss, M.; Maurand, R.; Trbovic, J.; Schönenberger, C. Spin symmetry of the bilayer graphene ground state. *Phys. Rev. B* **2013**, *87*, 161402.
(11) Nam, Y.; Ki, D.-K.; Soler-Delgado, D.; Morpurgo, A. F. A Family of Finite-Temperature Electronic Phase Transitions in Graphene Multilayers. *Science* **2018**, *362*, 324−328.
(12) Geisenhof, F. R.; Winterer, F.; Seiler, A. M.; Lenz, J.; Xu, T.; Zhang, F.; Weitz, R. T. Quantum Anomalous Hall Octet Driven by Orbital Magnetism in Bilayer Graphene. *Nature* **2021**, *598*, 53−58.
(13) Seiler, A. M.; Geisenhof, F. R.; Winterer, F.; Watanabe, K.; Taniguchi, T.; Xu, T.; Zhang, F.; Weitz, R. T. Quantum Cascade of Correlated Phases in Trigonally Warped Bilayer Graphene. *Nature* **2022**, *608*, 298−302.
(14) Hunt, B. M.; Li, J. I. A.; Zibrov, A. A.; Wang, L.; Taniguchi, T.; Watanabe, K.; Hone, J.; Dean, C. R.; Zaletel, M.; Ashoori, R. C.; Young, A. F. Direct Measurement of Discrete Valley and Orbital Quantum Numbers in Bilayer Graphene. *Nat. Commun.* **2017**, *8*, 948.
(15) Lee, K.; Fallahazad, B.; Xue, J.; Dillen, D. C.; Kim, K.; Taniguchi, T.; Watanabe, K.; Tutuc, E. Bilayer Graphene. Chemical Potential and Quantum Hall Ferromagnetism in Bilayer Graphene. *Science* **2014**, *345*, 58−61.
(16) Li, J.; Tupikov, Y.; Watanabe, K.; Taniguchi, T.; Zhu, J. Effective Landau Level Diagram of Bilayer Graphene. *Phys. Rev. Lett.* **2018**, *120*, 047701.
(17) Velasco, J.; Lee, Y.; Zhang, F.; Myhro, K.; Tran, D.; Deo, M.; Smirnov, D.; MacDonald, A. H.; Lau, C. N. Competing Ordered States with Filling Factor Two in Bilayer Graphene. *Nat. Commun.* **2014**, *5*, 4550.
(18) Shi, Y.; Lee, Y.; Che, S.; Pi, Z.; Espiritu, T.; Stepanov, P.; Smirnov, D.; Lau, C. N.; Zhang, F. Energy Gaps and Layer Polarization of Integer and Fractional Quantum Hall States in Bilayer Graphene. *Phys. Rev. Lett.* **2016**, *116*, 056601.
(19) Zhang, J.; Nandkishore, R.; Rossi, E. Disorder-tuned selection of order in bilayer graphene. *Phys. Rev. B* **2015**, *91*, 205425.
(20) Mayorov, A. S.; Elias, D. C.; Mucha-Kruczynski, M.; Gorbachev, R. V.; Tudorovskiy, T.; Zhukov, A.; Morozov, S. V.; Katsnelson, M. I.; Fal'ko, V. I.; Geim, A. K.; Novoselov, K. S. Interaction-Driven Spectrum Reconstruction in Bilayer Graphene. *Science* **2011**, *333*, 860−863.
(21) Li, J.; Fu, H.; Yin, Z.; Watanabe, K.; Taniguchi, T.; Zhu, J. Metallic Phase and Temperature Dependence of the N=0 Quantum Hall State in Bilayer Graphene. *Phys. Rev. Lett.* **2019**, *122*, 097701.
(22) Bolotin, K. I.; Sikes, K. J.; Jiang, Z.; Klima, M.; Fudenberg, G.; Hone, J.; Kim, P.; Stormer, H. L. Ultrahigh electron mobility in suspended graphene. *Solid State Commun.* **2008**, *146*, 351−355.
(23) Ju, L.; Shi, Z.; Nair, N.; Lv, Y.; Jin, C.; Velasco, J.; Ojeda-Aristizabal, C.; Bechtel, H. A.; Martin, M. C.; Zettl, A.; Analytis, J.; Wang, F. Topological Valley Transport at Bilayer Graphene Domain Walls. *Nature* **2015**, *520*, 650−655.
(24) Alden, J. S.; Tsen, A. W.; Huang, P. Y.; Hovden, R.; Brown, L.; Park, J.; Muller, D. A.; McEuen, P. L. Strain Solitons and Topological Defects in Bilayer Graphene. *Proc. Natl. Acad. Sci. U.S.A.* **2013**, *110*, 11256−11260.
(25) Zhang, F.; MacDonald, A. H.; Mele, E. J. Valley Chern Numbers and Boundary Modes in Gapped Bilayer Graphene. *Proc. Natl. Acad. Sci. U.S.A.* **2013**, *110*, 10546−10551.
(26) Li, X.; Zhang, F.; Niu, Q.; MacDonald, A. H. Spontaneous Layer-Pseudospin Domain Walls in Bilayer Graphene. *Phys. Rev. Lett.* **2014**, *113*, 116803.
(27) Jiang, L.; Shi, Z.; Zeng, B.; Wang, S.; Kang, J.-H.; Joshi, T.; Jin, C.; Ju, L.; Kim, J.; Lyu, T.; Shen, Y.-R.; Crommie, M.; Gao, H.-J.; Wang, F. Soliton-Dependent Plasmon Reflection at Bilayer Graphene Domain Walls. *Nat. Mater.* **2016**, *15*, 840−844.
(28) Sunku, S. S.; Ni, G. X.; Jiang, B. Y.; Yoo, H.; Sternbach, A.; McLeod, a. S.; Stauber, T.; Xiong, L.; Taniguchi, T.; Watanabe, K.; Kim, P.; Fogler, M. M.; Basov, D. N. Photonic Crystals for Nano-Light in Moiré Graphene Superlattices. *Science* **2018**, *362*, 1153−1156.

(29) Huang, S.; Kim, K.; Efimkin, D. K.; Lovorn, T.; Taniguchi, T.; Watanabe, K.; MacDonald, A. H.; Tutuc, E.; LeRoy, B. J. Topologically Protected Helical States in Minimally Twisted Bilayer Graphene. *Phys. Rev. Lett.* **2018**, *121*, 037702.
(30) Cao, Y.; Fatemi, V.; Fang, S.; Watanabe, K.; Taniguchi, T.; Kaxiras, E.; Jarillo-Herrero, P. Unconventional Superconductivity in Magic-Angle Graphene Superlattices. *Nature* **2018**, *556*, 43−50.
(31) Geisenhof, F. R.; Winterer, F.; Seiler, A. M.; Lenz, J.; Martin, I.; Weitz, R. T. Interplay between topological valley and quantum Hall edge transport. *Nat. Commun.* **2022**, *13*, 4187.
(32) Dhochak, K.; Shimshoni, E.; Berg, E. Spontaneous layer polarization and conducting domain walls in the quantum Hall regime of bilayer graphene. *Phys. Rev. B* **2015**, *91*, 165107.
(33) Kharitonov, M. Edge excitations of the canted antiferromagnetic phase of the ν=0 quantum Hall state in graphene: A simplified analysis. *Phys. Rev. B* **2012**, *86*, 075450.
(34) Ni, Z. H.; Yu, T.; Lu, Y. H.; Wang, Y. Y.; Feng, Y. P.; Shen, Z. X. Uniaxial Strain on Graphene: Raman Spectroscopy Study and Band-Gap Opening. *ACS Nano* **2008**, *2*, 2301−2305.
(35) San-Jose, P.; Gorbachev, R. V.; Geim, A. K.; Novoselov, K. S.; Guinea, F. Stacking Boundaries and Transport in Bilayer Graphene. *Nano Lett.* **2014**, *14*, 2052−2057.
(36) Geisenhof, F. R.; Winterer, F.; Wakolbinger, S.; Gokus, T. D.; Durmaz, Y. C.; Priesack, D.; Lenz, J.; Keilmann, F.; Watanabe, K.; Taniguchi, T.; Guerrero-Avilés, R.; Pelc, M.; Ayuela, A.; Weitz, R. T. Anisotropic Strain-Induced Soliton Movement Changes Stacking Order and Band Structure of Graphene Multilayers: Implications for Charge Transport. *ACS Appl. Nano Mater.* **2019**, *2*, 6067−6075.
(37) Guerrero-Avilés, R.; Pelc, M.; Geisenhof, F. R.; Weitz, R. T.; Ayuela, A. Relative Stability of Bernal and Rhombohedral Stackings in Trilayer Graphene under Distortions. *arXiv* (Mesoscale and Nanoscale Physics), 2021, 2110.06590v2, http://arxiv.org/pdf/2110.06590v2 (accessed September 12, 2022).
(38) Moser, J.; Barreiro, A.; Bachtold, A. Current-induced cleaning of graphene. *Appl. Phys. Lett.* **2007**, *91*, 163513.
(39) Abergel, D. S. L.; Min, H.; Hwang, E. H.; Das Sarma, S. dμdn in suspended bilayer graphene: The interplay of disorder and band gap. *Phys. Rev. B* **2011**, *84*, 195423.
(40) Rutter, G. M.; Jung, S.; Klimov, N. N.; Newell, D. B.; Zhitenev, N. B.; Stroscio, J. A. Microscopic polarization in bilayer graphene. *Nat. Phys.* **2011**, *7*, 649−655.
(41) Martin, J.; Feldman, B. E.; Weitz, R. T.; Allen, M. T.; Yacoby, A. Local Compressibility Measurements of Correlated States in Suspended Bilayer Graphene. *Phys. Rev. Lett.* **2010**, *105*, 256806.
(42) Ki, D.-K.; Morpurgo, A. F. High-Quality Multiterminal Suspended Graphene Devices. *Nano Lett.* **2013**, *13*, 5165−5170.
(43) Zhou, H.; Holleis, L.; Saito, Y.; Cohen, L.; Huynh, W.; Patterson, C. L.; Yang, F.; Taniguchi, T.; Watanabe, K.; Young, A. F. Isospin Magnetism and Spin-Polarized Superconductivity in Bernal Bilayer Graphene. *Science* **2022**, *375*, 774−778.
(44) de la Barrera, S. C.; Aronson, S.; Zheng, Z.; Watanabe, K.; Taniguchi, T.; Ma, Q.; Jarillo-Herrero, P.; Ashoori, R. Cascade of isospin phase transitions in Bernal-stacked bilayer graphene at zero magnetic field. *Nat. Phys.* **2022**, *18*, 771−775.

https://doi.org/10.1021/acs.nanolett.2c02119
Nano Lett. 2022, 22, 7378−7385

B Supplementary Material of the Publications

In the following, the Supplementary Information corresponding to the publications is provided.

B.1 Supplementary Information: Interplay between Topological Valley and Quantum Hall Edge Transport

Fabian R. Geisenhof, Felix Winterer, Anna M. Seiler, Jakob Lenz, Ivar Martin, and R. Thomas Weitz
Nat. Commun. **13**, 4187 (2022)
DOI: 10.1038/s41467-022-31680-y

Supplementary Information for

Interplay between topological valley and quantum Hall edge transport

Fabian R. Geisenhof[1], Felix Winterer[1], Anna M. Seiler[1],
Jakob Lenz[1], Ivar Martin[3], R. Thomas Weitz[1,2,4,5]*

Affiliations:

[1]Physics of Nanosystems, Department of Physics, Ludwig-Maximilians-Universität München, Geschwister-Scholl-Platz 1, Munich 80539, Germany

[2]1st Physical Institute, Faculty of Physics, University of Göttingen, Friedrich-Hund-Platz 1, Göttingen 37077, Germany

[3]Materials Science Division, Argonne National Laboratory, Lemont, Illinois 60439, USA

[4]Center for Nanoscience (CeNS), LMU Munich, Schellingstrasse 4, Munich 80799, Germany

[5]Munich Center for Quantum Science and Technology (MCQST), Schellingstrasse 4, Munich 80799, Germany

*Corresponding author. Email: thomas.weitz@uni-goettingen.de

Supplementary Note 1:

Identifying the emerging broken-symmetry quantum Hall states in the presence of a stacking domain wall

Since the conductance of the appearing quantum Hall states in device D1-DW differs quite significantly from usually observed values as in device D2, we have additionally recorded fan diagrams to examine the slope of transconductance fluctuations[1,2] (see Supplementary Fig. 1). As some of the emerging phases show an electric field dependence, we have measured the conductance at various applied fields (see Supplementary Fig. 1a – d). The slopes of the appearing broken-symmetry states fit very well to the expected $\nu = 0, \pm 1, \pm 2$ and ± 4 states, despite all having similar conductances of 3 – 4 $e^2\ h^{-1}$. Thus, additional charge transport along the domain wall in parallel to the quantum Hall edge states is unambiguously the cause for the higher conductance in the different states. Whereas the $\nu = 0$ phase is most stable for low and high electric field, consistent with a phase transition from the LAF/CAF to the LP phase[3,4], the $\nu = \pm 4$ is most stable for low electric field. Contrarily, the (partially) layer polarised $\nu = \pm 1, \pm 2$ phases appear only at intermediate electric field at these low magnetic field. Notably, since at $n = E = B = 0$ transconductance fluctuations with zero slope are visible, the layer antiferromagnetic phase is indeed present but masked owing to the quantum valley transport along the stacking domain wall.

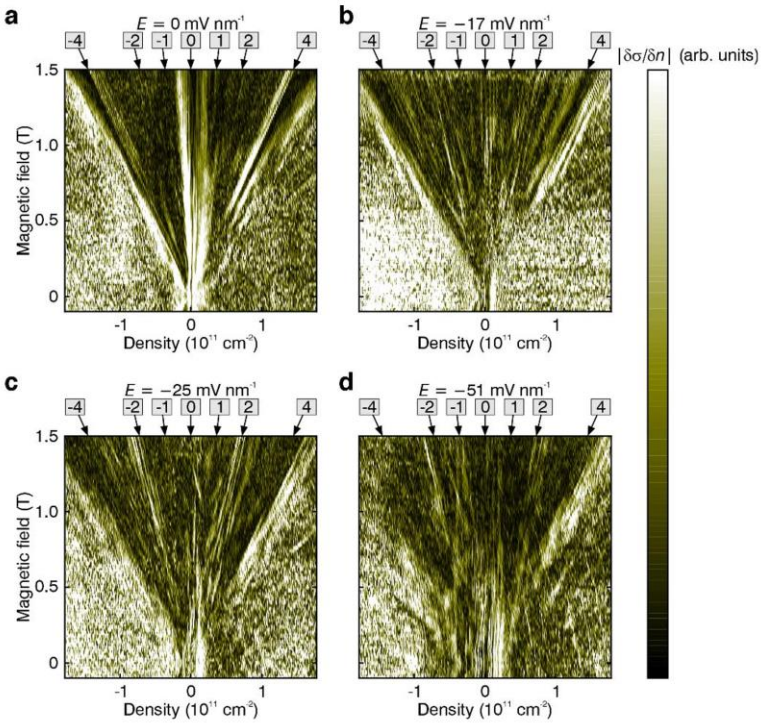

Supplementary Figure 1 | Fan diagrams measured at specific electric fields. a – d, Derivative of the differential conductance $\delta\sigma/\delta n$ as a function of magnetic field and charge carrier density for various electric fields. The slopes of the individual broken-symmetry $\nu = 0, \pm 1, \pm 2, \pm 4$ states are indicated with arrows.

Supplementary Note 2:

Phase transition between the fully layer polarised and the canted antiferromagnetic $\nu = 0$ phase in the presence of a stacking domain wall

When sweeping E as a function of B for zero charge carrier density (Supplementary Fig. 2a,b), the transition between the fully layer polarised and the canted antiferromagnetic phase appears as region with increased conductance in both devices, consistent with previous measurements[3,4]. However, in device D2 both phases are insulating, whereas in D1-DW the conductance remains finite at $\sigma \approx 2.9\, e^2\, h^{-1}$ (see Supplementary Fig. 2c) due to the kink states contributing to the charge transport. Within the CAF phase the conductance is slightly decreasing for increasing magnetic field (Supplementary Fig. 2d), consistent with the increase of canting and evolving energetic dispersion of the kink states (see main text). In Supplementary Fig. 2e, the band structure of the CAF and LP phase in the presence of a domain wall are schematically shown. In contrast to the minigap opening in the CAF phase owing to the hybridising of same valley states, the valley-helical kink states in the LP phase remain largely intact due to the suppression of intervalley scattering.

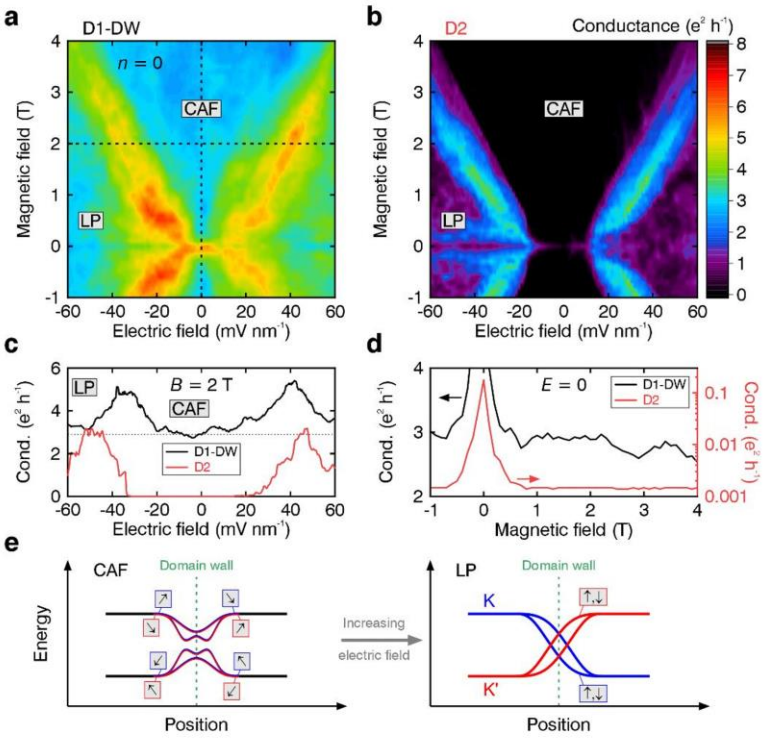

Supplementary Figure 2 | Phase transition between the fully layer polarised and the canted antiferromagnetic $\nu = 0$ phase. a,b, Conductance as a function of applied electric *E* and magnetic field *B* at zero charge carrier density for device D1-DW (a) and D2 (b). The first-order phase transition between the two $\nu = 0$ phases, the CAF and the LP phase, is characterized by a region with increased conductance. The dashed lines in (a) indicate the position of the data shown in (c) and (d). **c,** Line traces of the conductance across the $\nu = 0$ phase transition shown for sample D1-DW (black) and D2 (red) at *B* = 2 T. The dashed line marks the value $2.9\ e^2\ h^{-1}$. **d,** Conductance as a function of *B* for *n* = *E* = 0. The data of device D1-DW (D2) is shown in black (red). **e,** Schematic band structure as a function of position around a stacking domain wall shown for the CAF and LP phase.

Supplementary Note 3:

Impact of domain walls on the band structure beyond the zero energy Landau level

Supplementary Fig. 3 shows the influence of the domain wall on higher Landau levels. To this end, we have recorded a conductance map as a function of function of *E* and *n* at *B* = 1.5 T, see Supplementary Fig. 3a. At this low magnetic field, we can observe the $\nu = \pm 8, \pm 12$ quantum Hall states. While the conductance of the $\nu = \pm 8$ states show the expected conductance, the one of the $\nu = \pm 12$ state seems to be lower than 12 $e^2\ h^{-1}$. Moreover, we see an oscillating behaviour of the conductance when entering a new quantum Hall plateau (see Supplementary Fig. 3a,b). One possible explanation for these oscillations could be the rather low aspect ratio $L/W \approx 0.5$ of the device, with L and W being the length and width of the device channel, respectively. It has been shown that the shape of a sample can non-trivially affect the conductance at the quantum Hall transitions[5].

However, theoretical calculations of Landau levels energies (see Supplementary Fig. 3c,d) show that domain walls can cause the formation of ripples within higher Landau levels. For the band structure calculation, we used a linearized model of graphene layers near K/K' valley, with smoothly varying interlayer hybridisation across the domain wall; namely, hopping A1B2 gradually is being replaced by B1A2. The energies are calculated in a finite width strip, with the domain wall in the middle. In Landau gauge, the translational invariance in the direction of the strip is preserved, and the energies are plotted as a function of momentum along the strip. The rescaled momentum also corresponds to the locations x of the centres of individual states, when rescaled by $c/(eB)$, with c being the speed of light. Interestingly, if the expected increase of A1A2 and B1B2 hybridisation at the domain wall is not included, the zero energy Landau levels remain flat through the domain wall. In contrast, the higher Landau levels show

significant variations – "ripples" – near the domain wall. This could also be the possible reason for the observed oscillations of conductance as a function of density.

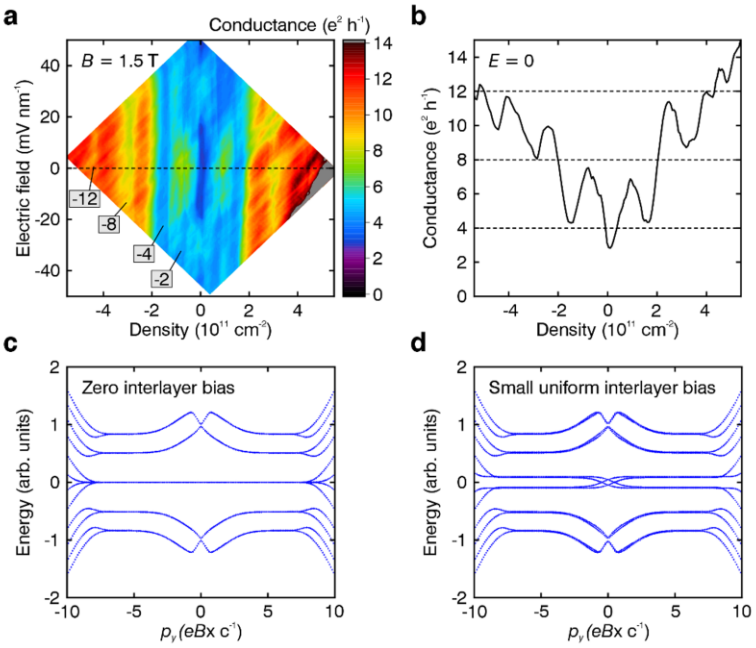

Supplementary Figure 3 | Influence of the domain wall on the energetic landscape of higher Landau levels. a, Conductance as a function of *E* and *n* at *B* = 1.5 T. The dashed line indicates the position of the data shown in (b). **b,** Line trace of the conductance as a function of charge carrier density for zero electric field. The dashed lines indicate multiples of $4\,e^2\,h^{-1}$. **c,** Schematic Landau level band structure computed in the presence of a domain wall, smoothly interpolating between AB and BA stacking. The horizontal axis is the momentum along the domain wall. In Landau gauge used here, it is proportional to the location of the centre of a given orbital, x. With zero interlayer bias, the zeroth Landau level is four-fold degenerate (valley and orbital index), and higher Landau levels are doubly degenerate owing to valley degeneracy (spin is ignored). Near the edges the Landau levels float away from zero energy. The behaviour near the domain wall ($x = 0$) depends on the precise way that domain wall interpolates between AB and BA stackings. Even when the zeroth Landau level is flat (when A1A2 and B1B2 hopping near domain wall is ignored), the higher Landau levels are sensitive to the presence of the stacking defect. **d,** same as in (c) but with a small uniform interlayer bias. Notably, valley-helical modes emerge at the domain wall.

Supplementary Note 4:

Full quantum transport data at low and high magnetic field in the presence of a stacking domain wall

Supplementary Fig. 4a – e shows the full conductance maps as a function of E and n for various magnetic fields in device D1-DW. Most prominently, the spectral minigap emerges for $B \geq 8$ T causing the conductance to drop, marked by the cross in Supplementary Fig. 4c – e and in the line traces in Supplementary Fig. 4f – h. Additionally, the conductances of the $\nu = 0, \pm 1, \pm 2$ states are dropping for increasing magnetic field. This can also be observed in the line traces shown in Supplementary Fig. 4f – h. For the $\nu = 0$ CAF phase, the decrease can be explained by the emergence of a minigap due to the hybridising of partially spin aligned counterpropagating modes in the same valley, as explained in the main manuscript. For the $\nu = 0, \pm 1, \pm 2$ states, we think the effect occurs owing to increased intervalley scattering, as explained in the main manuscript.

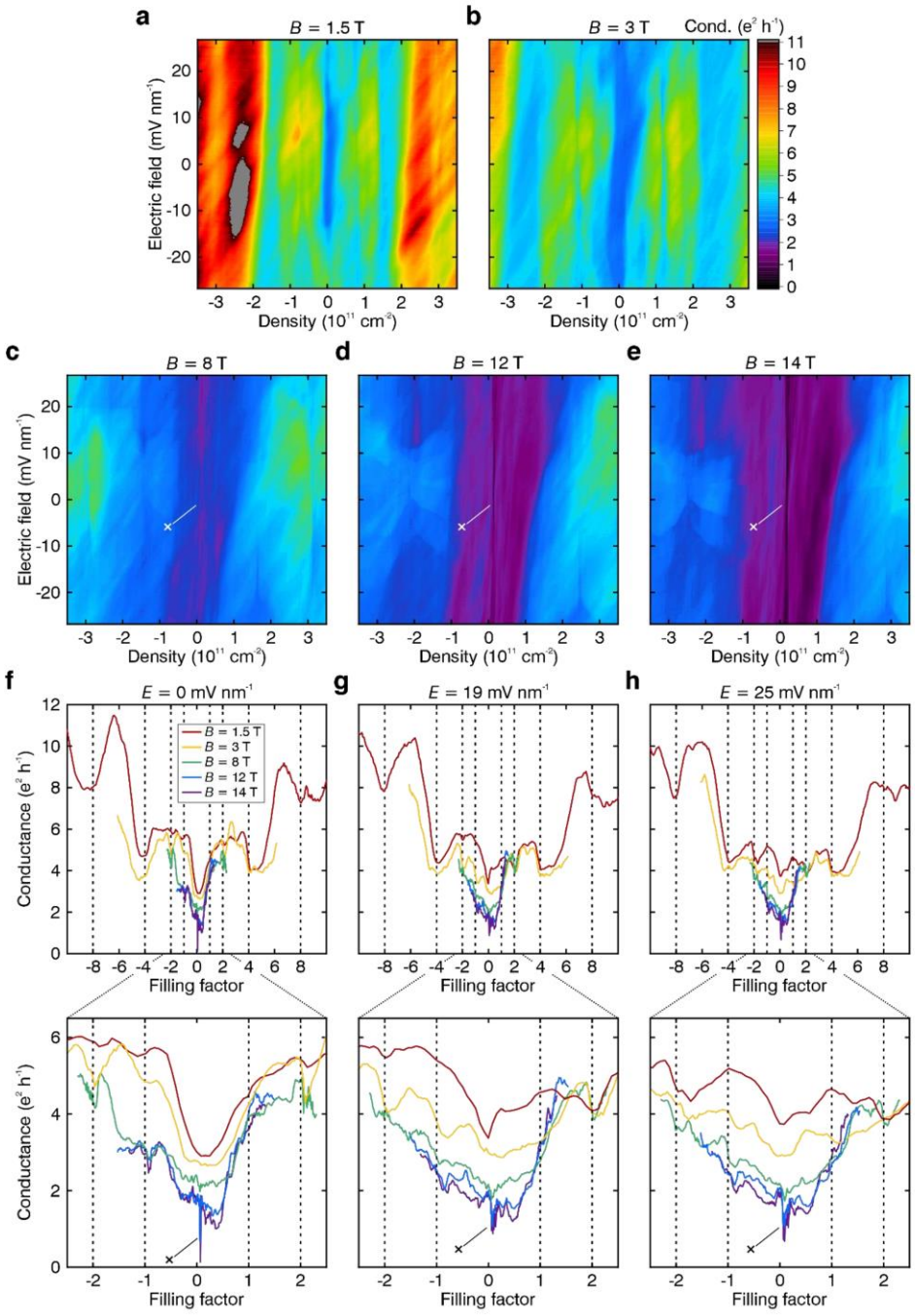

Supplementary Figure 4 | Topological valley and quantum Hall edge transport for low and high magnetic fields. a – e, Maps of the conductance as a function of electric field and charge carrier density for various magnetic fields in device D1-DW. The cross indicates the conductance dip caused by the appearing minigap. **f – h,** Line traces of the conductance as a

function of filling factor for E = 0, 19 mV nm^{-1} and 25 mV nm^{-1}. The lower panels are zoom-ins around small filling factors.

Supplementary Note 5:

Persistence of the spectral minigap for a different cooldown

Supplementary Fig. 5a shows a fan diagram recorded as a function of back gate voltage in device D1-DW. The graph shows the emergence of the spectral minigap within the $\nu = 0$ phase at $B \geq 8$ T, indicated by the cross. Moreover, its evolution for increasing magnetic field can be seen in Supplementary Fig. 5b, which shows line traces of the conductance for various high magnetic fields. The dip in conductance is increasing for increasing magnetic field, which matches the observations shown in Fig. 3 in the main manuscript.

It is worth noting that the data shown in Supplementary Fig. 5 was recorded during a different cooldown of the device than the data shown in the main manuscript. Most importantly, this demonstrates the persistence of the spectral minigap over multiple cooldowns. Since each cooldown involves a current annealing procedure, driving high currents through the device seem also to not affect the emergence of the feature. Notably, the device D1-DW was not as clean during the cooldown corresponding to Supplementary Fig. 5 as for the measurements shown in the main manuscript (in terms of residual charge disorder and contact resistance), which makes the direct comparison of absolute values of the conductance difficult.

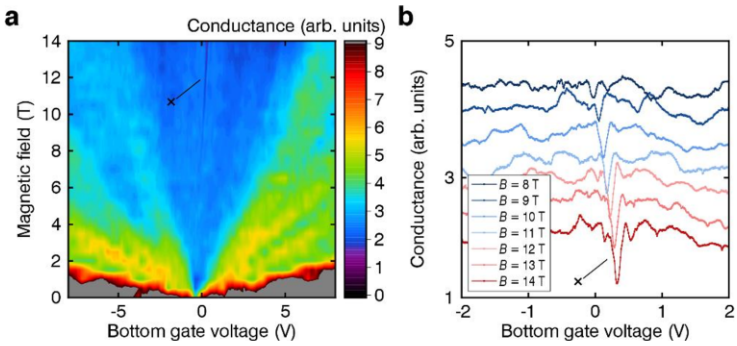

Supplementary Figure 5 | The emergence of a spectral minigap within the $\nu = 0$ phase for high magnetic field. a, Fan diagram showing the conductance as a function of magnetic field and bottom gate voltage. The cross indicates the conductance dip caused by the emergence of the spectral minigap. Note that the data was recorded with device D1-DW but during a different cooldown than the measurements shown in the main manuscript. **b,** Line traces of the conductance as a function of back gate voltage at various magnetic fields. The data is taken from the fan diagram shown in (a). The line cuts are offset for better visibility.

Supplementary Note 6:

Quantum transport measured in additional devices

Supplementary Fig. 6 shows the data from three additional devices with domain wall. Supplementary Fig. 6a – c shows the conductance of the $\nu = 0, -1, -2, -4$ quantum Hall states as a function of magnetic field measured in the devices D2-DW, D3-DW and D4-DW, respectively. Note that the conductance was averaged over the regime at which the respective state emerges, i.e. for the $\nu = 0$ CAF phase around zero electric field, for the $\nu = -1$ and -2 at $|E| \geq 10$ mV nm^{-1} and $|E| \geq 15$ mV nm^{-1} and the $\nu = -4$ state at all electric fields. The full conductance maps as a function of E and n for various magnetic fields are shown in Supplementary Fig. 6d – f for the three devices.

Similar to device D1-DW, all three samples show a decrease of the conductance for the quantum Hall states with increasing magnetic field. Although in device D2-DW (Supplementary Fig. 6a) and D3-DW (Supplementary Fig. 6b) the decrease is very prominent, sample D4-DW (Supplementary Fig. 6c) shows only a slight decrease of conductance. Moreover, a clear minigap can only be observed in device D2-DW (see Supplementary Fig. 6a,d). However, we have indications that the quality of the devices D3-DW and D4-DW is significantly lower than that of D2-DW or even D1-DW. In device D4-DW, even at low magnetic field, the conductances of the $\nu = 0, -2, -4$ states differ greatly. Evidently, the additional conductance originating from the kink states is highly reduced due to a low quality of the domain wall. In device D3-DW, the CAF phase can only be clearly observed for $B \geq 3$ T. Both observations indicate an overall lower quality of the two devices. Hence, the minigap can probably not be resolved due to disorder in both samples.

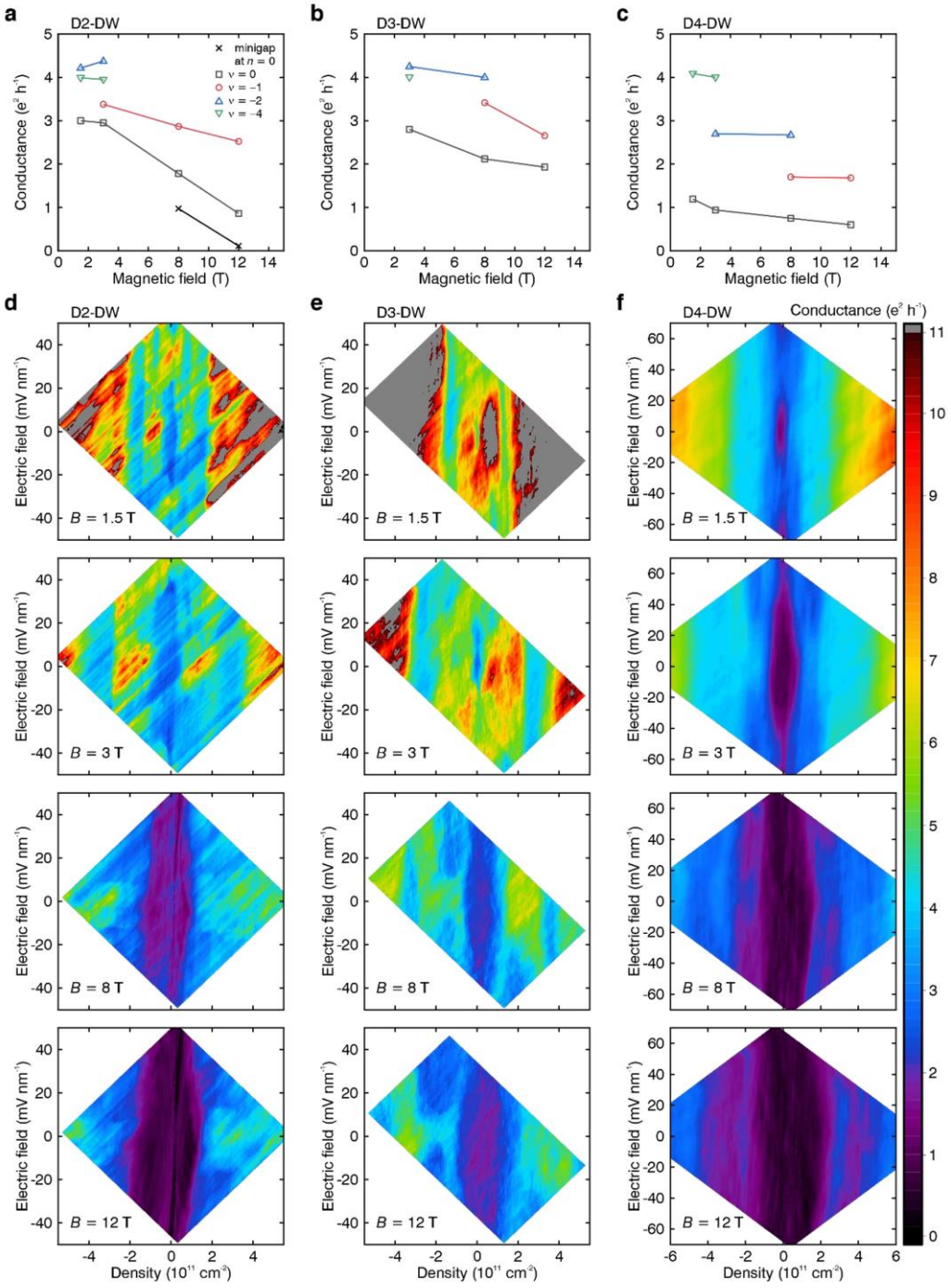

Supplementary Figure 6 | Data from additional devices. a – c, Conductance of the $\nu = 0, -1, -2, -4$ QH states as a function of B for the devices D2-DW (a), D3-DW (b) and D4-DW

(c). For device D2-DW, also the conductance within the spectral minigap is shown. **d – f,** Maps of the conductance as a function of E and n for various magnetic fields for the three devices.

References

1. Lee, D. S., Skákalová, V., Weitz, R. T., Klitzing, K. von & Smet, J. H. Transconductance fluctuations as a probe for interaction-induced quantum Hall states in graphene. *Phys. Rev. Lett.* **109**, 56602 (2012).
2. Geisenhof, F. R. *et al.* Quantum anomalous Hall octet driven by orbital magnetism in bilayer graphene. *Nature* **598**, 53–58 (2021).
3. Weitz, R. T., Allen, M. T., Feldman, B. E., Martin, J. & Yacoby, A. Broken-Symmetry States in Doubly Gated Suspended Bilayer Graphene. *Science* **330**, 812–816 (2010).
4. Maher, P. *et al.* Evidence for a spin phase transition at charge neutrality in bilayer graphene. *Nat. Phys.* **9**, 154–158 (2013).
5. Abanin, D. A. & Levitov, L. S. Conformal invariance and shape-dependent conductance of graphene samples. *Phys. Rev. B* **78**, 035416 (2008).

B.2 Supplementary Information: Impact of Electric Field Disorder on Broken-Symmetry States in Ultraclean Bilayer Graphene

Fabian R. Geisenhof, Felix Winterer, Anna M. Seiler, Jakob Lenz, Fan Zhang, and R. Thomas Weitz
Nano Lett. **22**, 7378 – 7385 (2022)
DOI: 10.1021/acs.nanolett.2c02119

Supplementary Materials for

Impact of Electric Field Disorder on Broken-Symmetry States in Ultraclean Bilayer Graphene

Authors: Fabian R. Geisenhof[1], Felix Winterer[1], Anna M. Seiler[1,5], Jakob Lenz[1], Fan Zhang[2], R. Thomas Weitz[1,3,4,5]*

Affiliations:

[1]Physics of Nanosystems, Department of Physics, Ludwig-Maximilians-Universität München, Geschwister-Scholl-Platz 1, Munich 80539, Germany

[2]Department of Physics, University of Texas at Dallas, Richardson, Texas, 75080, United States

[3]Center for Nanoscience (CeNS), Schellingstrasse 4, Munich 80799, Germany

[4]Munich Center for Quantum Science and Technology (MCQST), Schellingstrasse 4, Munich 80799, Germany

[5]1st Physical Institute, Faculty of Physics, University of Göttingen, Friedrich-Hund-Platz 1, Göttingen 37077, Germany

*Email: thomas.weitz@uni-goettingen.de

Methods:

Device fabrication:

Graphene flakes were exfoliated from a highly ordered pyrolytic graphite (HOPG) block onto Si/SiO_2 substrates. Suitable bilayer graphene flakes were preselected by examining their optical contrast under an optical microscope. Afterwards, infrared nano-imaging[1] was performed using a commercial scattering-type scanning near-field microscope (s-SNOM, neaspec GmbH) to detect stacking DWs within the flakes. Hereby, an infrared CO_2 laser beam with a wavelength of about 10.5 μm was focused onto a metal-coated atomic force microscopy tip (Pt/Ir, Arrow NCPT-50, Nanoworld) in tapping mode, providing topographic and infrared nano-images simultaneously. Oscillation frequency and amplitude of the tip were about 250 – 270 kHz and 50 – 80 nm, respectively. After fabricating the electrodes (Cr/Au, 5/100 nm), the top gate (Cr/Au, 5/160 nm) and a spacer (SiO_2, 140 nm) with multiple steps of standard electron-beam lithography and electron-beam evaporation, hydrofluoric acid was used to etch about 150 – 200 nm of the SiO_2 to suspend both the top gate and bilayer graphene flake. Subsequently, the suspended dually gated bilayer graphene devices were loaded in a dilution refrigerator and several cycles of current annealing at 1.6 K were performed. The devices were clean when a saturation of the drain current was well visible.

Quantum transport measurements:

We performed two-terminal conductance measurements with an AC bias current of 0.1 – 10 nA at 78 Hz using Stanford Research Systems SR865A and SR830 lock-in amplifiers. Keithley 2450 SourceMeters were used to apply the gate voltages.

Additionally, low-pass RC filters were used in series to reduce high frequency noise. For each device, a contact resistance was calculated and subtracted using the resistance of specific quantum Hall states[2].

Supplementary Note:

Discussion about the interaction-driven layer antiferromagnetic state in Bernal stacked bilayer graphene

In the following, we discuss why the observed spontaneous insulating ground state is the layer antiferromagnetic state in bilayer graphene: (i) Theoretically, all possible electron-electron interaction-driven insulating ground states relevant to BLG and its ABC variants at charge neutrality point have been classified[3]. (ii) As seen from Table I of ref.[3], the only two classes of states that do not have topologically protected edge states ($\sigma^{(\mathrm{CH})} = \sigma^{(\mathrm{SH})} = 0$) are the layer antiferromagnetic and the quantum valley Hall states (*i.e.* the fully layer polarized states). Thus, in our two-terminal charge transport measurements (the two-terminal conductance is given by $\sigma_{\mathrm{two-terminal}} = \sqrt{{\sigma_{\mathrm{xx}}}^2 + {\sigma_{\mathrm{xy}}}^2}$, with $\sigma_{\mathrm{xx}} \approx 0$ and σ_{xy} is given by $\sigma^{(\mathrm{CH})}$ or $\sigma^{(\mathrm{SH})}/2$ in Table I in ref.[3]) these two classes of states should exhibit insulating behavior with $\sigma_{\mathrm{CNP}} < 1\ e^2\ h^{-1}$ below their critical temperatures, while others should exhibit $\sigma_{\mathrm{CNP}} \geq 2\ e^2\ h^{-1}$. (iii) Since we observe an insulating state at $E = 0$ and two separate phase transitions at $E > 0$ and $E < 0$ to distinct insulating states, we can uniquely identify the insulating state at $E = 0$ as a layer antiferromagnetic state and the insulating states at $E \neq 0$ as two fully layer polarized states.

Supplementary Figures S1 – S8:

Eleven bilayer graphene devices scanned for stacking domain walls using scattering-type scanning near-field optical microscopy

Prior to fabricating the dually gated freestanding devices, the preselected bilayer graphene flakes were scanned for stacking domain walls using scattering-type scanning near-field optical microscopy. Fig. S1a – h shows eight different flakes. For each bilayer graphene flake, an atomic force microscopy (AFM) image as well as a s-SNOM amplitude and/or phase image is shown. The subsequently designed contacts are marked in blue, and the devices (one to three per flake) are labelled with letters or numerals. Any domain walls visible in the s-SNOM images are additionally indicated with yellow dashed lines in the corresponding topography images for greater visibility. A and B are the devices shown in the main manuscript. Two devices (devices 7 and 8) exhibit domain walls within their channel. For device 7, the two domain walls close to each other in the center of the channel presumably merged and annihilated, as we could not see any indications of topological valley transport along the domain walls in case an electric field is applied[4,5]. Apparently, when multiple structural domain walls are very close to each other, annihilation is possible.

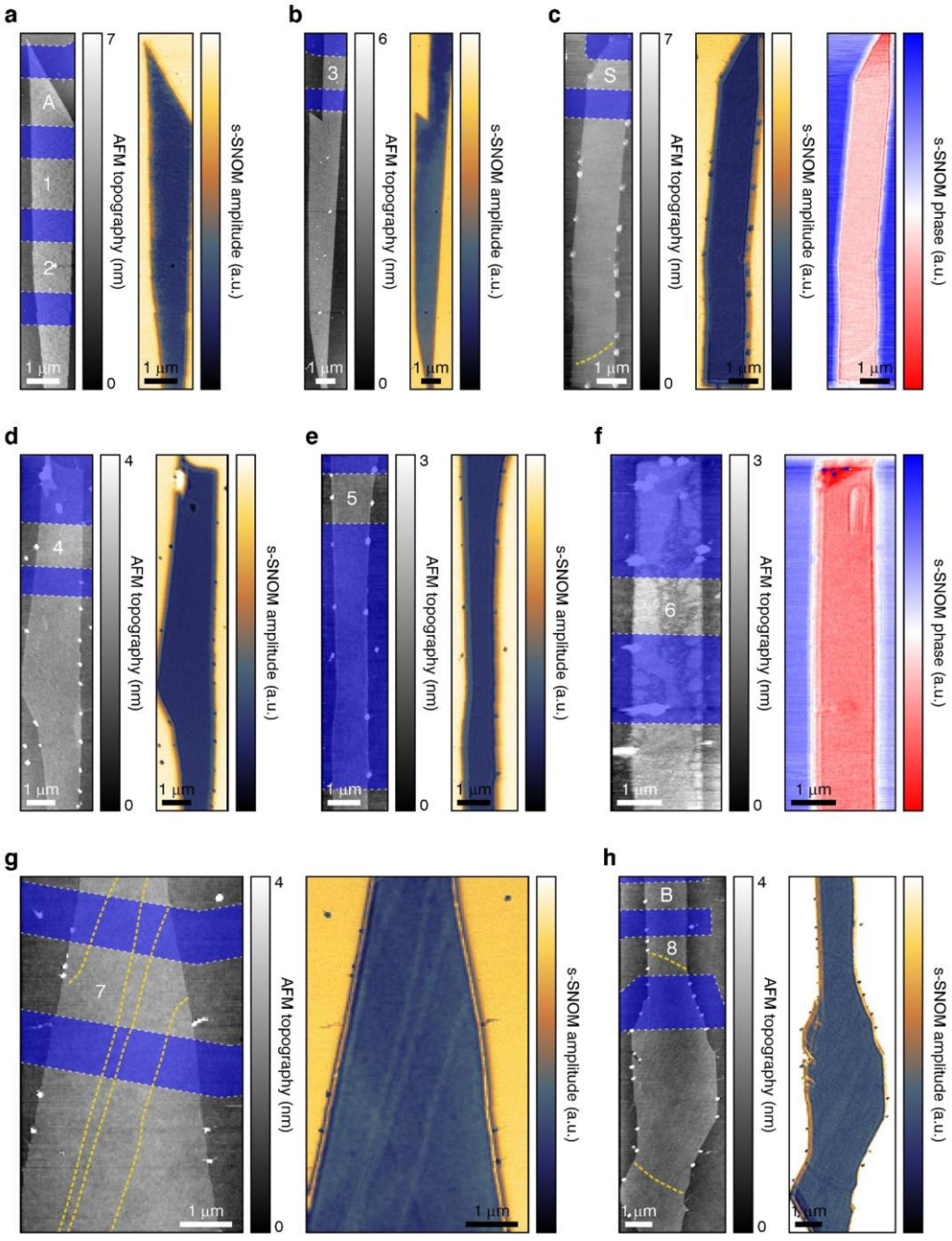

Supplementary Fig. S1 | AFM and s-SNOM images of the examined bilayer graphene flakes. a – h, AFM, and s-SNOM amplitude/phase images for all measured devices prior to processing. Subsequently designed contacts are highlighted in blue, and any present stacking domain walls are indicated with dashed yellow lines.

Current annealing and the appearance of fractional quantum Hall states

Prior to any measurements, the devices were cleaned using a current annealing procedure[6]. Multiple cycles of current annealing at 1.6 K were performed. During the ramp up of the d.c. voltage $V_{d.c.}$, the d.c. current $I_{d.c.}$ and resistance $R_{d.c.}$ were tracked (Fig. S2a). In case the device is clean, the current shows a saturation. More $V_{d.c.}$ is applied until the resistance has well increased.

After the current annealing process, we have looked for signs of fractional quantum Hall states, since the observation of such fragile phases[7,8] would indicate a high quality of our devices. To this end, in Fig. S2b, the conductance as a function of density and magnetic fields of $B = 8 - 14$ T is shown for one exemplary device. In the presented density range, besides the $\nu = \pm 1$ and ± 2 states, we can observe additional plateaus emerging for $B \geq 10$ T indicating the appearance of fractional quantum Hall states (illustrated by the black arrows in Fig. S2b). The most obvious appearing fractional states appear to be the 2/3 and 5/3 states, as reported in literature[7]. However, more detailed measurements would be needed to unequivocally identify the nature of these states. Nonetheless, these observations emphasize the high quality of our devices.

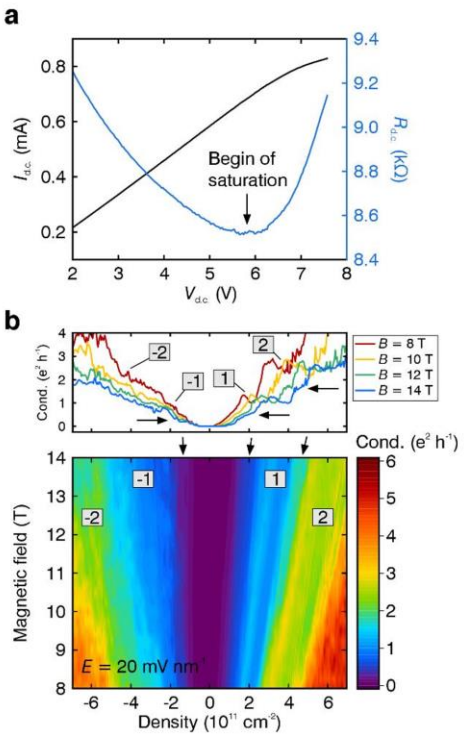

Supplementary Fig. S2 | Current annealing and fractional quantum Hall states. **a,** $I_{d.c.}$ and $R_{d.c.}$ as a function of $V_{d.c.}$ demonstrating the saturation of the current during annealing. **b,** Bottom: Fan diagram at $E = 20$ mV nm^{-1} for high magnetic fields. Top: line traces of the conductance as a function of charge carrier density for various B. The black arrows indicate emerging fractional quantum Hall states.

The correlation between σ_{CNP}, ΔE^{SP} and the critical temperature of the spontaneously insulating ground state

As discussed in the main text, we use σ_{CNP} and ΔE^{SP} as measures for the strength of the ground state. To support this, we show the resistance as a function of V_b measured for a series of V_t for four different devices at $T = 1.6$ K and $T < 10$ mK, as shown in Fig. S3. From top to bottom in Fig. S3, both the resistance at the CNP R_{CNP} and ΔE^{SP} consistently decrease. From the temperature dependent data in Fig. 2c in the main text, we know that device A (Fig. S3a) has the critical temperature T_c in the range of 5 K – 10 K. For the device shown in Fig. S3b, we can assign $T_c > 1.6$ K. For the device shown in Fig. S3c, 10 mK $< T_c < 1.6$ K, since it exhibits no spontaneously insulating state at the CNP at $T = 1.6$ K but features one at $T < 10$ mK. Lastly, for device B (Fig. S3d), we do not observe any insulating state even at $T < 10$ mK (see also the data in Fig. 2a in the main text), and its T_c should be below 10 mK. Therefore, we can conclude that T_c decreases from top to bottom in Fig. S3, which correlates with the decrease of R_{CNP} and ΔE^{SP}.

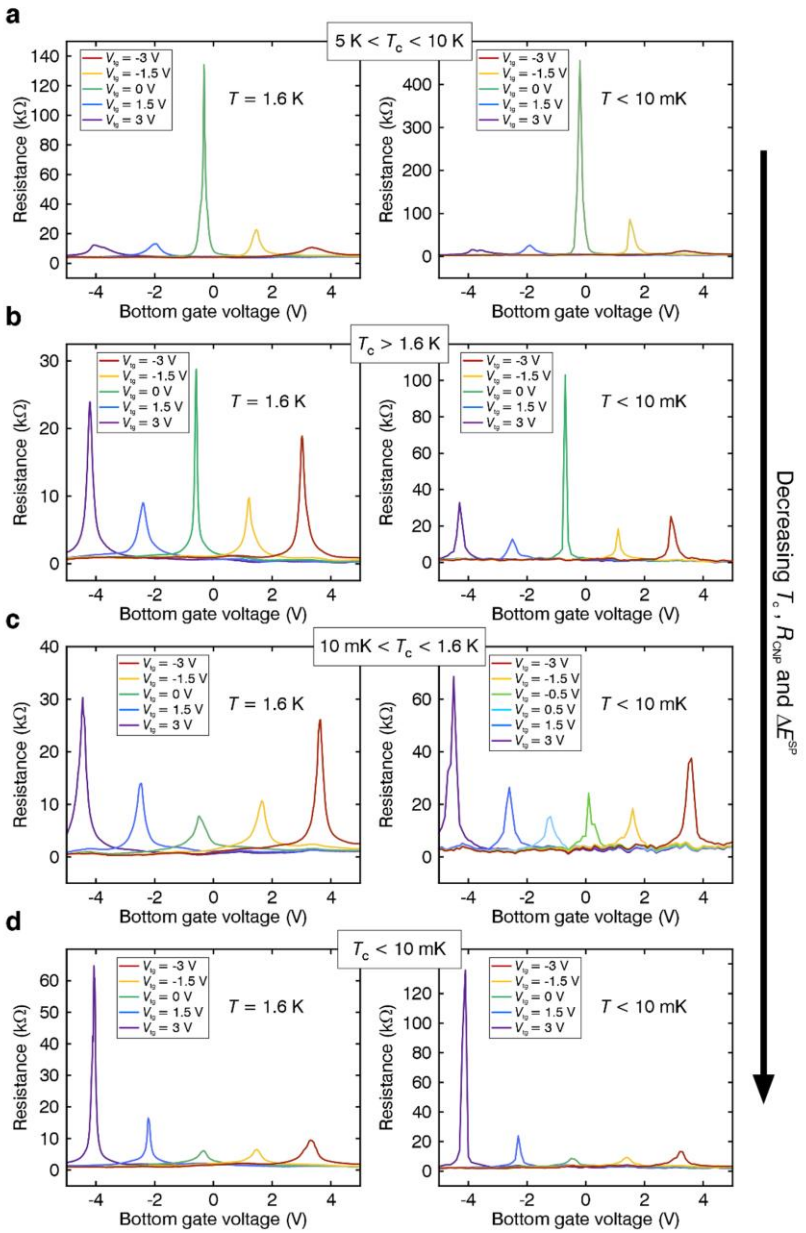

Supplementary Fig. S3 | Correlation between σ_{CNP}, ΔE^{SP} and T_c of the spontaneously insulating ground state. a – d, Resistance as a function of V_b measured for a series of V_t at T = 1.6 K (left) and T < 10 mK (right) for four different devices. Note that device A and B from the main text are shown in (a) and (d),

respectively. For each device, the corresponding T_c is indicated, and its respective contact resistance has been taken into account.

Behavior of the LAF phase with increasing magnetic field

After evaluating the data of eleven devices, it is reasonable to assume that the true ground state is the layer antiferromagnetic (LAF) phase at $n = E = B = 0$. However, an open question is still how the phase evolves into the canted antiferromagnetic phase for $n = E = 0$ but finite B. In literature, only once a non-monotonic behavior of the conductance for increasing magnetic field has been observed[9]. To investigate this further, we have recorded conductance maps as a function of electric field and around zero magnetic field for $n = 0$, see Fig. S4a,b. Most devices show (in case they exhibit a spontaneous gap opening at low temperatures) a monotonic decrease of the conductance for increasing magnetic field, see the data shown in Fig. S4b and the corresponding line trace in Fig. S4c for device S. Nonetheless, devices with a dominant LAF state (device A) show an indication of a non-monotonic behavior of the conductance for increasing B, see Fig. S4a,c. The conductance behaves asymmetrically around zero magnetic field at with maxima at +20 mT and -130 mT, which is consistent over multiple measurements. In the case of actually sweeping the magnetic field for constant E (see Fig. S4d,e) the two maxima of conductance appear symmetrically at $B \approx \pm$ 140 mT for low electric fields and rapidly shift towards zero magnetic field for E = -9.5 mV nm^{-1}. Possibly, this non-monotonic behavior comes from the differences in the edge transport between the LAF and CAF phase[10], however a phase transition, i.e. a closing of the bulk energy gap, is not expected.

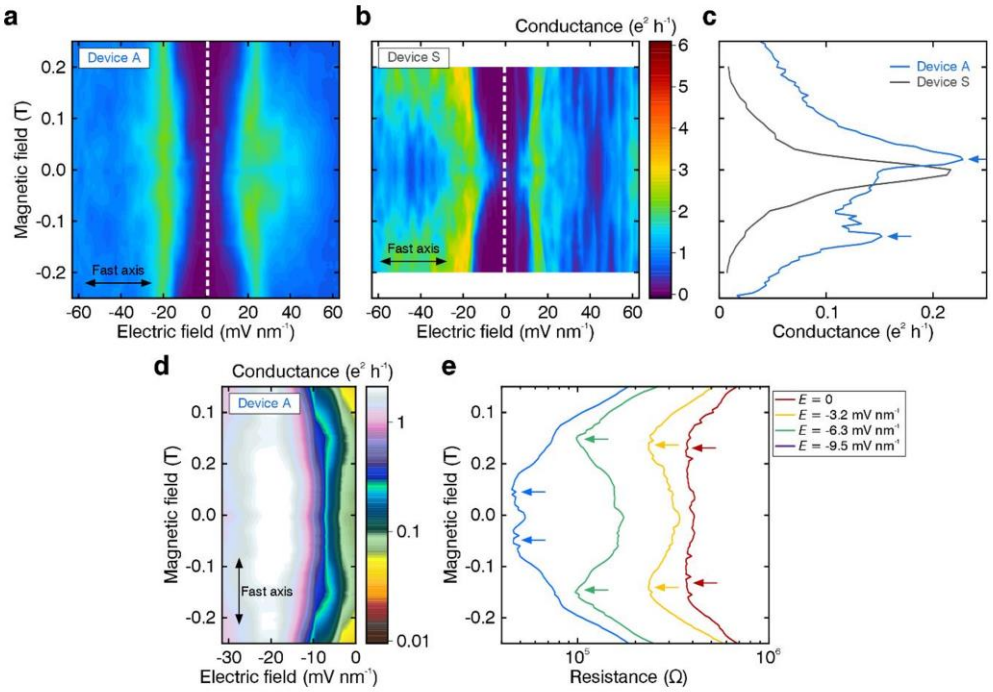

Supplementary Fig. S4 | Evolution of the LAF to the CAF phase. a,b, Maps of the conductance in units of e^2 h^{-1} as a function of applied electric and small magnetic fields at zero charge carrier density in devices A and S. **c,** Line traces of the conductance along the magnetic field direction at $E = 0$ shown for device A (blue) and S (black). **d,** Conductance as a function of E and B at zero charge carrier density for device A. Here, the magnetic field was swept at various electric fields. **e,** Line traces of the resistance along the magnetic field direction at various constant electric fields shown for device A.

Stability of stacking domain walls during processing

In multilayer graphene with a layer number of $N > 2$, mainly two stacking orders (Bernal and rhombohedral stacking) occur. Domain walls separating regions with different stacking can easily move due to the fabrication of contacts, since Bernal stacking is favoured during the process[11]. On the contrary, bilayer graphene naturally exhibits mainly Bernal stacking order. Stacking domain walls occurring in bilayer graphene flakes separate regions with AB and BA stacking[12], which are energetically equal[13]. Consequently, they are more unlikely to move. In fact, we have tested several devices without top gate, and could not observe any movement of the domain wall during fabricating the source-drain contacts by electron-beam lithography. Exemplarily, Fig. S5 shows AFM (a) and s-SNOM amplitude images (b) of a bilayer graphene flake prior (left and top panels) and after fabricating contacts (bottom panels). We can see that the domain wall remains at the exact same position. However, in the extreme case of multiple structural domain walls very close to each other, their annihilation seems still possible (see Fig. S1). We cannot conduct this test after any further step in the fabrication of the device since applying the top gate prevents the procedure.

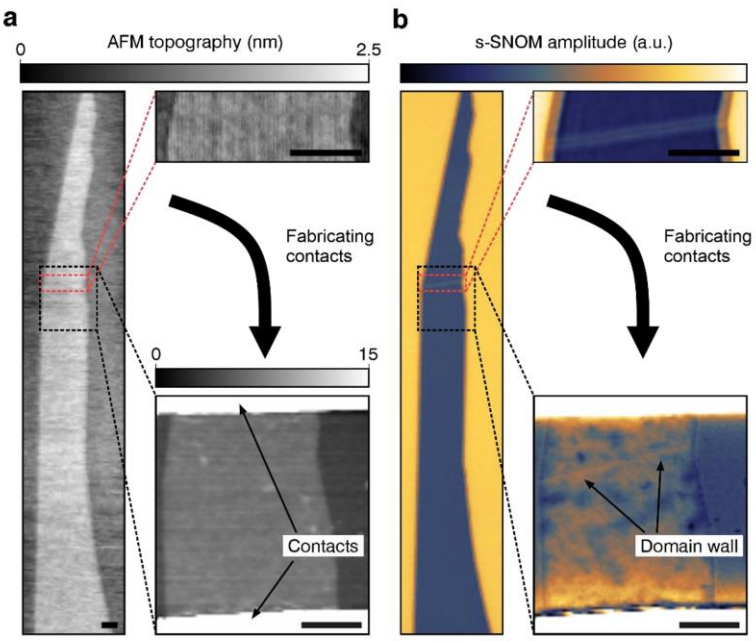

Supplementary Fig. S5 | Stability of stacking domain walls during processing. **a,b,** Atomic force microscopy image (a) and s-SNOM amplitude image (b) of a bilayer graphene flake. Left panels: bilayer graphene flake prior to processing. Top panels: high-resolution zoom-in scans showing the region of the domain wall prior to processing. Bottom panels: region of the domain wall after fabricating the source-drain contacts. The scale bars are 0.5 μm in all images.

Stability of stacking domain walls during current annealing

To investigate the stability and any possible new formation[14] of stacking domain walls during current annealing, we have fabricated multiple bilayer graphene devices on a SiO_2 substrate. The selected flakes each exhibited multiple stacking domain walls prior to contacting, as the s-SNOM images reveal (see Fig. S6a,c,e). Subsequently, the flakes were contacted and current annealing was performed at low temperatures ($T \approx 5$ K). Very high current densities J_{max} were applied between neighboring or next-neighboring contact pairs (even higher than in the suspended devices due to the presence of substrate), as indicated in Fig. S6. After the annealing procedure, the flakes were again scanned with near-field microscopy (Fig. S6b,d,f). Only one stacking domain wall (in the top panel of Fig. S6b) could not be observed anymore. However, it but might still be present but untraceable owing to residual dirt visible in the corresponding topography image. Besides this exception, all other stacking domain walls were still visible after current annealing and remained at the exact same spot. Moreover, even a complex s-shaped domain wall as in the top panels of Fig. S6f remained intact. Hence, stacking domain walls are very stable even when applying very high currents and the formation of new stacking domain walls seems very unlikely.

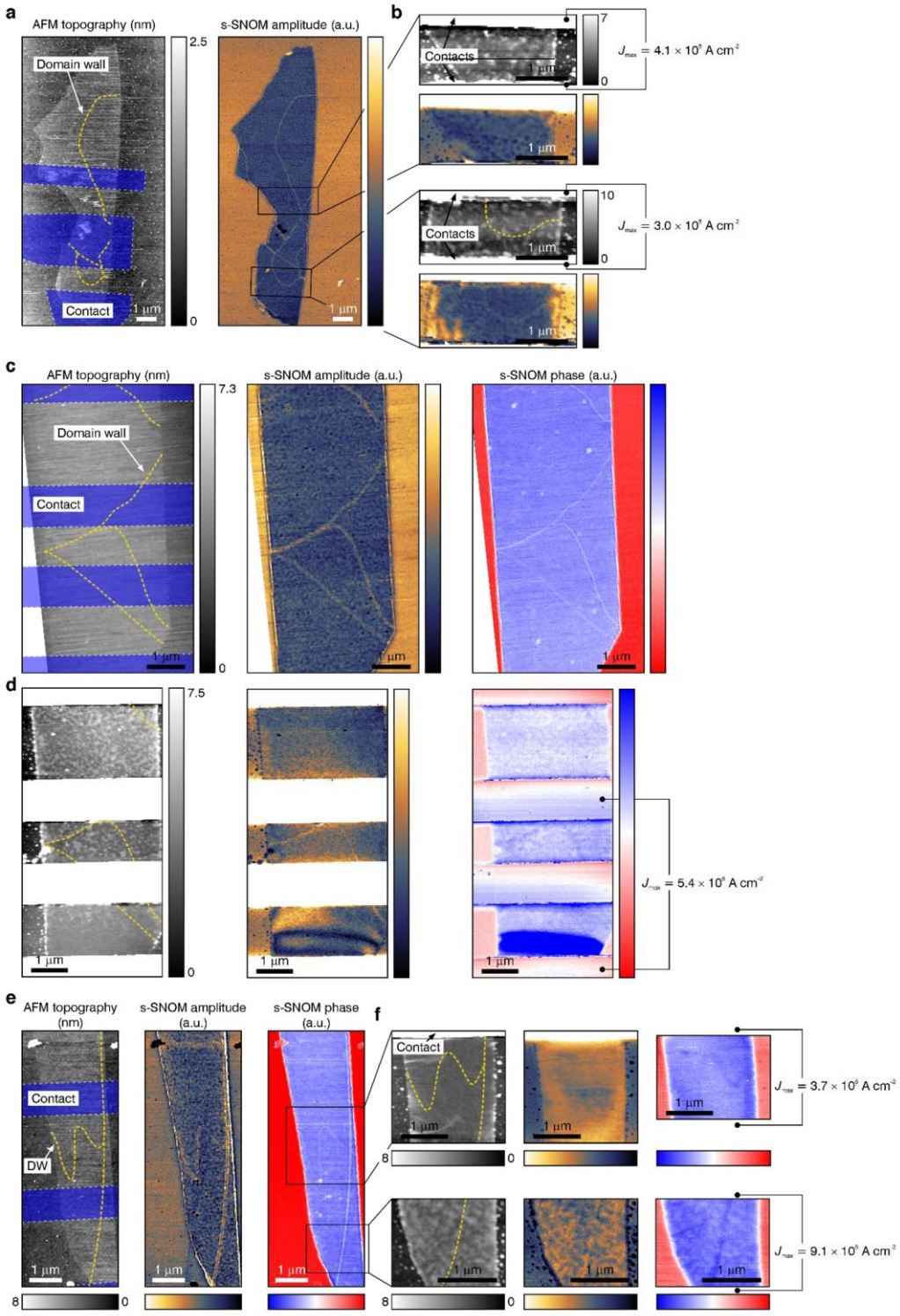
a
AFM topography (nm)
s-SNOM amplitude (a.u.)
Domain wall
Contact
2.5
0
1 μm
b
Contacts
7
0
$J_{max} = 4.1 \times 10^5$ A cm^{-2}
10
$J_{max} = 3.0 \times 10^5$ A cm^{-2}
c
AFM topography (nm)
s-SNOM amplitude (a.u.)
s-SNOM phase (a.u.)
7.3
d
7.5
$J_{max} = 5.4 \times 10^5$ A cm^{-2}
e
AFM topography (nm)
s-SNOM amplitude (a.u.)
s-SNOM phase (a.u.)
DW
8
f
$J_{max} = 3.7 \times 10^5$ A cm^{-2}
$J_{max} = 9.1 \times 10^5$ A cm^{-2}

Supplementary Fig. S6 | Tracking stacking domain walls prior and after current annealing. a,c,e, Topography as well as s-SNOM amplitude/phase images of three bilayer graphene flakes on SiO_2. Each of the flakes exhibits multiple stacking domain walls, visible in the s-SNOM images. In the topography images, subsequently designed contacts are highlighted in blue and stacking domain walls present are indicated with dashed yellow lines. **b,d,f,** Topography and s-SNOM images after current annealing. For the flake in (d), the complete flake is shown, whereas (b) and (f) show only zoomed-in images of the channel in between two contacts. The maximum current density applied during the cleaning procedure J_{max} in between two contacts is indicated. Again, the stacking domain walls are indicated by dashed yellow lines in the topography images for greater visibility.

Stability of the quantum transport signatures during multiple current annealing cycles

After multiple cleaning cycles, the charge neutrality point appears in the accessible V_b range, exemplarily shown for a device in Fig. S7a. Measuring conductance maps at $B = 0$ as a function of V_t and V_b (Fig. S7b) reveals that the device shows an intermediate strong spontaneous phase. Additional measurements at $B = 3$ T in dependence of n and E (Fig. S7c) as well as for $n = 0$ as a function of B and E (Fig. S7d) show medium-sized transition regions between states of different layer polarization confirming that the device has some disorder present. However, conductance fluctuations/spikes show that the device is not perfectly clean and it displays a high contact resistance (> 20 kΩ). Further annealing the device (about 3 % more d.c. current) drastically improves both aspects (Fig. S7e – h). Subsequently, only very few fluctuations are visible, and the contact resistance drops below 10 kΩ. Nonetheless, the overall transport signature has not changed. Therefore, the amount of disorder responsible for the strength of the LAF ground state and the width of phase transitions between different broken-symmetry states remains the same and is not changed by the additional current annealing.

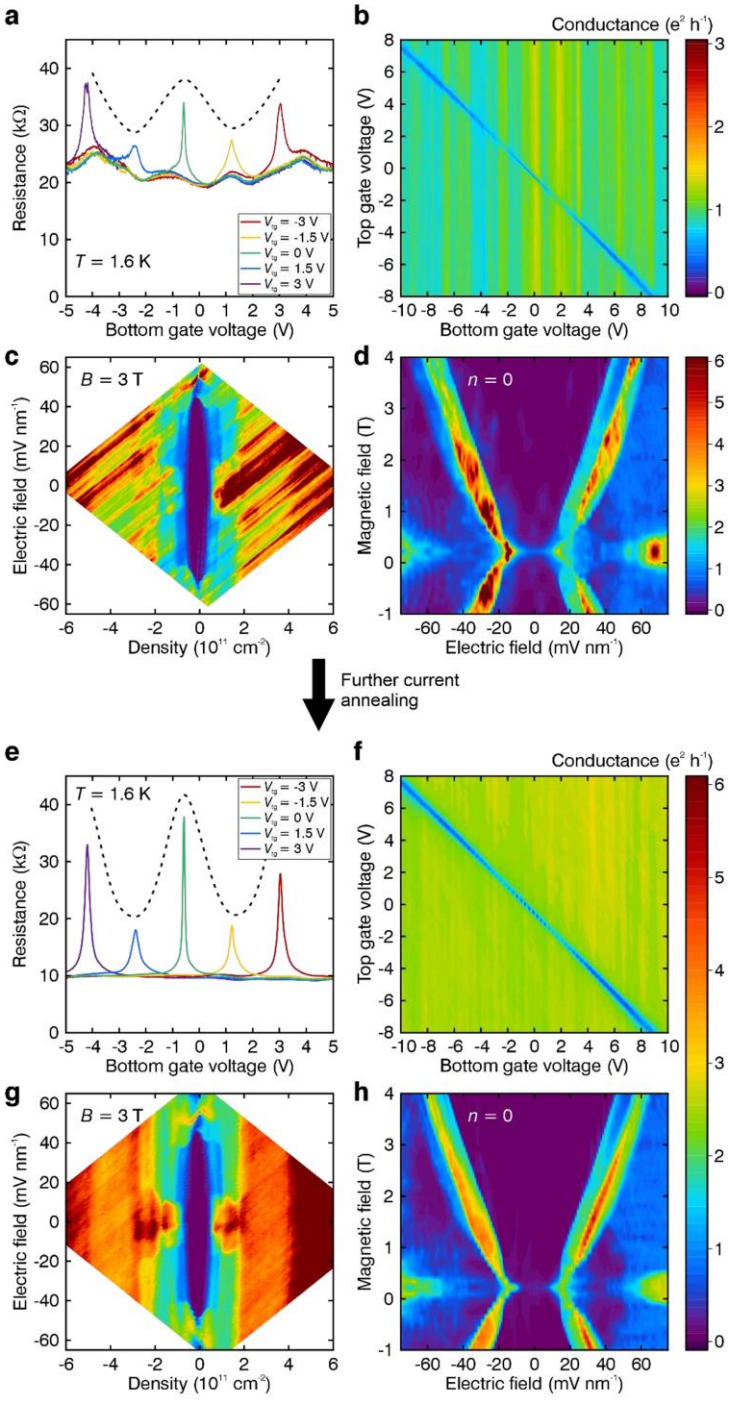

Supplementary Fig. S7 | The impact of current annealing on the quantum transport of a bilayer graphene device. a, Resistance as a function of V_b measured for certain V_t at T = 1.6 K. The dashed line is a guide to the eye. **b,** Map of the

conductance in units of $e^2 h^{-1}$ as a function of V_t and V_b for $T < 10$ mK. **c,** Conductance as a function of E and n measured at $B = 3$ T. **d,** Map of the conductance as a function of E and B at zero charge carrier density. The data shown in a – d was recorded after several current annealing steps but with some residual dirt present. **e – h,** Same data as in a – d but measured after additional current annealing steps, when the device was fully cleaned and the current showed a clear saturation.

Behavior of the quantum Hall states at $B = 1.5$ T

Besides the data shown for $B = 3$ T in the main manuscript, we have also conducted measurements at $B = 1.5$ T. Fig. S8a – b show maps of the conductance as a function of E and n at $B = 1.5$ T for device A and B. Similar to the observations in the main manuscript (see Fig. 4), layer unpolarized states (i.e., $\nu = \pm 4$) behave the same in both devices, whereas the (partially) layer polarized $\nu = \pm 1, \pm 2$ states differ in their electric field dependence, especially around zero electric field. Line traces of the conductance in electric field shown for constant filling factors $\nu = -2, -4$ illustrate the behaviors of the two devices, see Fig. S8c. In addition, at this low magnetic field, the distinct $\nu = 0$ phases and the corresponding phase transitions can be observed (see Fig. S8c). Their extend in electric field is distinct for the two devices, as discussed already in Fig. 4 in the main manuscript.

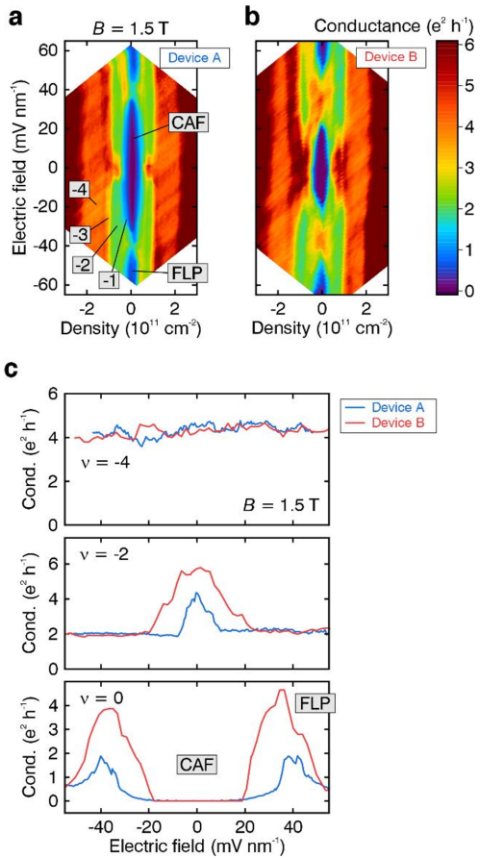

Supplementary Fig. S8 | The impact of electric field disorder on the quantum transport in bilayer graphene at *B* = 1.5 T. a – b, Maps of the conductance in units of e^2 h^{-1} as a function of applied electric field *E* and density *n* at a magnetic field of *B* = 1.5 T for device A (a) and B (b). **c,** Line traces of the conductance taken at constant filling factors ν = 0, -2 and -4 as a function of *E* for device A (blue) and B (red).

References

1. Keilmann, F.; Hillenbrand, R. Near-Field Nanoscopy by Elastic Light Scattering from a Tip. In *Nano-optics and near-field optical microscopy*; Zayats, A. V., Richards, D., Eds.; Artech House nanoscale science and engineering; Artech House: Boston, London; pp 235–265.
2. Geisenhof, F. R.; Winterer, F.; Seiler, A. M.; Lenz, J.; Xu, T.; Zhang, F.; Weitz, R. T. Quantum Anomalous Hall Octet Driven by Orbital Magnetism in Bilayer Graphene. *Nature* **2021**, *598*, 53–58.
3. Zhang, F.; Jung, J.; Fiete, G. A.; Niu, Q.; MacDonald, A. H. Spontaneous Quantum Hall States in Chirally Stacked Few-Layer Graphene Systems. *Phys. Rev. Lett.* **2011**, *106*, 156801.
4. Geisenhof, F. R.; Winterer, F.; Seiler, A. M.; Lenz, J.; Martin, I.; Weitz, R. T. Interplay between topological valley and quantum Hall edge transport. *Nat. Commun.* **2022**, *13*, 4187.
5. Ju, L.; Shi, Z.; Nair, N.; Lv, Y.; Jin, C.; Velasco, J.; Ojeda-Aristizabal, C.; Bechtel, H. A.; Martin, M. C.; Zettl, A.; Analytis, J.; Wang, F. Topological Valley Transport at Bilayer Graphene Domain Walls. *Nature* **2015**, *520*, 650–655.
6. Moser, J.; Barreiro, A.; Bachtold, A. Current-induced cleaning of graphene. *Appl. Phys. Lett.* **2007**, *91*, 163513.
7. Maher, P.; Wang, L.; Gao, Y.; Forsythe, C.; Taniguchi, T.; Watanabe, K.; Abanin, D.; Papić, Z.; Cadden-Zimansky, P.; Hone, J.; Kim, P.; Dean, C. R. Bilayer Graphene. Tunable Fractional Quantum Hall Phases in Bilayer Graphene. *Science* **2014**, *345*, 61–64.
8. Ki, D.-K.; Fal'ko, V. I.; Abanin, D. A.; Morpurgo, A. F. Observation of Even Denominator Fractional Quantum Hall Effect in Suspended Bilayer Graphene. *Nano Lett.* **2014**, *14*, 2135–2139.
9. Weitz, R. T.; Allen, M. T.; Feldman, B. E.; Martin, J.; Yacoby, A. Broken-Symmetry States in Doubly Gated Suspended Bilayer Graphene. *Science* **2010**, *330*, 812–816.
10. Kharitonov, M. Edge excitations of the canted antiferromagnetic phase of the ν=0 quantum Hall state in graphene: A simplified analysis. *Phys. Rev. B* **2012**, *86*, 075450.
11. Geisenhof, F. R.; Winterer, F.; Wakolbinger, S.; Gokus, T. D.; Durmaz, Y. C.; Priesack, D.; Lenz, J.; Keilmann, F.; Watanabe, K.; Taniguchi, T.; Guerrero-Avilés, R.; Pelc, M.; Ayuela, A.; Weitz, R. T. Anisotropic Strain-Induced Soliton Movement Changes Stacking Order and Band Structure of Graphene Multilayers: Implications for Charge Transport. *ACS Appl. Nano Mater.* **2019**, *2*, 6067–6075.
12. Jiang, L.; Shi, Z.; Zeng, B.; Wang, S.; Kang, J.-H.; Joshi, T.; Jin, C.; Ju, L.; Kim, J.; Lyu, T.; Shen, Y.-R.; Crommie, M.; Gao, H.-J.; Wang, F. Soliton-Dependent Plasmon Reflection at Bilayer Graphene Domain Walls. *Nat. Mater.* **2016**, *15*, 840–844.
13. Alden, J. S.; Tsen, A. W.; Huang, P. Y.; Hovden, R.; Brown, L.; Park, J.; Muller, D. A.; McEuen, P. L. Strain Solitons and Topological Defects in Bilayer Graphene. *Proc. Natl. Acad. Sci. U.S.A.* **2013**, *110*, 11256–11260.
14. San-Jose, P.; Gorbachev, R. V.; Geim, A. K.; Novoselov, K. S.; Guinea, F. Stacking Boundaries and Transport in Bilayer Graphene. *Nano Lett.* **2014**, *14*, 2052–2057.

References

1. Wallace, P. R. The Band Theory of Graphite. *Phys. Rev.* **71**, 622–634 (1947).
2. Geim, A. K. & Novoselov, K. S. The Rise of Graphene. *Nat. Mater.* **6**, 183–191 (2007).
3. Novoselov, K. S. Electric Field Effect in Atomically Thin Carbon Films. *Science* **306**, 666–669 (2004).
4. Castro Neto, A. H., Guinea, F., Peres, N. M. R., Novoselov, K. S. & Geim, A. K. The Electronic Properties of Graphene. *Rev. Mod. Phys.* **81**, 109–162 (2009).
5. Lee, C., Wei, X., Kysar, J. W. & Hone, J. Measurement of the Elastic Properties and Intrinsic Strength of Monolayer Graphene. *Science* **321**, 385–388 (2008).
6. Nair, R. R. *et al.* Fine Structure Constant Defines Visual Transparency of Graphene. *Science* **320**, 1308 (2008).
7. Geim, A. K. & Grigorieva, I. V. Van der Waals Heterostructures. *Nature* **499**, 419–425 (2013).
8. Liu, Y. *et al.* Van der Waals Heterostructures and Devices. *Nat. Rev. Mater.* **1**, 16042 (2016).
9. Dean, C. R. *et al.* Boron Nitride Substrates for High-Quality Graphene Electronics. *Nat. Nanotech.* **5**, 722–726 (2010).
10. Watanabe, K., Taniguchi, T. & Kanda, H. Direct-Bandgap Properties and Evidence for Ultraviolet Lasing of Hexagonal Boron Nitride Single Crystal. *Nat. Mater.* **3**, 404–409 (2004).
11. Mak, K. F., Lee, C., Hone, J., Shan, J. & Heinz, T. F. Atomically Thin MoS_2: a New Direct-Gap Semiconductor. *Phys. Rev. Lett.* **105**, 136805 (2010).
12. Radisavljevic, B., Radenovic, A., Brivio, J., Giacometti, V. & Kis, A. Single-Layer MoS_2 Transistors. *Nat. Nanotechnol.* **6**, 147–150 (2011).
13. Fatemi, V. *et al.* Electrically Tunable Low-Density Superconductivity in a Monolayer Topological Insulator. *Science* **362**, 926–929 (2018).
14. Wu, S. *et al.* Observation of the Quantum Spin Hall Effect up to 100 Kelvin in a Monolayer Crystal. *Science* **359**, 76–79 (2018).
15. Dean, C. *et al.* Graphene Based Heterostructures. *Solid State Commun.* **152**, 1275–1282 (2012).

16. Haigh, S. J. *et al.* Cross-Sectional Imaging of Individual Layers and Buried Interfaces of Graphene-Based Heterostructures and Superlattices. *Nat. Mater.* **11**, 764–767 (2012).

17. Ponomarenko, L. A. *et al.* Tunable Metal–Insulator Transition in Double-Layer Graphene Heterostructures. *Nat. Phys.* **7**, 958–961 (2011).

18. Pizzocchero, F. *et al.* The Hot Pick-up Technique for Batch Assembly of van der Waals Heterostructures. *Nat. Commun.* **7**, 11894 (2016).

19. Bolotin, K. I. *et al.* Ultrahigh Electron Mobility in Suspended Graphene. *Solid State Commun.* **146**, 351–355 (2008).

20. Mayorov, A. S. *et al.* Micrometer-Scale Ballistic Transport in Encapsulated Graphene at Room Temperature. *Nano Lett.* **11**, 2396–2399 (2011).

21. Balandin, A. A. *et al.* Superior Thermal Conductivity of Single-Layer Graphene. *Nano Lett.* **8**, 902–907 (2008).

22. Moser, J., Barreiro, A. & Bachtold, A. Current-Induced Cleaning of Graphene. *Appl. Phys. Lett.* **91**, 163513 (2007).

23. McCann, E. & Koshino, M. The Electronic Properties of Bilayer Graphene. *Rep. Prog. Phys.* **76**, 056503 (2013).

24. Novoselov, K. S. *et al.* Unconventional Quantum Hall Effect and Berry's Phase of 2π in Bilayer Graphene. *Nat. Phys.* **2**, 177–180 (2006).

25. Ohta, T., Bostwick, A., Seyller, T., Horn, K. & Rotenberg, E. Controlling the Electronic Structure of Bilayer Graphene. *Science* **313**, 951–954 (2006).

26. Zhang, Y. *et al.* Direct Observation of a Widely Tunable Bandgap in Bilayer Graphene. *Nature* **459**, 820–823 (2009).

27. Cao, Y. *et al.* Correlated Insulator Behaviour at Half-Filling in Magic-Angle Graphene Superlattices. *Nature* **556**, 80–84 (2018).

28. Cao, Y. *et al.* Unconventional Superconductivity in Magic-Angle Graphene Superlattices. *Nature* **556**, 43–50 (2018).

29. Serlin, M. *et al.* Intrinsic Quantized Anomalous Hall Effect in a Moiré Heterostructure. *Science* **367**, 900–903 (2020).

30. Sharpe, A. L. *et al.* Emergent Ferromagnetism near Three-Quarters Filling in Twisted Bilayer Graphene. *Science* **365**, 605–608 (2019).

31. Nandkishore, R. & Levitov, L. Quantum Anomalous Hall State in Bilayer Graphene. *Phys. Rev. B* **82**, 115124 (2010).

32. Zhang, F., Jung, J., Fiete, G. A., Niu, Q. & MacDonald, A. H. Spontaneous Quantum Hall States in Chirally Stacked Few-Layer Graphene Systems. *Phys. Rev. Lett.* **106**, 156801 (2011).

33. Zhang, F. Spontaneous Chiral Symmetry Breaking in Bilayer Graphene. *Synth. Met.* **210**, 9–18 (2015).

34. Barlas, Y., Côté, R., Nomura, K. & MacDonald, A. H. Intra-Landau-Level Cyclotron Resonance in Bilayer Graphene. *Phys. Rev. Lett.* **101**, 097601 (2008).

35. Ki, D.-K. & Morpurgo, A. F. High-Quality Multiterminal Suspended Graphene Devices. *Nano Lett.* **13**, 5165–5170 (2013).

36. Bao, W. *et al.* Evidence for a Spontaneous Gapped State in Ultraclean Bilayer Graphene. *Proc. Natl. Acad. Sci. U.S.A.* **109**, 10802–10805 (2012).

37. Freitag, F., Trbovic, J., Weiss, M. & Schönenberger, C. Spontaneously Gapped Ground State in Suspended Bilayer Graphene. *Phys. Rev. Lett.* **108**, 076602 (2012).

38. Nam, Y., Ki, D.-K., Soler-Delgado, D. & Morpurgo, A. F. A Family of Finite-Temperature Electronic Phase Transitions in Graphene Multilayers. *Science* **362**, 324–328 (2018).

39. Velasco, J. *et al.* Transport Spectroscopy of Symmetry-Broken Insulating States in Bilayer Graphene. *Nat. Nanotechnol.* **7**, 156–160 (2012).

40. Veligura, A. *et al.* Transport Gap in Suspended Bilayer Graphene at Zero Magnetic Field. *Phys. Rev. B* **85**, 1–8 (2012).

41. Weitz, R. T., Allen, M. T., Feldman, B. E., Martin, J. & Yacoby, A. Broken-Symmetry States in Doubly Gated Suspended Bilayer Graphene. *Science* **330**, 812–816 (2010).

42. Kotov, V. N., Uchoa, B., Pereira, V. M., Guinea, F. & Castro Neto, A. H. Electron-Electron Interactions in Graphene: Current Status and Perspectives. Current Status and Perspectives. *Rev. Mod. Phys.* **84**, 1067–1125 (2012).

43. Freitag, F., Weiss, M., Maurand, R., Trbovic, J. & Schönenberger, C. Spin Symmetry of the Bilayer Graphene Ground State. *Phys. Rev. B* **87**, 161402 (2013).

44. Martin, J., Feldman, B. E., Weitz, R. T., Allen, M. T. & Yacoby, A. Local Compressibility Measurements of Correlated States in Suspended Bilayer Graphene. *Phys. Rev. Lett.* **105**, 256806 (2010).

45. Chang, C.-Z. *et al.* Experimental Observation of the Quantum Anomalous Hall Effect in a Magnetic Topological Insulator. *Science* **340**, 167–170 (2013).

46. Mayorov, A. S. *et al.* Interaction-Driven Spectrum Reconstruction in Bilayer Graphene. *Science* **333**, 860–863 (2011).

47. Zhang, J., Nandkishore, R. & Rossi, E. Disorder-Tuned Selection of Order in Bilayer Graphene. *Phys. Rev. B* **91**, 205425 (2015).

48. Alden, J. S. *et al.* Strain Solitons and Topological Defects in Bilayer Graphene. *Proc. Natl. Acad. Sci. U.S.A.* **110**, 11256–11260 (2013).

49. Butz, B. *et al.* Dislocations in Bilayer Graphene. *Nature* **505**, 533–537 (2014).

50. Ju, L. *et al.* Topological Valley Transport at Bilayer Graphene Domain Walls. *Nature* **520**, 650–655 (2015).

51. Li, J. *et al.* Gate-Controlled Topological Conducting Channels in Bilayer Graphene. *Nat. Nanotechnol.* **11**, 1060–1065 (2016).

52. Li, X., Zhang, F., Niu, Q. & MacDonald, A. H. Spontaneous Layer-Pseudospin Domain Walls in Bilayer Graphene. *Phys. Rev. Lett.* **113**, 116803 (2014).

53. Martin, I., Blanter, Y. M. & Morpurgo, A. F. Topological Confinement in Bilayer Graphene. *Phys. Rev. Lett.* **100**, 036804 (2008).

54. Dhochak, K., Shimshoni, E. & Berg, E. Spontaneous Layer Polarization and Conducting Domain Walls in the Quantum Hall Regime of Bilayer Graphene. *Phys. Rev. B* **91**, 165107 (2015).

55. Keilmann, F. & Hillenbrand, R. Near-Field Microscopy by Elastic Light Scattering from a Tip. *Phil. Trans. R. Soc. Lond. A* **362**, 787–805 (2004).

56. Jiang, B.-Y. *et al.* Plasmon Reflections by Topological Electronic Boundaries in Bilayer Graphene. *Nano Lett.* **17**, 7080–7085 (2017).

57. Jiang, L. *et al.* Soliton-Dependent Plasmon Reflection at Bilayer Graphene Domain Walls. *Nat. Mater.* **15**, 840–844 (2016).

58. Zhou, H. *et al.* Isospin Magnetism and Spin-Polarized Superconductivity in Bernal Bilayer Graphene. *Science* **375**, 774–778 (2022).

59. Seiler, A. M. *et al.* Quantum Cascade of Correlated Phases in Trigonally Warped Bilayer Graphene. *Nature* **608**, 298–302 (2022).

60. de la Barrera, S. C. d. *et al.* Cascade of Isospin Phase Transitions in Bernal-Stacked Bilayer Graphene at Zero Magnetic Field. *Nat. Phys.* **18**, 771–775 (2022).

61. Dean, C. R. *et al.* Boron Nitride Substrates for High-Quality Graphene Electronics. *Nat. Nanotechnol.* **5**, 722–726 (2010).

62. Maher, P. *et al.* Evidence for a Spin Phase Transition at Charge Neutrality in Bilayer Graphene. *Nat. Phys.* **9**, 154–158 (2013).

63. Katsnelson, M. I. *Graphene. Carbon in Two Dimensions* (Camebridge University Press, 2012).

64. Katsnelson, M. I., Novoselov, K. S. & Geim, A. K. Chiral Tunnelling and the Klein Paradox in Graphene. *Nat. Phys.* **2**, 620–625 (2006).

65. Sarma, S. D., Adam, S., Hwang, E. H. & Rossi, E. Electronic Transport in Two Dimensional Graphene. *Rev. Mod. Phys.* **83**, 407–470 (2010).

66. Hatsugai, Y., Morimoto, T., Kawarabayashi, T., Hamamoto, Y. & Aoki, H. Chiral Symmetry and its Manifestation in Optical Responses in Graphene: Interaction and Multilayers. *New J. Phys.* **15**, 35023 (2013).

67. Di Xiao, Chang, M.-C. & Niu, Q. Berry Phase Effects on Electronic Properties. *Rev. Mod. Phys.* **82**, 1959–2007 (2010).

68. McCann, E. & Fal'ko, V. I. Landau-Level Degeneracy and Quantum Hall Effect in a Graphite Bilayer. *Phys. Rev. Lett.* **96**, 086805 (2006).

69. Klitzing, K. von. The Quantized Hall Effect. *Rev. Mod. Phys.* **58**, 519–531 (1986).

70. Klitzing, K. von *et al.* 40 Years of the Quantum Hall Effect. *Nat. Rev. Phys.* **2**, 397–401 (2020).

71. Hunklinger, S. *Festkörperphysik* (Oldenbourg, München, 2007).

72. Ibach, H. & Lüth, H. *Solid-State Physics. An Introduction to Principles of Materials Science.* 4th ed. (Springer, Dordrecht, 2009).

73. Suddards, M. E., Baumgartner, A., Henini, M. & Mellor, C. J. Scanning Capacitance Imaging of Compressible and Incompressible Quantum Hall Effect Edge Strips. *New J. Phys.* **14**, 083015 (2012).

74. Abanin, D. A. & Levitov, L. S. Conformal Invariance and Shape-Dependent Conductance of Graphene Samples. *Phys. Rev. B* **78**, 035416 (2008).

75. Lee, K. *et al.* Bilayer Graphene. Chemical Potential and Quantum Hall Ferromagnetism in Bilayer Graphene. *Science* **345**, 58–61 (2014).

76. Li, J., Tupikov, Y., Watanabe, K., Taniguchi, T. & Zhu, J. Effective Landau Level Diagram of Bilayer Graphene. *Phys. Rev. Lett.* **120**, 047701 (2018).

77. Zhao, Y., Cadden-Zimansky, P., Jiang, Z. & Kim, P. Symmetry Breaking in the Zero-Energy Landau Level in Bilayer Graphene. *Phys. Rev. Lett.* **104**, 066801 (2010).

78. Yin, L.-J., Shi, L.-J., Yang, L.-Z., Tong, L.-H. & He, L. Spectroscopic Characterization of Landau-Level Splitting and the Intermediate ν=0 Phase in Bilayer Graphene. *Phys. Rev. B* **101**, 165418 (2020).

79. Bao, W. *et al.* Stacking-Dependent Band Gap and Quantum Transport in Trilayer Graphene. *Nat. Phys.* **7**, 948–952 (2011).

80. Kharitonov, M. Edge Excitations of the Canted Antiferromagnetic Phase of the ν=0 Quantum Hall State in Graphene: A Simplified Analysis. *Phys. Rev. B* **86**, 075450 (2012).

81. Kharitonov, M. Antiferromagnetic State in Bilayer Graphene. *Phys. Rev. B* **86** (2012).

82. Velasco, J. *et al.* Competing Ordered States with Filling Factor Two in Bilayer Graphene. *Nat. Commun.* **5**, 4550 (2014).

83. Geisenhof, F. R. *et al.* Quantum Anomalous Hall Octet Driven by Orbital Magnetism in Bilayer Graphene. *Nature* **598**, 53–58 (2021).

84. Shi, Y. *et al.* Energy Gaps and Layer Polarization of Integer and Fractional Quantum Hall States in Bilayer Graphene. *Phys. Rev. Lett.* **116**, 056601 (2016).

85. Hunt, B. M. *et al.* Direct Measurement of Discrete Valley and Orbital Quantum Numbers in Bilayer Graphene. *Nat. Commun.* **8**, 948 (2017).

86. Maher, P. *et al.* Bilayer Graphene. Tunable Fractional Quantum Hall Phases in Bilayer Graphene. *Science* **345**, 61–64 (2014).

87. Li, J. *et al.* Metallic Phase and Temperature Dependence of the ν=0 Quantum Hall State in Bilayer Graphene. *Phys. Rev. Lett.* **122**, 097701 (2019).

88. Jiang, L. *et al.* Manipulation of Domain-Wall Solitons in Bi- and Trilayer Graphene. *Nat. Nanotech.* **13**, 204–208 (2018).

89. Zhang, F., MacDonald, A. H. & Mele, E. J. Valley Chern Numbers and Boundary Modes in Gapped Bilayer Graphene. *Proc. Natl. Acad. Sci. U.S.A.* **110**, 10546–10551 (2013).

90. Wang, Z., Cheng, S., Liu, X. & Jiang, H. Topological Kink States in Graphene. *Nanotechnology* **32**, 402001 (2021).

91. Qiao, Z., Jung, J., Niu, Q., MacDonald, A. H. & MacDonald, A. H. Electronic Highways in Bilayer Graphene. *Nano Lett.* **11**, 3453–3459 (2011).

92. Li, J. *et al.* A Valley Valve and Electron Beam Splitter. *Science* **362**, 1149–1152 (2018).

93. Chen, H. *et al.* Gate Controlled Valley Polarizer in Bilayer Graphene. *Nat. Commun.* **11**, 1202 (2020).

94. Geisenhof, F. R. *et al.* Interplay between Topological Valley and Quantum Hall Edge Transport. *Nat. Commun.* **13**, 4187 (2022).

95. Keilmann, F. & Hillenbrand, R. *Near-Field Nanoscopy by Elastic Light Scattering from a Tip,* in *Nano-Optics and Near-Field Optical Microscopy*. Zayats, A.; Richards, D., eds. (Artech House, Boston, London, 2009).

96. Abbe, E. Beiträge zur Theorie des Mikroskops und der Mikroskopischen Wahrnehmung. *Archiv f. mikrosk. Anatomie* **9**, 413–468 (1873).

97. Meyer, E. *Scanning Probe Microscopy. The Lab on a Tip* (Springer, Berlin, Heidelberg, 2004).

98. Binnig, Quate & Gerber. Atomic Force Microscope. *Phys. Rev. Lett.* **56**, 930–933 (1986).

99. Knoll, B. & Keilmann, F. Enhanced Dielectric Contrast in Scattering-Type Scanning Near-Field Optical Microscopy. *Opt. Commun.* **182**, 321–328 (2000).

100. Jackson, J. D., Witte, C. & Diestelhorst, M. *Klassische Elektrodynamik.* 5th ed. (De Gruyter, Berlin, Boston, 2014).

101. Cvitkovic, A., Ocelic, N. & Hillenbrand, R. Analytical Model for Quantitative Prediction of Material Contrasts in Scattering-Type Near-Field Optical Microscopy. *Opt. Express* **15**, 8550–8565 (2007).

102. Renger, J., Grafström, S., Eng, L. M. & Hillenbrand, R. Resonant Light Scattering by Near-Field-Induced Phonon Polaritons. *Phys. Rev. B* **71**, 075410 (2005).

103. Ni, G. X. *et al.* Fundamental Limits to Graphene Plasmonics. *Nature* **557**, 530–533 (2018).

104. Kim, D. S. *et al.* Stacking Structures of Few-Layer Graphene Revealed by Phase-Sensitive Infrared Nanoscopy. *ACS Nano* **9**, 6765–6773 (2015).

105. Basov, D. N., Fogler, M. M. & García de Abajo, F. J. Polaritons in van der Waals Materials. *Science* **354** (2016).

106. Low, T. *et al.* Polaritons in Layered Two-Dimensional Materials. *Nat. Mater.* **16**, 182–194 (2017).

107. Fei, Z. *et al.* Gate-Tuning of Graphene Plasmons Revealed by Infrared Nano-Imaging. *Nature* **487**, 82–85 (2012).

108. Chen, J. *et al.* Optical Nano-Imaging of Gate-Tunable Graphene Plasmons. *Nature* **487**, 77–81 (2012).

109. Schwierz, F. Graphene Transistors. *Nat. Nanotechnol.* **5**, 487–496 (2010).

110. Li, H. *et al.* Rapid and Reliable Thickness Identification of Two-Dimensional Nanosheets Using Optical Microscopy. *ACS Nano* **7**, 10344–10353 (2013).

111. Ocelic, N., Huber, A. & Hillenbrand, R. Pseudoheterodyne Detection for Background-Free Near-Field Spectroscopy. *Appl. Phys. Lett.* **89**, 101124 (2006).

112. Winterer, F. *Spontaneous Symmetry-Breaking in Trilayer Graphene. Dissertation* (Ludwig-Maximilians-Universität München, 2021).

113. Tenasini, G. *et al.* Giant Anomalous Hall Effect in Quasi-Two-Dimensional Layered Antiferromagnet $Co_{1/3}NbS_2$. *Phys. Rev. Res.* **2**, 023051 (2020).

114. Zhao, Y.-F. *et al.* Tuning the Chern Number in Quantum Anomalous Hall Insulators. *Nature* **588**, 419–423 (2020).

115. Polshyn, H. *et al.* Electrical Switching of Magnetic Order in an Orbital Chern Insulator. *Nature* **588**, 66–70 (2020).

116. Tschirhart, C. L. *et al.* Imaging Orbital Ferromagnetism in a Moiré Chern Insulator. *Science* **372**, 1323–1327 (2021).

117. Chen, G. *et al.* Tunable Correlated Chern Insulator and Ferromagnetism in a Moiré Superlattice. *Nature* **579**, 56–61 (2020).

118. Wang, L. *et al.* One-Dimensional Electrical Contact to a Two-Dimensional Material. *Science* **342**, 614–617 (2013).

119. Ki, D.-K., Fal'ko, V. I., Abanin, D. A. & Morpurgo, A. F. Observation of Even Denominator Fractional Quantum Hall Effect in Suspended Bilayer Graphene. *Nano Lett.* **14**, 2135–2139 (2014).

120. Freitag, F., Weiss, M., Maurand, R., Trbovic, J. & Schönenberger, C. Homogeneity of Bilayer Graphene. *Solid State Commun.* **152**, 2053–2057 (2012).

121. Lian, B., Sun, X.-Q., Vaezi, A., Qi, X.-L. & Zhang, S.-C. Topological Quantum Computation Based on Chiral Majorana Fermions. *Proc. Natl. Acad. Sci. U.S.A.* **115**, 10938–10942 (2018).

122. Geisenhof, F. R. *et al.* Anisotropic Strain-Induced Soliton Movement Changes Stacking Order and Band Structure of Graphene Multilayers. Implications for Charge Transport. *ACS Appl. Nano Mater.* **2**, 6067–6075 (2019).

123. Winterer, F., Geisenhof, F. R., Seiler, A. M., Zhang, F. & Weitz, R. T. Tunable Quantum Anomalous Hall States in Suspended Rhombohedral Trilayer Graphene. In preparation (2022).

124. Zarenia, M., Pereira, J. M., Farias, G. A. & Peeters, F. M. Chiral States in Bilayer Graphene: Magnetic Field Dependence and Gap Opening. *Phys. Rev. B* **84**, 125451 (2011).

125. Sunku, S. S. *et al.* Photonic Crystals for Nano-Light in Moiré Graphene Superlattices. *Science* **362**, 1153–1156 (2018).

126. Huang, S. *et al.* Topologically Protected Helical States in Minimally Twisted Bilayer Graphene. *Phys. Rev. Lett.* **121**, 037702 (2018).

127. Kharitonov, M. Canted Antiferromagnetic Phase of the ν=0 Quantum Hall state in Bilayer Graphene. *Phys. Rev. Lett.* **109**, 046803 (2012).

128. Killi, M., Wei, T.-C., Affleck, I. & Paramekanti, A. Tunable Luttinger Liquid Physics in Biased Bilayer Graphene. *Phys. Rev. Lett.* **104**, 216406 (2010).

129. Mazo, V., Shimshoni, E., Huang, C.-W., Carr, S. T. & Fertig, H. A. Helical Quantum Hall Edge Modes in Bilayer Graphene: a Realization of Quantum Spin-Ladders. *Phys. Scr.* **T165**, 014019 (2015).

130. Bockrath, M. *et al.* Luttinger-Liquid Behaviour in Carbon Nanotubes. *Nature* **397**, 598–601 (1999).

131. Yang, G. *et al.* Possible Luttinger Liquid Behavior of Edge Transport in Monolayer Transition Metal Dichalcogenide Crystals. *Nat. Commun.* **11**, 659 (2020).

132. Jiang, L., Wang, S., Zhao, S., Crommie, M. & Wang, F. Soliton-Dependent Electronic Transport across Bilayer Graphene Domain Wall. *Nano Lett.* **20**, 5936–5942 (2020).

133. Geisenhof, F. R. *et al.* Impact of Electric Field Disorder on Broken-Symmetry States in Ultraclean Bilayer Graphene. *Nano Lett.* **22**, 7378–7385 (2022).

134. San-Jose, P., Gorbachev, R. V., Geim, A. K., Novoselov, K. S. & Guinea, F. Stacking Boundaries and Transport in Bilayer Graphene. *Nano Lett.* **14**, 2052–2057 (2014).

135. Abergel, D. S. L., Min, H., Hwang, E. H. & Das Sarma, S. *dμ/dn* in Suspended Bilayer Graphene: The Interplay of Disorder and Band Gap. *Phys. Rev. B* **84**, 195423 (2011).

136. Rutter, G. M. *et al.* Microscopic Polarization in Bilayer Graphene. *Nat. Phys.* **7**, 649–655 (2011).

Danksagung

Ich möchte an dieser Stelle allen meinen herzlichen Dank aussprechen, die mich während meiner Promotion begleitet und unterstützt haben. Ohne euch wäre diese Arbeit nicht möglich gewesen. Lieber Thomas Weitz, ich möchte mich für deine herausragende Betreuung und immerwährende Unterstützung bedanken. Vielen Dank für die zahlreichen guten Diskussionen und deinen richtig liegenden Instinkt. Besonders geschätzt habe ich die Möglichkeit, jederzeit zu dir kommen zu können, ganz egal um was für ein Problem es sich handelte. Danke auch für deine ständige Zuversicht. Man würde kaum meinen, dass in dem schon seit mehr als einer Dekade untersuchtem Bilagen Graphen noch so viele spannende Dinge zu entdecken sind.

Von ganzem Herzen möchte ich mich bei meinen Kollegen und insbesondere Felix Winterer, Jakob Lenz, Lisa Walter, Anna Seiler, Lucca Kühner und Fabio del Giudice bedanken. Jeder von Euch hat maßgeblich zum Erfolg der Arbeit und zu einer unvergesslichen Zeit beigetragen. Felix, erst deine außerordentlich gute Betreuung in meiner Masterarbeit, dann deine unglaubliche Unterstützung als Doktorandenkollege. Deine konstruktiv kritische Denkweise, deine offene Art und die Tatsache, dass du dir jederzeit für einen Zeit nimmst und hilfst, schätze ich sehr. Vielen Dank dafür. Jakob, am meisten danke ich dir für dein offenes Ohr, du hast mir immer zugehört, egal um was es ging. Auch deine perfekte Beherrschung aller Geräte insbesondere im Reinraum, hat mich oft vorangebracht. Lisa, deine immerwährende gute Laune und Hilfsbereitschaft haben mir oft geholfen Motivation zu finden. Dein Mut, Probleme anzusprechen und deine gute Strukturierung haben definitiv zum Erfolg der Gruppe beigetragen. Anna, danke, dass du mir vor allem gegen Ende oft zugehört und mit mir sehr konstruktive Diskussionen geführt hast. Deine Unterstützung in vielen kleinen und großen Dingen hat mir sehr geholfen. Lucca, auch wenn du nur knapp ein Jahr bei uns in der Gruppe warst, die Diskussionen mit dir und zahlreichen Mittagessen im „Sarovar“ haben mir immer besonders Freude bereitet. Ein gemeinsames Wehklagen über doch ähnliche Probleme hat mir Mut gegeben. Fabio, danke für die vielen pointenreichen und philosophischen Diskussionen. Das hat meine Zeit am Anfang besonders bereichert.

Vielen Dank auch an Daniela Priesack, Stefan Wakolbinger, Maurice Larsson, Marco Dembecki, Francesca Falorsi und Jakob Riedel, die ich (teilweise) betreuen durfte. Ich hoffe ihr konntet etwas

von mir lernen. Ihr habt mir auf jeden Fall viel beigebracht, über physikalische Themen, Zusammenarbeit und Betreuung, aber auch über mich selbst.

Darüber hinaus möchte ich mich bei Noelia Fernández für die guten Diskussionen, bei Christian Eckel und Lukas Renn für die tatkräftige Unterstützung in vielen Angelegenheiten, bei Gilles Rodway-Gant für die philosophischen Gespräche zu Wortneuerfindungen, bei Maximilian Kögl für die mitreißende, motivierende Art und bei Lilian Schaffroth für inspirierende Gespräche über Geheimnisse bedanken. Ebenso gilt mein Dank allen gegenwärtigen und ehemaligen Mitgliedern der Gruppe, die bisher noch unerwähnt geblieben sind, insbesondere James Borchert, Martin Statz, Jonas Pöhls, Monica Kolek Martinez de Azagra, Jonas Schröder, Lucas Hille, Xin Huang, Patrick Ganswindt, Theresa Kammerbauer, Daniel Vitroler, Michael Hirler, Juri Crimmann, Jonas Biechteler, Jakob Braun, Florin Walter, Stefan Seebauer, Rayner Schelwald und Philipp Maier. Diese Arbeit wäre ohne die exzellente Teamarbeit, die in der AG Weitz immer großgeschrieben wurde, nicht möglich gewesen.

Außerdem möchte ich mir bei Tianyi Xu, Fan Zhang und Ivar Martin für die erfolgreiche Zusammenarbeit bedanken. Fan und Ivar, vielen Dank für eure Hingabe mir die doch recht komplexen theoretischen Zusammenhänge zu erklären und für eure Geduld, auch jede noch so triviale Frage von mir zu beantworten. Vielen Dank auch an Fritz Keilmann, Yasin Celaleddin Durmaz und Tobias Gokus bei der tatkräftigen Unterstützung in Bezug auf das Nahfeldmikroskop. Ohne eure Hilfe hätten die Messungen nie so gut funktioniert.

Zudem möchte mich auch für die hervorragende Unterstützung von vielen Personen der Universität bedanken. Vielen Dank an Bert Lorenz, Reinhold Rath und Anton Heindl für die Hilfe bei technischen Angelegenheiten und beim Aufbau der Labore. Liebe Martina Edenhofer, danke für die unglaubliche Hilfe bei aller Art von administrativen Aufgaben. Ein besonderer Dank geht an Stefan Manus, ohne dessen außerordentliche Kenntnisse und vielen lehrreichen Stunden hätten die sensiblen Messungen bis heute nicht funktioniert. Vielen Dank auch an Philipp Altpeter, Christian Obermayer und Charlott Leu, die bei unzähligen Problemen im Reinraum immer sofort zur Stelle waren.

Als letztes möchte ich mich noch bei meinen Freunden und meiner Familie bedanken, ohne sie wäre diese Arbeit nicht möglich gewesen. Insbesondere bei meinen Eltern, die mich immer bedingungslos unterstützt haben. Und natürlich bei Dara, danke, dass du für mich immer da bist, mich motivierst und an mich glaubst.